Analysis of the Structural and Optoelectronic Properties Of Semiconductor Materials and Devices Using Photoacoustic Spectroscopy and Synchrotron X-ray Topography

A Thesis Submitted in Partial Fulfillment of the
Requirements for the Degree of
Master of Engineering
(Electronic Engineering)

By
Donnacha Lowney
B.Eng., AMIEE, AMIEEE

School of Electronic Engineering
Faculty of Engineering and Design
Dublin City University

Research Supervisor
Dr. Patrick J. McNally
BE, ScM, PhD, CPhys, MInstP, CEng, MIEI, MIEEE

REFERENCE

April 2002

Declaration

I hereby certify that this material, which I now submit for assessment on the programme of study leading to the award of Master of Engineering is entirely my own work and has not been taken from the work of others save and to the extent that such work has been cited and acknowledged within the text of my work.

Signed: Donnacha Lowney Date: 24/4/2002

Acknowledgments

I'd like to thank my research supervisor and colleague Dr. Patrick McNally for all his support and advice over the duration of this thesis. Without his guidance and encouragement, this work would have invariably been a lot more difficult.

I would also like to thank Professor Charles McCorkell and Mr. Jim Dowling for their support in relation to all aspects of my work in Dublin City University.

I would like to thank Professor Turrka Tuomi for all his assistance during my X-ray topography experiments. His assistance and precision in the interpretation of the experimental data has proved invaluable. I would also like to acknowledge the help provided by many of my colleagues during beamtime at HASYLAB: Dr. Reko Rantamäki, Dr. Andreas Danilewsky, Mr. Mark O'Hare, Mr. Weimin Chen and Ms. Jarujit Kanatharana. The topographic measurements would not have been possible without the help of the beamline scientists: Dr. Thomas Wroblewski and Dr. Karsten Paulmann at beamline F-1 HASYLAB, Dr. Dmitri Novikov at beamline BW-1 HASYLAB, Dr. Hermann Franz at beamline PETRA-1 HASYLAB and Dr. Jürgen Häertwig at beamline ID-19 ESRF.

Many of the topographic investigations would not have been possible without the provision of samples. To this end I would like to thank Dr. Peter Becker for the silicon samples used in the Avogadro project, Professor Arthur Willoughby and Dr. Gabriela Dilliway for the silicon germanium hetero-structures, Dr. Tony Herbert for the ultra bright light emitting diodes, Dr. Tania Perova and Dr. Martina Nolan for the rapid thermally processed silicon samples and the accompanying micro-Raman data, and finally, Dr. Koen Jacobs and Dr. Laurence Considine for the gallium nitride samples.

The design and construction of the photoacoustic spectrometer was made easier by Professor Michael Slifkin of Jerusalem College of Technology, Israel who facilitated a visit to his laboratory. Without the knowledge gained from this short visit, the minute but important details concerning the design and construction of a photoacoustic spec-

trometer would never have been learned. I would like to thank Professor Vladimir Sandomirsky of Bar'Ilan University, Israel, for taking the time to answer my questions on the theoretical aspects of the photoacoustic effect in condensed matter samples.

I am very grateful to the technicians Conor Maguire, Robert Clare, John Whelan, Liam Meany, Paul Wogan and Theresa Collins for assisting me in various aspects of my work in Dublin City University. I would also like to thank the staff of the Mechanical Workshop, in particular Martin Johnson, for providing their expertise in the construction of the photoacoustic cell.

Although not a major influence in the results of this thesis, I would like to thank Dr. Bernhard Adams for introducing me to the fields of non-linear and ultrafast X-ray optics. My understanding of the dynamical theory of X-ray diffraction has significantly increased as a result of our discussions. I have also learned numerous experimental "tricks" from our collaborations.

Finally, the support of my family and friends cannot be underestimated. Mam, Dad, Fintan, Eilish, Ronan and all the warriors in the Aer Lingus diving club, Thanks!

Donnacha Lowney, April 2002.

Dedication

For a total of one year
and six months of her life
my mother was walking around
with either me or Fintan inside her.

Thanks Ma.

Adapted from "A Heavy Lot of Us" by Pat Ingoldsby

N'fheadar fós
an ar madin
nó an tráthnóna
a chonac ann é
ina sheasamh
leis an ngeta
bhi aimsir an dúluachair
ag teacht nó ag imeacht unainn
nó cuimhin liom
i ndáiríré
is nach taibhreamh
a d'fhan im' cheann
ach pé rud eile de
bhí se fuar fuar fuar fuar
bhí scáilí fada dorcha
is grian mhílítheach bhán
agus is ag imeacht
a bhí sé sin
mar ina dhiadh sin
ní raibh sé ann
is bhí mé a dó
nuar a tharla seo
nó a trí
ar an gcuid is mó
is níl a fhios agam
ach gur cuimhin liom
m'athair ag fágaint baile
maidin i mí Feabhra
nó tráthnóna sa bhfómhar

Adapted from "Athair" by Nuala Ní Dhomhaill

Abstract

Analysis of the Structural and Optoelectronic Properties Of Semiconductor Materials and Devices Using Photoacoustic Spectroscopy and Synchrotron X-ray Topography

Donnacha Lowney, *B.Eng.*, *AMIEE*, *AMIEEE*

This thesis deals with the characterisation of semiconductor materials and devices through two complimentary experimental modalities. Synchrotron X-ray topography and photoacoustic spectroscopy are rapid, non-destructive and non-invasive techniques. The former may be used to elucidate the strain within a crystalline material due to localised structural defects causing deviations in the recorded X-ray intensity; whilst the latter can indirectly probe the non-radiative de-excitation processes within the bandstructure by measuring pressure variations within the gas in contact with the sample.

In the first half of this work, a review of the theoretical description of the photoacoustic effect in condensed matter samples is presented. This classical review is extended to encompass the photoacoustic effect in semiconductor materials. Criteria governing the design of a spectrometer are then extracted. A photoacoustic spectrometer based on the gas-microphone technique, with a wide spectral range (0.5 eV to 6.2 eV) was designed and constructed. The spectrometer was characterised across its spectral range using common semiconductor materials.

The latter half of the thesis commences with a review of the kinematical and dynamical theories of X-ray diffraction. The properties of synchrotron radiation are discussed, with particular focus on their applicability to X-ray topography. The large area, section and grazing incidence topography techniques are presented. Several topographic studies of semiconductor materials and devices were performed. These included an analysis of the evolution of strain in ultra-bright light emitting diodes under varying degrees of electrical stress, strain induced by the epitaxial lateral overgrowth of gallium nitride on sapphire, stress due to rapid thermal processing of silicon wafers, characterisation of diamond crystals for use in a high energy monochromator, misfit dislocation generation at a Si/SiGe heterointerface and dynamical imaging of microdefects in nearly perfect silicon.

Contents

List of Tables

List of Figures

Chapter 1

Introduction and Overview

1.1 Introduction

Few could argue with the assertion that we live longer, healthier, more productive lives as a result of the microelectronics revolution that has taken place in the past fifty years. Advances in the microelectronics industry have been underpinned by improvements in the quality of the constituent device materials. Consider for example silicon: in the 1970s the dislocation density was of the order of 10^3 cm^{-2}, and today, defect free wafers with a diameter of fifteen inches are being used in the production of microprocessors [1]. Characterisation and understanding of defects within semiconductor materials is necessary if device performance is to be enhanced. The structural and optoelectronic properties of a material are interrelated and thus neither can be examined in isolation of the other. Of particular importance is the influence of structural defects on the optoelectronic properties of the material, as these are known to affect carrier diffusion lengths, radiative and non-radiative recombination processes.

In this thesis, two complementary non-destructive techniques will be used for the analysis of the optoelectronic and structural properties of common semiconductor materials

and devices. Photoacoustic spectroscopy is a non-invasive photocalorimetric technique that can probe the non-radiative thermal de-excitation channels of a sample and hence complements absorption and other spectroscopic methods [2]. Only light absorbed within the sample can generate a photoacoustic response and thus, this highly sensitive technique is not influenced by elastic scattering or transmission of light through the sample. Photoacoustic spectroscopy can be used to measure amongst others, the absorption spectrum, lifetime of photo-excited species and thermal properties of a sample. Synchrotron X-ray topography is a unique tool for the investigation of strain in semiconductor materials [3]. It is non-destructive but penetrating, sensitive to small defects and lattice orientations, possesses high spatial resolution and relatively large samples can be studied within a reasonable time. X-ray topography is mainly used for the study of strain, dislocations, planar defects, stacking faults, domain walls in ferroelectric and magnetic materials, growth defects or large precipitates.

1.2 Historical Overview

The photoacoustic effect was first reported in 1880 by Alexander Graham Bell in a report to the American Association for the Advancement of Science [4]. This report was primarily concerned with his work on the photo-phone; a device comprised of a voice-activated mirror, a selenium cell and an electrical telephone receiver. Bell observed that the electrical resistance of the selenium cell was dependent upon the intensity of the incident light. This work was further extended in 1881 when Bell detected an audible signal induced by intensity modulated light shone onto a diaphragm shaped

solid connected to a hearing tube [4]. Bell determined that the strength of the acoustic signal was dependent on the amount of light absorbed per unit time. These empirical results have been shown to be valid within the context of contemporary photoacoustic theories, making them all the more remarkable considering that the detector was the experimenter's ear.

After the work of Bell, the photoacoustic effect was largely ignored until this century because the technical equipment, such as phase sensitive amplifiers and microphones, necessary to obtain accurate results did not exist. The first theoretical description of the photoacoustic effect in non-gaseous samples was made by Parker [5] in 1973. This was quickly followed by the experimental and theoretical work of Rosencwaig and Gersho in 1976 [6]. Several classical extensions were made to this theory [7–9] before the first semi-classical description of the photoacoustic effect in semiconductors was formulated by Bandeira, Closs and Ghizoni in 1982 [10]. Essentially these theories describe how light absorbed in a sample following non-radiative de-excitation processes gives rise to a heat source in the sample that may be distributed throughout the sample volume or confined to its surface. This heat source generates both temperature and pressure fluctuations within the sample, which in turn induce measurable pressure variations within the gas in contact with the sample.

Research into X-ray radiation and its applications commenced about the same time Bell was investigating the photoacoustic effect, with the discovery of X-rays in 1895 by Röntgen [11]. Bells work was obviously familiar to Röntgen as he also performed experiments with spectrophones [4]. A similar time lag was present between the dis-

covery of X-rays and their application to the study of materials by diffraction methods. Von Laue, Friedrich and Knipping initiated the first experiments in this field when they recorded diffraction patterns from rock salt [12]. The theory of X-ray diffraction preceded that of the photoacoustic effect by approximately fifty years. Bragg, Von Laue, Darwin [13, 14] and Ewald [15] laid the theoretical foundations between 1911 and 1917. Contemporary theories of X-ray diffraction were developed by Lang, Authier [16], Takagi [17], Taupin and Kato [18]. A hierarchical summary of these may be found in [19].

Approximately twenty years after X-ray diffraction studies commenced the first X-ray diffraction topographs were recorded [20]. The original papers appear to have been published in 1931 when Berg [21] initiated studies on crystal perfection. With the advent of Lang topography images of individual dislocations were observed [22]. This method was complimented by the introduction of other topography techniques by Bonse and Klapper [23].

In 1974, Tuomi, Naukkarinen and Rabe [24] showed that synchrotron radiation could be applied to the study of materials using X-ray diffraction topography. Hart [25] subsequently showed that this method could be used for high-resolution imaging. This led to a major revolution in the type of experiment that could be performed and the nature of the data gathered. For example, long exposure times associated with monochromatic rotating anode experiments were replaced with a white beam source that could expose samples in seconds with the added benefit of multiple reflections.

1.3 Motivation and Thesis Aims

The desire to produce faster, less power consuming microelectronic devices has been the impetus behind the ongoing decrease in critical dimensions and increasing integration levels in current CMOS technology. With the advent of 0.18 μm technology, copper metallisation and 300 mm wafers, the semiconductor industry is continually seeking semiconductor materials with minimal defect densities. The performance of these materials *vis-á-vis* their structural and optoelectronic properties is directly attributable to the concentration of defects and their distribution. Hence the need for metrologic and diagnostic tools which are powerful and yet as comprehensive as possible, i.e. to characterise parameters critical to performance and yield, are non-destructive and can be applied readily to material qualification and process control.

The long-term goal, to which the work of this thesis ascribes to, is to determine the interrelationship between non-radiative de-excitation processes and structural defects in semiconductor materials. The principal tool used in the experimental investigations will be light: in the X-ray regime, the structural properties of the material can be probed and in the ultraviolet to infrared spectrum, the electronic bandstructure can be studied. Among characterisation methods, optical and X-ray techniques are unique in that, in general, they are contactless and non-destructive. This is crucial to the long-term focus of this work, as we want to investigate the influence of strain on the non-radiative de-excitation processes without altering the sample or its intrinsic stress.

Specifically, the focus of this thesis is on the applicability of the techniques photoa-

coustic spectroscopy and X-ray topography to such a study. As such, this is a thesis of two halves. In the first half, a photoacoustic spectrometer capable of spatial mapping for use in the photonic interval 0.5 eV to 6.2 eV is to be designed and constructed. This instrument will be utilised in the analysis of non-radiative de-excitation processes in narrow and wide bandgap semiconductors. The latter half of the thesis demonstrates the suitability of X-ray topography to the visualisation of stress in several contemporary semiconductor materials and devices. It is important to note that this thesis does not directly attempt to reveal any correlation between the structural defects and non-radiative recombination mechanisms, this is left for future investigations.

1.4 Thesis Organisation

The organisation of the thesis is as follows: Part I, consisting of Chapters 2 to 4, pertains to photoacoustic spectroscopy and Part II, comprising Chapter 5 to 13, deals with synchrotron X-ray topography. Part III provides conclusions from Parts I and II along with suggestions for future work that will serve to unite these currently disjoint subjects.

Chapter 2 reviews the main theories of the photoacoustic effect in condensed matter samples so the reader may understand the underlying physical mechanisms. Chapter 3 harnesses the results of these theories to extract a set of guidelines for the design of a photoacoustic spectrometer of the gas-microphone type. The calibration and characterisation of the spectrometer is the focus of Chapter 4, wherein photoacoustic investigations of silicon, gallium arsenide and gallium nitride are performed.

Part II of the thesis commences with a review of the kinematical and dynamical theories of X-ray diffraction in crystalline media. General properties of synchrotron radiation and their applicability to the techniques of X-ray diffraction topography are the focus of Chapters 6 and 7. The failure of light emitting diodes under increased levels of electrical stress is the theme of Chapter 8. Strain induced by the epitaxial lateral overgrowth of gallium nitride on sapphire is examined in Chapter 9. In Chapter 10 stress induced by rapid thermal processing of silicon wafers is investigated using X-ray topography. A good correlation is found with data obtained using micro-Raman spectroscopy. Synthetic diamond crystals are characterised in Chapter 11 for use in a high energy synchrotron monochromator. Stress relief in a silicon-silicon germanium heterostructure via misfit dislocation formation is examined using atomic force microscopy and grazing incidence diffraction topography in Chapter 12. The final topography study presented in Chapter 13 focuses on the imaging of microdefects in nearly perfect silicon.

In conclusion, Chapter 14 in Part III summarises the subject matter of the thesis and suggests future research directions.

PART I

Photoacoustic Spectroscopy

Chapter 2

Theory of the Photoacoustic Effect

2.1 Introduction

In the past thirty years, the photoacoustic effect has undergone something of a renaissance since its original discovery by Bell in 1880. This is largely attributable to the fact that the necessary experimental apparatus did not become available until *circa* 1970. The current renewed interest in photoacoustic studies appears to have started with the work of Kreuzer in 1971 [26]. Subsequently, much experimental and theoretical work has been reported in the literature to demonstrate not only spectroscopic applications, but also many other photoacoustic applications in the fields of physics, chemistry, materials science, biology, medicine and engineering. For a review of the applications of the photoacoustic effect the reader is referred to the excellent article by Tam [2].

The basic mechanism behind the photoacoustic effect is as follows. Intensity modulated monochromatic light is shone on a sample. Non-radiative de-excitation processes following light absorption consequently heat the sample. By convective processes, the sample in turn heats up the gas layer in the immediate vicinity of the point of light absorption. The modulated nature of the light induces corresponding pressure fluctu-

ations in the gas due to repetitive heating and cooling of the sample. These pressure fluctuations are detected in the case of indirect photoacoustic spectroscopy by a microphone and are called a photoacoustic signal. A photoacoustic spectrum may be obtained by determining the photoacoustic signal of the sample as a function of the wavelength and modulation frequency of the incident light. In the information of the signal, the optical and thermal properties of the sample play an important role.

In this chapter, the fundamental theories of the photoacoustic effect in condensed matter samples will be reviewed. The review aims to elucidate the underlying physical principles upon which each theory is based and to reap from this information a set of design criteria applicable to the spectrometer constructed in Chapter 3. The discussion of the theories is aspirational in some respects, as within the bounds of this thesis, it is not possible to investigate their every facet. To this end, we examine the original description as theorised by Rosencwaig and Gersho [6]. This theory is generally sufficient for interpretation of the bulk of experimental results. The failings of this theory and their implications on the design of a photoacoustic cell are highlighted through the analysis of the extended photoacoustic theories of McDonald *et. al* [7] and Korpiun *et. al* [8]. The theory of Bandeira, Closs and Ghizoni [10] accounts for the photoacoustic effect in semiconductor materials. Some theoretical and experimental procedures are interleaved to ascertain methods for the evaluation of the optical absorption coefficient and the bandgap energy of a semiconductor sample. The chapter concludes with an outline of some theoretical issues that need to be incorporated in a theory that relates the photoacoustic effect to structurally strained crystalline materials.

2.2 Theory of Rosencwaig and Gersho

The Rosencwaig Gersho theory is a relatively simple one-dimensional analysis of the production of a photoacoustic signal in a cylindrical cell. This theory, developed in the 1970s, is the cornerstone against which all experimental data is first evaluated [6, 27]. The theory will now be reformulated step by step for three reasons: (i) so that the reader may gain an insight into the essential physics surrounding the classical theory of the photoacoustic effect in condensed matter samples; (ii) it will make the discussion of the classical and semi-classical extensions to the theory easier to understand; and (iii) many of the design criteria for a photoacoustic spectrometer are implicitly embedded in it.

Rosencwaig and Gersho [6] obtained an expression for the pressure variation in the gas column in contact with the sample by first modeling the heat flow within the sample, gas and baking materials due to incident monochromatic light. Applying the appropriate boundary conditions, yielded the periodic temperature distribution within the cell. They found that a thermally excitable region of the gas column in contact with the sample underwent periodic compression and expansion due to convective heating from the sample. This "acoustic piston" induces the periodic acoustic pressure variation within the gas column. Couched in the expression obtained for the pressure variation in the gas are details of the thermal diffusion coefficients, specific heats and densities of the sample, gas and backing materials. The expression is quite involved. However, with some physical insight into the sample, the expression may be simplified into six categories depending on the optical absorption coefficient and thermal diffusion length of

the sample. We will now formally outline the theory of Rosencwaig and Gersho.

2.2.1 Theoretical Assumptions

Consider the one-dimensional photoacoustic cell shown in Figure 2.1. A one dimensional treatment is valid for situations where the cell's extension in the y- and z-directions is much larger than in the x-direction. The following assumptions have been made with regard to the system:

1. The length of the cell L is far greater than the acoustic wavelength Λ_g in the gas.
2. The incident light is monochromatic and sinusoidally chopped.
3. The gas and backing material do not absorb light.
4. The backing material is a poor thermal conductor.
5. The system is adiabatic.
6. The window is assumed to be optically and thermally transparent.

The following parameters of the system will be met frequently in the analysis: thermal conductivity k, density ρ, specific heat C, thermal diffusitivity $\alpha = k/\rho C$, chopping frequency ω, thermal diffusion coefficient $a = (\omega/2\alpha)^{0.5}$ and the thermal diffusion length $\mu = 1/a$. Where necessary, the parameter for a given material will be identified by the subscript s, g or b for the sample, gas or backing material, respectively. As the thermal diffusion length has a $\omega^{-0.5}$ dependence, by varying the modulation frequency

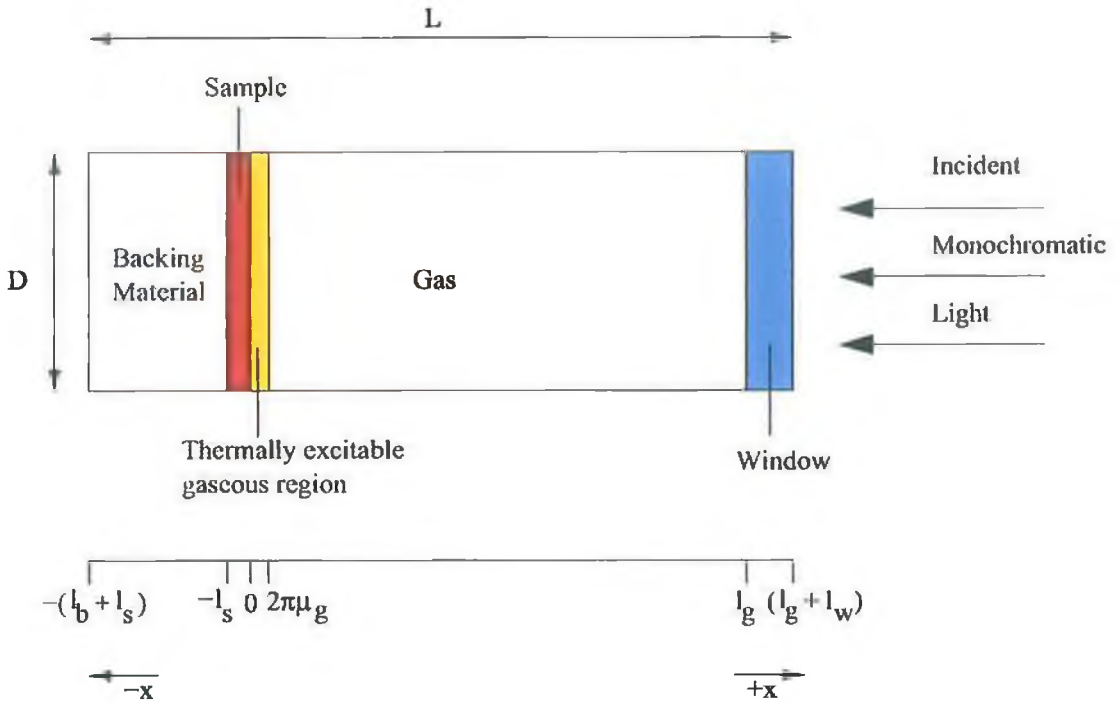

Figure 2.1: Schematic of one-dimensional photoacoustic cell. Shown in the gas column is the "thermal piston" that is formed following light absorption in the solid.

one can probe information from different thermal depths within the sample. Hence photoacoustic spectroscopy can be used for depth profiling studies.

2.2.2 Heat Diffusion Equations

The intensity of monochromatic light incident on the sample, modulated at frequency ω, with wavelength λ, and light flux I_0 is

$$I = \frac{I_0}{2}(1 + \cos \omega t) \tag{2.1}$$

Let β denote the optical absorption coefficient of the sample. Therefore, assuming purely classical analysis, i.e. in the case of semiconductor carrier diffusion and recombination being neglected, the density of heat generation at any point x in the sample due to the light absorbed is given by

$$H(x,t) = \frac{\beta I_0 e^{\beta x}}{2}(1+\cos\omega t) \tag{2.2}$$

By incorporating the effect of the distributed heat source due to the incident light into the one-dimensional heat equation the thermal diffusion in the sample can be described as follows:

$$\frac{\partial^2\phi(x,t)}{\partial x^2} = \frac{1}{\alpha_s}\frac{\partial\phi(x,t)}{\partial x} - Ae^{\beta x}\left(1+e^{j\omega t}\right) \quad ; \quad -l_s \le x \le 0 \tag{2.3}$$

where $\phi(x,t)$ is the spatially and temporally dependent temperature,

$$A = \frac{\beta I_0 \eta}{2k_s} \tag{2.4}$$

and η is the efficency with which light absorbed, of wavelength λ, is converted to heat by non-radiative de-excitation processes. $\eta = 1$ is a good approximation for solids at room temperature.

Applying assumption (3) facilitates a description of the thermal diffusion in the gas

and backing materials:

$$\frac{\partial^2\phi(x,t)}{\partial x^2} = \frac{1}{\alpha_g}\frac{\partial\phi(x,t)}{\partial x} \quad ; \quad -(l_b+l_s) \le x \le -l_s \tag{2.5}$$

$$\frac{\partial^2\phi(x,t)}{\partial x^2} = \frac{1}{\alpha_b}\frac{\partial\phi(x,t)}{\partial x} \quad ; \quad 0 \le x \le l_b \tag{2.6}$$

Solving the heat equations for the temperature distribution in the cell yields:

$$\phi(x,t) = \begin{cases} \frac{1}{l_b}(x+l+l_b)\,W_0 + We^{\sigma_b(x+l)}e^{j\omega t} & ; \quad -(l_s+l_b) \le x \le -l_s \\ e_1 + e_2 x + de^{\beta x} + \left(Ue^{\sigma_s x} + Ve^{-\sigma_s x} - Ee^{\beta x}\right)e^{j\omega t} & ; \quad -l_s \le x \le 0 \\ \frac{l_g - x}{l_g}\theta_0 + \theta e^{-\sigma_g x}e^{j\omega t} & ; \quad 0 \le x \le l_g \end{cases} \tag{2.7}$$

where $\sigma_i = (1+j)\,a_i$, $i \in \{s,b,g\}$, $W_0 \in \mathfrak{Re}$ is the time independent component of the temperature relative to the ambient temperature φ_0 at $x = -l_s$, $W \in \mathfrak{C}$ is the periodic component of the temperature at $x = -l_s$, $\theta_0 \in \mathfrak{Re}$ is the time independent component of the temperature relative to φ_0 at $x = 0$, $\theta \in \mathfrak{C}$ is the time dependent component of the temperature at $x = 0$,

$$d = \frac{I_0}{2\beta k_s}$$

and

$$E = \frac{\beta I_0}{2k_s\left(\beta^2 - \sigma_s^2\right)}$$

2.2.3 Temperature at Sample-Gas Interface

The real part of the thermal diffusion in the sample defines the temperature in the cell relative to the ambient.

$$\Rightarrow T(x,t) = \Re\mathrm{e}\{\phi(x,t)\} + \varphi_0 \tag{2.8}$$

We now want to solve for the θ term in Equation (2.7) since this is the time dependent temperature at the sample-gas interface. Applying the following temperature continuity and flux boundary conditions to $\theta(x,t)$:

$$\phi_g(0,t) = \phi_s(0,t) \tag{2.9}$$

$$k_g \frac{\partial \phi_g(0,t)}{\partial x} = k_s \frac{\partial \phi_s(0,t)}{\partial x} \tag{2.10}$$

$$\phi_b(-l_s,t) = \phi_s(-l_s,t) \tag{2.11}$$

$$k_b \frac{\partial \phi_b(-l_s,t)}{\partial x} = k_s \frac{\partial \phi_s(-l_s,t)}{\partial x} \tag{2.12}$$

yields:

$$\phi = U + V - E \tag{2.13}$$

$$W_0 = e_1 - l_s e_2 + de^{-l_s x} \tag{2.14}$$

$$\phi_0 = e_1 + d \tag{2.15}$$

$$W = Ue^{-l_s\sigma_s} + Ve^{l_s\sigma_s} - Ee^{-l_s\beta} \tag{2.16}$$

$$\frac{-k_g\theta_0}{l_g} = (e_2 + \beta d)\, k_s \tag{2.17}$$

$$\frac{k_b W_0}{l_b} = \left(e_2 + \beta d e^{-l_s\beta}\right) k_s \tag{2.18}$$

$$-k_g\sigma_g\theta = k_s\left(\sigma_s U - \sigma_s V - \beta E\right) \tag{2.19}$$

$$k_b\sigma_b W = k_s\left(\sigma_s U e^{-l_s\sigma_s} - \sigma_s V e^{l_s\sigma_s} - \beta E e^{-l_s\beta}\right) \tag{2.20}$$

Defining

$$r = \frac{\beta}{\sigma_s} \quad , \quad b = \frac{k_b\sigma_b}{k_s\sigma_s} \quad , \quad g = \frac{k_g\sigma_g}{k_s\sigma_s}$$

and solving equations (2.13) to (2.20) for θ yields:

$$\theta = \frac{\beta I_0}{2k_s\left(\beta^2 - \sigma_s\right)}\left[\frac{(r-1)(b+1)e^{l_s\sigma_s} - (r+1)(b-1)e^{-l_s\sigma_s} + 2(b-r)e^{-\beta l_s}}{(g+1)(b+1)e^{l_s\sigma_s} - (g-1)(b-1)e^{-l_s\sigma_s}}\right] \tag{2.21}$$

One would naturally conceive that there is a phase relationship between the incident exciting photons and the resulting temperature variation in the sample. It is therefore no surprise that θ is a complex valued function that may be expressed in terms of its real and imaginary components as follows:

$$\theta = \theta_1 + j\theta_2 \tag{2.22}$$

The temperature at the solid-gas interface may now be written as

$$T(0,t) = \varphi_0 + \theta_0 + \theta_1\cos\omega t - \theta_2\sin\omega t \tag{2.23}$$

2.2.4 The Acoustic Piston

Having derived an expression for the temperature at the solid-gas interface, Rosencwaig and Gersho proceeded to describe the production of the acoustic signal. Investigation of the temperature distribution in the gas column in Equation (2.7), shows that it is composed of temporally dependent and independent components. The time varying component is responsible for the creation of the pressure fluctuations in the gas and therefore, the time independent component may be neglected.

$$\phi_{g_{ac}}(x,t) = \theta e^{-\sigma_g x} e^{j\omega t} \tag{2.24}$$

The actual temperature variation in the cell is $T_{ac}(x,t) = \Re\mathrm{e}\{\phi_{g_{ac}}(x,t)\}$.

$$T_{ac}(x,t) = e^{-a_g x}\left[\theta_1 \cos\left(\omega t - a_g x\right) - \theta_2 \sin\left(\omega t - a_g x\right)\right] \tag{2.25}$$

Plotting Equation (2.25) for various different phases one can see that the time dependent component is almost fully damped out at a distance $x = 2\pi\mu_g$ from the sample-gas interface as shown in Figure 2.2. Therefore, one can define a boundary length in the gas that is thermally excitable by the sample. It is this region of the gas, wherein periodic expansion and contraction takes place, termed the "acoustic piston", that acts on the rest of the gas column producing an acoustic wave that travels the entire length of the gas column. The acoustic piston length as a function of frequency is shown in Figure 2.3. This has important ramifications for the design of an acoustic cell. In

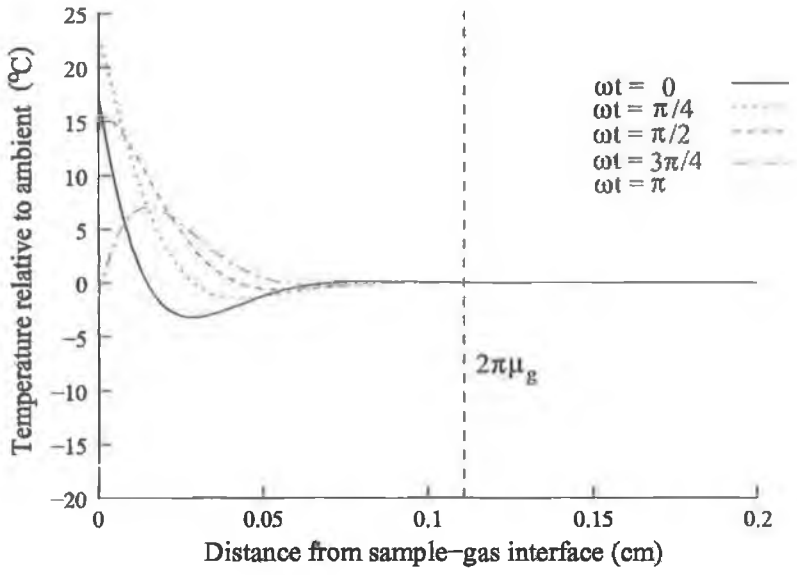

Figure 2.2: Spatial distribution of the time-dependent temperature within the gas layer adjacent to the solid surface for a 0.5 mm thick silicon sample, backing material aluminum and gas air. The incident light, modulated at 100 Hz, is provided by a 300 W arc lamp.

particular, the gas column length should be longer than the thermal diffusion length of the gas [28].

2.2.5 Pressure Variation in Gas Column

The spatially averaged temperature of the gas within the acoustic length is found by obtaining the spatial mean of Equation (2.24) as follows:

$$\overline{\phi_g(t)} = \frac{1}{2\pi\mu_g}\int_0^{2\pi\mu_g} \phi_{g_{ac}}(x,t)dx \tag{2.26}$$

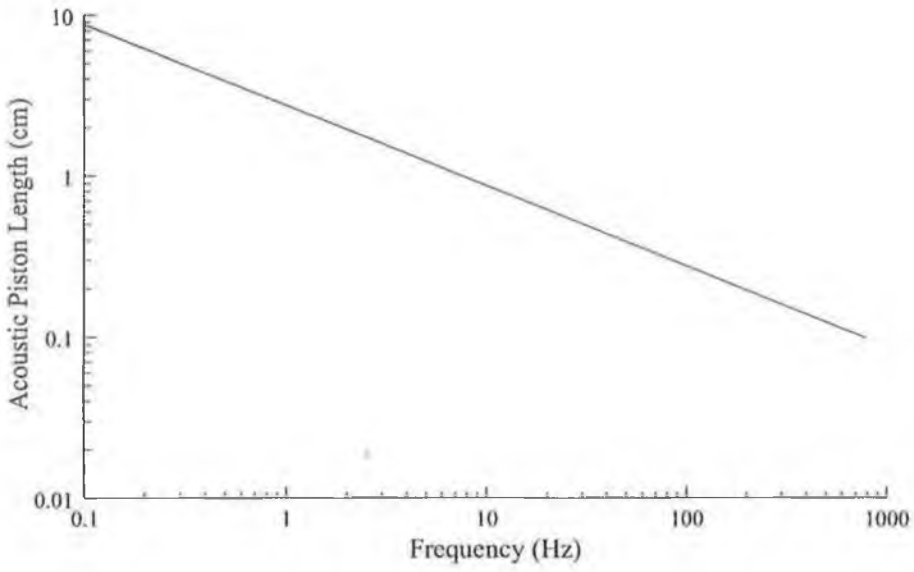

Figure 2.3: Acoustic piston length as a function of modulation frequency for an air gas column.

Using the approximation $e^{-2\pi} << 1$ yields:

$$\overline{\phi_g(t)} \approx \frac{1}{2\sqrt{2}\pi}\theta e^{j(\omega t - \pi/4)} \tag{2.27}$$

As the system is assumed to be adiabatic, the ideal gas law may be applied:

$$PV^{\gamma} = \text{constant} \tag{2.28}$$

where γ is the ratio of the molar specific heats at constant pressure and volume. The incremental pressure due to the action of the acoustic piston may be found through the following:

$$\ln\left(PV^{\gamma}\right) = \ln P + \gamma \ln V = \text{constant} \tag{2.29}$$

Taking the total derivative of the previous equation

$$\Rightarrow \partial P(t) = -\gamma \frac{P_0}{V_0} \partial V(t) \tag{2.30}$$

where P_0 and V_0 are the ambient pressure and volumes, respectively. Note that an increase in pressure in the gas induces a concomitant reduction in volume and vice versa. This is the mechanism by which the gas undergoes rarefaction and compression, thus spawning the acoustic wave.

The volume of gas displaced by the action of the gas piston can be found by appealing to the Maxwell relation

$$\left(\frac{\partial V}{\partial T}\right)_P = \beta_T V \tag{2.31}$$

where $\beta_T = 1/T_0$ is the thermal cubic expansion coefficient of the adiabatic gas.

$$\Rightarrow \partial V = V \frac{\partial T}{T_0} \tag{2.32}$$

As long as $2\pi\mu_g << l_g$ (assumption (1))

$$\Rightarrow \partial T \approx \frac{2\pi\mu_g \overline{\phi_{ac}(t)}}{l_g} \tag{2.33}$$

$$\Rightarrow \partial V(t) = \frac{2\pi\mu_g \overline{\phi_{ac}(t)}}{l_g} \frac{V_0}{T_0} \tag{2.34}$$

Inserting Equation (2.34) into (2.30) yields:

$$\partial P(t) = \frac{2\pi\mu_g}{l_g}\frac{P_0}{T_0}\gamma\overline{\phi_{g_{ac}}(t)} = Qe^{j\left(\omega t-\frac{\pi}{4}\right)} \tag{2.35}$$

By recalling Equation (2.21), the parameter Q is defined to be:

$$Q = \frac{\beta I_0 \gamma P_0}{2\sqrt{2}k_s l_g a_g T_0\left(\beta^2-\sigma_s\right)}\times \left[\frac{(r-1)(b+1)e^{l_s\sigma_s}-(r+1)(b-1)e^{-l_s\sigma_s}+2(b-r)e^{-\beta l_s}}{(g+1)(b+1)e^{l_s\sigma_s}-(g-1)(b-1)e^{-l_s\sigma_s}}\right] \tag{2.36}$$

Q is a complex number that specifies the complex envelope of the sinusoidal pressure variation and can be expressed in either of the following formats:

$$Q = \begin{cases} Q_1 + jQ_2 \\ q\angle\psi \end{cases} \tag{2.37}$$

The actual pressure variation as sensed by the microphone is thus:

$$\Delta P(t) = \Re\mathrm{e}\{\partial P(t)\} = q\cos\left(\omega t-\psi-\frac{\pi}{4}\right) \tag{2.38}$$

Figures 2.4 and 2.5 demonstrate the variations in photoacoustic amplitude and phase due to the photoacoustic effect in a 0.5 mm thick silicon sample at two different photonic energies as a function of modulation frequency.

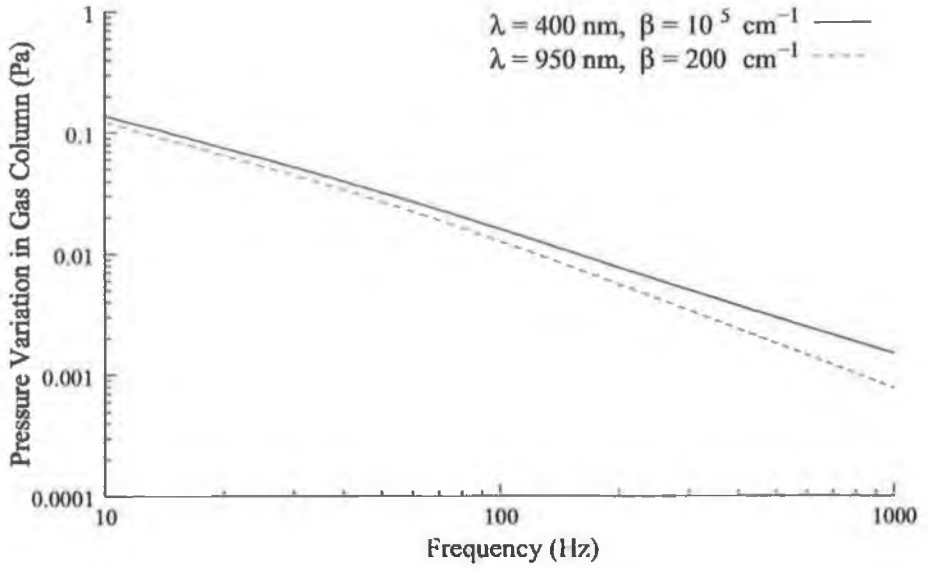

Figure 2.4: Amplitude of photoacoustic signal as function of chopping frequency for infrared and violet light incident on a silicon sample.

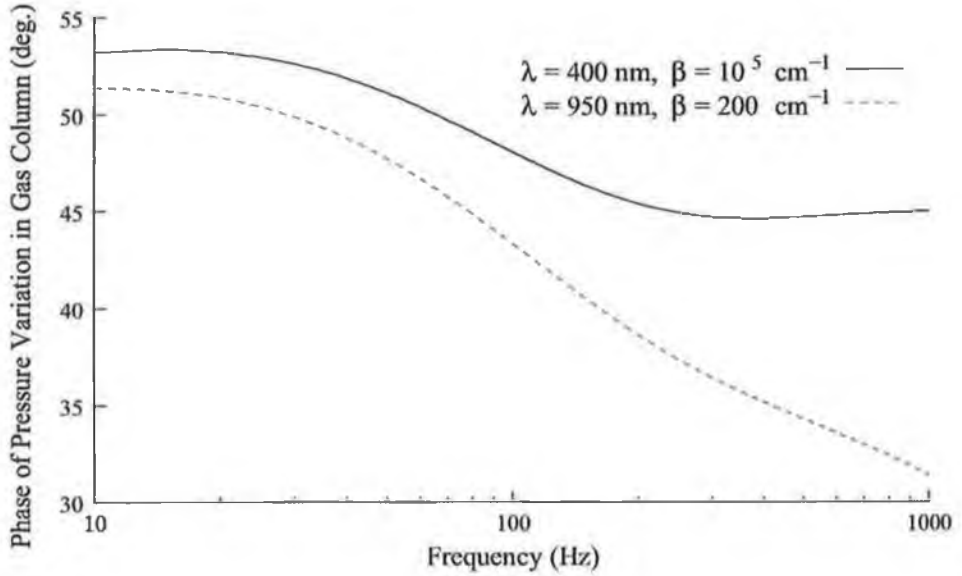

Figure 2.5: Phase of photoacoustic signal as function of chopping frequency for infrared and violet light incident on a silicon sample.

2.2.6 Special cases of the Rosencwaig Gersho Theory

From the previous section, it is obvious that an analytical solution for the pressure variation in the gas is quite cumbersome due to the complicated nature of Q. To overcome this problem, Rosencwaig and Gersho used physical insight to simplify Q for a number of special cases. These cases are grouped according to the optical opaqueness of the solid in relation to its thermal thickness. The optical absorption length, defined as $\mu_\beta = 1/\beta$, determines the optical opaqueness. The samples may be classed as either optically opaque $\mu_\beta << 1$ or optically transparent $\mu_\beta > 1$. Each category of optical transparency is further divided into three subcategories depending on the relative magnitude of the thermal diffusion length of the sample μ_s compared to the length of the sample l_s and the optical absorption length μ_β. Defining

$$Y \equiv \frac{\gamma P_0 I_0}{2\sqrt{2} T_0 l_g}$$

we will now investigate each of these categories in turn.

2.2.6.1 Optically Transparent Solids

In optically transparent solids, the length over which the light is absorbed is longer than the length of the sample. Consequently, light is absorbed throughout the entire volume of the sample.

1. Thermally thin solids $\mu_s >> l_s$, $\mu_s > \mu_\beta$:

   In Equation (2.36), the terms $e^{-\beta l_s} \approx 1 - \beta l_s$, $e^{\pm\sigma_s l_s} \approx 1$ and $|r| > 1$.

$$\therefore Q \approx \frac{(1-j)\beta l_s}{2a_g}\left(\frac{\mu_b}{k_b}\right) Y \tag{2.39}$$

   The acoustic signal is thus proportional to βl_s and since μ_b/a_g is proportional to ω^{-1}, the acoustic signal has an ω^{-1} dependence. For the thermally thin case of $\mu_s >> l_s$, the thermal properties of the backing material have to be taken into consideration. Therefore, in the design of a photoacoustic cell one should choose materials with low thermal conductivities.

2. Thermally thin solids $\mu_s > l_s$, $\mu_s < \mu_\beta$:

   In Equation (2.36), $e^{-\beta l_s} \approx 1 - \beta l_s$, $e^{\pm\sigma_s l_s} \approx 1 \pm \sigma_s l_s$ and $|r| < 1$.

$$\therefore Q \approx \frac{(1-j)\beta l_s}{2a_g}\left(\frac{\mu_b}{k_b}\right) Y \tag{2.40}$$

   As Equation (2.40) is identical to Equation (2.39), the same physical comments apply.

3. Thermally thick solids $\mu_s < l_s$, $\mu_s << \mu_\beta$:

   Now $e^{-\beta l_s} \approx 1 - \beta l_s$, $e^{\pm\sigma_s l_s} \approx 0$ and $|r| << 1$ in Equation (2.36).

$$\therefore Q \approx \frac{-j\beta\mu_s}{2a_g}\left(\frac{\mu_s}{k_s}\right) Y \tag{2.41}$$

   In this case, the signal is now proportional to $\beta\mu_s$ rather than βl_s as in the previ-

ous two cases. This implies, that only light absorbed within a thermal diffusion length μ_s contributes to the signal, in spite of the fact that light is being absorbed throughout the entire sample. The signal no longer depends on the properties of the backing material.

2.2.6.2 Optically Opaque Solids

In an optically opaque solid, the length over which the incident light is absorbed is far less than the length of the sample. This essentially means no light is transmitted through the sample.

1. Thermally thin solids $\mu_s >> l_s$, $\mu_s >> \mu_\beta$:

   In Equation (2.36) we set $e^{-\beta l_s} \approx 0$, $e^{\pm\sigma_s l_s} \approx 1$ and $|r| >> 1$.

$$\therefore Q \approx \frac{(1-j)}{2a_g}\left(\frac{\mu_b}{k_b}\right) Y \tag{2.42}$$

   In this case, we have photoacoustic "opaqueness" as well as optical opaqueness, in the sense that our signal is independent of β. A good example of a material that is both optically opaque and thermally thin is carbon black, universally used as a reference in photoacoustic measurements. One would anticipate a very strong signal from such a sample in comparison to the optically transparent and thermally thin samples as Q is now a factor βl_s larger. The signal also depends on the properties of the backing material and is inversely proportional to the chopping frequency ω.

2. Thermally thick solids $\mu_s < l_s$, $\mu_s > \mu_\beta$:

   In Equation (2.36) we set $e^{-\beta l_s} \approx 0$, $e^{\pm\sigma_s l_s} \approx 0$ and $|r| > 1$.

$$Q \approx \frac{(1-j)}{2a_g}\left(\frac{\mu_s}{k_s}\right) Y \tag{2.43}$$

   Equation (2.43) is analogous to Equation (2.42) except now the thermal properties of the backing material are replaced by those of the sample. Again the photoacoustic signal varies as ω^{-1} and is independent of the optical absorption coefficient.

3. Thermally thick solids $\mu_s << l_s$, $\mu_s < \mu_\beta$:

   In Equation (2.36) we set $e^{-\beta l_s} \approx 0$, $e^{\pm\sigma_s l_s} \approx 0$ and $|r| < 1$.

$$Q \approx \frac{-j\beta\mu_s}{2a_g}\left(\frac{\mu_s}{k_s}\right) Y \tag{2.44}$$

   This is a rather interesting case. The sample is optically very opaque. However, as long as $\beta\mu_s < 1$, the solid is not photoacoustically opaque and therefore, light absorbed within the thermal diffusion length μ_s will generate a photoacoustic signal.

2.3 The Generalised Classical Theory of the Photoacoustic Effect

McDonald and Wetsel expanded the Rosencwaig Gersho theory, wherein only the temperature in the sample was assumed to vary following absorption of photons, to include

the effect of a pressure variation in the sample as well [7]. The Rosencwaig-Gersho theory assumed adiabatic conditions throughout the cell, so one might expect valid results when the length of the gas column is far greater than the acoustic wavelength. However, when this criterion is not satisfied, or when the cell is operating near acoustic resonance, a break-down in the theory is to be anticipated.

The essential features of the generalised theory of the photoacoustic effect as derived by McDonald and Wetsel now follows. Absorption of amplitude modulated monochromatic light induces periodic heating within the sample. Respectively, the thermal wave is created in the sample and owing to thermoelasticity, pressure waves are formed and propagate in both directions inside the sample. Superposition of these waves at the sample surface gives rise to a surface motion, which then serves as a boundary condition for the acoustic waves in the gas. Periodic heat flow to the gas simultaneously causes expansion and contraction within a thin boundary layer next to the sample which Rosencwaig and Gersho characterised as the "acoustic piston." If the "acoustic piston" is now superimposed on the mechanical surface motion induced by the internal sample pressure variations, the resulting "composite piston" as defined by McDonald and Wetsel, produces the pressure variation in the gas detected by the microphone.

If one recalls the special case of the Rosencwaig Gersho theory for a thermally thick optically transparent solid (2.2.6.1), only light absorbed within a thermal diffusion length of the sample can contribute to the periodic heat flux at the sample-gas surface. However, in the generalised theory, the surface vibration in contrast, is proportional to the total energy absorbed in the sample. For experiments this has the following

implication. In transparent thermally thick samples, the "composite piston" model shows that the photoacoustic signal will be enhanced by increasing the sample thickness provided the factor βl_s remains sufficiently small to ensure optical transparency. In experimental regimes where the optical absorption coefficient may be small, the effect of acoustic coupling would be to increase the signal to noise ratio. However, one must now ensure that comparative spectra are recorded from samples possessing the same thickness to avoid ambiguities in interpretation.

2.3.1 Assumptions

Consider once more the one-dimensional schematic of a photoacoustic cell shown in Figure 2.1 on page 13. McDonald and Wetsel assumed that the incident light gave rise to an instantaneous source of thermal energy within the sample. Consequently, the equation for the density of heat generation is identical to Equation (2.2). As with the Rosencwaig and Gersho theory, it is assumed that the backing and window materials do not contribute to the acoustical processes. However, thermal diffusion within these materials is now included. This point is particularly important for cells with gas columns comparable to the acoustic wavelength. The gas is also assumed to be in-viscous. No reflective scattering of the incident light occurs.

2.3.2 Temperature and Pressure Fluctuations in System

The time-dependent pressure and temperature in the i^{th} medium in the system can be described by the following set of coupled differential equations derived from elemen-

tary fluid-mechanics:

$$\nabla^2 P_i - \frac{\rho_i}{B_i}\frac{\partial^2 P_i}{\partial t^2} = -\rho_i \beta_{T_i}\frac{\partial^2 T_i}{\partial t^2} \tag{2.45}$$

$$k\nabla^2 T_i - \frac{k_i}{\alpha_i} + S = -T_0 \beta_{T_i}\frac{\partial P_i}{\partial t} \tag{2.46}$$

where B is the isothermal bulk modulus, and S, present only in the sample, represents the thermal energy source due to optical absorption. The remaining parameters have the same meaning as in the Rosencwaig Gersho theory.

Assuming the temperature and pressure waves have an $e^{j\omega t}$ dependence, then the coupled system of equations may be re-written in one-dimension as follows:

$$\frac{d^2 P_i}{dx^2} + \frac{\rho_i \omega^2}{B_i} P_i = \rho_i \beta_T \omega^2 T \tag{2.47}$$

$$\frac{d^2 T_i}{dx^2} - \frac{j\omega T_i}{\alpha_i} + A e^{\beta x} e^{j\omega t} = -\frac{j T_0 \beta_{T_i} \omega P_i}{k_i} \tag{2.48}$$

In Equation (2.48), $A = 0$ in all regions except $l_s \leq x \leq 0$, wherein it has the same definition as in Equation (2.4) on page 14.

It can be shown that the general spatial solutions to the previous equations are, in the case of the sample:

$$T_s(x) = A_s e^{-jq_s x} + B_s e^{jq_s x} + C_s e^{-\sigma_s x} + D_s e^{\sigma_s x} + T'_A e^{\beta x} \tag{2.49}$$

$$P_s(x) = d_{as}\left[A_s e^{-jq_s x} + B_s e^{jq_s x}\right] + d_{ts}\left[C_s e^{-\sigma_s x} + D_s e^{\sigma_s x}\right] + d_\beta T'_A e^{\beta x} \tag{2.50}$$

in the case of the gas:

$$T_g(x) = A_g e^{-jq_g x} + B_g e^{jq_g x} + C_g e^{-\sigma_g x} + D_g e^{\sigma_g x} \tag{2.51}$$

$$P_g(x) = d_{ag}\left[A_g e^{-jq_g x} + B_g e^{jq_g x}\right] + d_{tg}\left[C_g e^{-\sigma_g x} + D_g e^{\sigma_g x}\right] \tag{2.52}$$

and, in the case of the window and backing materials:

$$T_i(x) = C_i e^{-\sigma_i x} + D_i e^{\sigma_i x} \qquad ; \qquad i \in \{w, b\} \tag{2.53}$$

In Equations (2.49) to (2.53), the letter q_i has been used to denote the wavenumbers of the acoustic waves propagating in the solid and gas, respectively. The standard nomenclature k has been neglected to avoid confusion with the thermal conductivity terms.

2.3.3 Results of the Generalised Photoacoustic Theory

Application of the boundary conditions between the different media to Equations (2.49)–(2.53) i.e. velocity of the acoustic waves, the continuity of temperature, heat flux and pressure, facilitates derivation of a set of twelve inhomogeneous linear equations in twelve unknown variables. These unknown variables are the coefficients $A_s, B_s, \cdots$. Thus the temperature and pressure spatial distributions can be defined everywhere in the cell. Normally one does not solve for the coefficients analytically as numerical computation via matrix algebra lends itself to an equally valid interpretation.

Figures 2.6 and 2.7 illustrate the respective photoacoustic amplitude as a function of high and low chopping frequencies for a dye-water solution. By varying the concentration of the dye in the solution, the optical absorption coefficient can be tuned accordingly. At high levels of optical absorption, the McDonald Wetsel theory agrees precisely with the Rosencwaig Gersho theory in the frequency range 0.1 Hz $\leq f \leq$ 10^3 Hz. Near cellular resonance or very low frequencies, the pressure variation in the sample contributes significantly to the photoacoustic signal and thus large deviations from the Rosencwaig Gersho theory occur. This is further compounded by samples possessing very small optical absorption coefficients.

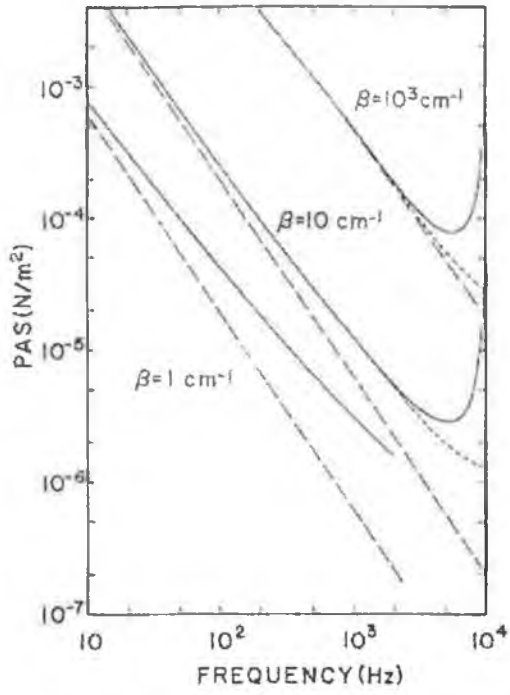

Figure 2.6: Photoacoustic amplitude verses chopping frequency for a dye-water solution, under normal to high modulation frequency. The results of the McDonald Wetsel theory are denoted by the solid curves and those of the Rosencwaig Gersho theory by the dashed lines. Reproduced from [7].

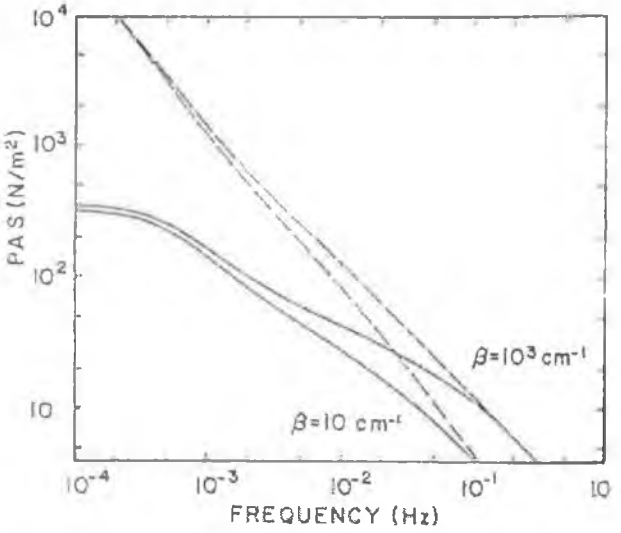

Figure 2.7: Photoacoustic amplitude verses chopping frequency for a dye-water solution, under low frequency modulation. The results of the McDonald Wetsel theory are denoted by the solid curves and those of the Rosencwaig Gersho theory by the dashed lines. Reproduced from [7].

2.3.4 Analytical Comparison with the Rosencwaig Gersho Theory

To further delineate the difference between the Rosencwaig Gersho theory and their own theory, McDonald and Wetsel derived a simpler expression for the spatial variation in pressure within the gas P_g. The simplified model, which is accurate to within 2% of the generalised model, is valid under normal to high frequency photoacoustic conditions i.e. in the interval 10 Hz $\leq f \leq 10^4$ Hz. The simplified model assumes that the temperature distribution in the system is hardly affected by the term coupling it to the pressure distribution and the surface motion of the sample is virtually independent of the periodic pressure variation in the gas. Under these conditions the pressure

variation possesses the following form:

$$P_g(x) \approx \frac{-j}{\omega}\frac{\gamma P_0}{l_g}\frac{I_0}{2\rho_s C_s}\left[\frac{\beta}{\sigma_g T_0\,(g+1)\,(r+1)} + \beta_T\left(1-e^{-\beta l_s}\right)\right] \times R_g(x) \quad (2.54)$$

where the term

$$R_g(x) = k_g l_g \frac{\cos\left(k_g l_g - k_g x\right)}{\sin\left(k_g l_g\right)} \quad (2.55)$$

is included to account for the spatial dependence of the photoacoustic signal. As the chopping frequency increases, the pressure amplitude becomes dependent upon position, since the acoustic wavelength is now comparable in size to the gas length l_g. This has important ramifications for placement of the microphone within the photoacoustic cell.

2.4 Further Extensions to the Classical Photoacoustic Theories

While a simple expression for the pressure variation in the gas column can be obtained using the McDonald Wetsel theory, no such analytical solution exists for low frequencies, i.e. below a modulation frequency of 10 Hz. Without any justification, and although their results agree with experimental measurements, the McDonald Wetsel theory inherently assumes that the pressure variation in the gas column at arbitrary low frequencies is adiabatic. Similar difficulties arise in the treatment of thermally thin gases.

Korpiun and Buchner eloquently resolve both these issues in their construction [8, 29] by taking into consideration the residual volume within the cell and that for small gas

columns, where $l_g \leq \mu_g$, a thermal wave is reflected by the optical window. The residual volume is defined as the volume that exists when the gas column length tends to zero, e.g. the volume of the antechamber in which the cell microphone is housed. The temperature variation due to the periodic heating of the sample induces a change in the internal energy of the illuminated gas volume, termed the active region, and also in the non-illuminated residual volume. Under such circumstances, Korpiun and Buchner experimentally determined that the system is better characterised by an isochoric process than an isobaric-adiabatic process. The isochoric variation of the internal energy leads to a pressure variation that is γ^{-1} times smaller than predicted by Rosencwaig and Gersho. Although the results of McDonald and Wetsel agree with this observation (see Figure 2.7 on page 33), the author believes the theoretical description presented by Korpiun and Buchner has a physically sounder basis.

The resultant expression for the pressure variation in the gas is:

$$\Delta P(t) = \frac{I_0 A_l P_0}{2\sqrt{2} A_t T_0} \frac{\beta K e^{j\left(\varphi - \frac{\pi}{4} + \omega t\right)}}{k_s a_s a_g l_g} \left(1 + \frac{V_r}{A_t l_g}\right)^{-1} \tag{2.56}$$

where the amplitude constant K and phase angle ϕ depend on the thermal properties of the sample and the cell; A_l is the area of the sample illuminated, A_t is the total cross sectional area of the cell and V_r is the residual volume of the cell. An investigation of this equation informs us that for sufficiently small gas columns or for photoacoustic systems operating at sufficiently low frequency, the pressure variation is independent of the gas used and the reflected thermal wave contributes to the signal. This is important

for the design of a photoacoustic cell. For example, if the gas used is air, then at a modulation frequency of 1 Hz, to avoid a reflected thermal wave from the optical window the length of the gas column would have to be far greater than $\mu_g = 4.5$ mm.

In another study, Korpiun and Bucher [9] examined the effect of the viscosity of the gas in the photoacoustic cell. Essentially, their results demonstrate that as the photoacoustic signal propagates away from the sample-gas interface it undergoes exponential damping of the form $e^{-\epsilon_v x}$ due to the viscosity of the gas [30] where

$$\epsilon_v = \frac{1}{v_g d_c}\sqrt{\frac{\eta_e \omega}{2\rho_0}} \tag{2.57}$$

In the previous formulae, d_c is the closest dimension between cell boundaries, v_g is the velocity of the acoustic wave and η_e is the effective viscosity. The salient feature of the investigation demonstrated that the viscosity is proportional to $\omega^{1/2}$, and therefore, for a gas such as air its effects become prominent upwards of 100 Hz.

2.5 The Bandeira, Closs and Ghizoni Theory of the Photoacoustic Effect in Semiconductors

In the aforementioned theories, an important feature which has so far been neglected, is that electron excitations, having a finite lifetime, are generated in the process of light absorption. The theories assumed that the evolution of heat is instantaneous at the point in the sample where the light is absorbed, so that at some time say Δt later, the heat source is governed by the light source whose intensity decreases away from the surface in an $e^{-\beta x}$ fashion. In reality, the absorption of light is accompanied by the

generation of electron-hole pairs, which exist for a finite lifetime and move within the sample, before transferring their energy back to the sample in the form of heat.

When the optical absorption coefficients are high, heating is basically provided by surface recombination of excess carriers which are generated very close to the illuminated surface of the sample. In such a case, the transport properties of the carriers will not greatly affect the photoacoustic response and one would obtain an expression similar to Equation (2.44) on page 26. However, in a sample possessing a small optical absorption coefficient, the light penetrates deep into the bulk of the material generating a substantial fraction of photoexcited carriers, and consequently, carrier diffusion effects can play an important role in the production of the photoacoustic signal.

The first theory of the photoacoustic effect in semiconductors was developed in the 1980s by Bandeira *et. al* [10]. Several groups tried to improve their theory, but all quintessentially possessed the same foundations [31–35].

In their study, Bandeira and co-workers were interested in enhancing the photoacoustic effect from samples with low optical absorption coefficients. To this end, they applied an electric field across the sample perpendicular to the direction the incident photons made with the sample. The subsequent Joule heating enhanced the contribution to the photoacoustic signal from photoexcited carriers in the bulk. In the following review of their work, the effect of the electric field will be neglected.

2.5.1 Temperature Fluctuation in Sample

The thermal distribution in the sample and gas may be found by solving the charge and thermal diffusion equations:

$$D\frac{\partial^2 n(x,t)}{\partial x^2} - \frac{n(x,t)}{\tau} - \frac{\partial n(x,t)}{\partial t} = -G(x,t) \tag{2.58}$$

$$\frac{\partial^2 \phi(x,t)}{\partial x^2} - \frac{1}{\alpha_s}\frac{\partial \phi(x,t)}{\partial x} = \frac{-P(x,t)}{k_s} \tag{2.59}$$

where $n(x,t)$, D, and τ are the density, diffusion constant, and recombination times of the photoexcited carriers, respectively.

The intensity of the source is the same as in the previous theories. The density of photoexcited carriers generated due to spatial dispersion of the incident light is given by:

$$G(x,t) = \frac{\eta\lambda}{hc}\frac{\partial I(x,t)}{\partial x} = \frac{\eta\lambda\beta}{2hc} I_0 e^{\beta x}\left(1 + e^{j\omega t}\right) \tag{2.60}$$

The density of heat generation $P(x,t)$ is attributable to the following nonradiative physical phenomena:

- Thermalisation of photoexcited carriers.
- Bulk recombination.
- Surface recombination.

It is important to note at this point that in the classical theories absorption of light caused heating of the sample. In this semi-classical theory, a subtle difference exists.

We now have two competing processes: incident absorbed light causes photoexcitation of carriers (not direct heating) and the subsequent interaction of these carriers with the sample causes heating.

2.5.1.1 Nonradiative thermalisation of photoexcited carriers

When electrons with energy $E = h\nu$ greater than the bandgap energy E_g are excited from the valence band to the conduction band the heat generated is:

$$\Delta Q_t = (h\nu - E_g)\, n_i(x,t) \tag{2.61}$$

Since interband transition or relaxation times τ_{IB} are of the order of a picosecond, the heat density generated by this process is:

$$\frac{dQ_t}{dt} \approx \frac{\Delta Q}{\Delta t} = \frac{(h\nu - E_g)\, n_i(x,t)}{\tau_{IB}} \tag{2.62}$$

Solving the carrier diffusion equation with the intrinsic carrier density $n_i(x,t) = \tau_{IB} G(x,t)$ reveals this process takes place within a *Debye length* $\sqrt{D\tau_{IB}}$ of the surface.

2.5.1.2 Nonradiative bulk recombination

For a steady-state population of photoexcited carriers particles $n_d(x,t)$, with energy $h\nu > E_g$, band to band recombination can occur within a diffusion length $\sqrt{D\tau_{BB}}$. Defining η_B to be the fraction of energy given up radiatively to the bulk in a recom-

bination time τ_{BB} gives us the nonradiative bulk recombination contribution to the density of heat generation:

$$\frac{dQ_{br}}{dt} \approx \frac{\Delta Q_{br}}{\Delta t} = \frac{\eta_B E_g n_d(x,t)}{\tau_{BB}} \tag{2.63}$$

2.5.1.3 Nonradiative surface recombination

In a manner similar to recombination in the bulk, surface recombination can also happen within a diffusion length $\sqrt{D\tau_{BB}}$ of the surface. In this case, η_S is the fraction of energy given up nonradiatively to the process.

$$\Rightarrow \Delta Q_{sr} = \eta_S E_g n_d(x,t) \tag{2.64}$$

The recombination interval Δt is characterised by the surface recombination velocity U. Note, this is not an actual velocity, rather it characterises the rate at which carriers recombine as τ_{BB}^{-1} did in the bulk.

$$\Delta t = [u_1\delta(x) + u_2\delta(x+l_s)]^{-1} \tag{2.65}$$

where u_1 and u_2 are the surface recombination velocities at the surface which the light impinges and the bottom surface of the sample, respectively. The contribution to the

total density of heat generation from this process is:

$$\frac{dQ_{sr}}{dt} \approx \frac{\Delta Q_{sr}}{\Delta t} = \eta_S E_g n_d(x,t)\left[u_1\delta(x) + u_2\delta(x+l_s)\right] \tag{2.66}$$

Therefore, the density of heat generation which is the sum of the contributions from Equations (2.62), (2.63) and (2.66) is:

$$P(x,t) = \frac{(h\nu - E_g)\, n_i(x,t)}{\tau_{IB}} + \frac{\eta_B E_g n_d(x,t)}{\tau_{BB}} + \eta_S E_g n_d(x,t)\left[u_1\delta(x) + u_2\delta(x+l_s)\right] \tag{2.67}$$

2.5.2 Solutions of the Thermal and Carrier Diffusion Equations

Now that all the terms necessary for a solution of Equations (2.58) and (2.59) have been ascertained, their solution can be found in a relatively straightforward manner. One must solve the charge diffusion equation first as a knowledge of the steady-state excess carrier concentration (both instrinsic and photoexcited) is required for solution of the thermal diffusion equation. Equation (2.58) is solved by applying the following boundary conditions to the surface recombination velocities at both surfaces:

$$D\frac{\partial n_d(x,t)}{\partial t}_{x=0} = -u_1 n_d(0,t) \tag{2.68}$$

$$D\frac{\partial n_d(x,t)}{\partial t}_{x=-l_s} = -u_2 n_d(-l_s,t) \tag{2.69}$$

The equation for the temperature distribution and subsequent pressure variation in the gas is solved in the much the same manner as in the Rosencwaig Gersho theory. However, one must now take into consideration the discontinuities in the heat flux at the gas-semiconductor and semiconductor-backing material interfaces due to the heat generated by surface recombination of excess carriers. Thus, the boundary condition is:

$$k(x)\frac{\partial^2\phi(x,t)}{\partial x^2}_{x=0 \text{ or } x=-l_s} = \rho(x)C(x)\frac{\partial\phi(x,t)}{\partial t} - \eta_S E_g H n_d(x,t)\left[\delta(x)+\delta(x+l_s)\right]_{x=0 \text{ or } x=-l_s} \tag{2.70}$$

where $H = 1$ if the incident photon energy is greater than the bandgap energy or zero if this is not the case.

Finally an expression for the pressure fluctuation in the gas may be derived:

$$\delta P(t) = \frac{\gamma P_0 I_0 \eta \lambda \beta}{2\sqrt{2}T_0 k_s l_g a_g hc}\frac{e^{j(\omega t-\pi/4)}}{R}\times \left[\frac{(h\nu - E_g)H}{1+j\omega\tau_{IB}}\frac{S}{\beta^2-\sigma_s^2} + \frac{\eta_B E_g H}{L^2(m^2-\beta^2)}\left\{\frac{S}{\beta^2-\sigma_s^2}-\frac{V}{m^2-\sigma_s^2}\right\} + \frac{\eta_s E_g H \tau_{BB}}{L^2(m^2-\beta^2)}W\right] \tag{2.71}$$

S, V and R are defined in [10]. The normalised photoacoustic spectrum from a silicon sample is illustrated in Figure 2.8. The most notable feature in the spectrum is the increase in photoacoustic intensity when the incident photonic energy is greater than the bandgap energy. In this part of the spectrum thermalisation and non-radiative deexcitation processes occurs.

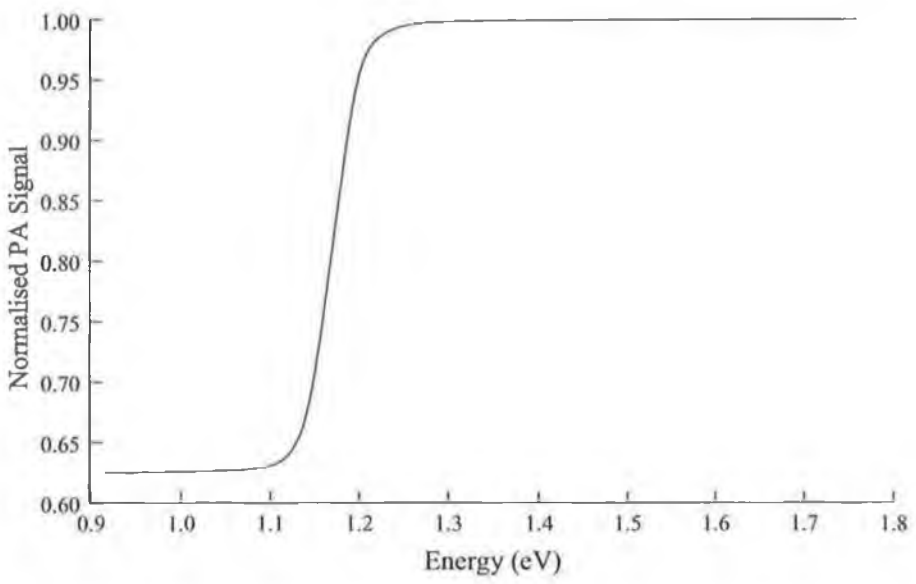

Figure 2.8: Normalised photoacoustic spectrum from a silicon sample according to the theory of Bandeira, Closs and Ghizoni. $E_g = 1.18$ eV.

2.6 Applications of the theory to experimental measurements

In the previous sections, the theory of the photoacoustic effect in condensed matter samples was reviewed. In this section, these theories will be utilised to create expressions for the optical absorption coefficient and energy of the bandgap in terms of the normalised photoacoustic spectrum.

2.6.1 Evaluation of the optical absorption coefficient β

Many of the semiconductor materials examined in this thesis may be considered optically opaque and thermally thick. This lets us reformulate the term for θ in Equation

(2.21) on page 17 as follows:

$$\theta = \frac{\beta I_0}{2k_s(\beta^2 - \sigma_s^2)} \frac{r-1}{g+1} \tag{2.72}$$

By further assuming that $g << 1$, the resulting photoacoustic signal as derived by Poulet *et. al* [36] may be written as:

$$\Delta P(t) = \frac{Z\beta\mu_s}{\omega\sqrt{(\beta\mu_s+1)^2+1}} e^{i\left(\omega t - \frac{\pi}{4} - \tan^{-1}\left(\frac{\beta\mu_s+2}{\beta\mu_s}\right)\right)} \tag{2.73}$$

where

$$Z = \frac{\gamma P_0 I_0 \sqrt{\beta_s \beta_g}}{2l_g T_0 k_g}$$

If one now solves Equation (2.73) for β in terms of the normalised photoacoustic amplitude one would get [36,37]:

$$\beta = \frac{1}{\mu_s} \frac{q^2 + q\sqrt{2-q^2}}{1-q^2} \tag{2.74}$$

where q is the normalised photoacoustic signal given by

$$q = \frac{|P_g(h\nu, t)|}{Z} \tag{2.75}$$

Therefore, through a knowledge of the normalised photoacoustic spectrum and the thermal diffusion length of the sample, it is possible to determine the optical absorption coefficient of the sample. However, one must be careful in the application of such a

formula. Ideally, it should be applied on the linear transition between the valence and conduction bands in the recorded spectrum. If it is applied in a region of the spectrum where the signal has saturated i.e. the normalised intensity is unity, then the procedure does not work as it would give an infinite value for the optical absorption coefficient which is obviously nonsensical.

2.6.2 Determination of the bandgap

Between the edges of the bandgap transition, the optical absorption coefficient in direct and indirect semiconductors is related to the energy of the bandgap according to [38]:

$$\beta = A_d \frac{\sqrt{h\nu - E_g}}{h\nu} \quad \ldots \text{direct} \tag{2.76}$$

$$\beta = A_{id} \frac{(h\nu - E_g)^2}{h\nu} \quad \ldots \text{indirect} \tag{2.77}$$

where A_d and A_{id} are constants independent of the photon energy. One can obtain the optical absorption coefficient based on the information presented in Section 2.6.1 and use this to generate, for example, a plot of $(h\nu\beta l_s)^2$ verses $h\nu - E_g$ in the case of a direct bandgap semiconductor. By extrapolating the data to $\beta = 0$ one can directly evaluate E_g. The procedure is similar for a semiconductor with an indirect bandgap.

2.7 Photoacoustic Effect in Strained Semiconductors

To date, very little has been published in the literature regarding the effect of structural strain on the photoacoustic spectrum. In a sufficiently strained crystalline material,

stress is relieved through the formation of dislocations. The effect of these structural dislocations is to alter the bandstructure of the material through the introduction of optoelectronic defect levels. These defect levels will obviously influence the behaviour of any photoexcited carriers within the sample by providing alternative paths for non-radiative de-excitation processes. This should manifest itself in the recorded photoacoustic spectrum. Photoacoustic spectroscopy has been used to analyse sub-bandgap defect levels [39–41]. However, no attempt has been made to correlate these results with the macroscopic sample stress. This is somewhat surprising as, inherent in the information recorded in the photoacoustic spectrum, is a wealth of information associated with the elastic and thermoelastic properties of the material under investigation.

Most of the papers in the literature are concerned with the effect of electronic strain i.e. the effect of photoexcited carriers on the photoacoustic response [42–44]. Perhaps for this discussion it is worth examining the effect of electronic strain before we speculate on the effects of structural strain. The photogenerated carriers can produce local strain that in turn generates an acoustic wave within the sample. The electronic strain ϵ_e changes linearly with excess carrier density $\Delta n(x,t)$ and is given by:

$$\epsilon_e(x,t) = d\Delta n(x,t) \tag{2.78}$$

where

$$d = \frac{1}{3}\left(\frac{\partial E_g}{\partial P}\right)_T \tag{2.79}$$

is the pressure dependence of the bandgap at constant temperature. For many semicon-

ductor materials d is negative, and therefore, electronic strain will induce a contraction of the lattice. This process will have to compete with the expansion of the lattice induced by non-radiative heating mechanisms. It is important to note that these studies are concerned with the influence of photoexcited carriers on the strain i.e. the $\Delta n(x,t)$ term of Equation (2.78) and not how the strain within the sample i.e. the d term modifies the signal.

Consider a perfect silicon crystal in an isolated ambient at 300 K. The bandgap of the material $E_g = 1.18$ eV. Suppose we induce a compressive stress within the material of the order 300 MPa. Given that $d_{Si} = -14.8 \times 10^{-12}$ eV / Pa [45], this implies the bandgap will narrow by approximately 4.4 meV. The question now posed is, would photoacoustic spectroscopy be capable of detecting such a shift? Given that the spectral resolution of a monochromator is governed by the product of the slit width and the linear dispersion of the diffraction grating, one would need a sufficiently small spectral bandwidth of the order of 1 meV to resolve the shift. For the monochromator used in this thesis, at $\lambda = 1050$ nm, the linear dispersion is 3.125 nm/mm (see Chapter 3 for details of the calculation). For a 0.5 mm slit, the bandpass of the monochromator is $\Delta\lambda/\lambda = \Delta E/E \approx 1.5$ meV. Therefore, in principle, it should be possible to measure such a shift. However, the low intensity resulting from the use of such a narrow slit would make the experiment difficult to implement. The obvious viable solution to this scenario would be to use a laser.

Potentially a much more productive investigation into the effect of structural strain on the photoacoustic spectrum would be found with epitaxial systems. In the unstrained

defect free substrate material, one should just observe an increase in the photoacoustic signal during the bandgap transition as described in the Bandeira, Closs and Ghizoni theory. As the epitaxial layer is grown on the substrate, induced strain will modify the bandstructure, possibly providing alternative non-radiative recombination paths for photoexcited carriers. The presence of such levels would be seen as peaks in the spectrum below the bandgap energy. The energy levels of these defects can be inferred directly from the spectrum. The strain within the material could be visualised using, for example, X-ray diffraction topography and a direct correlation between the strained structure and its sub bandgap defect levels performed.

The arguments of the previous paragraphs has innocently presumed perfect samples exist. In reality, this will never be the case. However, the introduction of extra defect levels or the removal of intrinsic levels in an imperfect sample follows essentially the same arguments.

2.8 Summary

In summary, the major theories of the photoacoustic effect in condensed matter samples have been reviewed. The underlying assumptions and physical principles were described at each stage. Failures and errors in the theories were highlighted. The theories were used to obtain methods for the extraction of the optical absorption coefficient and bandgap energy from normalised photoacoustic data. At each stage, physical criteria embedded in the theories governing the design of a photoacoustic cell were extracted. These will be formulated concisely in the next chapter as guidelines in the design of

a photoacoustic spectrometer possessing a spectral bandwidth from the infrared to the ultraviolet.

Chapter 3

Design of a Wide Bandgap Photoacoustic Spectrometer

3.1 Introduction

The previous chapter dealt with the theory of the photoacoustic effect in condensed matter samples. It is the purpose of this chapter to utilise the guidelines provided by the various theories in the design and construction of a photoacoustic spectrometer. This spectrometer, of the gas-microphone type, is to be used in the photonic energy range 0.5 eV to 6.2 eV for the observation and characterisation of non-radiative sub bandgap defects in narrow and large bandgap materials such as silicon and gallium nitride.

Photoacoustic spectrometers for the analysis of gaseous substances are commercially available. However, photoacoustic spectrometers for condensed matter analysis are difficult to obtain and are often unsuitable in their construction to the varied needs of an academic experimentalist. This has been the impetus for the development of in-house systems, which are quite often maximised for specific experimental conditions [46–49]. The construction of photoacoustic spectrometers for absolute measurements of

the photoacoustic effect is often quite arduous, expensive and very involved. However, one can develop a system at a reasonable cost with a lot less sophistication to acquire relative information by normalising the obtained spectra to that of a known sample such as carbon black. This chapter describes the design of a fully computerised high-resolution photoacoustic spectrometer similar to that developed by Zegadi *et. al* at the University of Salford circa 1994 [46, 47].

3.2 Photoacoustic Spectrometer Specifications

The system specifications are quite simple. Basically, the spectrometer should be capable of analysing samples with bandgap energies in the photonic interval 0.5 eV to 6.2 eV. The system should be capable of investigating samples of a reasonable size i.e. up to approximately 15 mm^2. The system should also have the potential to record spectra from large areas of a sample and also have the capability to perform photoacoustic mapping with a spatial resolution of approximately 1 mm^2. It is the purpose of the remainder of this chapter to design such a system. The system may be broken down into several independent sub-systems. These are the light source, the signal processing system, the data acquisition and processing system, and most importantly, the photoacoustic cell wherein the photoacoustic effect takes place.

3.3 Operational Overview of the Photoacoustic Spectrometer

Before presenting the reader with a detailed description of the sub-systems comprising the photoacoustic spectrometer, a general high-level description of its operation will be

provided. Consider the spectrometer illustrated in Figure 3.1 on page 54. A photograph of the system is shown in Figure 3.2 on page 55.

The operation of the system is quite simple. Polychromatic light from the 300 W Xenon arc lamp is modulated by the optical chopper as it is focused onto the entrance slit of the monochromator. The amplitude modulated light that enters the monochromator undergoes diffraction in accordance with the grating equation:

$$g\lambda = a \sin\theta \tag{3.1}$$

where g is the order of the reflection, λ the monochromatic diffracted wavelength, a the line spacing of the grating and θ the diffraction angle. The order sorting filter wheel at the output of the monochromator ensures that only light with wavelength λ is transmitted and the harmonic contribution from wavelengths λ/g where $g \geq 2$ are rejected. At this stage the monochromatic light enters the focusing sub-system, two of which have been designed in this thesis. The first quite simply is designed to maximise photonic throughput and thereby the intensity of light incident on the sample. This system is depicted in the photograph of Figure 3.2. The second focusing assembly is designed for spatial mapping of the photoacoustic signal within the sample. The light from each focusing sub-system is reflected into the photoacoustic cell using a plane mirror and the subsequent pressure variations in the gas are detected using an electret microphone. The resulting electrical signal is first pre-amplified in a low-noise pre-amplifier before detection of the signal is performed with a lock-in amplifier.

Pre-amplification and lock-in detection are used to circumvent the obvious problem associated with the low signal to noise ratio of the microphone signal. The reference frequency for the optical chopper is provided by an internal frequency generator in the lock-in amplifier – the motivation for this will be explained in Section 3.5.1.2. The entire system is controlled by the personal computer using LabView® software and the National Instruments IEEE 488.2 GPIB interfacing protocol.

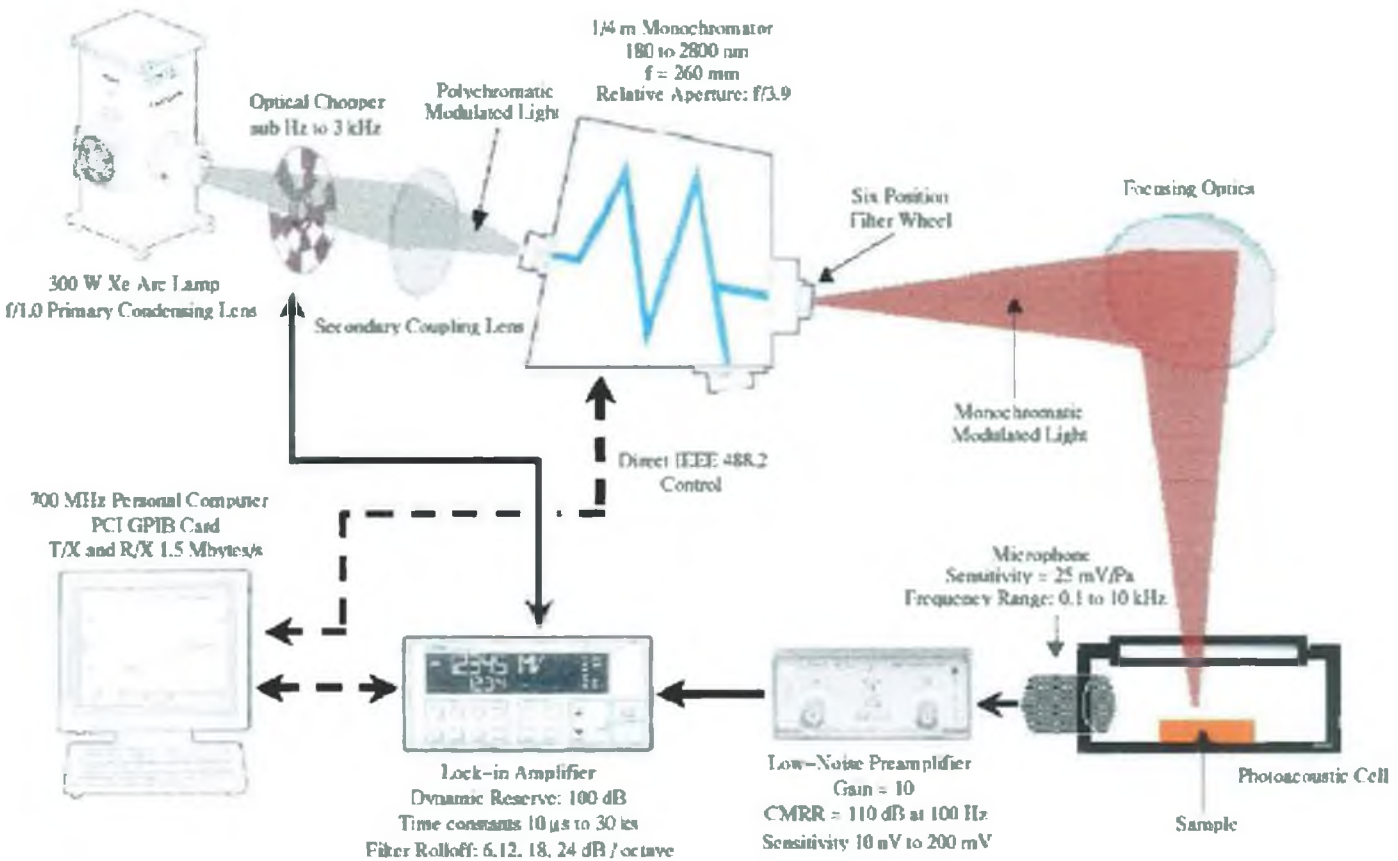

Figure 3.1: Schematic of photoacoustic spectrometer. Operational energy range 0.45 eV to 6.2 eV. Operational frequency range 25 Hz to 250 Hz.

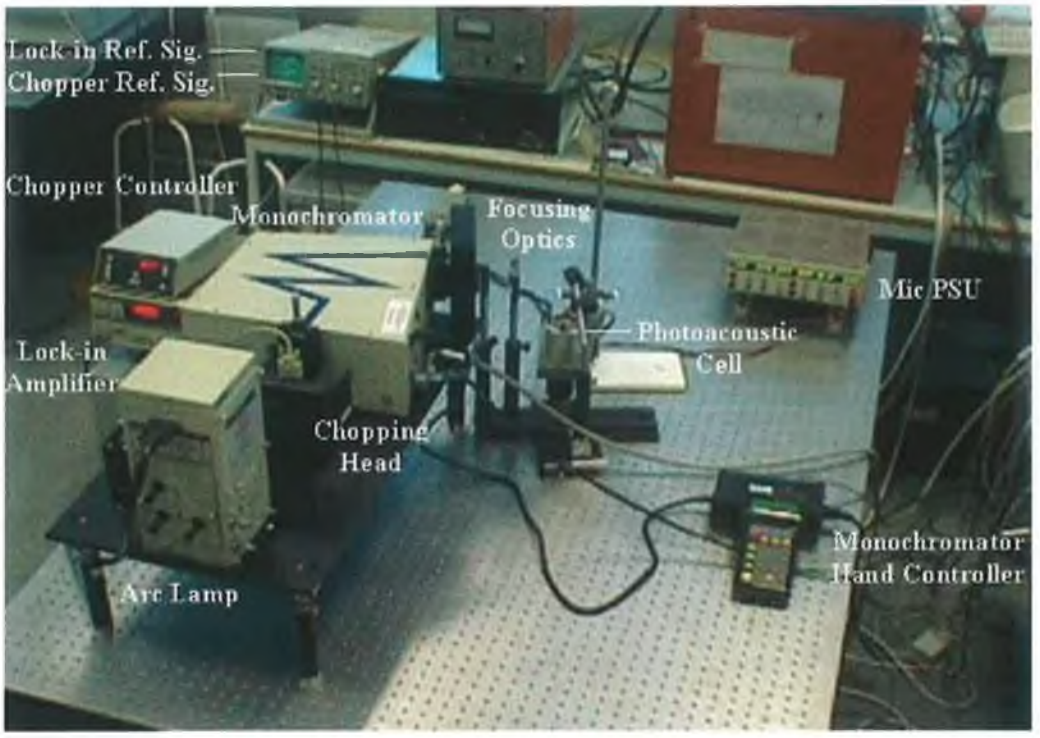

Figure 3.2: Photoacoustic spectrometer implemented in thesis. The spectrometer is configured in the maximal throughput operational mode.

3.4 Photoacoustic Cell

The heart of any photoacoustic spectrometer is the photoacoustic cell. Its design often involves complex optimisation in order to achieve the high signal-to-noise ratio required for the sample being examined. From Chapter 2 it is known that the photoacoustic signal reaching the microphone depends on the incident light intensity, on the thermal properties of the sample, gas and backing material, and on the details of the thermal diffusion processes responsible for the heat flow to the gas. We will now examine general design specifications for a photoacoustic cell of the gas-microphone

type before discussing the actual cell implemented in this work.

3.4.1 Performance Specifications

Rosencwaig identified several criteria governing the actual design of the photoacoustic cell [28]. These consisted of:

1. Acoustic isolation from the ambient.
2. Minimisation of extraneous photoacoustic signals arising from the interaction of the light beam with the cell proper.
3. Maximisation of the acoustic signal within the cell.
4. Optimal microphone configuration.

3.4.1.1 Acoustic Isolation from the Ambient

Acoustic isolation from external interference is not a major concern when lock-in detection is being used. However, one should obviously use chopping frequencies different from those present in the acoustic and vibrational spectrum of the environment. In this respect, the location of the optical chopper is of considerable importance. In the literature, the chopper is generally placed before the monochromator rather than at its exit port. This is to prevent or at least minimise acoustic coupling of the chopped air with the periodic pressure fluctuations in the cell gas column. The sample cell closure should provide an excellent acoustic seal. In practice, this is quite easy to obtain using high vacuum silicone grease and rubber O-rings. In conjunction, the cell walls should

be of sufficient thickness to form a good acoustic barrier [50]. Where possible, cooling fans from power supplies and the lamp should be directed away from the experimental region as the noise from these sources will be superimposed on the photoacoustic signal.

3.4.1.2 Minimisation of Scattered Light

McClelland and Kniseley investigated the effects of scattered light in photoacoustic spectroscopy [51]. In regions of low optical density and/or high reflectivity, where the photoacoustic signal is small due to the low absorption of incident light by the sample, they observed that scattered light could contribute significantly to the photoacoustic signal. In these regions, a fraction of light scattered from the surface or interior of the sample reaches the cell walls, where a portion may be absorbed. This scattered light contributes a spurious background component to the photoacoustic signal with a photon energy dependence on the optical properties of both the sample and the cell walls.

To minimise specious signals from the interaction of the light beam with the walls and windows of the cell, one should employ windows as optically transparent as possible for the photonic energy range of interest. The cell should also be constructed out of polished aluminum or stainless steel [28]. Though aluminum and stainless steel cell walls absorb some of the scattered light, the resulting photoacoustic signal will be quite weak as long as the thermal mass of the walls is large. The inside surfaces of the cell should be kept as clean as possible to minimise photoacoustic signals from surface

contaminants. Scattered light effects may be minimised by constructing large cells in such a way that scattered light is reflected outside, thus minimising its effect. However, the pressure variation is inversely proportional to the cell gas volume; hence a trade off must be made between scattered light effects and maximisation of the acoustic signal. The amount of scattered light reaching the microphone must also be minimised as absorption couples efficiently to the microphone diaphragm [52].

3.4.1.3 Maximisation of the Acoustic Signal Within the Cell

Since the signal in the photoacoustic cell used for solid samples varies inversely with the gas volume, one should attempt to minimise the gas volume. In accordance with the extended theories of the photoacoustic effect of Chapter 2, one should take care not to minimise the cell volume to the extent that the acoustic signal produced at the sample suffers appreciable dissipation to the cell window and walls before reaching the microphone. The distance between the sample and the cell window should always be greater than the thermal diffusion length of the gas, as this boundary layer acts as an acoustic piston generating the signal in the cell. Based on the analysis of the acoustic piston length in the previous chapter, the gas column length should be greater than 2 mm (see Figure 2.2 on page 19 of Chapter 2). Thermo-viscous damping also needs to be taken into consideration, the consequences of which imply the closest dimension between cell boundaries in a passageway should be greater than 1 mm. In accordance with the generalised theory of the photoacoustic effect developed by McDonald and Westsel one can avoid the effects of thermally reflected waves and thermo-viscous

damping by operating in the frequency range 10 Hz to 1000 Hz (see Figures 2.6 and 2.7 on pages 32–33 in Chapter 2).

The previous comments have presumed that the gas in the cell is air. The Rosencwaig Gersho theory has shown that the photoacoustic signal is proportional to $\sqrt{k_g}P_0/T_0$. Therefore, the acoustic signal may also be enhanced by using gases with high thermal conductivities, the use of higher gas pressures and lower gas temperatures.

3.4.1.4 Optimal Microphone Configuration

Various microphones can be used; the principle types being condenser and electret microphones. A condenser microphone consists basically of a thin metal diaphragm and a rigid back plate constituting the electrodes of an air dielectric capacitor. A constant charge is applied to the capacitor by a high DC voltage (the polarisation voltage). The variations in capacitance caused by the varying sound pressure on the thin diaphragm are transformed into voltage variations. Condenser microphones are generally accepted as being the best microphone type for sound measurements; however, owing to the large diameter of the devices, their use in small volume photoacoustic cells can be somewhat complicated [53].

Similar to condenser microphones, electret microphones use a variable plate capacitor as an acoustic transducer, the front electrode being the microphone diaphragm. As the diaphragm moves, the capacitance changes and a voltage proportional to the acoustic signal is produced. The stationary back electrode used in electret microphones is manufactured from a special synthetic material known as "electret." This material has

a unique quality of being able to store a permanent electric charge; the charge being "frozen" in the electret material. It therefore requires no high external polarising voltage and can be powered by low voltage batteries. The counter electrode is manufactured from a thin gossamer foil, with a thin gold coating. Such an ultralight diaphragm provides good transient response, high responsivity at low sound pressure levels, and ensures highly accurate sound reproduction with minimal distortion. Cylindrical electret microphones are relatively cheap and possess a large surface area with respect to their small size, thereby increasing their sensitivity. However, they usually do not have a flat frequency response. This can be quite troublesome if one intends to perform experiments at different chopping frequencies e.g. in depth profiling analysis. This apparent shortcoming can be turned to one's advantage if one is only going to operate at one chopping frequency. One can set the chopping frequency to take advantage of the non-flat frequency response and operate at its peak sensitivity.

The photoacoustic signal to noise ratio and experimental sensitivity can be increased by simply adding the signals from several microphones in the sample cell [53]. In such a configuration the signal increases with the number of microphones used, whereas the microphone random noise only increases with the square root of their number. For this purpose electret microphones are particularly suited due to their small size.

Based on the details of the Rosencwaig Gersho theory, in the frequency range of interest 10 Hz to 250 Hz, the microphone should be capable of sensing pressure variations of the order 10 mPa to 100 mPa (see Figure 2.4 on page 23 in Chapter 2). The microphone should be placed in an antechamber to minimise the effects of scattered light

and for general photoacoustic investigations of different samples, one should ensure that the cell is not operating near acoustic resonance.

3.4.2 Photoacoustic Cell Implementation

A three-dimensional illustration of the photoacoustic cell constructed in this thesis is shown in Figure 3.3. The working drawings can be viewed in Appendix A. The design is based on the individual designs of Zegadi *et. al* [46], Gray *et. al* [49] and Ferrell *et. al* [50]. It is the most common design adopted in the literature. Unlike Gray, the gas volume is fixed (typically 3.5 cm^3). The internal diameter of the active volume is 30 mm and the gas column length is 5 mm.

Air at atmospheric temperature and pressure was used as the gas in the cell. To reduce complexity, no other gases were used. Consequently, to avoid effects of thermally reflected waves and thermo-viscous damping, the usable chopping frequency range is 10 Hz to 1 kHz.

The cell is made large not only to accommodate large samples, but also to minimise the effect of reflected and scattered light from the sample on the cell walls. The cell was made from H-30 Aluminum supplied by Miko Metals, Cork, Ireland. When mechanically polished, this metal becomes highly reflective. Spectrosil WF (quartz) windows, manufactured by Oxford Cryogenic systems, with a thickness of 0.2 mm, have been used as they possess transmittance in excess of 99% for all incident light in the photon range 0.42 eV to 6.2 eV. The rubber O-ring and neoprene cushion provided a good acoustic seal from the ambient.

A single FG3329 electret microphone [54] manufactured by Knowles Electronics was used to detect the photoacoustic signal. This miniature cylindrical device, of dimension 2.59 mm in diameter and 3.22 mm in length, was housed in an antechamber under the sample stage. This ensured no scattered light induced noise from the microphone diaphragm. Only one microphone was used for experimental simplicity, but the cell can be easily modified in the future to accommodate a detector array. The microphone possessed a nominally high flat sensitivity of 25 mV/Pa in the frequency range 100 Hz to 10 kHz making the microphone ideal for studies at different chopping frequencies. Therefore, based on the estimated pressure variation due to the photoacoustic effect (see Figure 2.4 on page 23 in Chapter 2) one could estimate signal levels of the order of 250 μV to 2.5 mV to be produced.

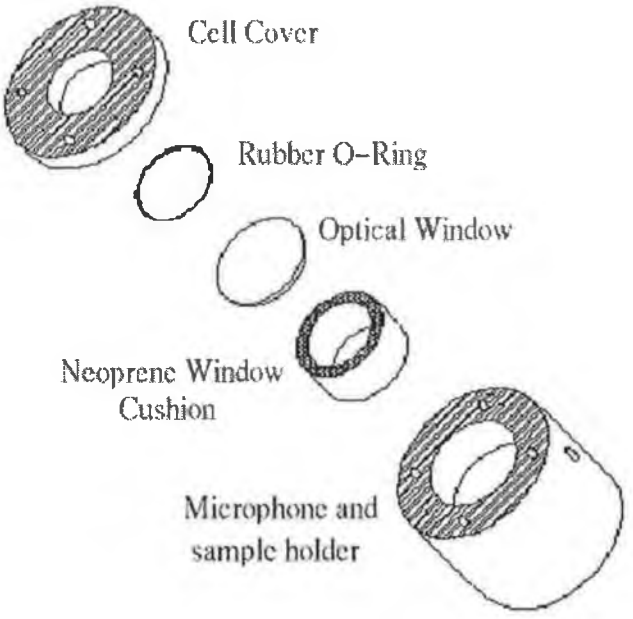

Figure 3.3: Photoacoustic cell used in thesis.

3.5 Optical Hardware

The primary purpose of the optical hardware in the photoacoustic spectrometer is to generate an intensity modulated monochromatic light source that will induce the photoacoustic effect in the semiconductor sample under investigation. To this end, the use of both pulsed and continuous wave lasers is very popular in the literature [55]. Although tunable lasers may be used to perform studies over a narrow photonic range, the more conventional and economic alternative is to use a high power short arc lamp in conjunction with a high-resolution monochromator. The secondary function of the optical hardware is to alter the characteristics of the incident beam. For example, through appropriate design, an optical system at the output of the monochromator could be used to vary the spatial resolution of the system. All of the optical hardware described below has been mounted on a RP Reliance vibrationally damped optical table manufactured by Newport.

3.5.1 Light Source

The intensity modulated light source simply consists of a high power spectrally broad arc lamp that is focused onto the entrance slit of a monochromator. On its way to the monochromator, the light is intensity modulated using an optical chopper. The details of these components are now presented.

3.5.1.1 Short Arc Xenon Lamp

A 300 W xenon short arc lamp manufactured by LOT Oriel, with an arc size of 0.7 mm × 2.4 mm, $f/1$ primary condensing optics, $f/4.6$ secondary coupling optics ($f =$ 150 mm) and high voltage power supply provide the radiation source. A parabolic reflector is situated behind the lamp to enhance device efficiency. As the arc lamp is at the focal point of the primary condensing lens, this lens provides a collimated beam for the secondary lens, which in turn performs the f-number matching with the monochromator situated at its focal point, thus maximising throughput. The lamp provides reasonable constant irradiance from 250 nm to 2400 nm. The lamp is ozone-free and consequently suffers from strong attenuation below 250 nm (above 4.96 eV). In comparison to other non-ozone free lamps of similar output, the constant irradiance above the oxygen cut-on wavelength makes the lamp quite suitable for photoacoustic spectroscopy [56]. The spectral irradiance of the lamp may be examined in Figure 3.4 on page 65.

3.5.1.2 Optical Chopper

A variable frequency enclosed optical chopper manufactured by LOT Oriel is inserted in the path of the collimated beam between the primary and secondary condensing lenses. Hence, the collimated light is intensity modulated before being focused on the entrance slit of the monochromator. An ancillary benefit of the enclosure is the minimisation of acoustic noise arising from the air being chopped. The enclosure surrounding the wheel also aids in safeguarding the user against hazardous scattered

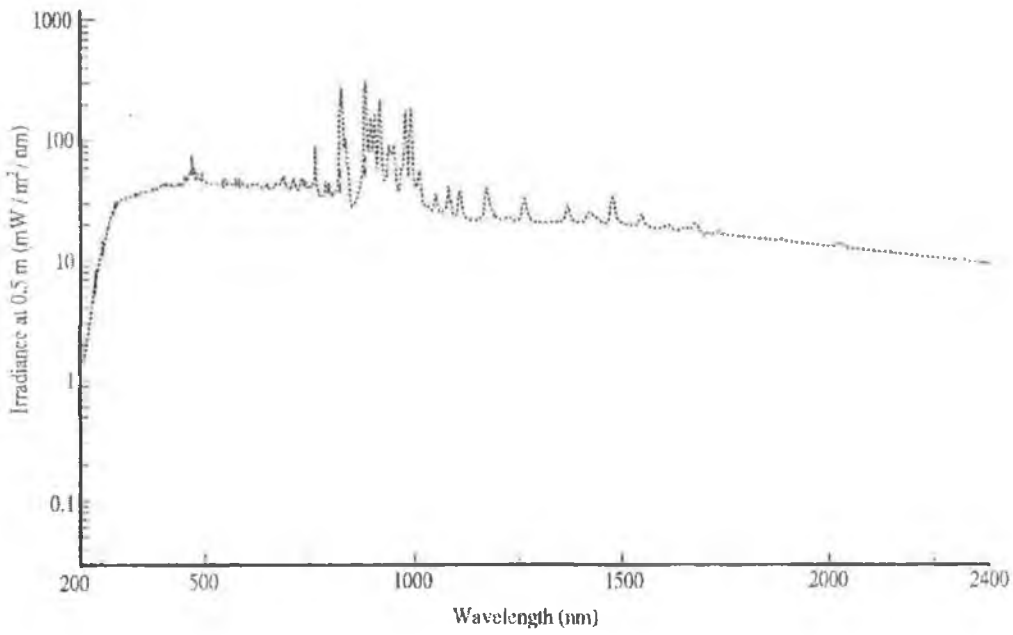

Figure 3.4: Spectral irradiance of 300 W ozone-free xenon arc lamp. Reproduced from [56].

light from the arc lamp. The chopping frequency may be varied from sub-Hz to 3 kHz by selection of an appropriate chopping wheel. Currently, the system is configured to operate at a maximum modulation frequency of 350 Hz. The device may operate in stand-alone mode or from a supplied external reference [56]. In the current system configuration, the reference signal for the optical chopper is supplied by an internal signal generator in the lock-in amplifier. The reason for this is twofold: firstly, it ensures that the detection frequency and excitation frequency are identical with a zero phase difference between them, and secondly, as the frequency generated by the lock-in amplifier is fully programmable this enables control software to be written where the modulation frequency can be varied at the user's discretion. To the best of the author's

knowledge, the latter has not yet been implemented in photoacoustic measurements.

3.5.1.3 High Resolution Monochromator

The Cornerstone 260 monochromator manufactured by LOT Oriel and used in the photoacoustic spectrometer is a true $1/4$ m monochromator. It has entrance and exit focal lengths of 260 mm, a relative aperture of $f/3.9$ and a potential spectral operating range of 180 nm to 20 μm depending on the diffraction gratings used. The limitations imposed by ozone attenuation below 250 nm may be overcome by purging the instrument with nitrogen. The device has a motorised triple grating turret, which facilitates rapid broad-spectrum scans at a maximum scan rate of 175 nm/s.

If monochromatic light strikes a grating, then a fraction of the light is diffracted into each order in accordance with the grating equation. The fraction diffracted into any order can be termed the efficiency of the grating in that order. Gratings are not equally efficient at all wavelengths for numerous reasons as the efficiency can be tuned by changing the number of grooves (or lines) in the grating, the groove facet angles and the shape or depth of the grating lines. The optimisation of efficiency by appropriate groove shaping is known as *blazing*. The blaze wavelength is the wavelength for which the grating is most efficient. Generally two types of grating are used: holographic and ruled. Holographic gratings provide good spectral resolution at the expense of reduced intensity, whilst ruled gratings offer increased intensity over the spectral range of interest at the expense of spectral resolution. The resolution of a grating increases and the throughput decreases with the number of grating lines. With these technical

points and knowledge of the arc lamp spectrum in mind the following gratings were used in the monochromator.

Grating No.	Type	No. of Grooves (l/mm)	λ range (nm)	Blaze λ (nm)
1	Holographic	1200	180 – 650	250
2	Ruled	1200	450 – 1400	750
3	Ruled	600	900 – 2800	1600

Table 3.1: Gratings used in monochromator.

The performance of a monochromator may be evaluated in terms of its resolution, accuracy, precision and dispersion. The bandpass is the spectral width of radiation passed by a monochromator when illuminated by a light source with a continuous spectrum. By reducing the width of the input and output slits of the monochromator, the bandpass may also be reduced until a limiting bandpass is reached. The limiting bandpass is termed the resolution of the device. In spectral analysis, the resolution is a measure of the ability of the instrument to separate two spectral lines that are close together. The resolution of the Cornerstone 260 is 0.15 nm for a 1200 l/mm grating when used with entrance and exit slits with dimension 10 μm $\times$ 2 mm. By judicious variation of the input and output slit widths, a relatively constant bandpass can be obtained for the entire wavelength range of a photoacoustic spectral scan. Attached to the monochromator input and output ports are continuously variable micrometer driven slits whose width may be varied from 4 μm to 3 mm and their height from 2 mm to 15 mm.

The monochromator has an accuracy of 0.35 nm and will reproduce wavelengths to a precision of 0.08 nm. It has an efficiency above 80% for blaze wavelengths and

exhibits high dispersion, typically 0.31 mm/nm and 0.16 mm/nm for the wavelength ranges 180 nm to 1400 nm and 900 to 2800 nm, respectively.

Coupled to the output slit of the monochromator is a six-position filter wheel. For the spectral range of interest, three filters are necessary to remove the effect of higher order harmonic contamination in the output spectrum. The filters and the associated grating wavelength ranges that they operate for are presented in Table 3.2. These order-sorting filters will also minimise the effect of stray re-entrant light in the monochromator. In a system with the potential to scan such a large range of wavelengths, this component becomes an integral part of the system. The filter change mechanism is controlled directly by the monochromator, which itself may be controlled using a dedicated hand controller, the IEEE 488.2 GPIB or the RS-232 communication protocols [56].

Filter No.	Cut-on wavelength (nm)	Grating No.	λ range (nm)
2	324	1	340 – 650
4	830	2	850 – 1200
6	1600	3	1750 – 2400

Table 3.2: Filters used with monochromator.

3.5.1.4 Photonic Power Incident from Light Source

The reader will now be presented with an order of magnitude estimation of the photonic power at the exit port of the light source. Suppose the monochromator is operating at 450 nm and the slits have been opened to their maximum (3 mm in width by 15 mm in height) to facilitate maximum throughput. Taking into consideration the irradiance of the lamp and geometrical factors such as the presence of a parabolic reflector, the

power provided by the arc lamp at 450 nm is 4.75 mW/nm. As the fused silica lens used in the primary and secondary condensers are approximately 90% transparent over the wavelength range of interest, this implies that 3.85 mW/nm power is provided at the output of the secondary condenser.

The magnification m of the condenser-secondary lens assembly is given by the ratio of their f-numbers as follows:

$$m = \frac{f/\#_{\text{secondary}}}{f/\#_{\text{condenser}}} = \frac{4.6}{1} = 4.6 \tag{3.2}$$

Therefore, the size of the image of the arc lamp source at the monochromator entrance slit will be 3.2 mm in width by 11.0 mm in height.

Assuming uniform image irradiance, the fraction of the image that passes through the entrance slit of the monochromator is given by the vignetting factor V. Since the image is wider but not taller than the entrance slit, the vignetting factor is found with respect to the horizontal beam size:

$$V = \frac{3}{3.2} = 0.93 \tag{3.3}$$

Therefore, the power entering the monochromator is given by the product of the vignetting factor with the power at the output of the secondary condenser. This is 3.58 mW/nm. The bandwidth $\Delta\lambda$ that a 3 mm slit will admit is given by the product of the reciprocal linear dispersion and the slit width w:

$$\Delta\lambda = w\frac{d\lambda}{dL} \tag{3.4}$$

where L is width of the spectral beam. Now the linear dispersion is given by the product of the focal length f of the monochromator and the angular dispersion of the grating. By differentiating Equation 3.1 with respect to λ one can obtain the angular dispersion.

$$\therefore \frac{d\theta}{d\lambda} = \frac{g}{a\cos\theta} \tag{3.5}$$

$$\Rightarrow \frac{dL}{d\lambda} = f\frac{d\theta}{d\lambda} = \frac{fg}{a\cos\theta} \tag{3.6}$$

Therefore, the reciprocal linear dispersion is:

$$\frac{d\lambda}{dL} = \frac{a\cos\theta}{fg} \tag{3.7}$$

At $\lambda = 450$ nm the reciprocal linear dispersion is 3.8 nm/mm. Therefore, the bandwidth passed is:

$$\Delta\lambda = w\frac{d\lambda}{dL} = 11.4 \text{ nm} \tag{3.8}$$

Consequently, the power admitted into the monochromator within this spectral bandwidth is:

$$P_i = 3.58 \text{ mW/nm} \times 11.4 \text{ nm} = 40.8 \text{ mW} \tag{3.9}$$

Assuming the grating has an efficiency of $\epsilon_g = 50\%$ at 450 nm and taking into consideration that the light undergoes reflection from four azimuthal aluminum mirrors with a reflectivity of $R = 88\%$ implies the power at the output port of the monochromator is:

$$P_o = P_i\epsilon_g R^4 = 12.95 \text{ mW} \tag{3.10}$$

In the previous analysis, the intensity modulation of the light by the chopper has not been taken into consideration.

3.5.2 Focusing Optics

Spectral resolution has not been a major design constraint in this system. In the future, if it does become important, then the experimenter can replace the hand driven slits with computer controlled motor driven slits. By varying the slit width according to the spectral position, one can achieve a constant spectral bandpass over the energy range of interest. This thesis has centered on the design of focusing optics for intensity maximisation and spatially resolved photoacoustic studies. In this section the operation of the focusing optics will be explained. The only major design constraint was that the materials used in the lenses had to be as optically transparent as possible over the wavelength range of interest, i.e. 200 nm to 2.4 μm.

3.5.2.1 Configuration A. Intensity Maximisation

As the photoacoustic effect is directly proportional to the intensity of the incident light source I_0, this implies that as much of the power from the output port of the monochromator should be focused into as small an area as possible. However, if this area is too small, insufficient heating of the gas volume in contact with the sample will occur, thus failing to generate an appreciable pressure variation that can be measured by the microphone. For this reason, it has been decided to focus the output beam by a magnification factor of approximately $m = 0.3$. Hence, the 3 mm by 12 mm output beam

will be converted into a beam approximately 1 mm by 4 mm in size.

Starting with the basic lens equation [57]:

$$\frac{1}{f} = \frac{1}{u} + \frac{1}{v} \tag{3.11}$$

and reformulating the magnification of a single lens yields:

$$m_{sl} = \frac{v}{u} = \frac{f_{sl}}{u_{sl} - f_{sl}} \tag{3.12}$$

where u is the object distance, v is the image distance and the subscript sl denotes single lens. This equation implies that for a real image to be formed by a single lens, two constraints must be satisfied:

1. The focal length $f_{sl} > 0$.

2. The object distance $u_{sl} > f_{sl}$.

If either of these constraints is ignored a virtual image will be generated. The second constraint implies $u_{sl} = \alpha f_{sl}$ for some $\alpha > 1$. Consequently, Equation (3.12) may be re-written as:

$$m_{sl} = \frac{1}{\alpha - 1} \tag{3.13}$$

Figure 3.5 demonstrates that a single lens only provides realistic real image focusing in the magnification range $1 \leq m \leq 2$. Outside this range the object distance becomes physically impractical with respect to the numerical aperture of the lens. Therefore, a

two lens imaging system must be considered.

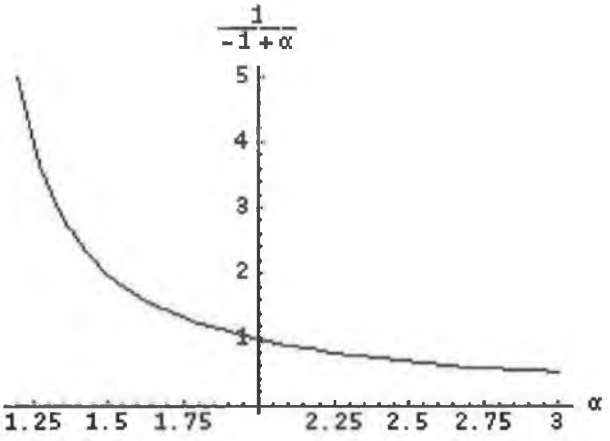

Figure 3.5: Plot of fractional variation in object distance versus magnification for a single lens.

Consider, the general optical system composed of two lenses as shown in Figure 3.6. The object distances have been chosen to be greater than the focal lengths of the lenses to ensure real images are created.

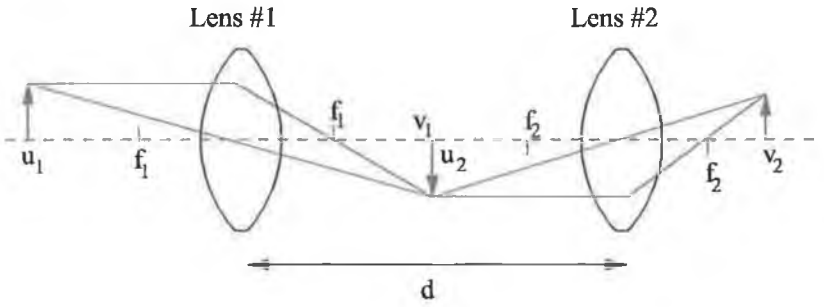

Figure 3.6: Optical system consisting of two lenses separated by a distance *d*. Biconvex lenses have been drawn, however the mathematical derivation in the text applies to lenses with both positive and negative focal lengths once the sign convention is adhered to.

The magnification of the system is the combined magnification of the individual lenses [58]:

$$m_{1,2} = m_1 m_2 = \frac{v_1}{u_1}\frac{v_2}{u_2} \tag{3.14}$$

Since

$$m_1 = \frac{f_1}{u_1 - f_1} \tag{3.15}$$

and $u_2 = d - v_1$

$$\Rightarrow m_{1,2} = \frac{f_1 v_2}{d\,(u_1 - f_1) - u_1 f_1} \tag{3.16}$$

Using a biconcave lens with a focal length $f_1 = -30$ mm and biconvex lens with a focal length $f_2 = 50$ mm one obtains a combined magnification $m_{1,2} = -0.32$ for an inter-lens separation distance of 50 mm. The minus sign in the magnification means the image of the source is inverted. This is inconsequential as we assumed equal irradiance in all parts of the beam, i.e. the beam is the same above and below the principal axis.

3.5.2.2 Configuration B. Spatial Resolution

In this subsection, the output optical configuration for spatially resolved photoacoustic studies will be examined. The goal of this sub-system is to focus the 3 mm by 12 mm rectangular beam at the output port of the monochromator into a circular shaped beam incident on the sample with a diameter variable between 1 mm and 12 mm. This design has been formulated in an iterative manner; we will therefore only examine the optimal solution.

Consider the completed lens and mirror assembly shown in Figure 3.7 on page 76. The

combination of the concave mirror and cylindrical lens (which focuses in one plane only) generate an image on the first plane mirror that is the same size in the horizontal and vertical directions. By varying the distance between the biconcave and biconvex lens one can vary the size of the beam that strikes the second plane mirror. Therefore, one can vary the size of the beam impinging on the sample. The photoacoustic cell is mounted on a computer controlled X-Y translational stage. Thus fully automated spatially resolved photoacoustic scans are possible. Using paraxial ray theory analysis, general component specifications will be derived. Ray tracing analysis will then be used to determine the size of the beam striking the mirror as a function of the inter-lens distance.

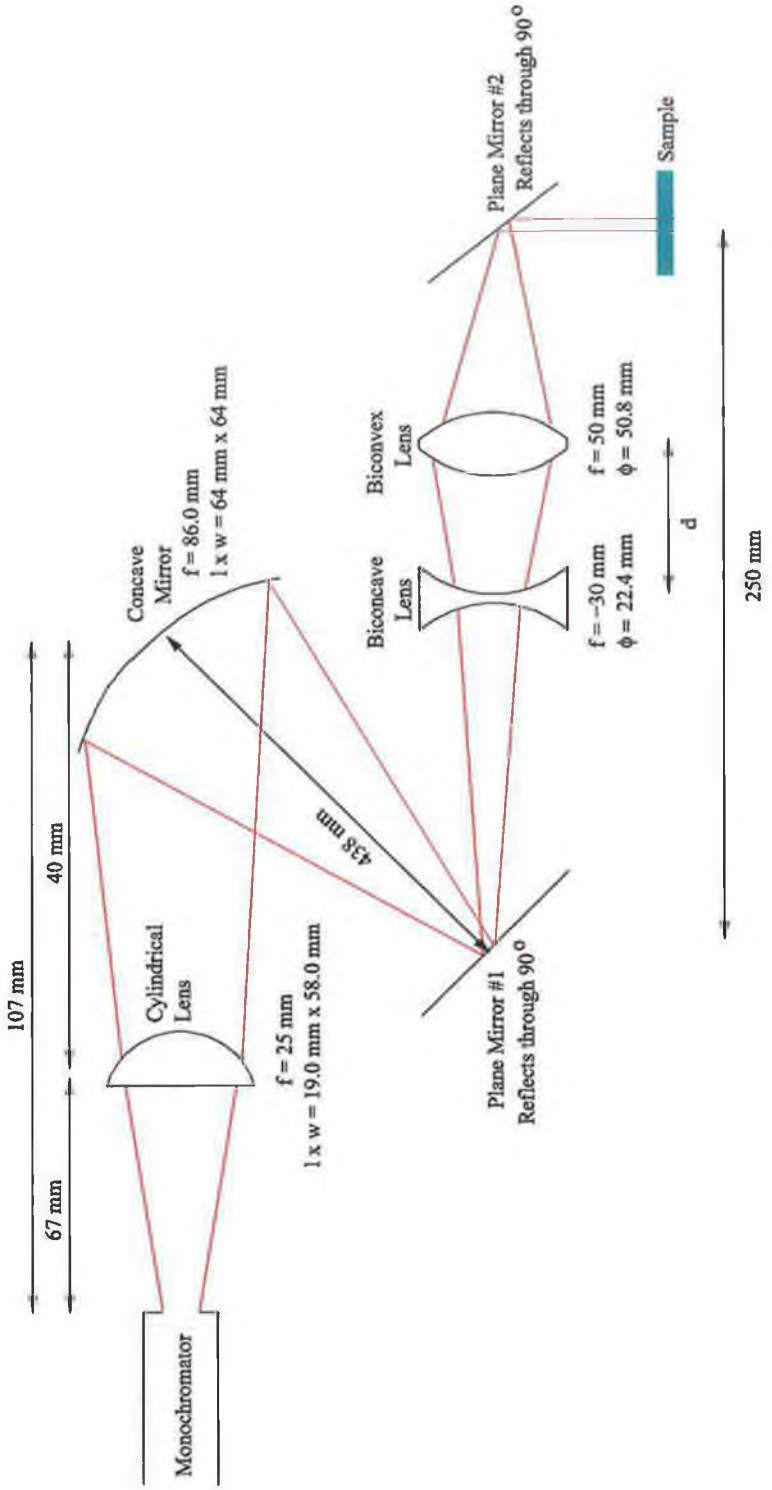

Figure 3.7: Output optical configuration for spatially resolved photoacoustic studies.

Paraxial Ray Theory Analysis

At a distance u from the output of the monochromator, the beam size has been experimentally ascertained to be:

$$w = 0.15u + 0.5 \qquad \text{Horizontal size in mm} \qquad (3.17)$$

$$h = 0.166u + 6.76 \qquad \text{Vertical size in mm} \qquad (3.18)$$

Now the magnification of the cylindrical lens may be written as:

$$m_{cyl} = \frac{w}{h} \qquad (3.19)$$

Inserting Equations (3.17) and (3.18) into Equation (3.19) and solving for the system parameters results in $u_{cyl} = 67$ mm, $v_{cyl} = 40$ mm and $m_{cyl} = 0.6$. Using Equation (3.12) we ascertain that the focal length of the cylindrical lens must be 25 mm. The beam size hitting the cylindrical lens prior to de-magnification in the vertical plane is 11 mm × 18 mm. A UV grade fused silica cylindrical lens with $f_{cyl} = 25.4$ mm possessing dimensions of 19.0 mm by 50.8 mm satisfying these design requirements is used in the optical train.

The object distance for the concave mirror $u_m = u_{cyl} + v_{cyl} = 107$ mm. The image size on the concave mirror is approximately 17 mm^2. Using the lens equation for this mirror results in $v_m = 438$ mm and $m_m = 4.1$. Consequently, the image size on the first plane mirror is approximately 12 mm^2.

The combination of the biconcave and biconvex lenses focuses the image on the first plane mirror onto the second plane mirror. From Section 3.5.2.1 it is known that a single lens is incapable of providing the magnification requirement $0.1 \leq m \leq 1.0$. Therefore, two lenses are required. Re-consider Equation (3.16) and its application to Figure 3.6. In paraxial ray analysis it is not possible to estimate the magnification at a fixed distance from the source as the inter-lens distance is varied; one can only estimate the magnification at the point the light rays come to focus. The focusing optics consists of a biconcave lens with $f_1 = -30$ mm and a biconvex lens with $f_2 = 50$ mm. The following constraints ensure real images are formed. For the diverging lens $\alpha u_1 = f_1$ where $\alpha < 1$ and for the converging lens $\zeta u_2 = f_2$ where $\zeta > 1$.

$$\Rightarrow v_2 = \frac{\zeta}{\zeta - 1} f_2 \tag{3.20}$$

For simulation purposes Equation (3.16) reduces to:

$$m_{1,2} = \frac{\zeta f_2}{[d(\alpha - 1) - \alpha f_1](\zeta - 1)} \tag{3.21}$$

Figure 3.8 shows the magnification of the system as a function of the object distance u_1 and inter-lens distance d for a biconvex and biconcave lens system with focal lengths $f_1 = -30$ mm and $f_2 = 50$ mm, respectively. Figure 3.9 shows the total distance from the source to the point of focus as a function of the object and inter-lens distances. From both figures, one can see that the magnification requirement is satisfied. Also the total object to image distance is less than 30 cm making implementation on a standard

optical table quite easy.

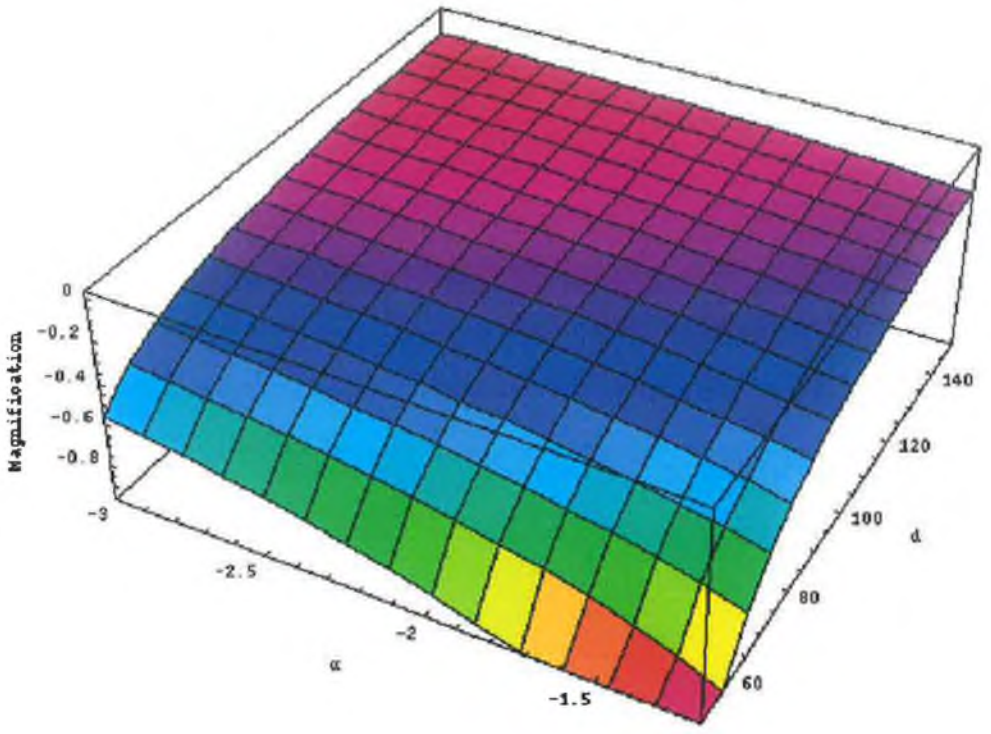

Figure 3.8: Magnification of two lens system as a function of object distance $u_1 = \alpha f_1$ and inter-lens distance d. The biconcave lens has a focal length $f_1 = -30$ mm and the biconvex lens has a focal length $f_2 = 50$ mm. A negative magnification indicates an inverted image.

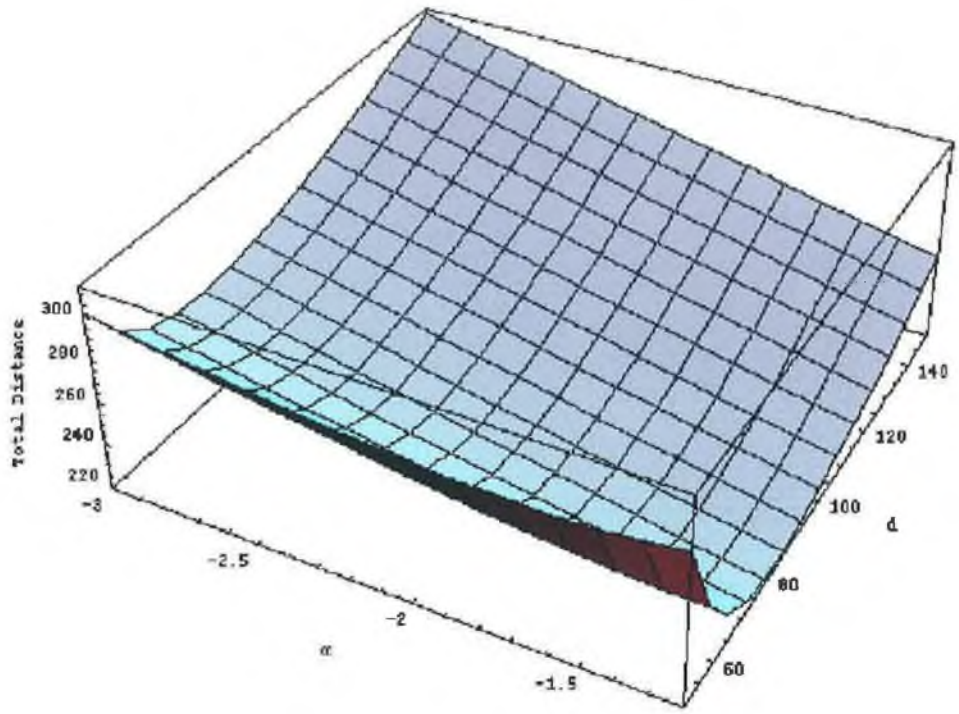

Figure 3.9: Total distance $(u_1 + d + v_2)$ of two lens system from object to image as a function of object distance u_1 and inter-lens distance d. The total distance demonstrates that all images are real.

Ray Tracing Analysis

The proceeding analysis is only valid for paraxial rays. Unfortunately, the reflected beam from the first plane mirror will be divergent. For most applications it would be desirable to leave the sample cell and plane mirrors in the same position on the optical table and vary the spatial resolution via the inter-lens distance. All of these requirements preclude the use of ray tracing for the analysis of the system magnification.

As the beam has been conditioned by the combination of the cylindrical lens and concave mirror to possess uniform divergence, the analysis will be confined to meridional rays and the effects of skew rays will be neglected. The beam reflected from the first plane mirror in Figure 3.7 diverges at an angle α_{i_1} and strikes the biconcave lens at a position y_{i_1} as illustrated in Figure 3.10. In the following derivation, all heights above the optical axis are defined positive and those below, negative. Similarly, all anticlockwise angles above the optical axis are defined positive and all clockwise angles below the optical axis are defined negative.

Applying *Snell's Law* at the entrance to the biconcave lens yields:

$$n_{i_1} \sin \theta_{i_1} = n_{t_1} \sin \theta_{t_1} \tag{3.22}$$

where

$$\begin{aligned} \theta_{i_1} &= \alpha_1 - \alpha_{i_1} \\ \theta_{t_1} &= \alpha_1 - \alpha_{t_1} \end{aligned} \tag{3.23}$$

$$\therefore \alpha_{t_1} = \alpha_1 - \sin^{-1}\left[\frac{n_{i_1}}{n_{t_1}} \sin\left(\alpha_1 - \alpha_{i_1}\right)\right] \tag{3.24}$$

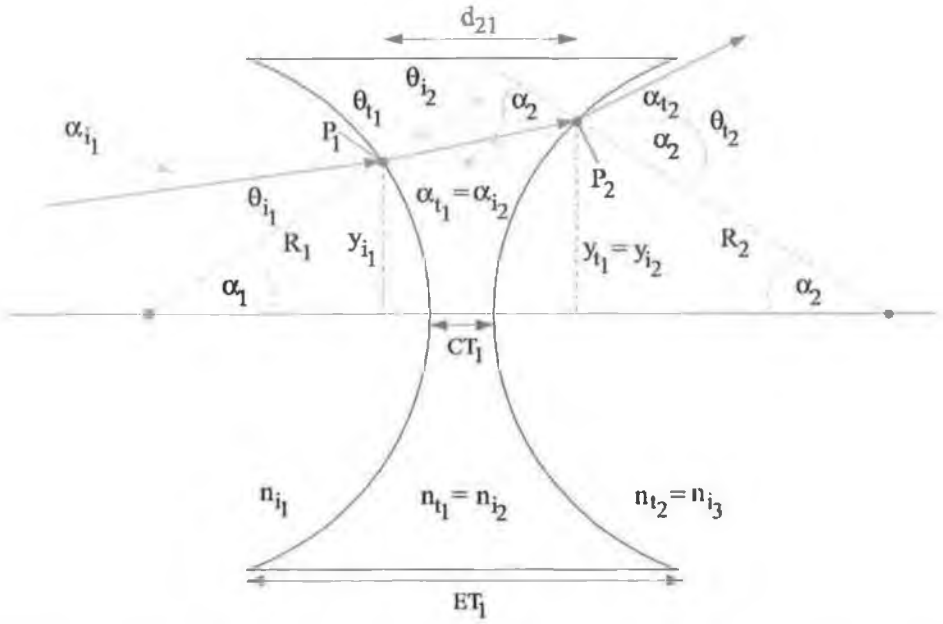

Figure 3.10: Optical path of meridional ray through biconcave lens. The ray strikes the lens surface at position P_1 making an angle θ_{i_1} with respect to the surface normal. The object distance is always greater than the focal length. The lens has centre thickness $CT_1 = 1.5$ mm, refractive index $n_{i_2} = 1.4649$, diameter $\phi_1 = 22.4$ mm and radius of curvature $R_1 = R_2 = 30.92$ mm.

The height of the beam above the optical axis at the exit of the lens is:

$$y_{t_1} = y_{i_1} + \Delta y_{i_1} \tag{3.25}$$

The derivation for Δy_{i_j} where $j \in \{1, 2, 3, 4\}$ can be found in Appendix B.

Similarly at the exit of the lens *Snell's Law* yields:

$$n_{i_2} \sin \theta_{i_2} = n_{t_2} \sin \theta_{t_2} \tag{3.26}$$

$$\theta_{i_2} = \alpha_2 + \alpha_{i_2}$$
$$\theta_{t_2} = \alpha_2 + \alpha_{t_2} \tag{3.27}$$

$$\therefore \alpha_{t_2} = \sin^{-1}\left[\frac{n_{i_2}}{n_{t_2}} \sin\left(\alpha_2 + \alpha_{i_2}\right)\right] - \alpha_2 \tag{3.28}$$

$$y_{t_2} = y_{i_2} + \Delta y_{i_2} \tag{3.29}$$

The ray trajectories through the biconvex lens are illustrated in Figure 3.11.

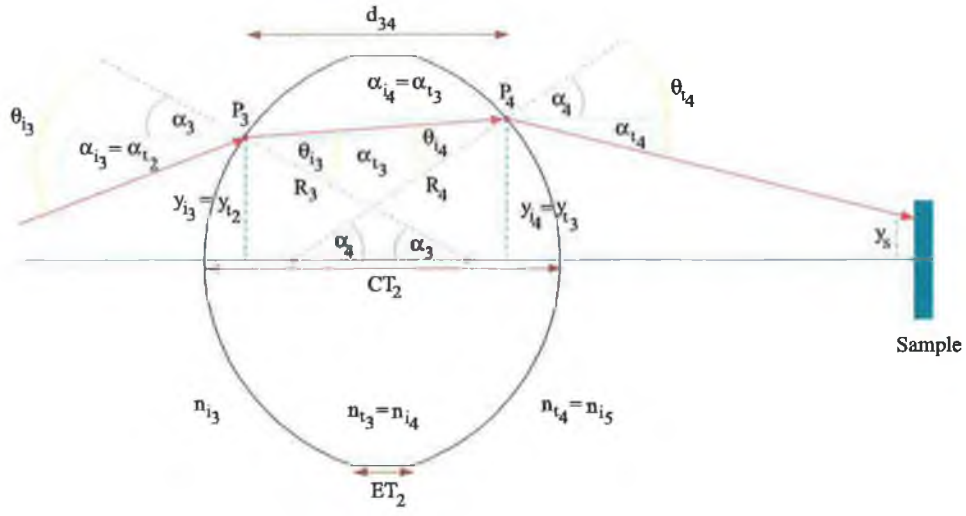

Figure 3.11: Optical path of meridional ray through biconvex lens. The ray strikes the lens surface at position P_3 making an angle θ_{i_3} with respect to the surface normal. The object distance is always greater than the focal length. The lens has a centre thickness $CT_2 = 19.73$ mm, diameter $\phi_2 = 50.8$ mm, refractive index $n_{i_4} = 1.4649$ and radius of curvature $R_3 = R_4 = 42.73$ mm.

Applying Snell's Law with respect to the incident ray yields:

$$n_{i_3} \sin\theta_{i_3} = n_{t_3} \sin\theta_{t_3} \tag{3.30}$$

$$\begin{aligned} \theta_{i_3} &= \alpha_3 + \alpha_{i_3} \\ \theta_{t_3} &= \alpha_3 + \alpha_{t_3} \end{aligned} \tag{3.31}$$

$$\therefore \alpha_{t_3} = \sin^{-1}\left[\frac{n_{i_3}}{n_{t_3}}\sin\left(\alpha_3 + \alpha_{i_3}\right)\right] - \alpha_3 \tag{3.32}$$

$$y_{t_3} = y_{i_3} + \Delta y_{i_3} \tag{3.33}$$

Now

$$n_{i_4}\sin\theta_{i_4} = n_{t_4}\sin\theta_{t_4} \tag{3.34}$$

$$\begin{aligned} \theta_{i_4} &= \alpha_4 - \alpha_{t_3} \\ \theta_{t_4} &= \alpha_4 + \alpha_{t_4} \end{aligned} \tag{3.35}$$

$$\therefore \alpha_{t_4} = \sin^{-1}\left[\frac{n_{i_4}}{n_{t_4}}\sin\left(\alpha_4 - \alpha_{i_4}\right)\right] - \alpha_4 \tag{3.36}$$

As the ray governed by the angle α_{t_4} travels downwards with respect to the optical axis, it should be defined as negative in any simulation. Only the size of the angle is provided by Equation (3.36).

$$\therefore y_s = y_{i_4} + \Delta y_{i_4} \tag{3.37}$$

See Appendix B for y_{i_4}.

In Figure 3.10, the ray is indicated as hitting the sample. In the actual experimental configuration, the ray will be reflected onto the sample by a plane mirror. As the sample to mirror distance will be smaller with respect to the mirror to biconvex lens

distance, any convergence or divergence of the beam will be negligible. Consequently, the size of the beam impinging on the mirror may be considered to be the size of the beam impinging on the sample.

The magnification of the system according to the ray tracing analysis may be defined as

$$m_{rt} = \frac{y_o}{y_s} \tag{3.38}$$

where y_o and y_s are the heights of the object and image above the principal optical axis respectively.

The previous analysis was simulated for an object with height 6 mm above the optical axis. The ray incident on the first lens was parallel to the principal axis so a quantitative comparison with the results of Figure 3.8 could be made. The total distance of the system was defined to be 250 mm. This is unlike the paraxial ray theory analysis where the final image distance v_2 was taken to be the point where the rays came to focus. That is, in the paraxial ray theory analysis, the position of the sample was variable and in the ray tracing analysis, it is fixed. The results are shown in Figure 3.12.

An analysis of the results clearly demonstrates that the output optical system meets the system specifications i.e. it is capable of providing magnification over an order of magnitude from 0.1 to 1.

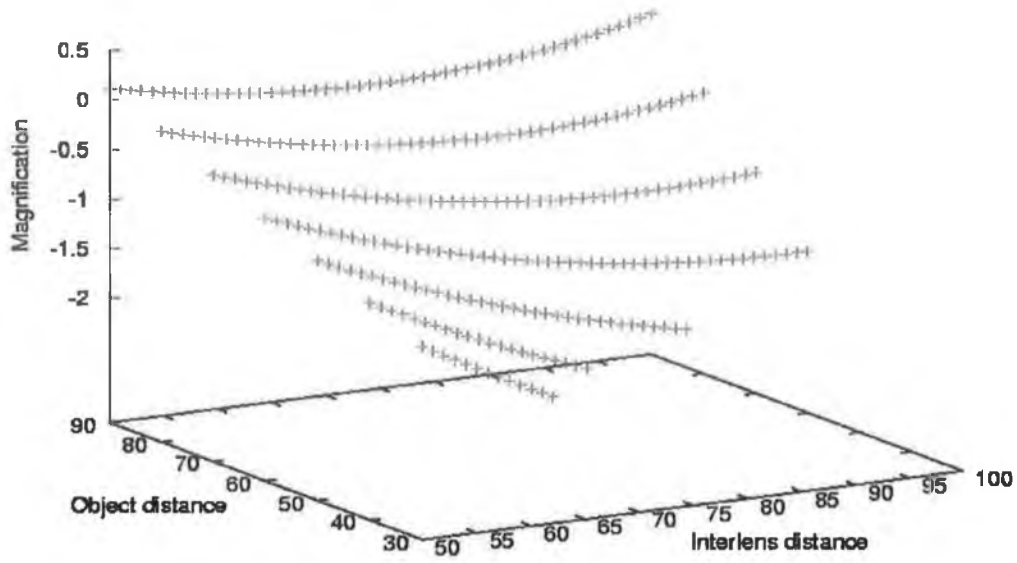

Figure 3.12: Ray tracing results for object 6 mm above the principal axis. The total distance between the object and the image was 250 mm. A negative magnification implies an inverted image.

3.6 Electrical Hardware

Data from early spectrometers was recorded using X-Y plotters or very basic microcomputers [59]. Real time spectra normalisation was only a dream with these systems. Modern photoacoustic spectrometers do not suffer from these drawbacks as personal computers are relatively cheap and can be used to acquire data from the lock-in amplifiers whilst simultaneously controlling the monochromator.

3.6.1 Lock-in Amplifier

Periodic AC signals as low as a few nanovolts can be detected using lock-in amplification. This is achieved by a technique known as phase sensitive detection, whereby it is possible to single out the component of a signal at a specific reference frequency and

phase. An important part of this process is that noise signals at frequencies other than the reference frequency are rejected. Hence, they do not affect the measurement.

The following example will help to illustrate the process. In the following hypothetical experiment, the reference signal to the lock-in amplifier is a square wave with frequency ω_{ref} [60]. Now suppose the output signal from the experiment is a sine wave of frequency ω_{sig}. Using a phase-locked-loop (PLL), the amplifier generates a reference signal with the same frequency as the sine wave but with a fixed phase shift θ_{ref}. Since the PLL actively tracks the external reference, changes in the external reference frequency do not affect the measurement. The experimental signal is multiplied by the reference signal using a phase sensitive detector (PSD). The output of the PSD is the product of the two sine waves in this example:

$$V_{\text{psd}} = V_{\text{sig}} V_{\text{lock-in}} \sin(\omega_{\text{ref}} t + \theta_{\text{sig}}) \sin(\omega_{\text{lock-in}} t + \theta_{\text{ref}}) \tag{3.39}$$

This signal is amplified and low pass filtered. When $\omega_{\text{ref}} = \omega_{\text{lock-in}}$ a DC component will remain. In this case the output of the PSD will be:

$$V_{\text{psd}} = \frac{1}{2} V_{\text{sig}} V_{\text{lock-in}} \cos(\theta_{\text{sig}} - \theta_{\text{ref}}) \tag{3.40}$$

Therefore, using lock-in detection one can obtain a DC signal proportional to the experimental signal amplitude without any noise superimposed on it.

The overall performance of a lock-in amplifier is largely determined by the perfor-

mance of its phase sensitive detectors. In virtually all respects, the digital PSD outperforms its analogue counterpart. Analogue PSD's have many problems associated with them, namely harmonic rejection, output offsets, limited dynamic reserve and gain error [60]. The lock-in amplifier used in the photoacoustic spectrometer is the Stanford Research Systems SR830 digital signal processing amplifier. The amplifier converts the amplified experimental signal using a 16 bit ADC that has a sampling frequency of 256 kHz. An anti-aliasing filter prevents higher frequency inputs from aliasing below 102 kHz. Using the digital PSD's linear multipliers, the digitised experimental signal is multiplied with the digitally computed reference signal. The reference sine wave may be considered "pure" as all harmonics are attenuated with a dynamic reserve of 100 dB. The lock-in amplifier has time constants from 10 μs to 30 ks with 6 dB to 24 dB per octave filter rolloff. The internally generated reference signal is accurate to within 25 ppm and phase measurements can be made with a resolution of 0.01°. The amplifier provides dual inputs and outputs in conjunction with an output reference port. Inputs can be supplied in differential or single ended mode. The two data displays can be used for the display of X and Y or R and θ. The amplifier is fully programmable under the IEEE 488.2 GPIB protocol [60].

3.6.2 Low-noise Preamplifier

To further enhance the electrical signal generated by the microphone, the use of a Stanford Research Systems SR552 low-noise bipolar input voltage preamplifier has been employed. The preamplifier is designed to supply gain to the experimental detector,

before the signal to noise ratio is permanently degraded by cable capacitance and noise pick-up. The amplifier has an input impedance of 100 kΩ + 25 pF and a common mode rejection ratio of 110 dB at 100 Hz. Signals can be supplied in differential or single-ended mode. It has a full-scale sensitivity from 10 nV to 200 mV. Thus the preamplifier minimises noise and reduces measurement time in noise limited experiments making it an ideal addendum to the photoacoustic spectrometer. The power and control signals for the device are supplied directly by the SR830 lock-in amplifier. When used in conjunction with the lock-in amplifier, the gain is set to 10. It is therefore necessary to divide all output measurements by 10 to obtain the true measurement value [61, 62].

3.6.3 Electrical Connections

Due to the small size of the microphone and its positioning within the photoacoustic cell, attachment of coaxial cables to the signal lines was not possible. Therefore, small insulated wires from the microphone were connected inside a Gaussian shield to a twisted coaxial network that was fed to the input preamplifier in a differential mode configuration. The output from the preamplifier was also fed to the lock-in amplifier through twisted pair coaxial cables in a differential mode configuration. The microphone requires a supply voltage of 0.9 V to 1.6 V volts and this was supplied from a standard laboratory power supply. All of the electronic circuitry i.e. the microphone and its power supply, the lock-in amplifier, the optical chopper driver and the monochromator were all powered from a mains voltage supply independent to that supplying the arc lamp power supply. This ensured any potential voltage variations

due to the operation of the lamp did not couple into the rest of the system.

3.7 Control Hardware

The full potential of the optical and electrical equipment previously described can only be harnessed by placing the entire system under the control of a personal computer. All the equipment in the system may be controlled directly or indirectly via the IEEE 488.2 GPIB or RS-232 communication standards. Conventional GPIB provides a modular robust approach for interfacing up to fifteen devices on a single data bus. Unlike RS-232, where parameters such as baud rate, parity and the number of stop bits have to be known, any device adhering to the GPIB standard may be connected to the bus with little or no knowledge of its communication requirements. In conjunction, RS-232 does not readily permit simultaneous communication with several devices without the use of sophisticated hardware or software routines.

GPIB devices communicate with each other by sending device-dependent messages and interface messages through the interface system. Device-dependent messages, commonly known as data messages, contain device specific information such as programming instructions that control its operation. Interface messages are primarily concerned with bus management. Interface messages perform functions such as initialising the bus and addressing devices. GPIB devices may be categorised as *talkers*, *listeners* and *controllers*. Listeners are devices that may receive data transmitted by a talker. For example, in the spectrometer, the lock-in amplifier acts as both a talker (transmitting data to the computer) and a listener (acquiring data from the microphone via

the preamplifier). The controller, a PCI card in this application, manages the flow of information on the bus by sending commands to all the devices.

Devices are usually connected via a shielded 24-conductor cable with both a plug and receptacle connector at each end. The bus uses negative logic with standard TTL levels. In order to achieve the high data transmission rates, nominally 1.5 Mbytes/s when using a PCI controller, the physical distance between devices is limited as follows. The maximum separation between any two devices should be less than 4 m and the average device separation must not be greater than 2 m over the entire bus. The total cable length must not exceed 20 m. This will clearly not be a problem for the photoacoustic spectrometer implemented in this thesis [63].

3.8 Software

The software developed for the photoacoustic spectrometer essentially falls into two functional categories, that of data acquisition and data processing. The data acquisition software is responsible for the communication and control of all the experimental apparatus. Due to the low signal to noise ratio inherent in photoacoustic spectroscopy, once spectra have been recorded they normally have to undergo processing of some sort before they can be interpreted correctly.

3.8.1 Data Acquisition Software

An ancillary benefit of the IEEE 488.2 GPIB standard is that several companies have developed sophisticated high-level application development tools to enable engineers

to provide application specific user interfaces to their GPIB fostered systems. LabView®, a product of National Instruments Inc., is a graphical program development environment. LabView® programs are called virtual instruments, or VIs for short, because their appearance and operation mimic the actual operation of the device they communicate with. A VI consists of an interactive user interface, a data-flow diagram that serves as the source code and icon connections that allow the VI to be called from higher level VIs. When amalgamated with LabView® GPIB compliant instrument drivers, sophisticated control systems may be developed with little time overhead [64].

Several VIs have been written to control both the monochromator and the lock-in amplifier. Tables 3.3 and 3.4 describe the main virtual instruments that have been implemented to date. Each VI is referenced by a unique number and letter so that the inter-dependence of various VIs on one another can be illustrated.

Ref. No.	VI name	Function	Dependence
M1	MonoSendMessage.vi	Sends a command to the monochromator	
M2	MonoReceiveMessage.vi	Receives a string from the monochromator	
M3	MonoGetLambda.vi	Finds the current wavelength	M1,M2
M4	MonoGoLambda.vi	Changes to a specific wavelength	M1,M5,M7,M8
M5	MonoGetGrating.vi	Finds the current grating	M1, M2
M6	MonoGoGrating.vi	Changes to a specific grating	M1
M7	MonoFindGratingLambda.vi	Finds grating applicable to a given λ	
M8	MonoGetFilter.vi	Finds which filter is operating	M1,M2
M9	MonoGoFilter.vi	Changes to a given filter	M1, M2
M10	MonoFindFilterLambda.vi	Finds filter applicable to a given λ	
M11	MonoShutter.vi	Opens or closes the shutter	M1

Table 3.3: Monochromator virtual instruments and their inter-dependence.

Ref. No.	VI name	Function	Dependence
L1	LockInSendMessage.vi	Sends a command to the amplifier	
L2	LockInReceiveMessage.vi	Receives a string from the amplifier	
L3	LockInAmplifierSetup.vi	Configures the amplifier	L1, L2
L4	LockInReadDisplay.vi	Reads a specified display	L1, L2
L5	LockInReadAuxIn.vi	Reads a specified analogue auxiliary input	L1, L2

Table 3.4: Lock-in Amplifier virtual instruments and their inter-dependence.

3.8.1.1 Photoacoustic Energy Scan

The impetus behind this part of the thesis was to design a photoacoustic spectrometer for the characterisation of sub-bandgap absorption defects. The most common VI used for such studies will be examined. The actual graphical interface as seen by the user is shown in Figure 3.13. Consider the flowchart for the photoacoustic energy scan VI illustrated in Figure 3.14. Prior to starting the VI, the user enters the start wavelength, end wavelength and wavelength increment for the scan. The user specifies the number of scans that are to be performed and also provides the details of where the data is to be stored. The VI is then started and proceeds according to the flowchart.

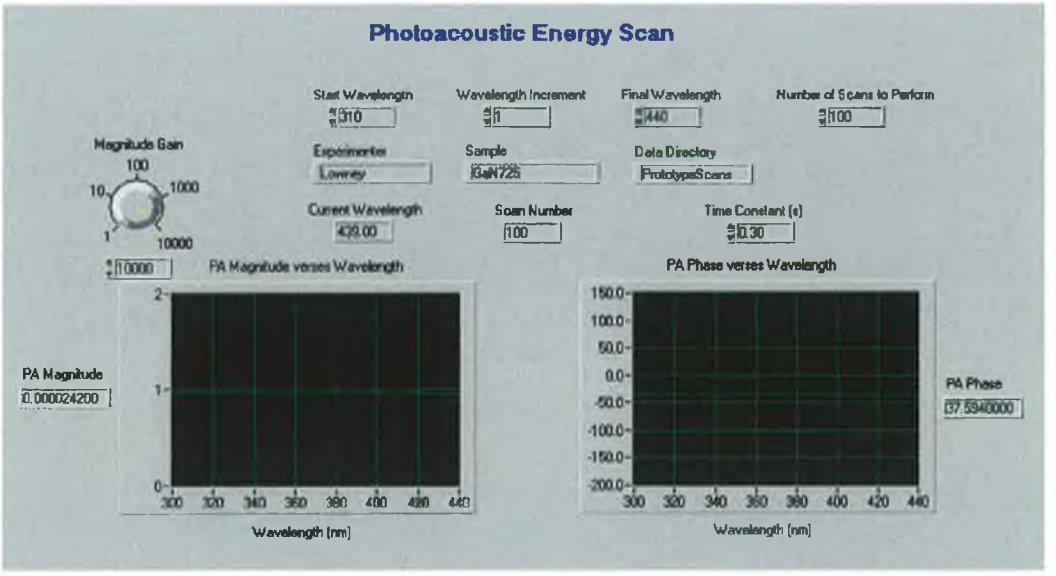

Figure 3.13: Graphical user interface for photoacoustic energy scan.

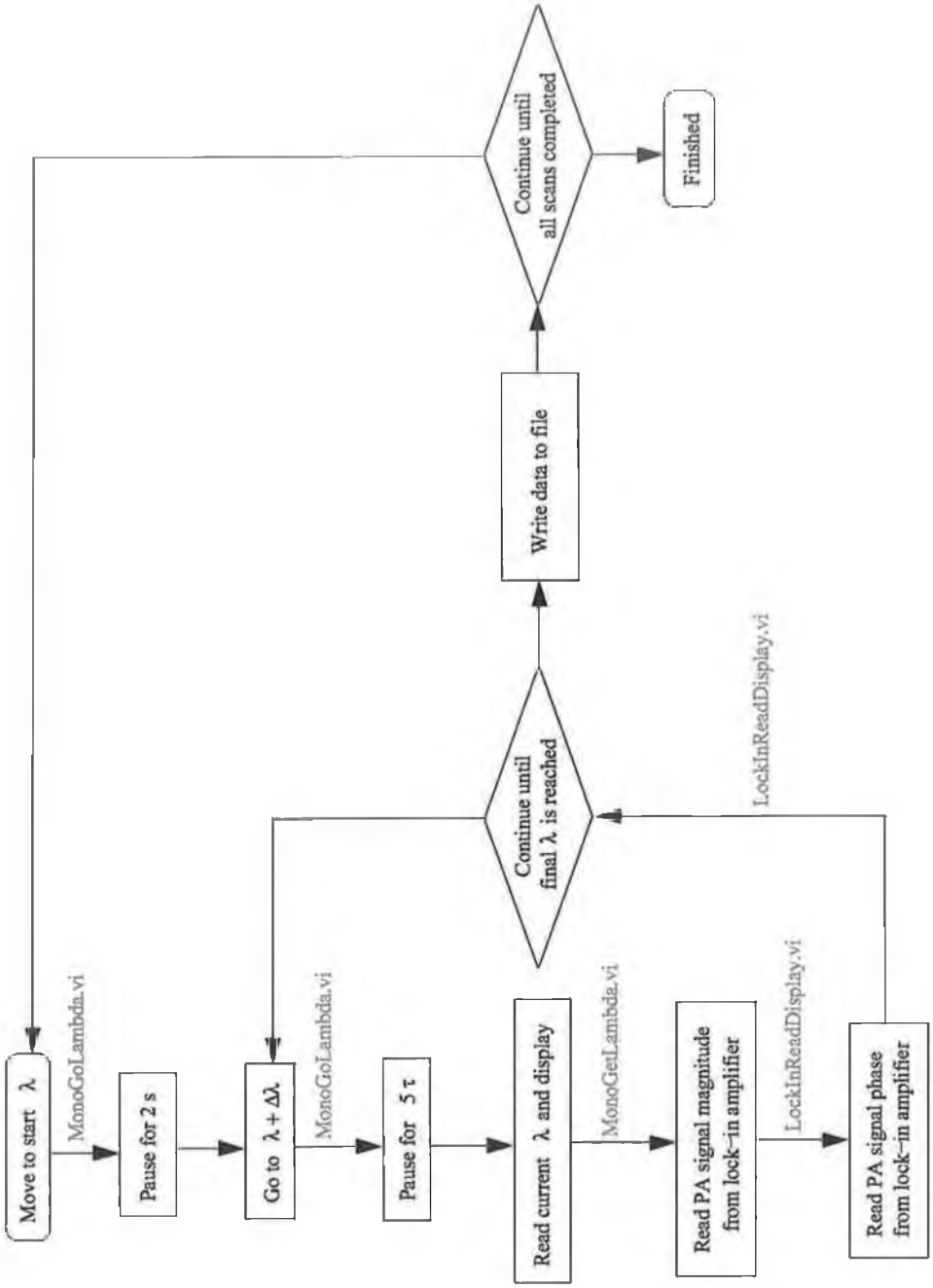

Figure 3.14: Flowchart depicting operation of photoacoustic energy scan VI.

3.8.2 Data Processing Software

In a normal photoacoustic energy scan, the data is collected from a number of different spectra. Since the noise is assumed to be Gaussian in nature simple statistical averaging should improve the signal to noise ratio. The averaged spectrum is next normalised to an averaged spectrum of a known sample such as carbon black powder. As averaging cannot remove all of the spectral noise, some filtering is necessary at this stage. All of these processes will now be examined.

3.8.2.1 Spectral Averaging

During a photoacoustic energy scan, the signal magnitude and phase are read from the lock-in amplifier as the wavelength of the incident light is varied. These three elements are recorded in an ASCII text file. For a spectrum from a carbon black powder where the photoacoustic effect is quite strong, nominally five scans across the wavelength range of interest are recorded. For a semiconductor sample it is necessary to record twenty or more scans to minimise the effect of noise. Having recorded the spectra, they are statistically averaged. A *C* program has been written that reads the directory where the spectra are stored, loads them into memory and takes the simple average. The average is then stored in a separate file for normalisation.

3.8.2.2 Spectral Normalisation

When a photoacoustic spectrum is recorded, superimposed on the signal from the sample itself is a photoacoustic signal due to the spectral distribution of the optical system,

the cell and the microphone. Normalisation is the process where these errors are corrected. This is performed by normalising the photoacoustic response of the specimen with that of a fine powder of carbon black. The latter acts as a true light trap with a flat response at all wavelengths. During the normalisation procedure the user is asked to enter the name of the averaged spectrum to be normalised along with the name of the averaged carbon black spectrum used in the process. Each sample spectral point is divided by its corresponding carbon black point. The normalised data is then stored in a file for filtering.

3.8.2.3 Spectral Filtering

Due to the fact that the constructed spectrometer is a single beam type therefore, by the process of normalisation, fluctuations in the normalised photoacoustic spectrum are bound to happen. The previous averaging and normalisation processes in themselves could enter some element of noise which could alter the final result to some extent. It is therefore desirable to perform some form of spectral filtering or smoothing to remove any noise. Two filters have been developed for use with the data.

The first is a simple n-point smoothing window where each spectral point is replaced by a local average of the n_L data points to the left and n_R data points to right of it. The user specifies the number of points to be averaged. In general, it is not recommended to average more than five points at a time or the spectrum may be corrupted.

Mathematically the form of this filter may be expressed as follows:

$$g_i = \sum_{n=-n_L}^{n_R} c_n f_{i+n} \tag{3.41}$$

where g_i is the filtered value for the spectral point f_i. The coefficient $c_n = 1/(n_L + n_R + 1)$. This moving average filter works quite well for carbon black powders as their signal to noise ratio is quite high.

However, for spectra from semiconductor samples it is dangerous to use such a filter. Suppose the spectrum could be approximated by a function that is sufficiently differentiable such that its second order derivative exists. In such cases, the moving average filter has the mathematical property of reducing the value of the function when a local maximum occurs. In a spectroscopy application, this implies a narrow spectral line will have its height reduced and its width increased. Since these parameters are themselves of physical interest, such filtering is obviously erroneous. Note however, that a moving average filter will preserve the area under the peak of interest i.e. the zeroth moment [65].

For spectroscopy applications a filter is required that preserves the zeroth and higher order moments. One such filter that has been implemented in this thesis is the Savitzky-Golay [65] filter. This type of filter has the advantage that it operates directly in the time-domain, and therefore, data does not have to be transferred back and forth between the Fourier domain. This avoids the risk of any loss of information, i.e. introduction of noise, due to algorithms such as the fast Fourier transform that might be

used for such a process. The basic idea behind the Savitzky-Golay filter is to find filter coefficients c_n that preserve higher order moments. Equivalently, the idea is to approximate the underlying function with a moving polynomial window. At each point f_i a polynomial is least-squares fitted to all n points in the moving window, and then g_i is set to be the value of that polynomial at position i. The technical details of the filter implementation can be found in [65].

3.9 Summary

In this chapter, the design and construction of a photoacoustic spectrometer for use in the infrared to ultraviolet part of the electromagnetic spectrum was described. Starting with the basic design criteria, each of the constituent systems was examined in the context of the theories of Chapter 2 and practical realisation issues were also discussed when appropriate. Particular emphasis was placed on the design of the photoacoustic cell. Potential enhancements to the system were alluded to as we progressed through the chapter; these will be expanded upon further in the conclusions of Chapter 14. Now we will progress to Chapter 4, where initial results of the spectrometer will be presented for materials such as carbon black, silicon and gallium nitride.

Chapter 4

Characterisation of Photoacoustic Spectrometer

4.1 Introduction

In this chapter the photoacoustic spectrometer designed in Chapter 3 will be calibrated and its performance evaluated by obtaining photoacoustic spectra from several common semiconductor materials. Calibration of the spectrometer essentially entails accounting for photoacoustic signals in the spectrum recorded from a sample that are attributable to the system itself. With a knowledge of these effects, an elementary verification of the theory of the photoacoustic effect in condensed matter samples is performed. Sub-bandgap absorption spectra are recorded for silicon ($E_g = 1.12$ eV), gallium arsenide ($E_g = 1.44$ eV) and gallium nitride ($E_g = 3.4$ eV). This data is then used to determine the energy of defect levels within the bandstructure and their influence on the optical absorption spectra. Finally, manipulation of the absorption spectra provides a measured value for the bandgap energy for each of the materials.

4.2 Calibration of Spectrometer

From Chapter 2 it is known that in a gas-microphone photoacoustic spectrometer, the photoacoustic signal is dependent on system parameters such as the light source, gas, backing materials, microphone and the photoacoustic cell geometry. Since the basic aim of a photoacoustic spectroscopy experiment is to determine the properties of the sample under investigation, these cell-dependent features are obvious experimental impediments. We therefore need to calibrate the spectrometer to account for system-dependent effects recorded in the photoacoustic spectra.

Using a photothermophone, Murphy and Aamodt [66], performed absolute calibration of their photoacoustic cell. In their experiment, they mimicked the photoacoustic signal produced by a carbon film by periodically heating the sample with a square wave current source. The absolute energy absorbed by the sample due to the incident light was determined by varying the electrical power supplied to the sample. The energy required to induce the photoacoustic effect was evaluated when the same pressure fluctuation was recorded in the gas from both the electrical and photoacoustic heating. The absolute calibration of a photoacoustic spectrometer is unnecessary for our purposes as we are only interested in obtaining relative information from a sample.

4.2.1 Light Source Power Spectrum

One of the most obvious and important predictions of the theories of the photoacoustic effect is that the photoacoustic signal is always linearly proportional to the intensity of the incident beam. It has been shown in Chapter 2 Section 2.2.6.2 that for an opti-

cally opaque, thermally thin sample such as carbon black, the photoacoustic spectrum is simply the power spectrum of the light source. Figure 4.1 illustrates the normalised photoacoustic spectrum of a carbon black powder sample measured at a chopping frequency of 100 Hz as a function of the photonic spectrum from 200 nm to 2400 nm (0.52 eV to 6.2 eV). One can see that most of the photonic power is concentrated in the spectral interval 300 nm to 2000 nm (0.62 eV to 4.1 eV). Below 300 nm the arc lamp suffers from ozone attenuation and in the deep infrared the efficiency of the respective monochromator grating is very poor.

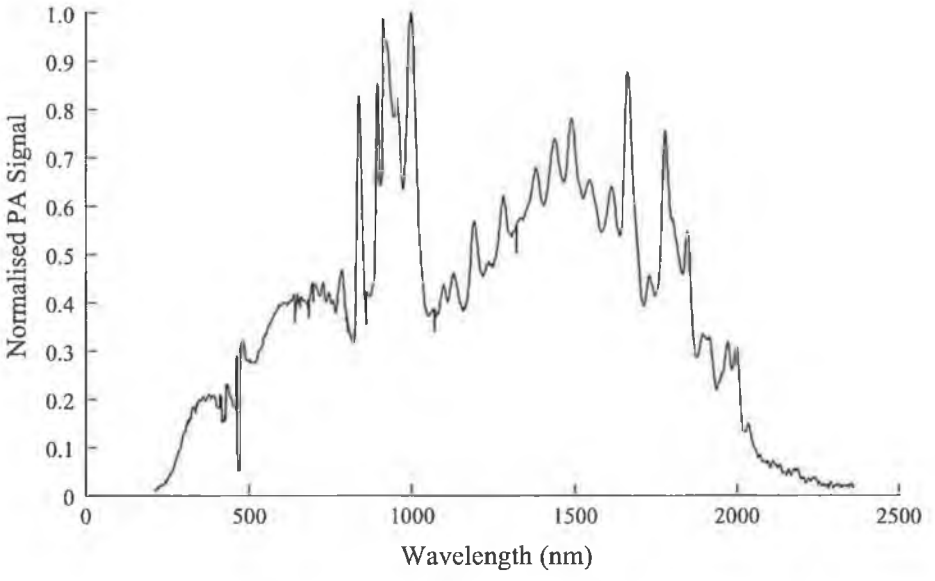

Figure 4.1: Spectral dependence of the normalised photoacoustic (PA) signal measured at a modulation frequency of 100 Hz from a carbon black powder sample. The wavelength increment between points is 1 nm.

Figure 4.2 illustrates the normalised power spectrum of the light source recorded with a Photodyne 33XLA chopped light multimeter. The recorded spectrum is quite coarse as the wavelength increment between points is 10 nm. Macroscopically both spectra

demonstrate the same features as one would expect. However, closer comparison of the two spectra reveals subtle differences. Consider for example, the wavelength range 500 nm to 800 nm. The photoacoustic spectrum displays more photonic power in this region compared to the data from the silicon photodiode. The differences arise from the fact that the power meter does not act like the perfect light trap with flat frequency response at all photon energies. Therefore, the results from carbon black which absorbs all incident light at all photonic energies could be potentially used for spectroscopic calibration from the X-ray to far infrared spectral regions.

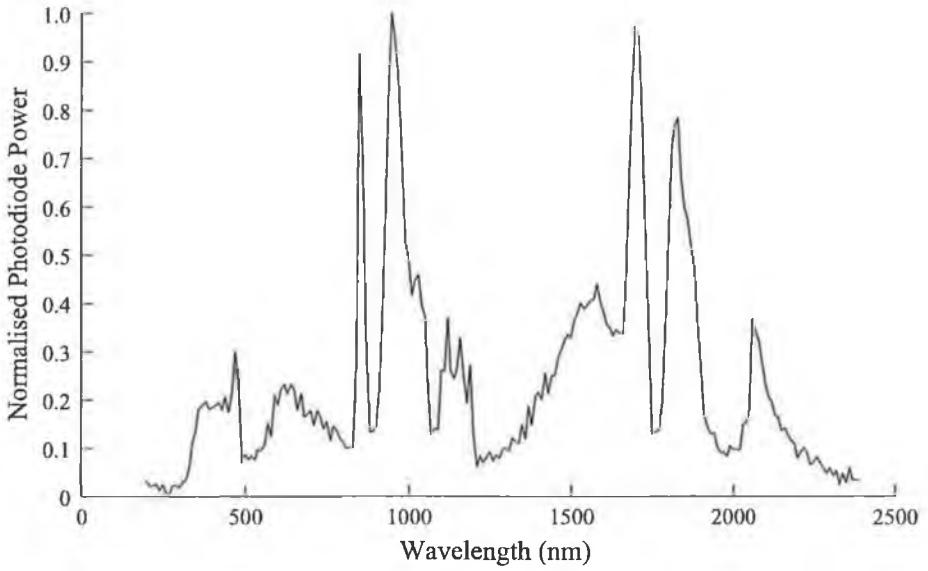

Figure 4.2: Normalised power spectrum of the light source measured at a modulation frequency of 100 Hz using a photodiode.

The results from the carbon black powder, which possesses an optical absorption coefficient $\beta \approx 10^6$ cm^{-1}, demonstrate that we are dealing with a situation where the optical absorption length $\mu_\beta \approx 1$ μm is very small compared to the sample length $l \approx 1$

mm. At the same time the thermal diffusion length μ_s is far greater than the sample length for the modulation frequencies usable in the spectrometer i.e. 25 Hz to 350 Hz. For example, $\mu_s \approx 1.6$ mm at a modulation frequency of 100 Hz.

4.2.2 Frequency Dependence of Photoacoustic Effect

The simplest way of verifying the theory of the photoacoustic effect in condensed matter samples is to examine the effect of the modulation frequency on the photoacoustic signal. For an optically opaque and thermally thin sample such as carbon black, it is known that the photoacoustic signal should be independent of the optical absorption coefficient β and inversely proportional to the chopping frequency ω (see Section 2.2.6.2 in Chapter 2).

Consider the chopping frequency dependence of the photoacoustic signal amplitude from a carbon black powder sample shown in Figure 4.3. Please note that over the modulation frequency range of interest, silicon is also optically opaque and thermally thin. Since the photoacoustic response from a powdered sample is much stronger than a crystalline sample, carbon black has been used as the material for the experimental study. One can clearly see the ω^{-1} dependence of the photoacoustic signal. This is in direct agreement with the theoretical predictions for a silicon sample shown in Figure 2.4 in Chapter 2. As the photoacoustic signal is supposed to be independent of the optical absorption coefficient for this class of materials, one would have imagined that the photoacoustic response at 700 nm should have been the same as at 1300 nm. One can clearly see that this is not the case. The long wavelength infrared radiation

is producing a much stronger photoacoustic signal compared to that produced by the visible radiation. The origin of the difference lies in the intensity of the light source at the two energies. The intensity of the light source is one and a quarter times greater at 1300 nm than at 700 nm (see Figure 4.1). Therefore, bearing this point in mind, one can see that the response of the photoacoustic signal is inversely proportional to ω and independent of β in accordance with the theoretical predictions.

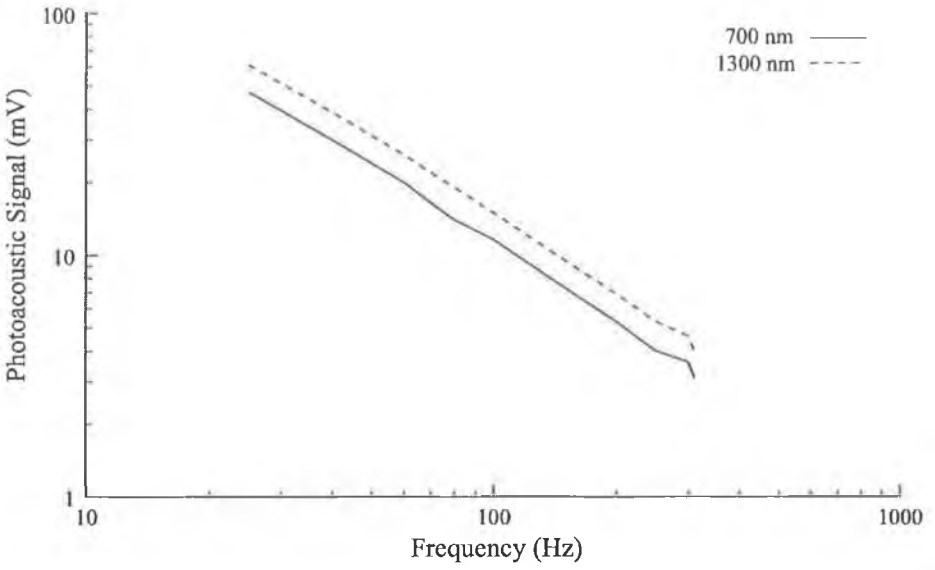

Figure 4.3: Dependence of the photoacoustic signal amplitude on chopping frequency for a carbon black powder sample. The study was performed in the visible (700 nm) and infrared (1300 nm) parts of the electromagnetic spectrum.

4.3 Data Acquisition Process

In a typical photoacoustic experiment wherein the photoacoustic signal is recorded as a function of the energy of the incident radiation, one normally averages the data over several spectra prior to normalisation. Once the data is normalised it is often

necessary to filter it to further suppress the effect of noise on the spectrum. Each of these processes will now be examined for a silicon sample so that the reader will have a greater understanding of the spectrometer's operation.

4.3.1 Averaging

The sample used for this study was a 15 mm^2 piece of silicon cut from a four inch p-type <100> wafer. Boron dopant was used and the 0.5 mm thick wafer possessed a nominal resistivity of 9 Ω cm to 12 Ω cm. Photoacoustic energy scans were performed from 0.95 eV to 1.8 eV (690 nm to 1380 nm) in wavelength increments of 1 nm. The modulation frequency was 55 Hz yielding a thermal diffusion length $\mu_s = 708\ \mu$m, which is greater than the sample thickness. A typical scan from this optically opaque, thermally thin sample is shown in Figure 4.4. Superimposed on the photoacoustic response of the sample is the power spectrum of the light source and Gaussian noise. As the noise is statistically distributed, averaging over several spectra will reduce its influence on the results. The simple average of thirty scans is presented in Figure 4.5. One can clearly see that the noise is significantly reduced.

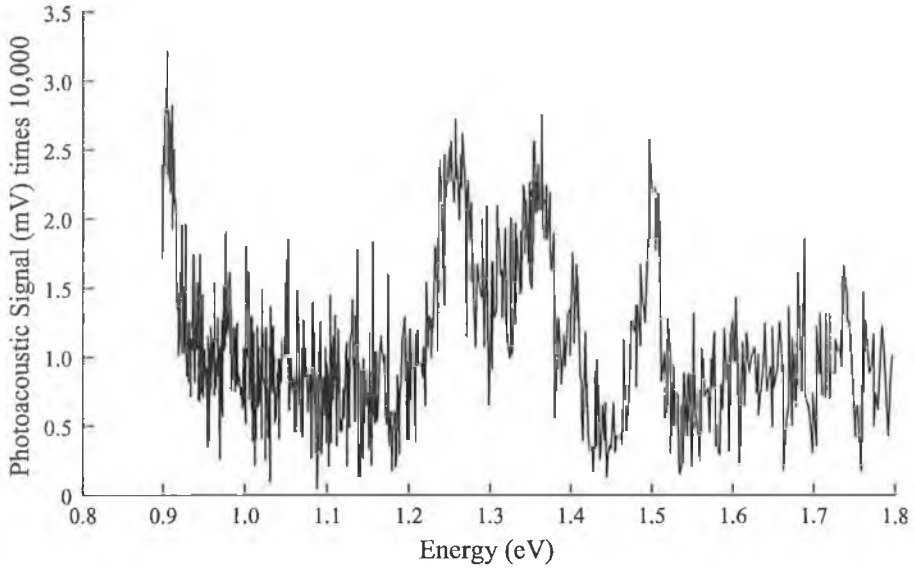

Figure 4.4: Typical raw spectrum data recorded from a silicon sample.

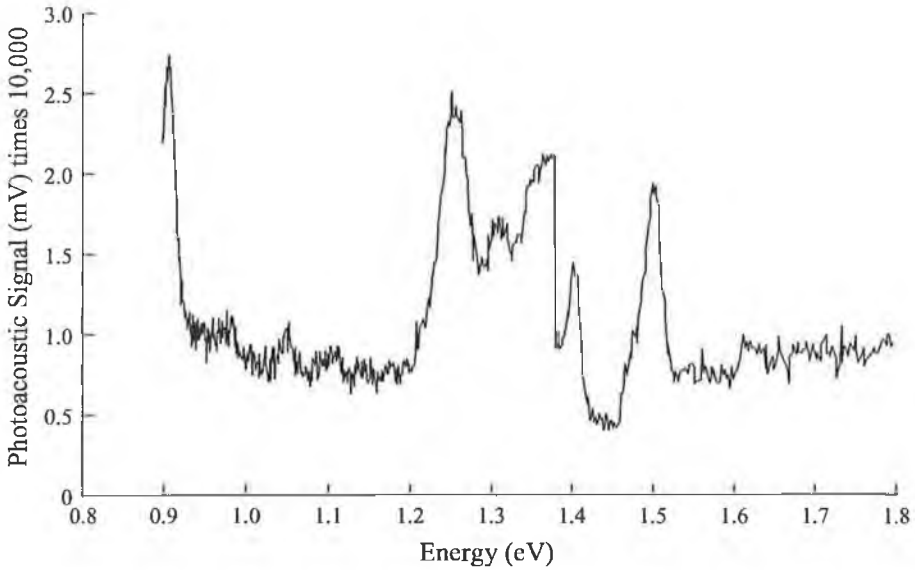

Figure 4.5: Increase in photoacoustic signal to noise ratio by averaging 30 spectral scans recorded from a silicon sample.

4.3.2 Normalisation

To remove the photoacoustic signal due to the spectrometer itself the averaged sample spectrum is divided by an averaged carbon black spectrum recorded from the same photonic interval and modulation frequency as the sample itself. Figures 4.6 and 4.7 show the carbon black spectrum used for the process and the resulting normalised photoacoustic spectrum for the silicon sample.

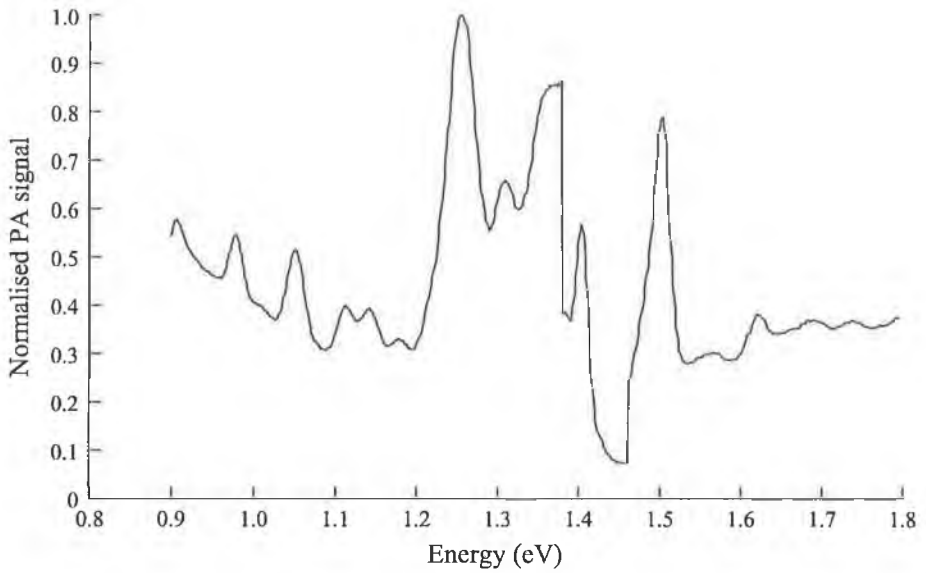

Figure 4.6: Carbon black spectrum used in the normalisation of an averaged silicon spectrum. The spectrum has been normalised to unity to aid clarity.

4.3.3 Filtering

In the normalised spectrum of Figure 4.7 one can see the presence of a defect level approximately 80 meV below the bandgap at 1.2 eV. This is highlighted by the arrow labeled D. However, a lot of noise is present in the spectrum and to elucidate the

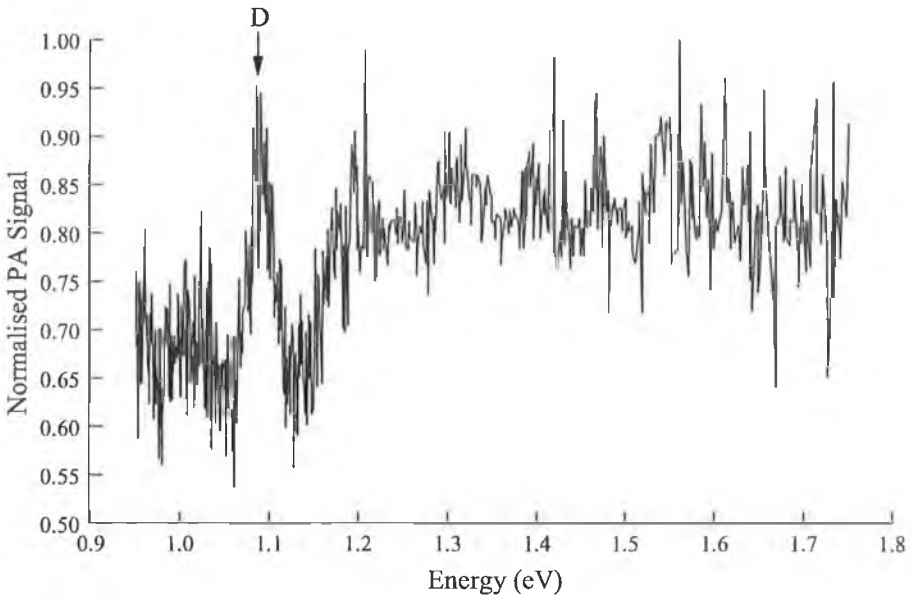

Figure 4.7: Normalised photoacoustic spectrum from p-type silicon sample. A non-radiative defect approximately 80 meV below the bandgap is indicated by the arrow labeled D.

photoacoustic data in a more understandable manner filtering has been applied. In order to preserve as much of the spectroscopic information as possible a seventh order Savitzky-Golay filter, utilising 11 data points either side of the filtered point, was applied to the spectrum. The results are shown in Figure 4.8. Due to the low signal to noise ratio one can see that the photoacoustic spectrum is still quite coarse. This problem cannot be overcome by further filtering; rather one must increase the information by increasing the number of spectral scans recorded.

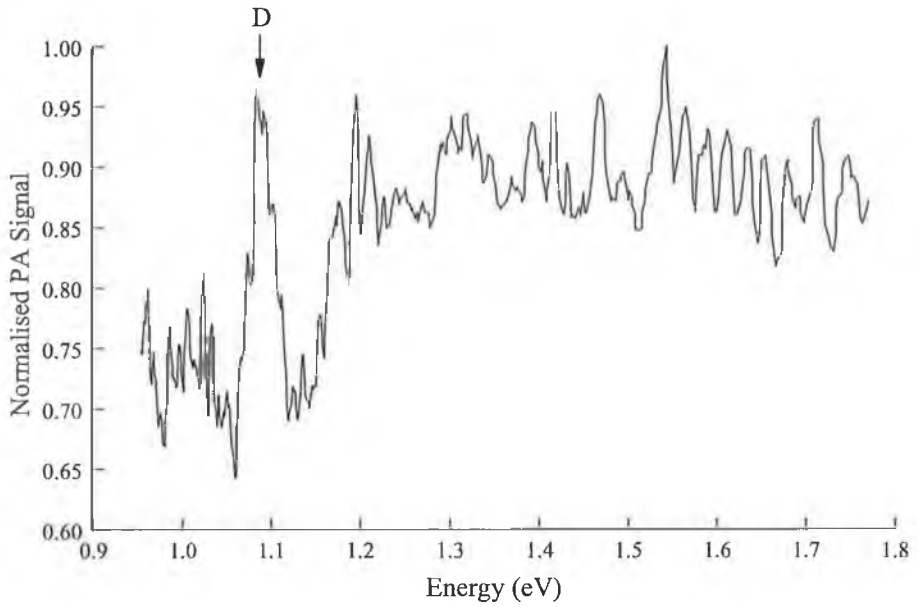

Figure 4.8: Normalised photoacoustic spectrum from p-type silicon sample after filtering with a 7 th order Savitzky-Golay filter. 11 data points either side of the filtered point were used to generate the polynomial coefficients. A non-radiative defect approximately 80 meV below the bandgap is indicated by the arrow labeled D.

4.4 Photoacoustic Spectroscopy of Common Semiconductors

In this section, the spectrometer will be characterised across its spectral range using the common semiconductor materials silicon, gallium arsenide and gallium nitride. For each material, the sub-bandgap absorption spectrum will be recorded, the bandgap energy and optical absorption coefficient determined. A good agreement between these results and those recorded in the literature has been obtained.

4.4.1 Silicon

The non-radiative sub-bandgap absorption spectrum for the silicon sample studied in this thesis has been presented in Figure 4.8. In line with the theory of Bandeira, Closs

and Ghizoni [10], there is a significant increase in the amplitude of the photoacoustic signal for energies greater than the bandgap energy E_g. From Figure 4.8 one could estimate the bandgap energy to be approximately 1.2 eV. However, a much more precise value can be obtained through a knowledge of the optical absorption coefficient as a function of the incident photonic energy. The optical absorption coefficient near the band to band transition can be obtained using the normalised photoacoustic amplitude q as follows:

$$\beta = \frac{1}{\mu_s}\frac{q^2 + q\sqrt{2 - q^2}}{1 - q^2} \tag{4.1}$$

The near-edge optical absorption spectrum for silicon is shown in Figure 4.9. The values presented here agree quite well with those obtained in [67–69].

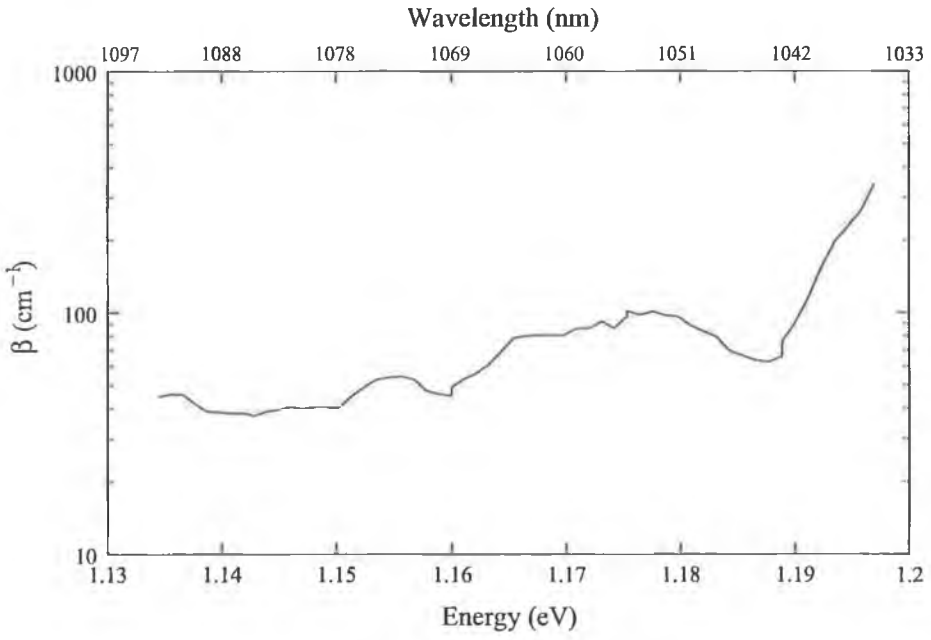

Figure 4.9: Near band edge optical absorption spectrum for silicon.

Re-iterating Equation (2.77) for an indirect bandgap semiconductor:

$$\beta = A_{id}\frac{(h\nu - E_g)^2}{h\nu} \tag{4.2}$$

enables one to obtain the bandgap energy by plotting $\sqrt{\beta h\nu}$ against $h\nu - E_g$. The value for which $\beta = 0$ gives the corresponding energy of the bandgap. In Figure 4.10 $\sqrt{\beta l h\nu}$ is plotted on the ordinate axis rather than $\sqrt{\beta h\nu}$. The sample thickness l, which is constant, does not change the end result, it only makes the magnitude of the figures more manageable. The bandgap of silicon has been evaluated to be $E_g = 1.187$ eV. This is approximately 63 meV greater than the theoretical value of 1.126 eV for a measurement at room temperature [45]. To a large degree, the experimental error can be attributed to the large dispersion of the monochromator which results in a nominal bandpass of approximately 25 nm at 1.12 eV.

4.4.2 Gallium Arsenide

The optical properties of two different gallium arsenide samples grown by the Vertical Gradient Freeze (VGF) and Liquid Encapsulated Czochralski (LEC) techniques were examined through their non-radiative decay branches. The samples studied were taken from p-type four inch wafers oriented in the <100> direction. The photoacoustic spectra were recorded over the photonic energy range 1.1 eV to 2.0 eV. The wavelength increment between data points was 1 nm and the modulation frequency was 55 Hz. Figures 4.11 and 4.12 show the respective spectra from the LEC and VGF samples. In both spectra, the direct bandgap transition at $E_g \approx 1.4$ eV can be seen. The spectrum

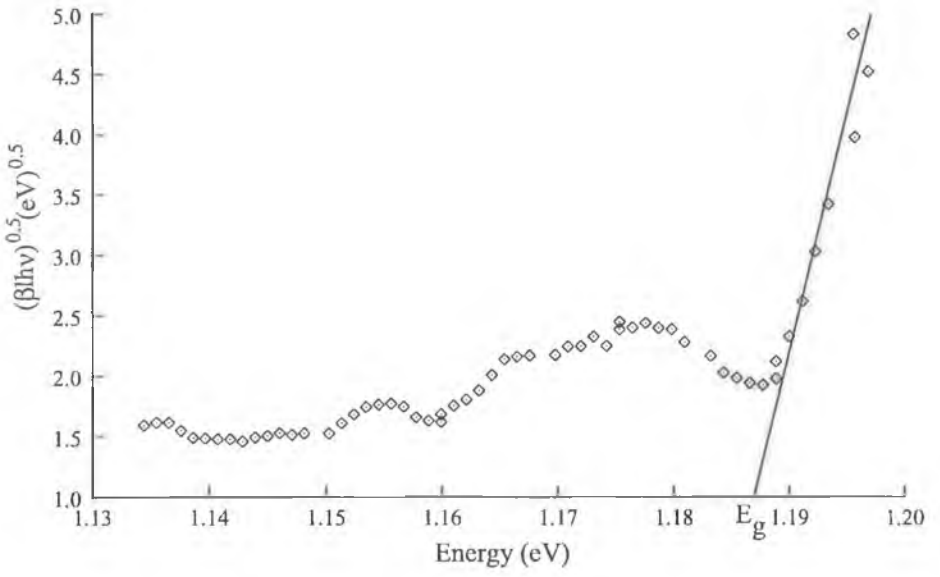

Figure 4.10: Evaluation of the bandgap energy for silicon.

recorded from the VGF sample possesses significantly more noise than the LEC spectrum. This point is very important for comparison of the spectra. For example, there would appear to be two defect levels present in the VGF spectrum at $E_1 = 1.17$ eV and $E_2 = 1.22$ eV. These defect levels also appear to be present in the LEC spectrum but their contribution to the photoacoustic signal is somewhat smaller. Therefore, due to the statistical nature of the VGF data it is most probable that these defects are actually the same in both samples. The energies associated with the four defect levels present in the spectra are summarised in Table 4.1. Determination of the nature of these defects is beyond the scope of this thesis. However, several investigations into sub-bandgap defect levels in semi-insulating gallium arsenide have been performed using piezoelectric photoacoustic spectroscopy by Fukuayama *et. al* [70, 71] and Ikari *et. al* [41, 72]. Their studies were able to determine the nature, i.e. their activation energies and trap-

ping cross-sections, of the electron non-radiative defect levels EL2, EL6, and EL7. It is envisaged that the spectrometer constructed in this thesis will be applied to similar studies in the near future.

Sample	E_1 (eV)	E_2 (eV)	E_3 (eV)	E_4 (eV)
LEC GaAs	1.17	1.20	1.33	1.42
VGF GaAs	1.17	1.22	1.33	1.41

Table 4.1: Energy levels associated with the non-radiative de-excitation centres in GaAs samples.

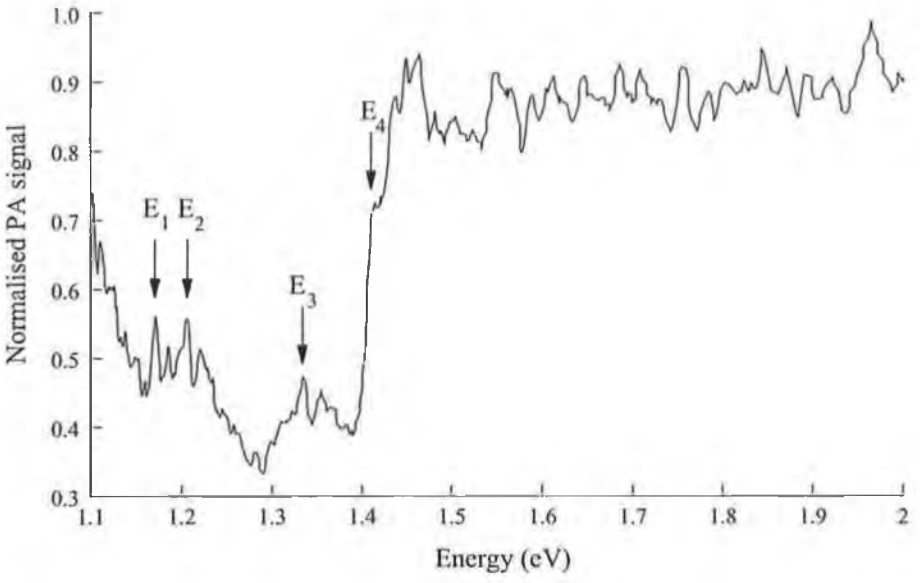

Figure 4.11: Normalised photoacoustic spectrum recorded from LEC grown GaAs. The data has been averaged over 20 spectral scans and filtered using an 11 point 7^{th} order Savitzky-Golay filter. Four non-radiative defect levels are indicated in the spectrum.

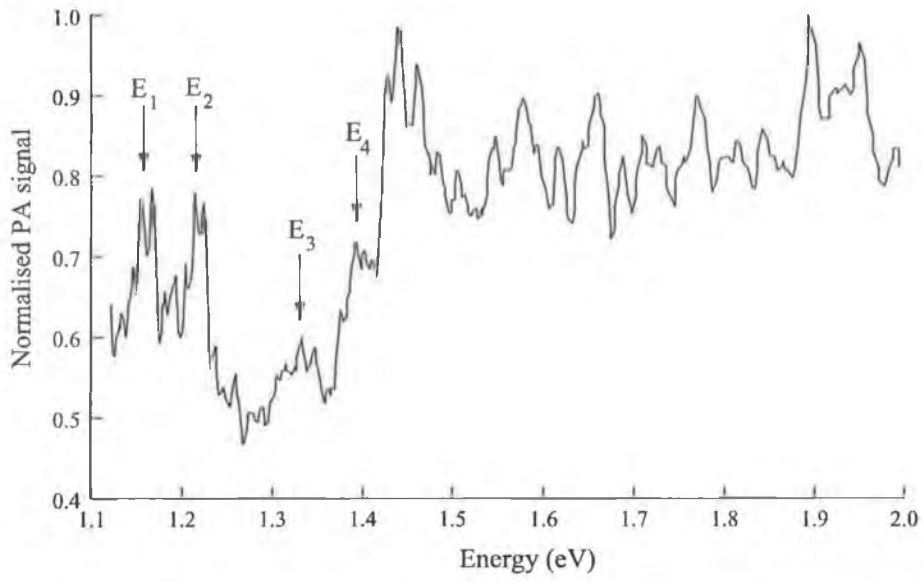

Figure 4.12: Normalised photoacoustic spectrum recorded from VGF grown GaAs. The data has been averaged over 20 spectral scans and filtered using an 11 point 7th order Savitzky-Golay filter. Four non-radiative defect levels are indicated in the spectrum.

The near band edge optical absorption coefficient has been evaluated using Equation (2.76), re-iterated here:

$$\beta = A_d \frac{\sqrt{h\nu - E_g}}{h\nu} \tag{4.3}$$

The results are presented for the LEC and VGF samples in Figure 4.13 and 4.14, respectively. Both sets of data demonstrate reasonable agreement with each other and with previous optical absorption spectra recorded in the literature [73, 74]. The effect of the sub-bandgap defect level E_4 in the VGF sample induces an appreciable localised variation in the optical absorption coefficient as indicated in Figure 4.14. Therefore, the information contained within a photoacoustic spectrum could be utilised, for example, in the design and construction of infrared transmitters and detectors.

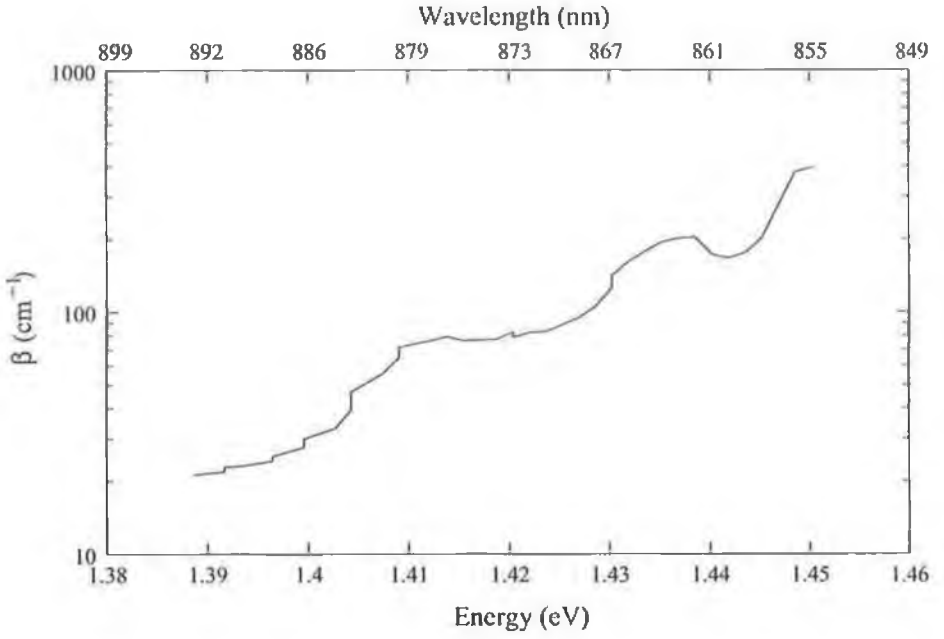

Figure 4.13: Near band edge optical absorption spectrum for LEC grown GaAs.

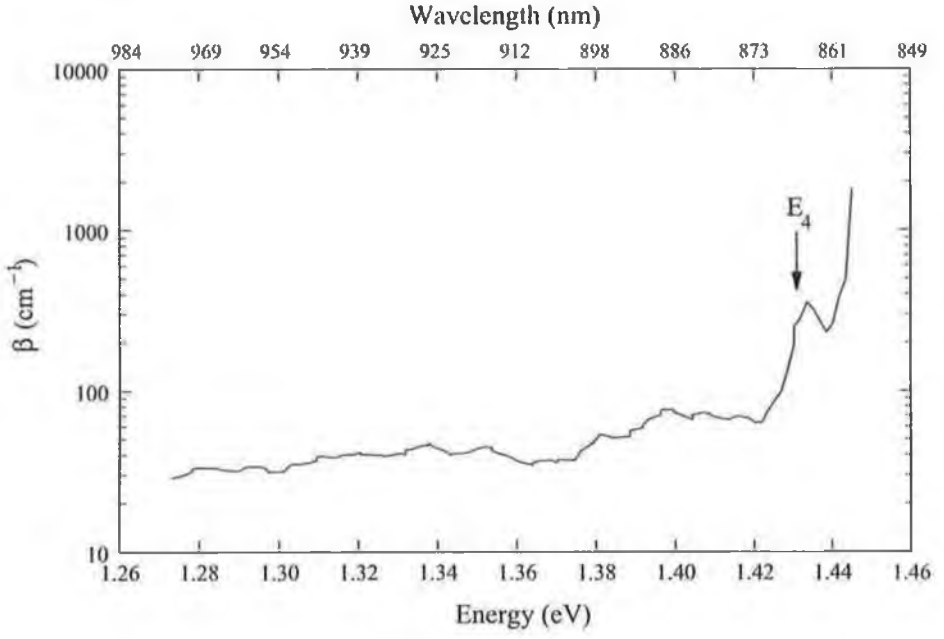

Figure 4.14: Near band edge optical absorption spectrum for VGF grown GaAs.

One can determine the bandgap energy by manipulation of Equation (4.3) and plotting $(\beta l h\nu)^2$ verses $h\nu - E_g$. Extrapolating to $\beta = 0$ yields $h\nu = E_g$; hence the bandgap energy can be determined. Both sets of data, plotted in Figures 4.15 and 4.16, yielded $E_g = 1.441$ eV in precise agreement with the literature [45].

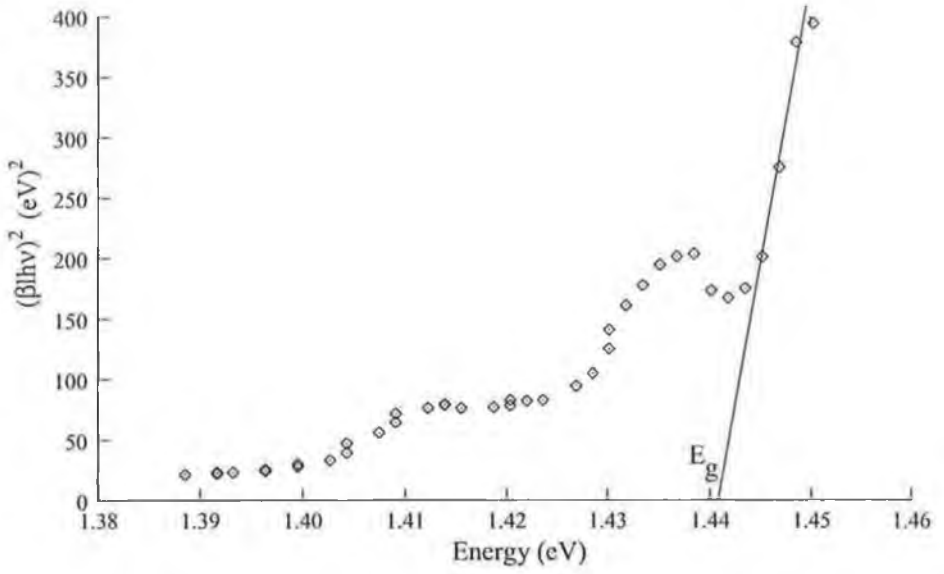

Figure 4.15: Evaluation of the bandgap energy for LEC grown GaAs.

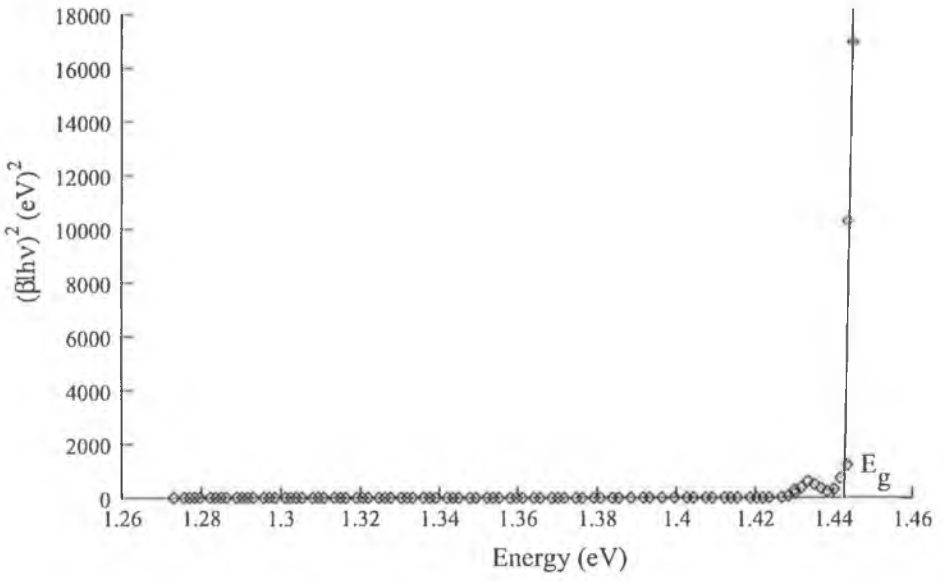

Figure 4.16: Evaluation of the bandgap energy for VGF grown GaAs.

4.4.3 Gallium Nitride

Group III-nitrides have been considered a promising system for semiconductor device applications since the early 1970s, especially for the development of blue and ultraviolet lasers due to their large photonic bandgap [75]. It has been a necessity for investigators in the III-nitride community to grow films of gallium nitride using heteroepitaxial routes because of the dearth of bulk substrates of this material. This results in films containing dislocation densities of the order of 10^8 cm^{-2} to 10^{10} cm^{-2} because of: (i) mismatches in the lattice parameters, and (ii) differences in the coefficients of thermal expansion between the film and the substrate. These high concentrations of dislocations limit the performance, efficiency and lifetime of optical devices via carrier recombination, increased leakage currents and decreased breakdown strength [76].

To the author's knowledge the first ever study of the non-radiative de-excitation processes in gallium nitride using photoacoustic spectroscopy is presented in this thesis. Two samples were investigated. The first, henceforth referred to as the "reference" sample consisted of 1.2 μm thick GaN epilayer grown on a 50 nm GaN buffer layer that had been deposited on a 400 μm thick (001) sapphire substrate. The second sample, henceforth called the "pendeo-epitaxy" sample consisted of a 400 μm thick sapphire substrate. On top of this a 50 nm GaN nucleation layer and a 1.2 μm thick GaN epilayer were grown using metal organic chemical vapor deposition (MOCVD). The combination of these two layers form the seed layer for the pendeo-epitaxy growth. Afterwards a 150 nm thick SiO_2 layer was deposited. Stripes were then defined using conventional photolithography and dry etching. Reactive ion etching (RIE) was used to create GaN stripes, measuring 2 μm wide with a period of 6 μm, by etching until the sapphire substrate was exposed. A new form of growth termed *pendeo-epitaxy* was used to grow 6 μm of GaN over the silicon dioxide mask layer. Pendeo-epitaxy (from the Latin: *pendeo* – to hang, or to be suspended) incorporates mechanisms of growth exploited by the conventional epitaxial lateral overgrowth technique [77] by using the SiO_2 mask to prevent vertical propagation of threading dislocations and extends this technique to employ the substrate itself as a pseudomask. This technique differs from conventional ELO growth in that the growth does not initiate through the window openings in the silicon dioxide mask but begins on the side-walls etched in the GaN seed layer. As the lateral growth from the sidewalls continues, vertical GaN growth begins from the newly formed (0001) face of the continuously extending lat-

eral growth front. Subsequently, once the vertical growth reaches the top of the seed mask, lateral growth over the mask itself begins through the conventional ELO technique. Allowing pendeo-epitaxial growth to continue will result in coalescence over and between each seed front, producing a continuous layer of GaN [78, 79].

The dependence of the photoacoustic signal on the energy of the incident light was investigated in the photonic interval 2.8 eV to 4.1 eV at a modulation frequency of 55 Hz. Consequently, the thermal diffusion length $\mu_s \approx 500$ μm implies data was recorded throughout the entire sample volume i.e. a signal contribution from the sapphire substrate, nucleation and buffer layers is to be expected. In its present form, the spectrometer is incapable of probing only the gallium nitride layers within the material, as modulation frequencies of the order 130 kHz to 3.4 MHz are required to achieve thermal diffusion lengths as shallow as 2 μm to 10 μm. The respective sub-bandgap absorption spectra for the reference and pendo-epitaxy samples are shown in Figures 4.17 and 4.18. The spectra are relatively free of noise due to the large information set that was recorded. However, it is difficult to discern the exact energy at which the direct bandgap transition occurs in the samples.

In the photoacoustic spectra of the silicon and gallium arsenide samples examined in the previous sections (see Figures 4.8 and 4.11), one could clearly see a large increase in the normalised photoacoustic signal during the transition from the valence band to the conduction band. This is directly attributable to the thermalisation of electrons from the valence band to the conduction band and their subsequent non-radiative relaxation mechanisms. Progressing this analysis one step further, one can also see that

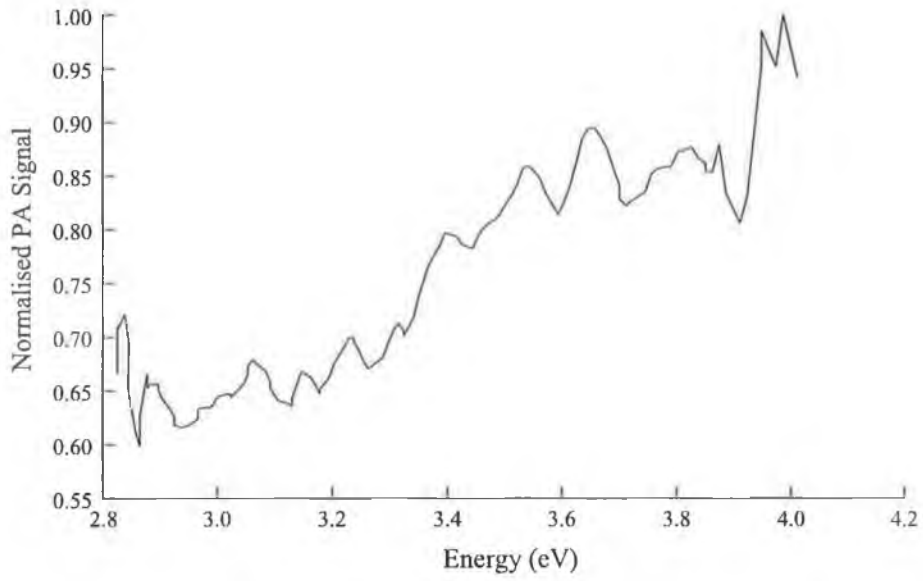

Figure 4.17: Normalised photoacoustic spectrum recorded from GaN reference sample. The data has been averaged over 100 spectral scans and filtered using an 11 point 7^{th} order Savitzky-Golay filter.

the difference in the photoacoustic signal strength between the valence and conduction bands is much larger for the gallium arsenide sample than for the silicon sample. This is a direct consequence of the thermal electrons requiring more energy to cross the bandgap in gallium arsenide than in silicon. All of this analysis seems to be incorrect when applied to gallium nitride. As the bandgap of gallium nitride is approximately three times larger than that of silicon, one would have envisaged a noticeable transition in the photoacoustic spectrum at an energy of approximately 3.4 eV.

Inherent in the discussion of the previous paragraph was an assumption that the materials under investigation are perfect. Although the photoacoustic spectra of silicon and gallium arsenide demonstrated the presence of some defect levels, their spectra and degree of crystallinity is sufficiently pure that to a first order the arguments presented

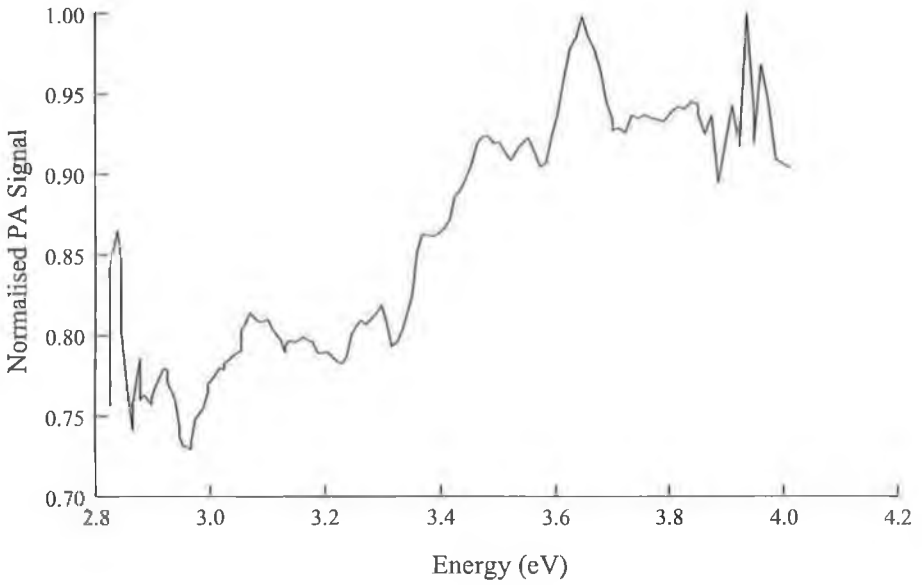

Figure 4.18: Normalised photoacoustic spectrum recorded from GaN pendeo-epitaxy sample. The data has been averaged over 100 spectral scans and filtered using an 11 point 7th order Savitzky-Golay filter.

are reasonably plausible. This is not the case for gallium nitride. The reference sample is heavily dislocated by virtue of the lattice mismatch inherent in the heteroepitaxial growth. The pendeo-epitaxy sample will have a reduced number of dislocations compared to the reference sample, but for the purposes of this discussion the number is still sufficiently large that both materials may be classed heavily dislocated. The dislocations induce modifications of the bandstructure such that alternative paths for non-radiative thermalisation and recombination of the electrons are introduced. Therefore, one could imagine that in their transition between the valence and conduction bands, the carriers undergo small transitions between the defect levels rather than large discrete transitions between the bands. Consequently, the carriers generate small amounts of heat within the lattice and a small photoacoustic signal. To first order, this qualita-

tive discussion explains the gradual transition from the valence band to the conduction band seen in the recorded spectra.

The most amazing feature of the III-nitrides is that although they are heavily dislocated, carriers in the materials and their constituent devices are capable of undergoing radiative recombination. To date a large amount of interest has been placed on the radiative recombination mechanisms in gallium nitride [80, 81]. Sugahara *et. al* [82] have shown that the efficiency of light emission remains high as long the minority carrier diffusion length is shorter than the dislocation spacing. Only a small number of investigations have examined the non-radiative properties and in particular, the influence of dislocations on the non-radiative centres [83]. By correlating the location of the defects in a transmission electron micrograph with a spatially mapped photoluminescence scan, Miyajima *et. al* [84] have determined that screw, edge and mixed dislocations act as strong non-radiative recombination centres in gallium nitride. They also determined that device efficiency is improved when the dislocation density is reduced. However, the location of the non-radiative centers within the bandstructure has yet to be determined.

In the interval between 3.4 eV and 3.5 eV, i.e. where one would expect the bandgap transition to take place, the rate of change of the photoacoustic signal strength with respect to the change in energy is greater for the pendeo-epitaxy sample than for the reference material. In light of the discussion of the previous two paragraphs, this suggests fewer non-radiative recombination centres are present in the pendeo-epitaxy sample compared to the reference sample.

The optical absorption coefficient of the materials in the energy range 2.9 eV to 3.5 eV was evaluated using the same procedure that was described for gallium arsenide. The results for both samples are shown in Figures 4.19 and 4.20. The optical absorption coefficient of the reference sample is lower than that of the pendeo-epitaxy sample over the spectral range examined. The higher dislocation density in the reference sample is responsible for the creation of a higher number of non-radiative recombination centres which serve to reduce the measured optical absorption coefficient. These results support the observations of Miyajima *et. al* [84] and the discussion thus far. The measured optical absorption spectrum for the pendeo-epitaxy sample agrees with the data of Ambacher *et. al* [85] and Muth *et. al* [86].

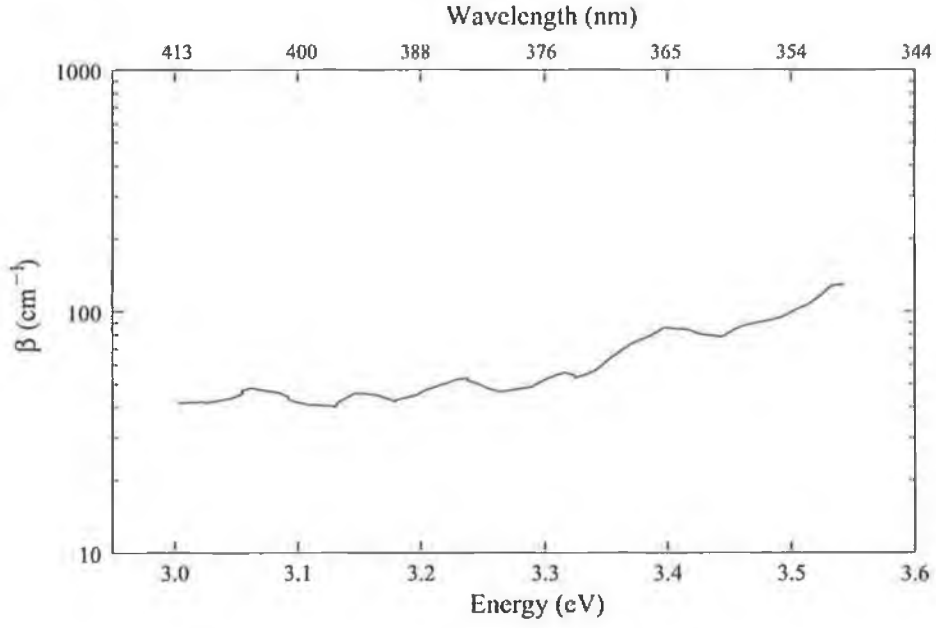

Figure 4.19: Near band edge optical absorption spectrum for the GaN reference sample.

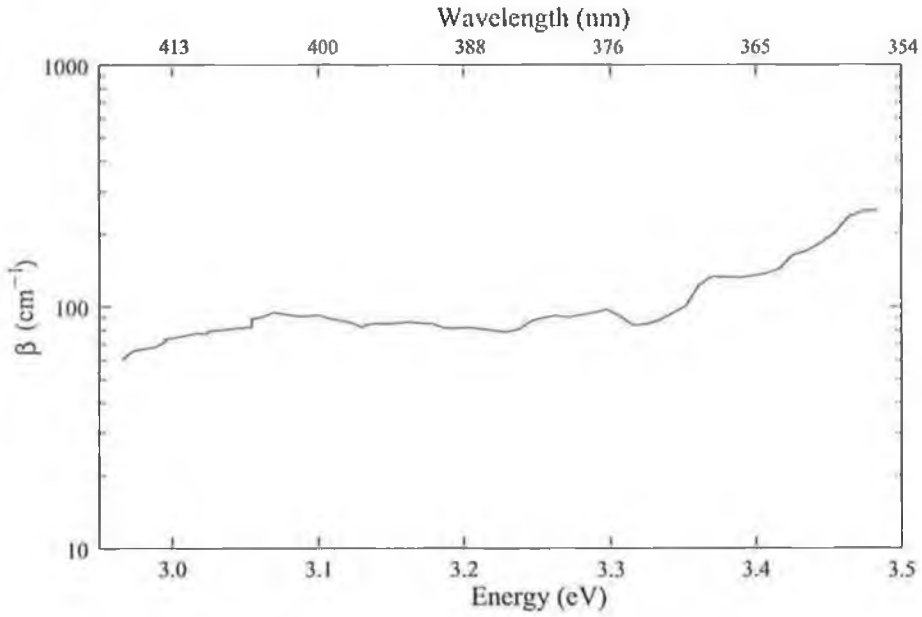

Figure 4.20: Near band edge optical absorption spectrum for the pendeo-epitaxy GaN sample.

By plotting $(\beta l h\nu)^2$ verses the photon energy the measured bandgap energy for both samples was found to be $E_g = 3.35$ eV which is in close agreement with the value of 3.42 eV reported in the literature [87]. The 70 meV difference may be accounted for through intrinsic stress in the samples due to their heteroepitaxial nature and also by system effects such as dispersion in the monochromator. The data is shown in Figures 4.21 and 4.22.

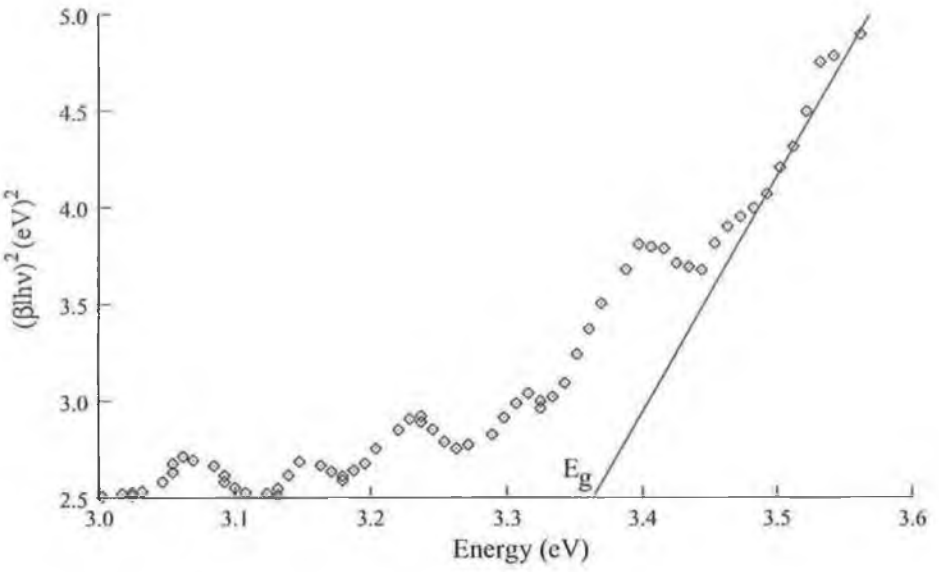

Figure 4.21: Evaluation of the bandgap energy for GaN reference material.

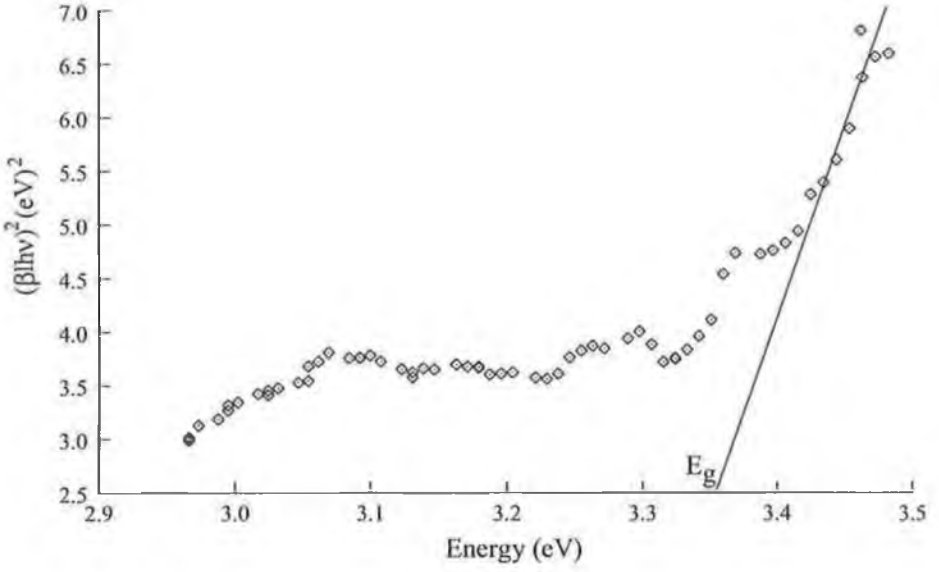

Figure 4.22: Evaluation of the bandgap energy for pendeo-epitaxy GaN material.

4.5 Conclusions

The results of this chapter have demonstrated clearly that the high resolution spectrally broad photoacoustic spectrometer, designed in Chapter 3 and based on the theories of Chapter 2, is capable of analysing narrow to wide bandgap semiconductor materials. The power spectrum of the system was measured using carbon black powder, and the inherent advantage of the method's flat frequency response, demonstrated its superiority to the conventional silicon photodiode. The Rosencwaig-Gersho theory was analysed in the frequency range 25 Hz to 350 Hz. No deviations from the theoretical predictions were found once system effects such as the spectral dependence of the light intensity had been taken into consideration. The spectrometer was used to measure the optical absorption spectra of silicon and gallium arsenide, from which it was possible to extrapolate their bandgap energies. All results were shown to be in agreement with those published in the literature.

The first investigation, using photoacoustic spectroscopy, into the non-radiative de-excitation processes in the wide bandgap semiconductor gallium nitride, have been performed in this thesis. Although these studies are in their infancy, it was possible to qualitatively demonstrate that the pendeo-epitaxy material possessed fewer non-radiative recombination centres compared to a heteroepitaxial reference sample. One may also infer from previous work that there are fewer dislocations in the pendeo-epitaxy material.

At present, there appear to be no publications in the literature correlating the nature of

the non-radiative optoelectronic defects in gallium nitride with the structural defects from which they originate. The spatially resolved photoacoustic optics designed in Chapter 3 have not been used to date in spatially resolved studies. In the near future such studies will be undertaken and it is envisaged the location of the structural defects will be found using synchrotron X-ray topography, the focus of part two of this thesis, to which we now turn.

PART II

Synchrotron X-ray Topography

Chapter 5

Theory of X-ray Diffraction

5.1 Introduction

X-ray diffraction has been used extensively for studying crystalline materials possessing varying degrees of lattice perfection. Developments in the theories of X-ray diffraction have been motivated by interest in the underlying physical phenomena and the need of the semiconductor industry to increase the quality of the materials used for electronic devices.

Two theories are generally used to describe the interaction of X-rays with crystalline materials for the purposes of understanding X-ray diffraction topographs. The conceptually easier theory, the kinematical theory, treats the scattering from each unit cell in the lattice as being independent from every other unit cell. The resulting diffracted intensity is the sum of the scattered radiation from all unit cells in the sample with geometrical phase differences taken into consideration. The second theory, the dynamical theory, takes into account all wave interactions within the crystal and must be used whenever diffraction from large perfect crystals is being considered.

Historically, several descriptions of the dynamical theory of X-ray diffraction exist.

The Darwin theory [13, 14] is based on the resolution of recurrence equations describing the partial reflection and transmission of waves at each lattice plane. Its formalism is not very convenient for the study of the propagation of X-rays and therefore for the study of defect images on X-ray topographs. Ewald's theory [88] investigates the interaction of an electromagnetic wave with a discrete triply periodic set of electromagnetic dipoles. Von Laue's theory [89] is based on the interaction of X-rays with a continuous medium characterised by a triply periodic dielectric susceptibility.

Today, Laue's theory is used for the explanation of dynamical diffraction effects in perfect crystals. For deformed crystals several theories exist. An excellent review of these theories and their relationship to one another can be found in [19]. In this chapter, the kinematical and dynamical theories of X-ray diffraction will be reviewed in the case of perfect crystals. In the topographic investigations of later chapters these will be modified and extended where necessary to account for effects seen in imperfect crystals. In the review that follows much of the physics of diffraction has been derived from first principles. In the case of the kinematical theory the review loosely follows the work of Zachariasen [90] and Azároff *et. al* [91]. Various aspects have been drawn from the works of Batterman and Cole [92], Authier [93–95] and Sutter [96] in the description of the dynamical theory of X-ray diffraction.

5.2 Kinematical Diffraction Theory

In the kinematical theory of X-ray diffraction a photon with wavelength λ and frequency ω_O is represented by a plane wave that transverses the entire sample. Scattering

occurs at points within the sample and the scattered radiation travels in straight lines without undergoing further scattering. In a crystal, a distinct phase relationship that is dependent on the geometrical path difference exists between the scattered radiation from each scattering centre. The radiation detected at some distant point is the sum of the scattered radiation from the entire sample, the phase differences due to the different path lengths being taken into consideration. The result is that the distribution of diffracted amplitudes in reciprocal space is the Fourier transform of the distribution of diffracting centres in physical space. The integrated reflected intensities calculated this way are proportional to the square of the structure factor and to the volume of the crystal bathed in the incident beam.

5.2.1 Theoretical Assumptions

For the description outlined above, a number of assumptions have been made:

- Plane wave approximation

  The source of the radiation and the detector are far away from the sample, compared to the distance between scattering centres in the sample. This allows the reader to assume that the incident radiation acts like a plane wave rather than a spherical wave. Therefore, waves scattered from different points in the sample travel toward the detector parallel to one another.

- Small scattering amplitude

  The total radiation diffracted into any one direction is assumed to be a very small portion of the incident beam. The interaction between the scattered and incident

radiation is ignored. It is also assumed that the intensity of the beams is diminished slowly as they pass through the sample by combined isotropic absorption and scattering processes. This point is violated in highly crystalline materials and under such circumstances the diffracted beam has an intensity comparable to the incident radiation. The assumed weakness of the scattered radiation implies that multiple scattering is negligible.

- Coherent scattering

  Changes in the wavelength of the radiation due to scattering are not considered. In an atom, the electrons are responsible for the scattering and consequently, the very small energy gains or losses due to interaction with the atomic nuclei are also ignored.

  These assumptions are generally valid in very thin or highly disordered crystalline samples. The thickness of a perfect crystal must be less than the Pendellösung distance (see Section 5.3.4 on page 165) for the kinematical theory to be applicable, otherwise coupling of energy between the diffracted and forward diffracted beams occurs. As many of the materials examined in this part of the thesis are highly strained, application of the kinematical approximation is generally valid. We will now review the theory.

5.2.2 X-ray Interactions with Matter

Consider an isolated electron with elemental charge e and mass m_e, located at the origin interacting with an electromagnetic wave (photon) with frequency ω_O and wavevec-

tor $|\vec{k_O}| = 1/\lambda$. It is assumed that no forces act on the particle other than that arising from the electric field and this force is sufficiently weak that the electron does not move relativistically. The oscillating electric field may be written as:

$$\vec{E}(\vec{r},t) = \vec{E}_O e^{i(\omega_O t - 2\pi \vec{k}_O \cdot \vec{r})} \tag{5.1}$$

Therefore, the electron is subject to a force:

$$\vec{F}(\vec{r},t) = -e\vec{E}(\vec{r},t) \tag{5.2}$$

From Newton's laws of motion, the electron acquires an acceleration:

$$\vec{a}(\vec{r},t) = \frac{-e}{m_e}\vec{E}(\vec{r},t) \tag{5.3}$$

and its displacement is given by:

$$\vec{d}(\vec{r},t) = \int\int \vec{a}(\vec{r},t)dt = \frac{e}{4\pi^2\omega_O^2 m_e}\vec{E}(\vec{r},t) \tag{5.4}$$

The resulting dipole moment is:

$$\vec{M}_O = -e\vec{d}(\vec{r},t) = \frac{-e^2}{4\pi^2\omega_O^2 m_e}\vec{E}(\vec{r},t) \tag{5.5}$$

Such an oscillating dipole, according to classical electrodynamics, produces its own propagating electromagnetic wave i.e. the scattered wave. At large displacements $\vec{R}$

from the dipole, the electric field of the scattered radiation is given by [97]:

$$\vec{E}_e(\vec{r},t) = \frac{Z_O\omega_O^2}{4\pi^2 c|\vec{R}|}e^{-i\left(\omega_O t - 2\pi\vec{k}\cdot\vec{R}\right)}\left[\left(\vec{n}\times\vec{M}_O\right)\times\vec{n}\right] \tag{5.6}$$

where $Z_O = \sqrt{\mu_O/\epsilon_O}$ is the impedance of free space, μ_O is the permeability of free space, ϵ_O the permittivity of free space, c the speed of light, $\vec{k}$ the wavevector of the scattered wave and $\vec{n} = \vec{k}\lambda$ is a unit vector in the scattering direction.

We will now extend the scattering from a single electron to an atom with Z electrons whose nucleus is assumed to be at the origin. As only the Z electrons of the atom contribute significantly to the X-ray scattering process, by ignoring the interaction between the electrons, one can determine the total scattered electric field by simply adding the scattered fields from each of the individual electrons:

$$\vec{E}_{at}(\vec{r},t) = \frac{Z_O\omega_O^2}{4\pi^2 c}\sum_{j=1}^{Z}\frac{1}{|\vec{R}_j|}e^{-i\left(\omega_O t - 2\pi\vec{k}_j\cdot\vec{R}_j\right)}\left[\left(\vec{n}_j\times\vec{M}_j\right)\times\vec{n}_j\right] \tag{5.7}$$

where the index j refers to a particular electron within the atom. The dipole moment from the j^{th} electron, located at position $\vec{r}_j$ is given by:

$$\vec{M}_j = \vec{M}_O e^{-i2\pi\vec{k}_O\cdot\vec{r}_j} \tag{5.8}$$

If the distance from the nucleus to the point of observation is much larger than that from the nucleus to any of the electrons, the distances $|\vec{R}_j|$ can be replaced by an average R, the wave vectors $\vec{k}_j$ with an average $\vec{k}_H$, and the unit vectors $\vec{n}_j$ with an average

$\vec{n}$. In the exponential, the phase relationship must be preserved as the displacements $\vec{r}_j$ between atoms are of the order of the wavelength of the incident radiation. Consequently, Equation (5.7) reduces to:

$$\vec{E}_{at}(\vec{r},t) = \vec{E}_e \sum_{j=1}^{Z} e^{-i2\pi(\vec{k}_O - \vec{k}_H)\cdot\vec{r}_j} \tag{5.9}$$

Due to the Heisenberg uncertainty principle, it is not possible to know the exact position of an electron at a specified time. Therefore we should represent the presence of each electron in the atom by its probability density p_j so that $p_j d\tau$ represents the probability of finding the electron j within the volume $d\tau$. The scattering of the incident electromagnetic radiation by all the electrons in the atom may be characterised by the atomic form factor:

$$f_0 = \sum_{j=1}^{Z} \int p_j e^{-i2\pi(\vec{k}_O - \vec{k}_H)\cdot\vec{r}_j} d\tau \tag{5.10}$$

such that

$$\vec{E}_{at}(\vec{r},t) = f_0 \vec{E}_e \tag{5.11}$$

It is known that X-rays have sufficient energy to excite inner shell electrons from one level to another. The effect of the electronic resonances and absorption can be included by modifying the atomic form factor to include the anomalous dispersion (Hönl) corrections f' and f''. Hence, for a given atom

$$f = f_0 + f' + if'' \tag{5.12}$$

The scattering from an atom will now be extended to a crystal i.e. a medium possessing a continuous distribution of electrons. If $\rho(\vec{r})$ is the electron density distribution, the charge of a small volume element is $e\rho(\vec{r})d\tau$. Therefore using the arguments that were used in the derivation of Equation (5.5), this differential volume possesses an electric moment equal to:

$$d\vec{M}(\vec{r},t) = -\rho(\vec{r})\frac{e^2}{4\pi^2\omega_O^2 m_e}\vec{E}(\vec{r},t)d\tau \tag{5.13}$$

The medium is thus polarised, and its polarisation $\vec{P}$ is equal to the electric moment per unit volume:

$$\vec{P}(\vec{r},t) = \frac{d\vec{M}(\vec{r},t)}{d\tau} = -\rho(\vec{r})\frac{e^2}{4\pi^2\omega_O^2 m_e}\vec{E}(\vec{r},t) = \chi_e(\vec{r})\epsilon_0\vec{E}(\vec{r},t) \tag{5.14}$$

where the dielectric susceptibility:

$$\chi_e(\vec{r}) = -\frac{\rho(\vec{r})e^2}{4\pi^2\epsilon_0\omega_O^2 m_e} \tag{5.15}$$

Since the dielectric susceptibility is proportional to the electron density, it is triply periodic in the case of a perfect crystal and may be expanded as a Fourier series over the reciprocal lattice:

$$\chi_e(\vec{r}) = \sum_{\vec{H}} \chi_{\vec{H}} e^{-i2\pi\vec{H}\cdot\vec{r}} \tag{5.16}$$

where $\vec{H}$ is a reciprocal lattice vector. The coefficients $\chi_{\vec{H}}$ are given by the inverse Fourier transform:

$$\chi_{\vec{H}} = \frac{1}{V}\int \chi_e(\vec{r})e^{i2\pi\vec{H}\cdot\vec{r}}dV \tag{5.17}$$

where V is the volume of the unit cell.

For a perfect crystal, one may determine the ratio of the scattering amplitude of the unit cell to that of a single free electron i.e. the structure factor F. In general, most semiconductors of interest do not possess a monoatomic basis and therefore, the structure factor for a given unit cell must take into consideration the scattering from the different types of constituent atoms. Hence

$$F = \sum_k f_k e^{-i2\pi(\vec{k}_O - \vec{k}_H)\cdot\vec{r}_k} e^{-M_j} \tag{5.18}$$

where f_k is the atomic form factor associated with the k^{th} atom in the unit cell. Anomalous dispersion has been implicitly taken into consideration in f_k. The term e^{-M_j} is the Debye-Waller factor and it accounts for the thermal motion of atoms in a crystal, and thus produces a lower intensity of coherently scattered radiation as the temperature increases.

Inserting Equation (5.15) into Equation (5.17) and comparing the result with Equation (5.18) one can reveal the relationship between the charge distribution and macroscopic scattering processes when $\vec{k}_O - \vec{k}_H = \vec{H}$:

$$\chi_{\vec{H}} = \frac{-r_e\lambda^2}{\pi V} F_{\vec{H}} \tag{5.19}$$

where the classical electron radius is given by:

$$r_e = \frac{e^2}{4\pi\epsilon_O m_e c^2} \tag{5.20}$$

Now suppose the sample is a rectangular parallelepiped with dimensions $N_1\vec{a_1}$, $N_2\vec{a_2}$ and $N_3\vec{a_3}$ containing $N_1N_2N_3$ atoms, where $\vec{a_1}$, $\vec{a_2}$ and $\vec{a_3}$ are non co-planar unit vectors in real space. Then the scattered radiation from the sample, is the sum of the radiation from all the individual unit cells in the crystal, with the phase contributions being taken into consideration:

$$\vec{E}_{cr}(\vec{r},t) = \vec{E}_e(\vec{r},t)F\sum_{n_1=0}^{N_1-1} e^{in_1 2\pi\left(\vec{k}_O-\vec{k}_H\right)\cdot\vec{a_1}}\sum_{n_2=0}^{N_2-1} e^{in_2 2\pi\left(\vec{k}_O-\vec{k}_H\right)\cdot\vec{a_2}}\sum_{n_3=0}^{N_3-1} e^{in_3 2\pi\left(\vec{k}_O-\vec{k}_H\right)\cdot\vec{a_3}} \tag{5.21}$$

Since each summation term is a finite geometric series the previous equation may be re-written as:

$$\vec{E}_{cr}(\vec{r},t) = \vec{E}_e(\vec{r},t)F\prod_i^3 \frac{e^{iN_i 2\pi\left(\vec{k}_O-\vec{k}_H\right)}-1}{e^{i2\pi\left(\vec{k}_O-\vec{k}_H\right)}-1} \tag{5.22}$$

Only the scattered X-ray intensity, which is the average of the Poynting vector, can be measured. Therefore

$$I_{cr} = \frac{1}{2c\mu_0}|\vec{E}_{cr}(\vec{r},t)||\vec{E}^*_{cr}(\vec{r},t)| = I_e|F|^2\prod_i^3 \frac{\sin^2 N_i\pi\left(\vec{k}_O-\vec{k}_H\right)}{\sin^2\pi\left(\vec{k}_O-\vec{k}_H\right)} \tag{5.23}$$

where $\vec{E}^*_{cr}(\vec{r},t)$ is the complex conjugate of the scattered electric field and I_e is the intensity of the scattered radiation from an electron.

One can see that the scattered intensity reaches a maximum when $\vec{k}_O - \vec{k}_H = \vec{H}$. This is the Laue criterion for diffraction. Consider Figure 5.1 on page 142 where a beam with wavevector $\vec{k}_O$ incident on a crystalline sample makes an angle β to the normal of the (hkl) lattice plane i.e. the reciprocal lattice vector $\vec{H}_{hkl}$. The real space

lattice spacing is d_{hkl}. Assuming no energy loss upon scattering, the magnitudes of the diffracted wavevector $\vec{k}_H$ and incident wavevector $\vec{k}_O$ are identical. According to the Ewald construction, this implies $\vec{k}_H$ must fall on a sphere about the origin of radius $1/\lambda$ and $-\vec{k}_O$ must end on a sphere of the same radius about the $\vec{H}_{hkl}$ terminal point. Thus the intersection of these two spheres defines the only allowable orientations of $\vec{k}_O$ and $\vec{k}_H$ for diffraction to occur at a given wavelength. From simple symmetry arguments, the angle the incident and diffracted beams make with the lattice planes is θ, one-half of the total scattering angle 2θ. By simple geometry

$$\sin\theta = \frac{|\vec{H}_{hkl}|}{2|\vec{k}_O|} \tag{5.24}$$

and by definition

$$|\vec{H}_{hkl}| = \frac{n}{d_{hkl}}; \qquad n \in \mathbb{Z} \tag{5.25}$$

Combining Equations (5.24) and (5.25) yields the Bragg criterion for diffraction:

$$n\lambda = 2d_{hkl}\sin\theta \tag{5.26}$$

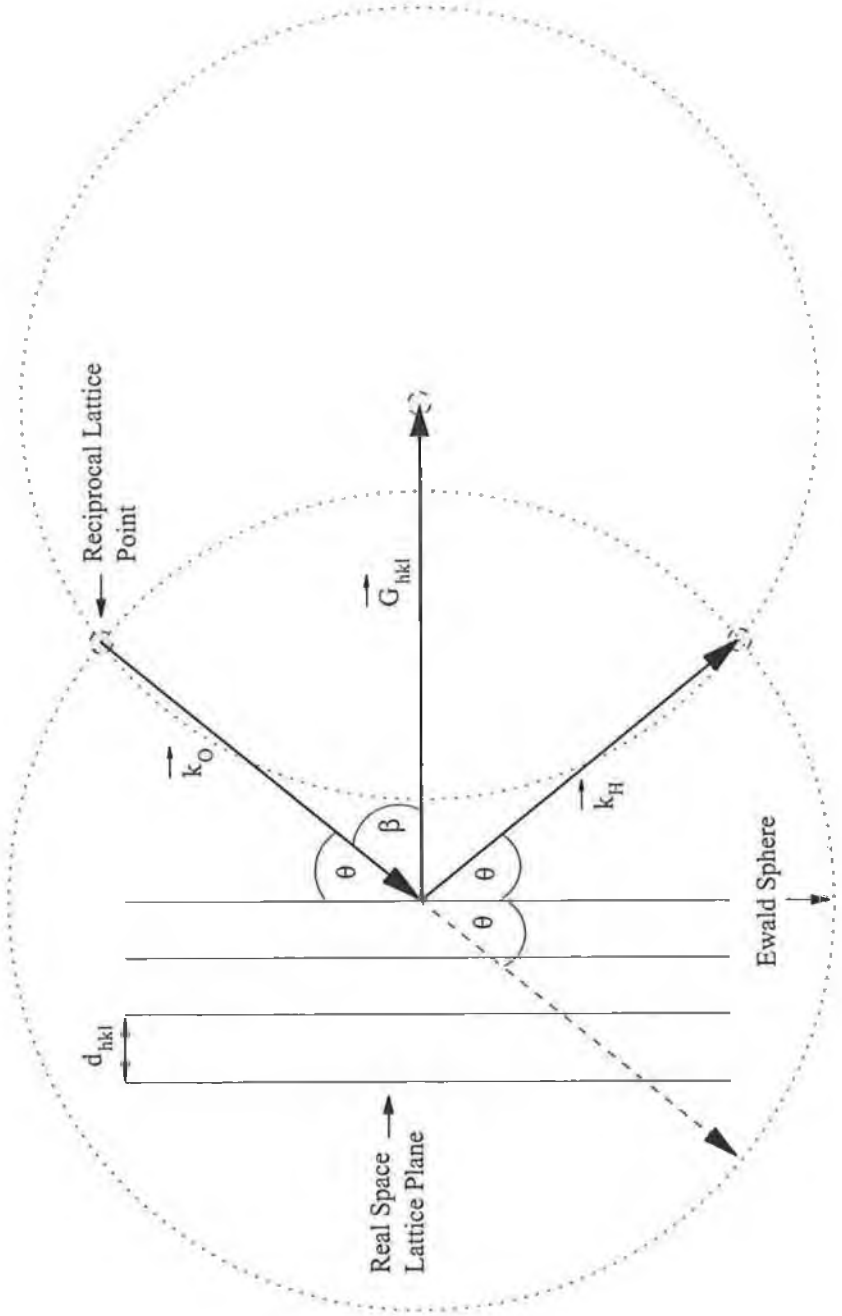

Figure 5.1: Ewald construction for diffraction from a crystal.

5.2.3 Kinematical Theory Failings

Consideration of the rocking curve profile reveals flaws in the kinematical theory. Under the exact Bragg condition

$$|\vec{k}_H| = \frac{2\sin\theta_B}{\lambda} \tag{5.27}$$

where $2\theta_B$ is the scattering angle. Now let the incident wavevector $\vec{k}_O$ remain unchanged so we can investigate the scattering at a slightly different angle $2\theta_B + \epsilon$. The new diffraction vector is $\vec{k}_{H'} = \vec{k}_H + \vec{\delta}$, and simple geometrical considerations of the wavevectors shows that

$$|\vec{\delta}| = \frac{\epsilon}{\lambda}\cos\theta_B \tag{5.28}$$

The intensity of the scattering close to a maximum may be given the form:

$$I_H = I_e|F_H|^2 \prod_i^3 \frac{\sin^2 \pi N_i \vec{\delta}\cdot\vec{a_i}}{\sin^2 \pi \vec{\delta}\cdot\vec{a_i}} \tag{5.29}$$

The

$$\frac{\sin^2 \pi N_i \vec{\delta}\cdot\vec{a_i}}{\sin^2 \pi \vec{\delta}\cdot\vec{a_i}}$$

terms are now replaced by a function $N_i^2 e^{-\frac{N_i^2 x_i^2}{4\pi}}$ as it possesses the same maximum value and area. In this manner, Equation (5.29) becomes

$$I_H \approx I_e|F_H|^2 N^2 e^{-\frac{1}{4\pi}\left(2\pi\vec{\delta}\cdot\vec{A}_d\right)^2} \tag{5.30}$$

where $\vec{A}_d$ is the diagonal of the crystal parallelipied. We may now set $\vec{\delta} \cdot \vec{A}_d = |\vec{\delta}|D$ where D is the average linear dimension of the crystal. Therefore,

$$I_H(\epsilon) \approx I_e |F_H|^2 N^2 e^{-\frac{\pi}{\lambda^2}\epsilon^2 D^2 \cos^2\theta_B} \tag{5.31}$$

Hence, the full-width at half-maximum may be approximated by

$$\Delta(2\theta_B) = 2\epsilon_{\frac{1}{2}} \approx 2\sqrt{\frac{\ln 2}{\pi}} \frac{\lambda}{D\cos\theta_B} \tag{5.32}$$

The maximum intensity of the rocking curve peak is found from Equation (5.23) at the exact Bragg condition to be

$$I_{cr}^{max} = I_e |F_H|^2 N^2 \tag{5.33}$$

where $N = N_1 N_2 N_3$ is the total number of unit cells in the crystal.

As the size of the sample increases the rocking curve width decreases and the peak intensity increases. For sufficiently large N the rocking curve will approximate a delta function which obviously does not make physical sense. Therefore, the kinematical theory is flawed.

The fundamental flaw in the kinematical theory is the assumption inherent in Equation (5.23) that the incident wave is the same for each unit cell of the crystal and only a phase difference exists between the scattered radiation. This assumption is clearly untenable. An X-ray beam traversing through a crystalline medium will undergo absorption due to photoelectric and scattering processes. The scattering processes con-

sist of coherent scattering and incoherent (Compton) scattering. For situations where $\vec{k}_O - \vec{k}_H \approx \vec{H}_{hkl}$ the energy of the incident wave is coupled into the diffracted wave and coherent scattering results. For situations where the Laue or Bragg diffraction conditions are not satisfied Compton scattering dominates. Therefore, kinematical theory is only valid for crystals where the scattering effects and absorption processes are negligible i.e. for sufficiently thin or highly disordered crystals. For relatively thick highly crystalline samples, the dynamical theory of X-ray diffraction must be used.

5.2.4 Application to X-ray Topography

It is not the purpose of this section to describe kinematical imaging in X-ray diffraction topography as this will be treated in Chapter 7 with the techniques of X-ray topography. Many of the semiconductor materials and devices examined in this thesis are sufficiently strained that application of the kinematical theory is justified. For Bragg geometries it is often useful to know the depth the X-ray penetrates into the material and therefore, the depth from which information is being recorded. The kinematical penetration depth t_p, which is measured perpendicular to the surface as illustrated in Figure 5.2, at which the intensity of the outgoing reflected beam has dropped to $1/e$ times that of the incident beam due to absorption is given by geometrical analysis to be

$$t_p = \left[\mu_O(\lambda)\left(\frac{1}{\sin\alpha_o} + \frac{1}{\sin\alpha_h}\right)\right]^{-1} \tag{5.34}$$

where $\mu_O(\lambda)$ is the linear absorption coefficient, α_O and α_H are the incident and reflected angles measured with respect to the sample surface, respectively.

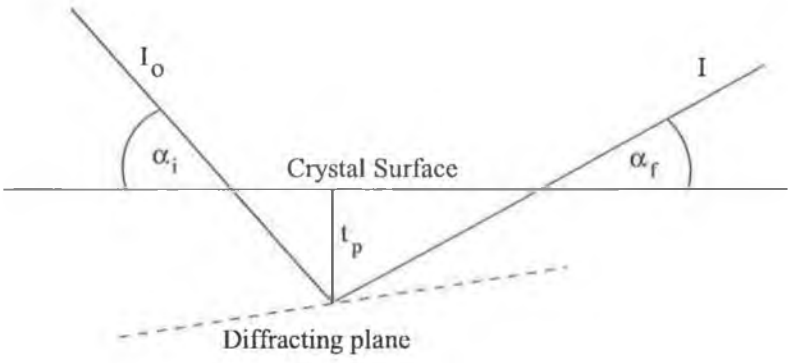

Figure 5.2: Penetration depth t_p at which the intensity of the outgoing reflected beam has dropped to $1/e$ times that of the incident beam due to absorption.

5.3 Dynamical Diffraction Theory

In the dynamical theory of X-ray diffraction one describes the propagation of the X-ray field outside and inside the crystal using Maxwell's equations. This is analogous to the band theory of solids where one solves the Schrödinger equation to ascertain the allowable energies of the electrons as a function of their wave number. In dynamical diffraction, one solves for the allowable wavevectors as a function of their position in reciprocal space. In electronic band theory concepts such as particle momentum in the valence and conduction bands are replaced in dynamical theory by the position of the tie-points on the dispersion surface. The tie-point characterises a given mode of propagation for an electric displacement field within the crystal and thus this geometrical construct can elucidate information about the diffraction processes taking place. Maxwell's equations will now be solved in a medium possessing a triply periodic di-

electric susceptibility i.e. a crystal. The solution will be used to develop the concept of the dispersion surface which in turn will elucidate some of the rather interesting features of dynamical diffraction such as Pendellösung and anomalous transmission of X-rays through thick crystals.

5.3.1 Solutions to Maxwell's Equations that Satisfy Bragg's Law

Maxwell's equations can be used to describe the macroscopic interaction between an electromagnetic wave with wavevector $|\vec{k}| = 1/\lambda$ and a crystal with triply periodic dielectric susceptibility $\chi_{\vec{H}}$. These equations are now presented in their general form:

$$\nabla \cdot \vec{D} = \rho, \qquad \nabla \cdot \vec{B} = 0 \tag{5.35}$$

$$\nabla \times \vec{E} = \frac{-\partial \vec{B}}{\partial t}, \qquad \nabla \times \vec{H}_{\text{mag}} = \vec{j} + \frac{\partial \vec{D}}{\partial t} \tag{5.36}$$

$$\vec{D} = \epsilon_0 \vec{E} + \vec{P} = \epsilon_0 \left(1 + \chi_e\right) \vec{E}, \qquad \vec{B} = \mu_0 \vec{H}_{\text{mag}} + \vec{M} \tag{5.37}$$

where $\vec{E}$ is the electric field strength, $\vec{D}$ is the electric displacement, $\vec{H}_{\text{mag}}$ is the magnetic field strength, $\vec{B}$ is the magnetic flux density, ρ is the charge density, $\vec{j}$ is the electrical current density and $\vec{P}$ is the polarisation density of the medium.

As the crystal is electrically neutral, the local charge distribution and current density is zero. As the magnetic interaction is extremely weak it can be neglected. Therefore,

$$\nabla \times \vec{E} = \frac{-\partial \vec{B}}{\partial t} \tag{5.38}$$

Now

$$\nabla \times \left(\nabla \times \vec{E}\right) = \nabla\left(\nabla \cdot \vec{E}\right) - \nabla^2 \vec{E} = \frac{-\partial}{\partial t}\left(\nabla \times \vec{B}\right) \tag{5.39}$$

Since

$$\nabla \times \vec{B} = \mu_0 \epsilon_0 \frac{\partial \vec{E}}{\partial t} \tag{5.40}$$

$$\Rightarrow \nabla^2 \vec{E} - \frac{1}{c^2}\frac{\partial^2 \vec{E}}{\partial t^2} = 0 \tag{5.41}$$

The solution to the wave equation is a plane wave of the form:

$$\vec{E} = E_0 e^{i(\omega_0 t - 2\pi \vec{k}\cdot\vec{r})} \tag{5.42}$$

Substituting

$$\vec{E} \approx \frac{\vec{D}}{\epsilon_0}(1 - \chi_e) \tag{5.43}$$

into the wave equation and applying the following property of the curl operator

$$\nabla^2 \vec{D} = \nabla(\nabla \cdot \vec{D}) - \nabla \times (\nabla \times \vec{D}) = 0 \tag{5.44}$$

yields an equation that describes the propagation of an electromagnetic wave through a medium with dielectric susceptibility χ_e:

$$\nabla^2 \vec{D} + \chi_e \nabla \times \left(\nabla \times \vec{D}\right) + 4\pi^2 |\vec{k}|^2 \vec{D} = 0 \tag{5.45}$$

This is a linear homogeneous partial differential equation and any linear combination

of special solutions

$$\vec{D} = \sum_{j} A_j \vec{D}_j \tag{5.46}$$

is also a solution. As the medium we are dealing with is a crystal and therefore possesses a triply periodic dielectric susceptibility, according to Floquet's theorem the simplest special solution of Equation (5.45) is a Bloch wave:

$$\vec{D}_j = e^{-i2\pi\vec{k}_{oj}\cdot\vec{r}} \sum_{\vec{H}} \vec{D}_{\vec{H}_j} e^{i2\pi\vec{H}\cdot\vec{r}} = \sum_{\vec{H}} \vec{D}_{\vec{H}_j} e^{-i2\pi\vec{k}_{H_j}\cdot\vec{r}} \tag{5.47}$$

This is the *wavefield* i.e. the electric displacement field which propagates through the crystal and excites the scattering centres. This may be expressed as the sum of plane waves with amplitude $|\vec{D}_{\vec{H}_j}|$ and wave vector $\vec{k}_{\vec{H}_j}$. The concept of the wavefield underlies the whole theory of dynamical diffraction. Wavefields have a physical reality and all the propagation properties of X-rays in crystals may be interpreted in terms of wavefields.

Under the Laue condition for diffraction:

$$\vec{k}_{O_j} - \vec{k}_{H_j} = \vec{H}_j \tag{5.48}$$

Therefore, all the wavevectors of a given wavefield can be deduced from one another by a translation in the reciprocal lattice. If we draw these wavevectors from the various reciprocal lattice points we find they intersect at a common extremity called the *tie-point*. The tie-point characterises the wavefield and its geometrical construction is

illustrated in Figure 5.3.

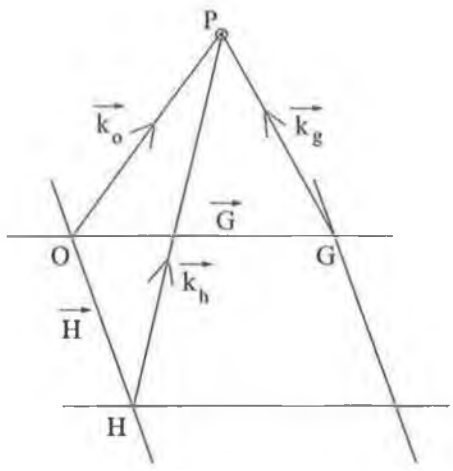

Figure 5.3: Wavevectors $\vec{k}_O$, $\vec{k}_H$ and $\vec{k}_G$ originating from three reciprocal lattice sites O, H and G intersect at a common point P, the tie-point.

5.3.2 n-Beam Diffraction and the Dispersion Surface

Consider now a single wavefield $\vec{D}_j$ within the crystal. Since $\vec{D}_j = \epsilon_0 (1 + \chi_e) \vec{E}_j$, inserting Equation (5.19) into Equation (5.16) lets one express Equation (5.47) as:

$$\sum_{\vec{H}_j} \vec{D}_{\vec{H}_j} e^{-i2\pi \vec{k}_{\vec{H}_j} \cdot \vec{r}} = \epsilon_0 \left[1 - \frac{r_e \lambda^2}{\pi V} \sum_{\vec{H}'_j} F_{\vec{H}'_j} e^{-i2\pi \vec{H}'_j \cdot \vec{r}} \right] \sum_{\vec{H}_j} \vec{E}_{\vec{H}_j} e^{-i2\pi \vec{k}_{\vec{H}_j} \cdot \vec{r}} \qquad (5.49)$$

where the index $\vec{H}'_j$ has been used to distinguish it from $\vec{H}_j$. Since each wavevector is displaced by a reciprocal lattice vector from its neighbour, one can say $\vec{k}_{\vec{H}'_j} + \vec{H}_j = \vec{k}_{\vec{H}'_j + \vec{H}_j} = \vec{k}_{\vec{H}_j - \vec{H}'_j}$. After appropriate changes in the indices of summation the previous

equation can be rewritten as:

$$\sum_{\vec{H}_j} \vec{D}_{\vec{H}_j} e^{-i2\pi\vec{k}_{H_j}\cdot\vec{r}} = \epsilon_0 \sum_{\vec{H}_j} \vec{E}_{\vec{H}_j} e^{-i2\pi\vec{k}_{\vec{H}_j}\cdot\vec{r}} - \frac{\epsilon_0 r_e \lambda^2}{\pi V} \sum_{\vec{H}_j} \left[\sum_{\vec{P}_j} F_{\vec{H}_j - \vec{P}_j} \vec{E}_{\vec{P}_j} \right] e^{-i2\pi\vec{k}_{\vec{H}_j}\cdot\vec{r}} \tag{5.50}$$

Since this relationship must hold for all $\vec{r}$ it must also hold for each Fourier component.

$$\begin{aligned} \therefore \vec{D}_{\vec{H}_j} &= \epsilon_0 \vec{E}_{\vec{H}_j} - \frac{\epsilon_0 r_e \lambda^2}{\pi V} \sum_{\vec{P}_j} F_{\vec{H}_j - \vec{P}_j} \vec{E}_{\vec{P}_j} \\ &= \epsilon_0 \chi_{\vec{H}_j} \vec{E}_{\vec{H}_j} - \frac{\epsilon_0 r_e \lambda^2}{\pi V} \sum_{\vec{P}_j \neq \vec{H}_j} F_{\vec{H}_j - \vec{P}_j} \vec{E}_{\vec{P}_j} \end{aligned} \tag{5.51}$$

Inside the crystal $\vec{D}_{\vec{H}_j}$ is predominantly equal to its vacuum value; however, it is slightly modified by small contributions from the other Fourier components of the electric field inside the crystal. By analysing the rotation of the Bloch function for the electric field using Maxwell's equations, Batterman and Cole [92] ascertained the following condition:

$$\vec{k}_{\vec{H}_j} \times \vec{E}_{\vec{H}_j} = \omega_0 \mu_0 \vec{H}_j \tag{5.52}$$

Taking the cross product of this equation with the diffracted wavevector $\vec{k}_{\vec{H}}$ yields:

$$\vec{k}_{\vec{H}_j} \times \left(\vec{k}_{\vec{H}_j} \times \vec{E}_{\vec{H}_j} \right) = -\omega_0^2 \mu_0 \vec{D}_{\vec{H}_j} = -\omega_0^2 \mu_0 \epsilon_0 \left(\vec{E}_{\vec{H}_j} - \frac{r_e \lambda^2}{\pi V} \sum_{\vec{P}_j} F_{\vec{H}_j - \vec{P}_j} \vec{E}_{\vec{P}_j} \right) \tag{5.53}$$

Using the vector identity for a triple cross product

$$\vec{k}_{\vec{H}_j} \times \left(\vec{k}_{\vec{H}_j} \times \vec{E}_{\vec{H}_j} \right) = -\left(\vec{k}_{\vec{H}_j} \cdot \vec{k}_{\vec{H}_j} \right) \vec{E}_{\vec{H}_j} + \left(\vec{k}_{\vec{H}_j} \cdot \vec{E}_{\vec{H}_j} \right) \vec{k}_{\vec{H}_j} \tag{5.54}$$

with Equation (5.53) and re-arranging yields

$$\left[k^2\left(1+\chi_0\right)-\left(\vec{k}_{\vec{H}_j}\cdot\vec{k}_{\vec{H}_j}\right)\right]\vec{E}_{\vec{H}_j}+k^2\chi_{\vec{P}_j}\vec{E}_{\vec{P}_j}+\left(\vec{k}_{\vec{H}_j}\cdot\vec{E}_{\vec{H}_j}\right)\vec{k}_{\vec{H}_j}=0 \qquad (5.55)$$

where k is the magnitude of the wavevector of the incident radiation impinging upon the crystal. Equations (5.55) are the fundamental set of equations describing the j fields propagating inside the crystal. It is important to note, that physically all the waves exist within the crystal; however, only some of them have appreciable intensity. We will therefore look at two cases of interest to this thesis, that of a single beam propagating in the crystal ($j \in \{0\}$ i.e. no diffraction taking place) and that of two beams propagating in the crystal ($j \in \{0,1\}$ i.e. the diffracted and forward diffracted waves exist). To simplify the notation the forward diffracted beam will be defined $\vec{E}_O = \vec{E}_{\vec{H}_{j=0}}$ and the diffracted beam $\vec{E}_H = \vec{E}_{\vec{H}_{j=1}}$.

5.3.2.1 Single Beam Case $j \in \{0\}$

In the single beam case Equation (5.55) reduces to:

$$|\vec{k}_0|^2 = k^2\left(1+\chi_0\right) \qquad (5.56)$$

This equation simply describes the influence of the material's index of refraction on the propagation of the beam. The equation suggests two possible values for the wavevector $\vec{k}_0$ inside the crystal. The first is the refracted beam and the second is a reflected wave from the interface of the vacuum and the crystal exit surface. As the reflected wave

will only have appreciable intensity for samples that are thinner than the material's absorption length its effects can be neglected as such samples will not be studied in later chapters.

Consider the refraction of the X-ray beam in the crystal as shown in Figure 5.4. The wavevector of the beam inside the crystal only impinges on one reciprocal lattice site associated with the Ewald sphere and therefore diffraction does not occur. Applying Snell's law yields:

$$\mathfrak{Re}(n)\sin\psi_0 = \sin\psi_i \tag{5.57}$$

where the real component of the refractive index of the material is given by:

$$\mathfrak{Re}(n) = \mathfrak{Re}\left\{\sqrt{\frac{\mu\epsilon}{\mu_0\epsilon_0}}\right\} = \mathfrak{Re}\left\{\sqrt{1+\chi_e}\right\} \approx 1 + \frac{\chi_0}{2} \tag{5.58}$$

At the critical angle ω_c, the refracted angle $\psi_0 = \pi/2$ and $\psi_i = \pi/2 - \omega_c$.

$$\therefore \cos\omega_c = 1 + \frac{\chi_0}{2} \tag{5.59}$$

In the X-ray regime the critical angle is far less than unity and we may expand $\cos\omega_c \approx 1 - \omega_c^2/2$

$$\Rightarrow \omega_c = \sqrt{-\chi_0} = \lambda\sqrt{\frac{r_e F_0}{\pi V}} \tag{5.60}$$

For angles less than the critical angle total external reflection occurs giving rise to a specularly reflected Fresnel wave in conjunction to a evanescent wave within the

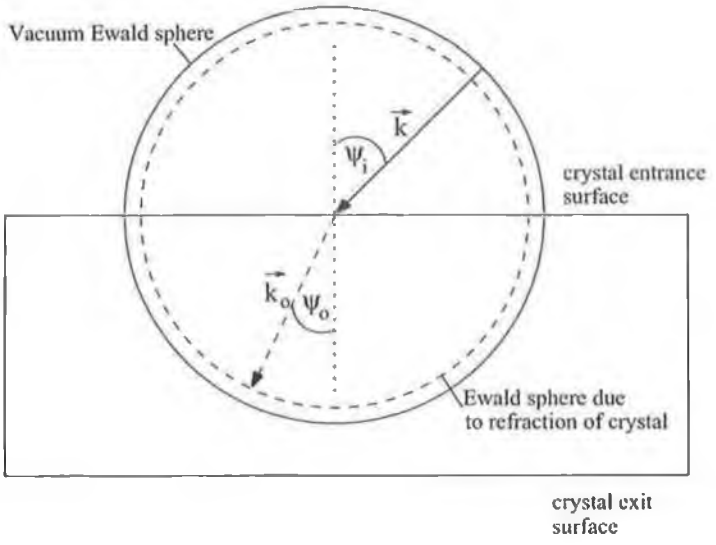

Figure 5.4: Refraction of X-ray beam by crystal with refractive index n. Due to the effect of the refractive index the radius of the Ewald sphere is smaller inside the crystal compared to vacuum.

sample whose electric field is exponentially damped within the scattering depth defined by Dosch [98]:

$$\Lambda = \frac{\lambda}{2\pi\left(l_i + l_o\right)} \tag{5.61}$$

where

$$l_{i,o} = \sqrt{\frac{\left(2\delta - \sin^2\psi_{i,o}\right) + \left[\left(\sin^2\psi_{i,o}\right)^2 + (2\beta)^2\right]^{\frac{1}{2}}}{2}} \tag{5.62}$$

In equation (5.62) the subscripts i and o refer to the incident and forward diffracted beams respectively,

$$\beta = \frac{\lambda\mu_0(\lambda)}{4\pi}$$

$$\delta = \frac{\overline{\rho_e}e^2\lambda^2}{2m_e\epsilon_0\left(2\pi c\right)^2}$$

and $\overline{\rho_e}$ is the mean electron density.

5.3.2.2 Two Beam Case $j \in \{0, 1\}$

Under the two beam approximation two reciprocal lattice points lie on the Ewald sphere associated with the vector $\vec{k}_O$ and diffraction occurs. Therefore, Equation (5.55) reduces to:

$$\left[k^2\left(1+\chi_O\right) - \left(\vec{k}_O\vec{k}_O\right)\right]|\vec{E}_O| + k^2 C\chi_{\overline{H}}|\vec{E}_H| = 0 \tag{5.63}$$

$$k^2 C\chi_H|\vec{E}_O| + \left[k^2\left(1+\chi_O\right) - \left(\vec{k}_H\vec{k}_H\right)\right]|\vec{E}_H| = 0 \tag{5.64}$$

where the different polarisation states are taken into consideration through $C = 1$ for σ polarisation or $C = \cos 2\theta$ for π polarisation.

For the incident and diffracted field amplitudes to have nontrivial solutions, the determinant of the previous set of equations must equal zero.

$$\begin{vmatrix} k^2(1+\chi_0) - \vec{k}_0 \cdot \vec{k}_0 & k^2 C\chi_{\overline{H}} \\ k^2 C\chi_H & k^2(1+\chi_0) - \vec{k}_H \cdot \vec{k}_H \end{vmatrix} = 0 \tag{5.65}$$

The resulting secular equation determines the permissable wavevectors inside the crystal:

$$\left[\vec{k}_0^2 - k^2\left(1+\chi_0\right)\right]\left[\vec{k}_H^2 - k^2\left(1+\chi_0\right)\right] = k^4 C^2 \chi_H \chi_{\overline{H}} \tag{5.66}$$

This equation can be interpreted as the equation of the locus of the tie-point P_j which is determined by the wavevectors $\vec{k}_O$ and $\vec{k}_H$. This locus is a surface called the *dispersion surface*. Essentially Equation (5.66) describes two spheres of radii equal to $|\vec{k}_O| =$

$|\vec{k}_H| = k\,(1 + \chi_0/2)$ centered around two reciprocal lattice sites displaced from each other by a reciprocal lattice vector. The dispersion surface is illustrated in Figure 5.5.

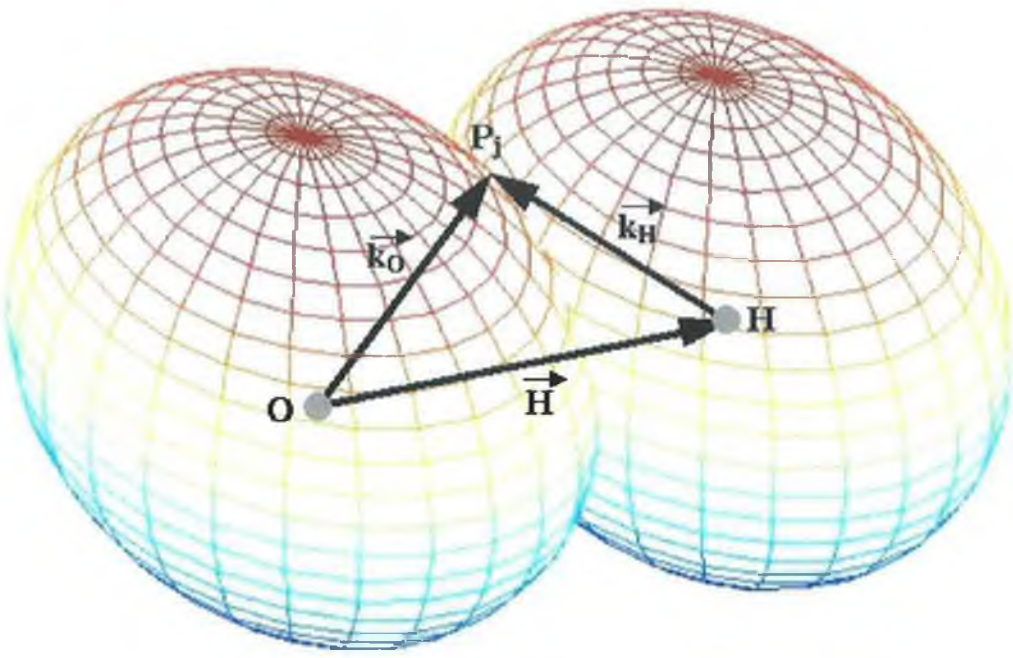

Figure 5.5: Three dimensional illustration of the dispersion surface. The wavevectors $\vec{k}_O$ and $\vec{k}_H$ intercept at the tie-point P_j. Each Ewald sphere has a radius $k\,(1 + \chi_0/2)$.

Since each term in square brackets in Equation (5.66) is the difference of two squares, we may simplify the equation to:

$$4k^2 \left[\vec{k}_0 - k\left(1 + \frac{\chi_0}{2}\right)\right]\left[\vec{k}_H - k\left(1 + \frac{\chi_0}{2}\right)\right] = k^4 C^2 \chi_H \chi_{\overline{H}} \qquad (5.67)$$

Consider the term in the first square bracket of the previous equation. This describes the distance X_O between the tie-point P_j and the Ewald sphere centered about the reciprocal lattice point O. Similarly, the term in the second set of square brackets

describes the distance X_H between the tie-point and the Ewald sphere centered on the reciprocal lattice point H. Equation (5.67) reduces to:

$$X_O X_H = \frac{k^2}{4} C^2 \chi_H \chi_{\overline{H}} \tag{5.68}$$

Far from the Laue diffraction condition either X_O or X_H must be large, implying the other quantity is small and hence only one beam exists inside the crystal. Close to the Laue condition for diffraction $X_O \approx X_H$ and both the diffracted and forward diffracted beams have appreciably values. At the exact Bragg condition $X_0 = X_H$ and this implies

$$X_0 = \pm \frac{k}{2} \sqrt{\chi_H \chi_{\overline{H}}} \tag{5.69}$$

The significance of the two values for X_0 implies two branches exist on the dispersion surface; the outer and inner branches being called the β and α branches, respectively. As the distances X_O and X_H are approximately 10^{-5} times smaller than the radii of the two Ewald spheres, examination of Figure 5.5 does not reveal the presence of the two branches. Rather we must zoom in around the point of intersection of the spheres, the Lorentz point L_O, as shown in Figure 5.6. The small size of X_O and X_H compared to the radius of their respective Ewald sphere, facilitates approximation of the Ewald spheres in the vicinity of the Lorentz point by tangential planes T_O and T_H. The tangential plane T through the Laue point L parallel to the α branch of the dispersion surface describes the locus of the incident vacuum wavevectors.

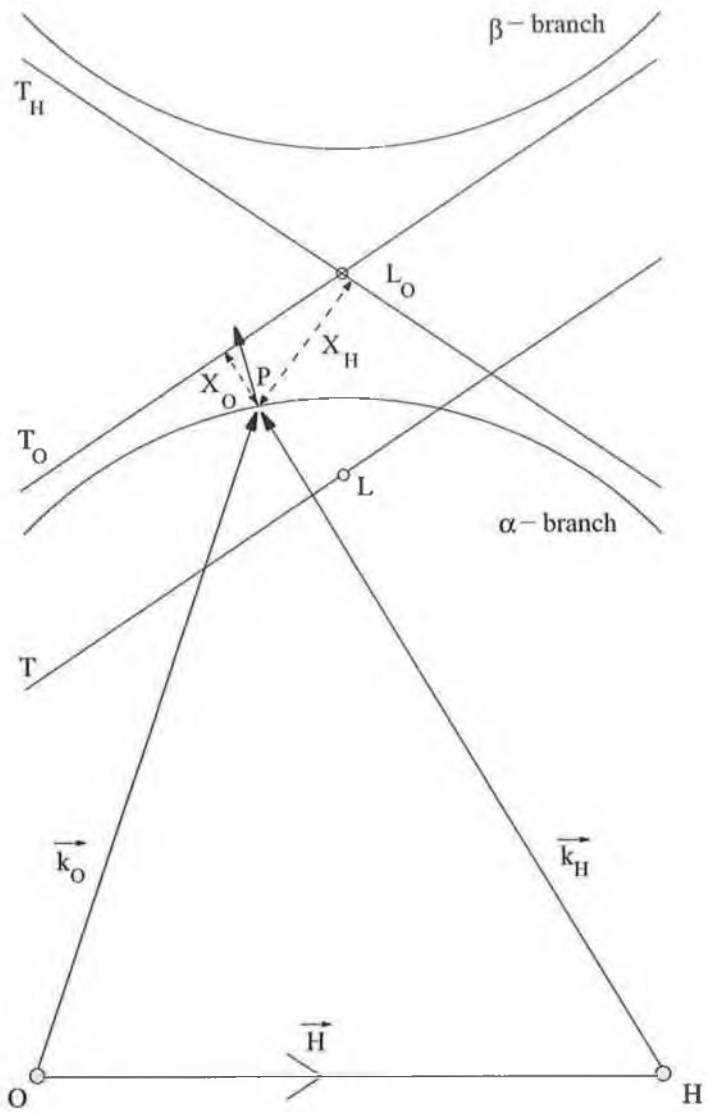

Figure 5.6: Asymptotic approximation to the Ewald sphere's about the Lorentz point L_O. Strictly speaking two asymptotes should be drawn for the polarisation states associated with the diffracted and forward diffracted beams; only one asymptote corresponding to the real part of the dispersion surface has been drawn for the sake of clarity. The drawing is not to scale.

The angle between the asymptotes in Figure 5.6 is $2\theta_B$. From Equation (5.68) it follows that the distance between the apexs of the hyperbola of each branch of the dispersion surface, the so called Bragg gap, is:

$$G_B = \frac{k|C|\sqrt{\chi_H \chi_{\overline{H}}}}{\cos\theta_B} = \frac{r_e \lambda |C| \sqrt{F_H F_{\overline{H}}}}{\pi V \cos\theta_B} \tag{5.70}$$

The Bragg gap is proportional to the structure factor and therefore, the size of the X-ray interaction with the sample. The larger the structure factor, the greater the interaction and the larger the Bragg gap. In real space the reciprocal of the Bragg gap gives Λ_0: the Pendellösung distance and extinction distance in the transmission and reflection geometries, respectively.

$$\Lambda_0 = \frac{1}{G_B} = \frac{\lambda\sqrt{\gamma_O|\gamma_H|}}{C\sqrt{\chi_H \chi_{\overline{H}}}} \tag{5.71}$$

where γ_0 and γ_H are the cosines of the angles between the normal to the crystal surface and the incident and reflected directions, respectively.

5.3.3 Boundary Conditions

A particular solution of Equation (5.45) that describes the propagation of the electromagnetic wave through the crystal is represented geometrically by its corresponding tie-point on the dispersion surface. The wavefield will consist of contributions from the diffracted wave $\vec{k}_H$ and the forward diffracted wave $\vec{k}_O$; the extent of these contributions is dependent on the boundary conditions. The direction of energy flow within the crystal is governed by the Poynting vector $\vec{S}_T$ for the total wavefield that is ex-

cited. This in turn depends on the energy flow associated with tie-points on the α and β branches of the dispersion surface, $\vec{S}_\alpha$ and $\vec{S}_\beta$, respectively. A particular and elegant property of the energy flow $\vec{S}_T$ is that the direction of energy flow corresponding to a tie point on a particular tangential sheet of the dispersion surface, is that of the normal to the surface at that point.

The appropriate tie-points can be selected in accordance with the boundary conditions imposed upon Maxwell's equations due to the vacuum-crystal interface:

$$\vec{E}_{T_{\text{vac}}} - \vec{E}_{T_{\text{cryst}}} = 0 \qquad \vec{D}_{N_{\text{vac}}} - \vec{D}_{N_{\text{cryst}}} = 0 \tag{5.72}$$

$$\vec{H}_{T_{\text{vac}}} - \vec{H}_{T_{\text{cryst}}} = 0 \qquad \vec{B}_{N_{\text{vac}}} - \vec{B}_{N_{\text{cryst}}} = 0 \tag{5.73}$$

where the indices T and N refer to the tangential and normal components at the interface of the respective field. These boundary conditions can be summarised concisely by stating if $\vec{n}$ is a unit vector normal to the crystal surface, whatever the values of the incident wavevector $\vec{k}$ or the resulting Bloch wave inside the crystal, then

$$\vec{k}_O - \vec{k} = \delta\vec{n}; \qquad \delta \in \mathbb{N} \tag{5.74}$$

5.3.3.1 Laue Diffraction

The selection of tie-points for the Laue geometry is illustrated in Figure 5.7. In this case two tie-points are always excited, one on each branch of the dispersion surface. At each tie-point wavevectors directed toward the O and H reciprocal lattice sites are

generated. Four wavevectors are generated in the crystal for each polarisation state, eight in total. The energy flow in the crystal is in the direction of the Poynting vector, that is, normal to the dispersion surface at the tie-points, and only at the exit surface do the waves split up into the diffracted and forward diffracted beams.

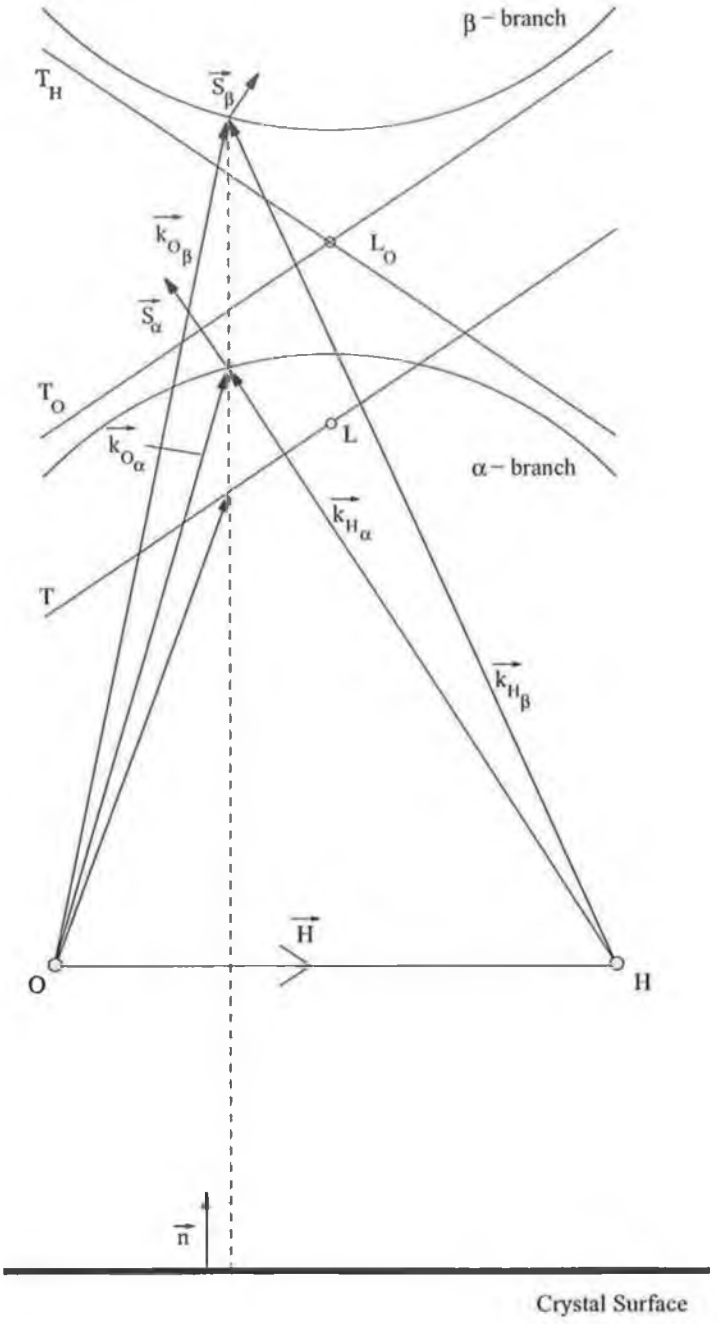

Figure 5.7: Selection of tie-points on dispersion surface for Laue geometry. Only the real parts of the wavevectors are considered in the analysis; the effects of absorption are neglected. Only one polarisation state is considered. A tie-point is selected on each branch of the dispersion surface. The Poynting vectors associated with the α and β branches are normal to the dispersion surface at the tie point.

5.3.3.2 Bragg Diffraction

The tie-points associated with Bragg diffraction are shown in Figure 5.8. In strict Bragg diffraction the normal to the crystal surface intersects two points on one of the branches of the dispersion surface. The Poynting vectors associated with the two tie-points are different; the energy flow from one point is directed into the crystal, but that from the other is directed outwards. No wavefields are generated within crystal from the tie-point whose Poynting vector is directed outwards and thus its effects can be ignored. Therefore a single wavefield is generated within the crystal for each polarisation state.

The penetration depth under the Bragg geometry for an imperfect crystalline sample was given by the kinematical theory in Section 5.2.4. For a perfect crystal extinction occurs and the resulting penetration depth is shallower than anticipated by purely photoelectric absorption processes. Over an extinction distance all the energy is coupled from the forward diffracted beam to the diffracted beam and back again (see Pendellösung discussion in Section 5.3.4). Therefore, the maximum transfer of energy from the forward diffracted to diffracted beam takes place over half the extinction distance Λ_0 described by Equation (5.71). This is therefore the penetration depth from which information is recorded in a Bragg reflection from a perfect crystal.

$$t_p = \frac{\Lambda_0}{2} \tag{5.75}$$

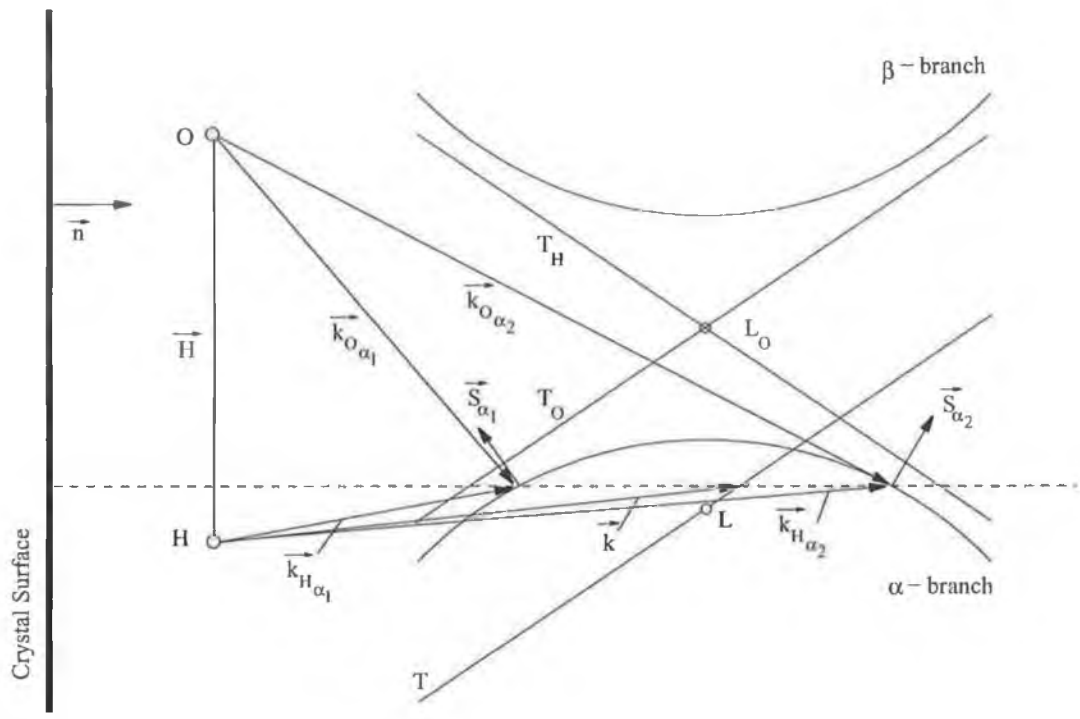

Figure 5.8: Selection of tie-points on dispersion surface for Bragg geometry. Only the real parts of the wavevectors are considered in the analysis; the effects of absorption are neglected. Only one polarisation state is considered. Only one branch of the dispersion surface is excited. The Poynting vectors associated with the α and β branches are normal to the dispersion surface at the tie point.

5.3.3.3 Total External Reflection

The mechanism of tie-point selection in the case of Bragg diffraction is only applicable to situations where the incident angle between the X-ray beam and the normal to the diffracting planes lies in the interval $\omega_c \leq \theta_B < \pi/2$. An interesting case occurs for $\theta_B = \pi/2$. In this situation multiple beam effects come into consideration with the excitation of other Bragg reflections apart from the backscattered one [99]. Further discussion of this situation is beyond the scope of this thesis. For angles below the

critical angle no tie-points are selected as shown in Figure 5.9 and therefore, no wavefields exist within the crystal. As seen in the one-beam analysis of Section 5.3.2.1 an evanescent wave is generated within the sample.

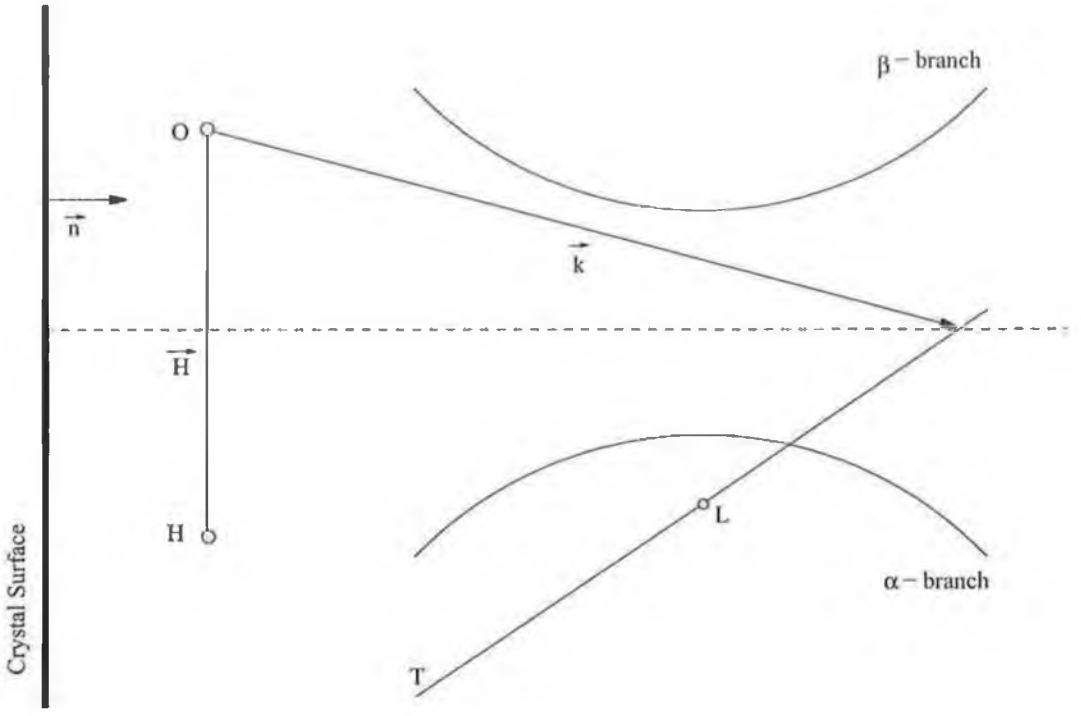

Figure 5.9: Dispersion surface under the condition of total external reflection. No tie-points are selected on the dispersion surface and therefore only an evanescent wave exists within the sample. In this geometry it is not accurate to approximate the α and β branches of the dispersion surface using the tangential planes T_O and T_H.

5.3.4 Energy Flow and Pendellösung Fringes

The energy flow in the crystal is described in terms of the Poynting vector for the total wavefield. The temporal average of the Poynting vector is given by:

$$< \vec{S} >= \frac{1}{2}\mathfrak{Re}\left(\vec{E} \times \vec{H}^{*}_{\text{mag}}\right) \tag{5.76}$$

where $\vec{H}^*_{\text{mag}}$ is the complex conjugate of the magnetic field strength. By spatially averaging over the unit cell one can find a relationship describing the interchange of energy between the diffracted and forward diffracted beams in the crystal. Batterman and Cole [92] have shown the result of this calculation to be:

$$\begin{aligned}
\vec{S}_T &= \sqrt{Z_0} << \vec{S} >> \\
&= \frac{1}{2} e^{-4\pi \Im\mathrm{m}\left(\vec{k}_{O_\alpha}\right)\cdot\vec{R}} \left(|\vec{E}_{O_\alpha}|^2 \vec{s}_O + |\vec{E}_{H_\alpha}|^2 \vec{s}_H \right) \\
&\quad + \frac{1}{2} e^{-4\pi \Im\mathrm{m}\left(\vec{k}_{O_\beta}\right)\cdot\vec{R}} \left(|\vec{E}_{O_\beta}|^2 \vec{s}_O + |\vec{E}_{H_\beta}|^2 \vec{s}_H \right) \\
&\quad + e^{-2\pi\left[\Im\mathrm{m}\left(\vec{k}_{O_\alpha}\right)+\Im\mathrm{m}\left(\vec{k}_{O_\beta}\right)\right]\cdot\vec{R}} \left[|\vec{E}_{O_\alpha}||\vec{E}_{O_\beta}|\vec{s}_O + |\vec{E}_{H_\alpha}||\vec{E}_{H_\beta}|\vec{s}_H \right] \times \\
&\qquad \times \cos 2\pi \left[\left(\Re\mathrm{e}\left(\vec{k}_{O_\alpha}\right) - \Re\mathrm{e}\left(\vec{k}_{O_\beta}\right) \right) \cdot \vec{R} \right] \\
&= \vec{S}_\alpha + \vec{S}_\beta + \vec{S}_{\alpha\beta}
\end{aligned} \tag{5.77}$$

where $\vec{R}$ is a vector within the unit cell and $\vec{s}_O$ and $\vec{s}_H$ are unit vectors in the directions of $\vec{k}_O$ and $\vec{k}_H$.

In general, the imaginary parts of the wavevectors i.e. the components of the wavevectors associated with absorption, do not play an important part in the directional properties of the Poynting vector $\vec{S}_T$. Consequently, $\vec{S}_\alpha$ and $\vec{S}_\beta$ are independent of depth below the surface of the crystal whilst $\vec{S}_{\alpha\beta}$ demonstrates a sinusoidal dependence. For the symmetric Laue case satisfying the exact Bragg condition, the sinusoidal period is equal to the Pendellösung distance Λ_0. Equation (5.77) shows how $\vec{S}_{\alpha\beta}$ periodically shifts the energy around the average direction of the Poynting vector $\vec{S}_\alpha + \vec{S}_\beta$. Such coupling of the energy back and forth between the two branches of the dispersion

surface is termed the Pendellösung effect.

Section transmission X-ray topographs from highly crystalline samples can demonstrate an intensity variation due to this effect. Black white fringes, termed Pendellösung fringes, are recorded in the reflections. The topograph essentially records the intensity variation at the base of the Borrman fan, i.e. the exit surface of the crystal, due to the Pendellösung effect associated with the α and β branches of the respective (hkl) reflection. When Pendellösung fringes are seen, excellent crystalline quality can be automatically inferred.

5.3.5 Anomalous Transmission

In the two-beam approximation a solution to the propagation of the electromagnetic wave in the crystalline medium may be written using Equation (5.47) as:

$$\vec{D} = e^{-i2\pi\vec{k}_O\cdot\vec{r}}\left(\vec{D}_O + \vec{D}_H e^{i2\pi\vec{H}\cdot\vec{r}}\right) \tag{5.78}$$

The intensity of the electromagnetic wave is equal to:

$$|\vec{D}|^2 = e^{4\pi\vec{k}_O\cdot\vec{r}}\left[|\vec{D}_O|^2 + |\vec{D}_H|^2 + 2C|\vec{D}_O||\vec{D}_H|\cos 2\pi\vec{H}\cdot\vec{r}\right] \tag{5.79}$$

The previous equation demonstrates that interference between the diffracted and forward-diffracted waves occurs (the Pendellösung phenomena) resulting in a wavefield that produces a set of standing waves within the lattice. As the intensity of the diffracted

beam is governed by the ratio:

$$R = \frac{\vec{D}_H}{\vec{D}_O} = \frac{k\chi_H C}{2X_H} = \frac{2X_O}{k\chi_{\bar{H}} C} \tag{5.80}$$

one can see that the sign of $|\vec{D}_O||\vec{D}_H|$ in Equation (5.79) is the opposite of the sign of X_O, since the coefficients of the dielectric susceptibility are negative. Therefore, X_O is positive when the tie-point is on the α branch of the dispersion surface and negative when its on the β branch. Consequently the antinodes of the electric field lie on the lattice planes when the tie-point lies on the β branch and the nodes of the electric field lie on the lattice planes when the tie-point lies on the α branch. Hence, wavefields belonging to the α branch of the dispersion surface will experience weaker absorption compared to wavefields belonging to the β branch. In a thick perfect crystal where the product of the linear absorption coefficient and the thickness of the crystal $\mu_O(\lambda)t > 5$ the wavefields associated with the β branch of the dispersion surface are completely absorbed in the crystal and only wavefields corresponding to the α branch are transmitted. Due to the cosine term in Equation (5.79) the effect is strongest for the β brach when the exact Bragg condition is satisfied and decreases as the tie-point moves away from the middle of the reflection domain approaching the asymptotes of the dispersion surface. This is the effect of anomalous transmission.

The effective absorption coefficient for the α and β branches of the dispersion surface has the following dependence on the real part of the deviation parameter η_r from the

ideal Bragg condition:

$$\mu_j = \mu_O(\lambda)\left[1 \mp \frac{|C|\frac{\Im m(\chi_H)}{\Im m(\chi_O)}\cos\psi}{\sqrt{1+\eta_r^2}}\right] \tag{5.81}$$

where ψ is the phase difference between the real and imaginary parts of the dielectric susceptibility for the given reflection. The upper sign corresponds to the α branch and the lower sign corresponds to the β branch.

5.4 Summary

In this chapter the salient features of the kinematical and dynamical theories of X-ray diffraction were presented to the reader. Many of the samples investigated in this thesis possess such large defect densities that application of the kinematical theory to obtain a qualitative understanding of the diffraction topograph is permissible. The assumptions underlying the kinematical theory are valid for most experimental configurations in synchrotron X-ray topography. This theory was formulated by considering the scattering process of a photon incident on an isolated electron. Scattering from an atom occurs essentially from the electron cloud. The result is simply the sum of the scattering contributions from the individual electrons. The next iteration is to consider scattering form a collection of atoms i.e. a crystal. The kinematical theory correctly predicts that diffraction occurs when either the Bragg or Laue criteria are satisfied but fails to determine the intensity of the diffracted beam or its spectral bandpass. These failings were surmounted using the dynamical theory of X-ray diffraction. Maxwell's

equations were solved in a medium possessing a triply periodic dielectric susceptibility. In the one-beam approximation the effect of the material's refractive index on the incident radiation was examined. In particular, the criteria governing the angle of incidence for total external reflection to occur were investigated. This analysis will be applicable to the study of silicon germanium heteroepitaxy on silicon in Chapter 12. In the two-beam approximation, the concept of the dispersion surface was developed. The inherent beauty of the dispersion surface is that it allows the propagation of a wavefield to be described by appropriate tie-points selected in accordance with the boundary conditions imposed on the electromagnetic fields at the vacuum-crystal interface. This geometrical description of the propagation of the wavefield will become particularly useful in Chapter 13 when the effect of microdefects on anomalously transmitted wavefields in nearly perfect silicon is considered. Other dynamical effects such as Pendellösung fringes in section transmission topographs and extinction in Bragg experimental geometries were also considered.

Chapter 6

Synchrotron Radiation

6.1 Introduction

For research in the fields of physics, chemistry, biology and materials science, photons ranging from radio frequencies to hard γ-rays provide some of the most important tools for scientists. Within the bounds of radio waves and gamma rays one covers the spectrum with visible light, ultraviolet light and X-rays. Since their discovery by W.C. Röntgen in 1895 [11], X-rays have become an invaluable tool to probe the structure of matter. They have revolutionised our lives by helping scientists to unravel such mysteries as the structure of DNA [100] and in more recent times, the structure of proteins. The main reason for this unprecedented success is that the X-ray wavelength, which determines the smallest distance one can study with such a probe, is comparable to the inter-atomic dimension.

However, developments in the fields of X-ray physics were limited by the source. Until circa 1970, this was simply the X-ray tube or a variant thereof. In the late 1960s new fields of scientific endeavour were born driven by a new radiation source, namely synchrotron radiation [101]. Synchrotron radiation owes its name to the energy emitted

by relativistically accelerated particles as they are bent in a magnetic field. The early pioneers of synchrotron radiation were thus considered "parasitic users" by their particle physics counterparts who had no use for this wasted energy. The interest in using synchrotron radiation as a tool for scientific investigation caught on almost immediately, with the first dedicated storage ring sources being commissioned in the early 1970s. Today there are forty four dedicated synchrotrons in operation in the world, with new sources being planned on an on-going basis to satisfy the demands of the user community.

Synchrotron radiation provides the user with a continuous spectrum of radiation from the infrared to the hard X-ray region, with an intensity at least ten orders of magnitude higher than can be achieved with a conventional laboratory based rotating anode generator. Other important properties that appeal to different experiments performed within the user community are its high degree of polarisation, pulsed time structure and low divergence.

In this chapter, a basic investigation of the properties of synchrotron radiation will be performed. The interested reader can find much more detailed information in [102–104] and the references provided therein. A good overview of the properties of synchrotron radiation and their applicability to X-ray diffraction topography can be found in [24]. As much of the topography experiments described in this thesis were undertaken at the DORIS storage ring at HASYLAB am DESY, Germany, particular attention will be paid to the parameters pertaining to this synchrotron. However, the analysis applies to the operation of all synchrotrons. Having imparted some knowl-

edge on the fundamental differences between synchrotron radiation and ordinary non-relativistic radiation, the apparatus to generate such electromagnetic energy, i.e. the synchrotron, will be examined. The chapter concludes with some of the shortcomings of current synchrotron radiation sources and alludes to the potential of the proposed X-ray free electron lasers that will surely be the focus of scientific investigations in the very near future.

6.2 Properties of Synchrotron Radiation

6.2.1 Instantaneous Power Radiated

Schwinger [105] determined the instantaneous radiation power emitted by a monoenergetic electron with energy E travelling at relativistic speeds in a circular orbit per unit interval at wavelength λ into the unit interval of the angle ψ between the emitted radiation and the orbit axis to be

$$\frac{\delta^2 I\left(\lambda,\psi,E\right)}{\delta\lambda\delta\psi} = \frac{27}{128\epsilon_0\pi^4}\frac{e^2c}{\rho^3}\left(\frac{\lambda_c}{\lambda}\right)^4\left(\frac{E}{mc^2}\right)^8\left(1+\left(\frac{E}{mc^2}\psi\right)^2\right)^2 \times\left[K_{2/3}^2(\eta)+\frac{\left(\frac{E}{mc^2}\psi\right)^2}{1+\left(\frac{E}{mc^2}\psi\right)^2}K_{1/3}(\eta)\right] \tag{6.1}$$

where I is the intensity of the synchrotron radiation, ρ is the radius of curvature of the circular orbit, $K_{1/3}$ and $K_{2/3}$ are modified Bessel functions of the second kind, e is the elementary charge, m is the rest mass of the electron, c is the speed of light, ϵ_0 the

permittivity of free space and

$$\eta = \frac{\lambda_c}{2\lambda}\left[1+\left(\frac{E}{mc^2}\psi\right)^2\right]^{3/2} \tag{6.2}$$

$$\lambda_c = \frac{4\pi\rho}{3}\left(\frac{mc^2}{E}\right)^3 \tag{6.3}$$

λ_c is the so-called "critical wavelength". This is the characteristic wavelength of the observed radiation, i.e. above λ_c, the brilliance of the source falls off with an exponential type dependence as illustrated in Figure 6.3 on page 177.

6.2.2 Polarisation

The first and second terms in the square brackets in Equation (6.1) give the intensities of the components of light polarised parallel and perpendicular to the electron orbit. The radiation is predominantly polarised with the electric vector parallel to the acceleration vector. In the electron's direction of motion the radiation is 100% polarised with the electric vector in the instantaneous orbital plane. Integration over all angles and all wavelengths yields about 75% polarisation in the orbital plane. However, when many electrons are present, the incoherent vertical and radial betatron oscillations result in a range of angles for the electron beam at each point in the orbit. This angular divergence reduces the polarisation. Off the orbit plane the polarisation is elliptical. One of the axes of the polarisation ellipse is always in the orbital plane because the phase difference between the parallel and perpendicular polarisation components is always 90°.

6.2.3 Beam Divergence

The divergence of the beam can be investigated by plotting Equation (6.1) as a function of ψ for various wavelengths. The simulated results for the DORIS storage ring, wherein $E = 4.45$ GeV, $\rho = 12.1849$ m and $\lambda_c = 0.77$ Å are shown in Figure 6.1. Below the critical wavelength the energy is focused into a narrow cone with opening angle less than

$$\gamma = \frac{mc^2}{E} \tag{6.4}$$

For the DORIS storage ring $\gamma \approx 0.11$ mrad. Therefore, below the critical wavelength one has a highly directed, highly collimated beam. The divergence of the beam is of particular importance for X-ray topography, the implications of which will be discussed in Chapter 7 Section 7.3.2.

The angular distribution of radiated power integrated over all wavelengths is simply the integral of Equation (6.1) over λ. If one examines Figure 6.2 one can see that most of the radiation is contained within a cone with opening angle less than γ.

$$\frac{\delta I(\psi, E)}{\delta \psi} = \frac{7}{64\pi\epsilon_0}\frac{e^2 c}{\rho^2}\left(\frac{E}{mc^2}\right)^5 \left[1 + \left(\frac{E}{mc^2}\psi\right)^2\right]^{-5/2} \left[1 + \frac{5}{7}\frac{\left(\frac{E}{mc^2}\psi\right)^2}{1 + \left(\frac{E}{mc^2}\psi\right)^2}\right] \tag{6.5}$$

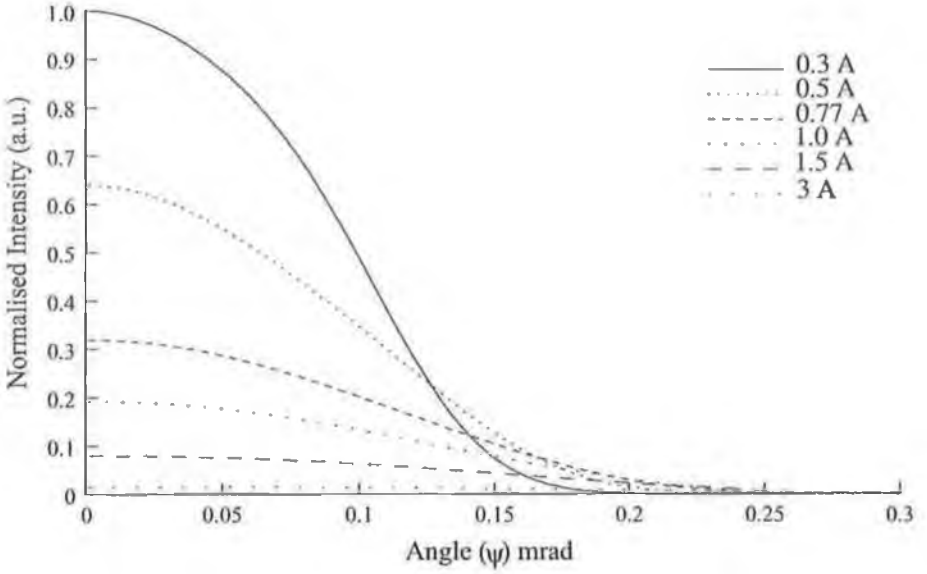

Figure 6.1: Angular distribution of instantaneous synchrotron radiation power at various wavelengths for DORIS storage ring bending magnet. $E = 4.45$ GeV, $\rho = 12.1849$ m and $\lambda_c = 0.77$ Å.

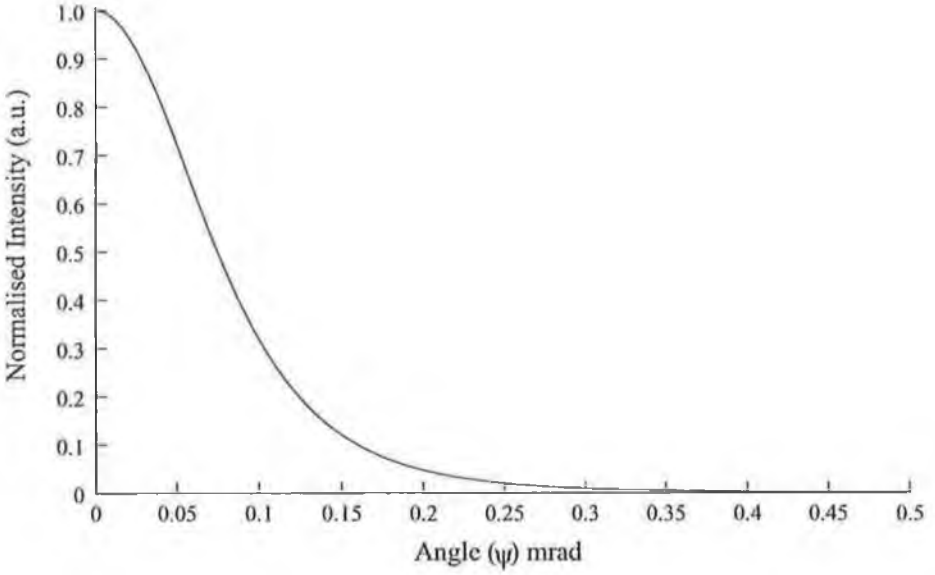

Figure 6.2: Angular distribution of synchrotron radiation power over all wavelengths for DORIS storage ring bending magnet. $E = 4.45$ GeV, $\rho = 12.1849$ m and $\lambda_c = 0.77$ Å.

6.2.4 Spectral Distribution of Emitted Radiation

Integrating Equation (6.1) over ψ one obtains the spectral distribution of synchrotron radiation.

$$\frac{\delta I(\lambda, E)}{\delta \lambda} = \frac{9\sqrt{3}}{64\pi^3 \epsilon_0} \frac{e^2 c}{\rho^3} \left(\frac{E}{mc^2}\right)^7 \left(\frac{\lambda_c}{\lambda}\right)^3 \int_{\lambda_c/\lambda}^{\infty} K_{5/3}(\zeta) d\zeta \tag{6.6}$$

The simulated spectral distribution of the DORIS storage ring is shown in Figure 6.3. One can clearly see that a broad spectral range is achievable with synchrotron radiation. No other source can produce such a spectrum at such high intensities. The spectrum has a maximum at 0.42 λ_c and a full width at half-maximum of 0.84 λ_c.

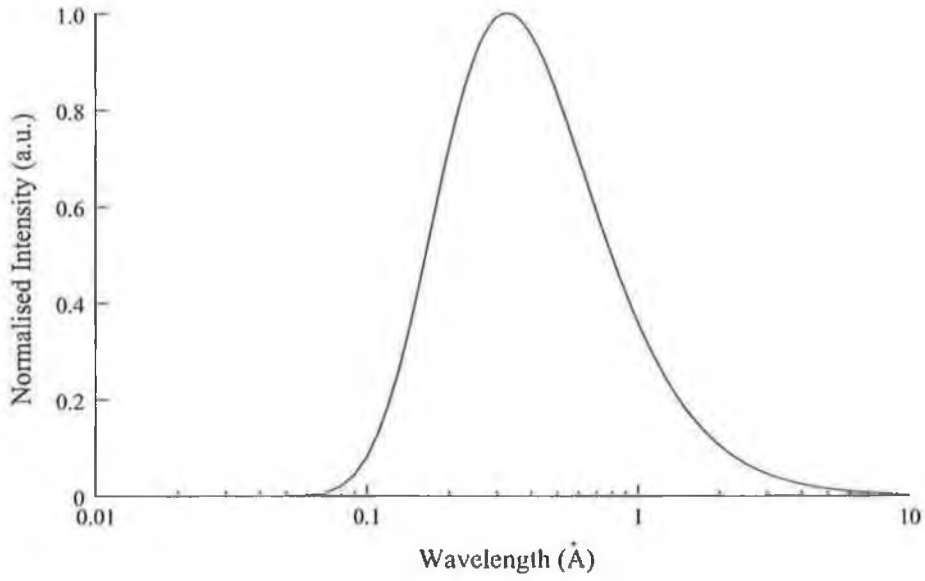

Figure 6.3: Spectral dependence of normalised intensity for DORIS storage ring bending magnet. $E = 4.45$ GeV, $\rho = 12.1849$ m and $\lambda_c = 0.77$ Å.

6.2.5 Total Intensity of Synchrotron Radiation

The total intensity of the synchrotron radiation may be obtained by integrating Equation (6.1) over both variables of integration. The result is

$$I = \frac{1}{6\pi\epsilon_0}\frac{e^2 c}{\rho^2}\left(\frac{E}{mc^2}\right)^4 \tag{6.7}$$

Therefore, one can see that the intensity is proportional to the fourth power of the electron energy, which implies a very intense source of electromagnetic radiation at the expense of high power losses. One can also see that for a given energy E, the synchrotron radiation intensity and corresponding power loss produced by an electron will be approximately 3×10^6 times greater than that caused by a proton due to the m^4 term. This is the fundamental reason why particle physicists can accelerate protons up to energies of the order 460 GeV [106] and electrons/positrons are rarely accelerated above 50 GeV.

6.2.6 Time Structure

Electrons/positrons in synchrotrons are grouped in *bunches* whose length is determined by the radio frequency system that replenishes the radiated energy. Thus, the radiation is pulsed with each pulse typically about 10% of the RF period. To ensure destructive interference does not occur, the orbital period must be an integer multiple of the RF period. This integer is called the *harmonic number* of the ring. Often this number is very large so that a large number of discrete bunches (and corresponding high currents)

can be used.

At DORIS, which is now approximately 25 years old, only five equidistant bunches are used providing a peak beam current of 140 mA. The circumference of the storage ring is 289.2 m, yielding a temporal bunch separation of 192 ns. Far more esoteric bunch modes are used at the current third generation synchrotron sources such as the European Synchrotron Radiation Facility (ESRF), the Advanced Photon Source (APS) and Spring8. For example, in one of the hybrid modes at the ESRF, one 7 mA bunch can be injected such that it is diametrically opposed to a 193 mA multi-bunch beam that is spread over one third of the storage ring circumference. Such a bunch pattern is often used in time-resolved pump probe measurements; the single bunch being employed as a timing fiducial.

For the main stay of X-ray topographic investigations the time structure of the beam is not important. The intensity, which is directly related to the beam current, is the crucial factor as it governs exposure times. However, stroboscopic X-ray topographic investigations [107] have been undertaken and these obviously appealed to the time structure of the ring.

In every synchrotron in the world, with the exception of the APS in Chicago USA, the beam current of the ring falls off exponentially after injection of the bunches because the RF system cannot provide sufficient energy to maintain their peak velocity. With the aim of providing a more stable beam for their users, in September 1998, the APS began commissioning a new operating mode called "top-up" [108]. In this mode, the beam current does not decay but is maintained at a high level using frequency injection,

while the photon shutters are open and the photon beams are delivered to the users. The APS achieved their goal and now "top-up" is a standard operating mode with a nominal beam current of 100 mA. This mode of operation would be beneficial to topographers as the constant intensity would facilitate greater control of the exposure times.

6.2.7 Comparison with Laboratory Based Sources

In the previous subsections synchrotron radiation was demonstrated to be a source of highly directional, focused, very intense, linearly polarised light, possessing a time structure in the picosecond regime. This is in stark contrast to laboratory based sources. The spectrum generated by a conventional rotating anode [109] or laser based plasma X-ray source [110, 111], consists of a continuous spectrum known as *Bremsstrahlung* radiation with the spectrally sharper and more intense elemental fluorescent lines superimposed on it. One generally uses the radiation associated with the fluorescent lines in the experiment and the *Bremsstrahlung* is normally filtered using a double crystal monochromator or some suitable alternative. The radiation from such sources is emitted over a solid angle of 2π and consequently, inefficient use is made of the unpolarised radiation that is produced. Rotating anodes generate radiation continously, whilst the laser driven sources have a pulsed time structure, as the high intensities necessary to induce plasma formation cannot be achieved by lasers operating in continous mode.

6.3 Synchrotron Structure

6.3.1 Fundamental Operation

Typically, synchrotron radiation facilities operate as follows. The charged particles, be they positrons or electrons, are accelerated by a linear accelerator before they gain further energy in a booster ring. The storage ring then accumulates the particles that have been pre-accelerated and transported from the injection system. The stored particles traverse the ultra-high vacuum storage ring in bunches, the size of which is determined by the injection sequence and the radio frequency system of the ring. The system compensates for energy lost through radiation using the RF system.

6.3.2 Magnet System

In order to guide the beam in a curved trajectory around the ring, dipole or bending magnets, whose magnetic field is perpendicular to the direction of motion and is uniform in the region occupied by the beam, steer the beam in accordance with the Lorentz force law. The radiation from such magnets has been described in Section 6.2.1. If the bending magnets were the only steering elements in the ring, particles with spatial coordinates different from those of the ideal orbit would move progressively away from this orbit. To improve the characteristics of the beam, focusing elements are required; namely the quadrupole and sextupole magnets. In a quadrupole magnet, particles are focused in one plane and defocused in the other plane. Therefore a sequence of focusing and defocusing quadrupole magnets, appropriately designed, can focus the beam in

both planes. Sextupole magnets are needed to control the electron beam's chromaticity, i.e. the variation in focusing with electron momentum.

At this stage the reader may be thinking that a lot of the previous discussion about quadrupole and sextupole magnets sounds more like conventional optics than relativistic particle acceleration. In fact, this is the case. The system of magnetic "lenses" that guide and focus an electron beam is called the *lattice*. Fundamentally the lattice lets the accelerator physicist describe the machine section by section by an appropriate matrix element much in the same way a ray passing through a lens can. In much of the literature concerned with the design of modern day synchrotrons [112], one can find lattice names such as the double focusing achromat (DFA), the triple achromat and the FODO lattice. The choice of lattice will depend on such factors as the cost and user requirements. For example, the FODO lattice is commonly used by high energy physicists and the DFA lattice has been used in the National Synchrotron Light Source and Advanced Light Source storage rings in the USA.

6.3.3 Radio Frequency System

Interspersed between the magnets are drift or acceleration cavities. The accelerating cavities or resonant cavities comprise the RF system. The cavity is energised from a power amplifier at an appropriate frequency so as to establish the necessary acceleration voltage across the gap. The dynamic interaction of the beam with the cavity is such that as long as the voltage is larger than the minimum necessary, a state of "phase stability" exists and those electrons captured at injection automatically receive, on average

over many orbits, the energy increment per turn which they require to counterbalance their energy loss. Current state of the art superconducting RF cavities, constructed out of niobium for the TESLA project [113, pp. 29–30], cooled to an operation temperature of 2 K, can achieve nominal potential gradients of 23.4 MV/m, with the best cell performance yielding gradients as high as 42 MV/m. The power required by the cavity consists of two sources: the power required by the beam itself and sufficient power to compensate the resistive losses of the cavity wall itself. When a "beam-dump" is performed, in general the safest way to do so, is by turning off the power supplied to the RF system.

6.3.4 Vacuum System

A storage ring is a high-vacuum device. In order for the stored beam decay to be of the order of many hours, the average pressure in the ring must be of the order 10^{-9} Torr. Particles circulating in a storage ring suffer collisions due to residual gas within the ring. This induces betatron oscillations and if the scattering angle is too large, the particle is lost by absorption in the vacuum pipe wall. In order to maintain such high vacuums, special delivery systems are required to transmit the radiated photons to the experimental hutch. In the X-ray region, beryllium windows which are transparent to X-rays and can withstand the high vacuum-atmospheric pressure gradient are used.

6.3.5 Insertion Devices

It is known from Section 6.2 that a relativistic electron or positron travelling in a circular orbit emits a continuous spectrum of radiation with opening angle γ in a direction perpendicular to the direction of motion. As the users of synchrotrons became more sophisticated, their demands for greater intensities and tailored radiation characteristics increased in parallel. This was the impetus for the development of special magnetic structures known as wigglers and undulators. These two classes of insertion devices are thus known because they are inserted in straight sections of the storage ring. Both devices fundamentally consist of a periodic alternating magnetic array that is perpendicular to the direction of motion of the electrons. The electrons moving in such an array are forced to wiggle or undulate about their nominal central position thus causing them to radiate. The magnetic field strength can be adjusted through variation of the separation gap z between both arrays and consequently, the desired radiation properties such as intensity and wavelength can be chosen at the user's discretion.

The periodic magnetic field perpendicular to the direction of motion of the particles in an insertion device may be written as

$$B(z) = B_0 \cos\left(\frac{2\pi z}{\lambda_{id}}\right) \tag{6.8}$$

where λ_{id} is the period of the magnetic array and B_0 is the peak magnetic field given by

$$B_0 = \frac{2\pi mcK}{e\lambda_{id}} \tag{6.9}$$

The parameter K characterises the deflection of the electron at each turning point in the device and fundamentally describes the difference in operation between wigglers and undulators.

6.3.5.1 Wigglers

The instantaneous angular distribution of radiated power as a function of wavelength for a particle following a curved trajectory was described in Equation (6.1). In a wiggler where the magnetic structure is designed such that a device with $2N$-poles causes the positron to undergo $2N$ wiggles; the deflection angle $\varphi = K/\gamma$ at each turning point is greater than the natural emission angle of the synchrotron radiation ($\gamma \approx 0.11$ mrad for the DORIS storage ring). Hence $K >> 1$. Thus the wiggler produces incoherent radiation that is $2N$ times more intense than can be achieved with a normal bending magnet.

6.3.5.2 Undulators

Undulators cause small electron or positron deflections, comparable in magnitude to the natural emission angle of the synchrotron radiation. The radiation emitted by an individual particle at the various poles in the magnetic array thus interferes coherently resulting in a very narrow beam of radiation that is spectrally peaked at harmonics of the fundamental wavelength of the undulator. At a nonzero horizontal observation

angle ϑ, the fundamental wavelength of the undulator radiation is given by

$$\lambda_{u1}(\vartheta,\psi) = \frac{\lambda_{id}}{2}\left(\frac{mc^2}{E}\right)^2\left[1+\frac{K^2}{2}+\left(\frac{E}{mc^2}\right)^2(\vartheta^2+\psi^2)\right] \tag{6.10}$$

Assuming the angular divergence of the electron beam is smaller than the natural emission angle of the synchrotron radiation i.e. $K \leq 1$, due to the partial constructive interference the radiation beams opening angle is decreased by $\sqrt{N}$ at a given wavelength and thus the radiation intensity per solid angle increases as N^2. The angular distribution of the nth harmonic radiation intensity is given by

$$\frac{\delta^2 I_n}{\delta\theta\delta\phi} = \frac{I_B}{127e}\frac{\Delta\omega}{\omega}\frac{N^2K^2n^2}{(1+K^2/2)^2}\left[J_{\frac{n-1}{2}}\left(\frac{nK^2}{4(1+K^2/2)}\right) - J_{\frac{n+1}{2}}\left(\frac{nK^2}{4(1+K^2/2)}\right)\right] \tag{6.11}$$

where I_B is the beam current in Amperes, $\Delta\omega/\omega$ is the relative bandwidth and the J's are modified Bessel functions of the first kind. The normalised photon flux for the first, third and fifth harmonics of 127 pole undulator at beamline BW-1, HASYLAB am DESY is shown in Figure 6.4. This was calculated in accordance with [114, 115]. Due to the large beam size at beamline BW-1 (2.141 mm $\times$ 0.252 mm) each harmonic possesses very prominent side lobes.

6.4 Summary

In this chapter, the radiative properties of a relativistic particle moving in a circular orbit due to the presence of a magnetic field were examined. Synchrotron radiation from a bending magnet was shown to be a spectrally broad, intense, polarised, highly

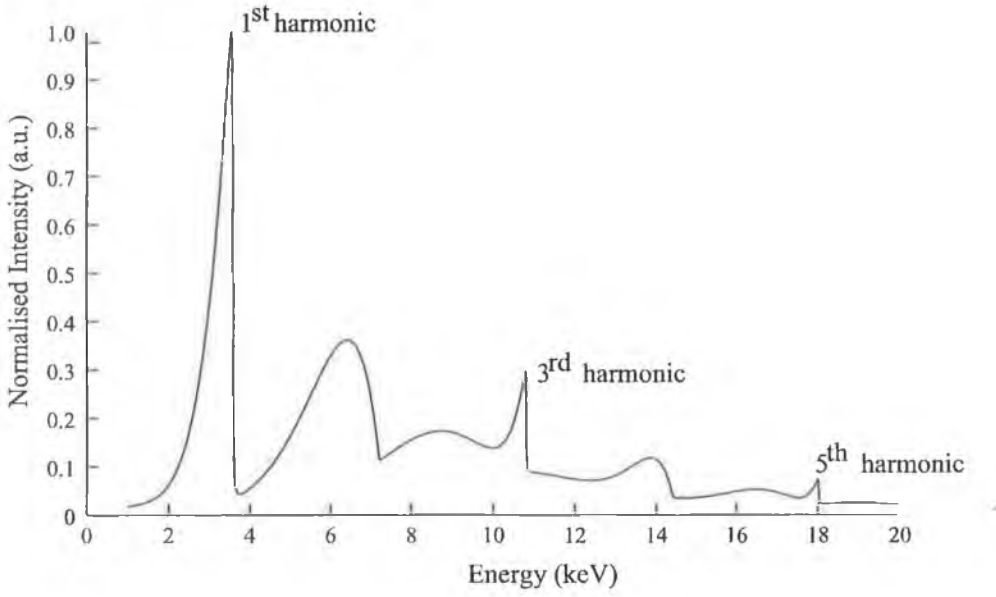

Figure 6.4: Normalised photon flux for the undulator beamline BW-1 at HASYLAB am DESY. $I = 150$ mA, $B_0 = 0.46$ T and $K = 1.34$.

directional source of electromagnetic radiation. The main elements of the synchrotron comprising the magnet system, RF system and vacuum system were briefly examined. The chapter concluded with an examination of the motion of an electron/positron in a periodic magnetic array. Due to its large emission angle, the wiggler behaves as a dipole magnet albeit $2N$ times more intense. Within an undulator, the angle of spontaneously emitted radiation is smaller than the natural emission angle γ, and consequently, in an undulator interference occurs producing harmonically related radiation. It is important to note that there is no fixed phase relationship between the radiated photons. Therefore, the total radiation power is the sum of the single-particle radiation power from all of the particles in the beam.

In a free electron laser (FEL), the aim is to introduce a fixed phase relationship between

all the radiating photons in the undulator [116]. Such total coherence, implies the radiation amplitudes rather than the radiative powers become additive and the radiation power becomes proportional to the square of the number of electrons until saturation occurs. To introduce such coherence in a SASE (Self Amplified Spontaneous Emission) based FEL [117, 118], it is necessary to introduce a longitudinal density modulation of the electrons such that, whilst travelling along one period of the undulator, the electrons slip by one radiation wavelength with respect to the faster electromagnetic field. Depending on the relative phase between the radiation and electron oscillation, electrons experience either a deceleration or an acceleration. The resulting cigar shaped bunch has a micro-bunched structure superimposed on it; the distance between each micro-bunch being equal to the wavelength of the emitted photons. These fourth generation radiation sources will offer extremely intense, polarised, short-pulse duration ($\sim$ 100 fs), transversely coherent, tunable radiation from ca. 0.1 Å to 5 Å. The peak brilliance of these sources will be approximately 10 orders of magnitude higher than current third generation synchrotron sources [119]. It is expected, that owing to the special properties of such radiation whole new avenues of experimental investigation, currently unfeasible at third generation radiation sources, will become possible.

Chapter 7

X-ray Topography

7.1 Introduction

In Chapter 5 elementary kinematical and dynamical diffraction was reviewed before the properties of synchrotron radiation were investigated in Chapter 6. These two fields now merge on the stage of X-ray diffraction topography. From Section 5.2 it is known that when a crystalline material is immersed in a white X-ray beam, diffraction occurs in accordance with Bragg's law for different sets of diffracting lattice planes. Due to the parallel two-dimensional extrusion of a synchrotron radiation beam, each of the respective diffraction spots is actually an X-ray topograph which can be recorded on a fine grain emulsion film. Localised imperfections within the sample modify the diffraction condition and this manifests itself as an intensity variation within the topograph. It is important to note that the defects themselves are not being imaged; rather it is the strains they induce that modify the Bragg condition with respect to the perfect sample regions. This is essential to an understanding of the mechanism of defect imaging.

X-ray topography is a non-destructive, non-invasive technique. It is sensitive to strain

fields extending over more than several micrometres within the sample and therefore X-ray topography is used mainly to image the strain fields associated with dislocations, planar defects, stacking faults, domain walls in ferroelectric and magnetic materials, growth defects and large precipitates [3].

In this chapter the techniques of white beam X-ray diffraction topography will be analysed. Extensive reference to and some expansion of these techniques will be made in the remaining chapters of this thesis. Experimental facets such as resolution and exposure time in conjunction with their relationship to synchrotron radiation will also be described. The chapter concludes with an introduction to the fundamental imaging mechanisms of X-ray topography.

7.2 Techniques of Synchrotron X-ray Topography

The original topographic investigations were performed using the Berg-Barett or Lang techniques. In the Berg-Barett technique [120, 121] an extended X-ray source such a rotating anode generator was used as the radiation source. The sample had to be cut and oriented such that the incident X-ray beam that contained both the $K\alpha_1$ and $K\alpha_2$ fluorescent lines made a very small angle with the diffracting planes. The topograph was recorded on a photographic film placed within 1 mm of the sample surface. One of the problems with this method included double images of defects due to the presence of both the $K\alpha_1$ and $K\alpha_2$ lines. Lang [22] overcame the problem of "double diffraction" by generating the X-ray beam from a fine focus source and collimating the beam to a height of ca. 10 μm. The ribbon of $K\alpha_1$ radiation thus produced a section transmission

image of the crystal under investigation. Lang invented a goniometer that facilitated simultaneous traversal of the film and sample across the beam. Thus, a projection topograph could be produced. The major drawback with Lang's technique is the long exposure time.

Synchrotron radiation produces a very intense, highly collimated beam of X-ray radiation. This radiation can be collimated to provide large area beams of approximately 5 mm^2 down to micro-focus beams of approximately 10 μm^2. By simple collimation of the beam using a pair of computer controlled slits, one can obtain Lang section and projection topographs without any need for special alignment or traversal of the sample. Since its first demonstration in 1974 [24] the field of synchrotron X-ray topography has blossomed into a mature area of scientific investigation. Its growth is directly attributable to the ultra-low divergence and high intensities provided by a synchrotron light source. During its growth, experimental techniques such as back reflection and grazing incidence topography were developed and implemented. The reader will now be presented with a review of the techniques of X-ray topography applicable to this thesis.

All of the topography experiments mentioned below were performed at the Hamburger Synchrotronstrahlungslabor at the Deutsches Elektronen-Synchrotron (HASYLAB am DESY), Hamburg, Germany, utilising the continuous spectrum of synchrotron radiation from the DORIS III positron storage ring bending magnet at beamline F-1. Currents of 60 mA to 150 mA were used and the positron energy was 4.45 GeV.

7.2.1 Large Area Transmission Topography

In large area transmission topography, the incident beam size is collimated anywhere from 0.5 mm × 0.5 mm to 4 mm × 8 mm in size. The whole volume of the sample bathed in the beam contributes to the topographs recorded on the film. The information in the images originates from within the same sample volume, albeit from different diffracting planes. Therefore different information may be present in different topographs. The sample may be tilted to obtain information from specific reflections [122]. This geometry is demonstrated in Figure 7.1.

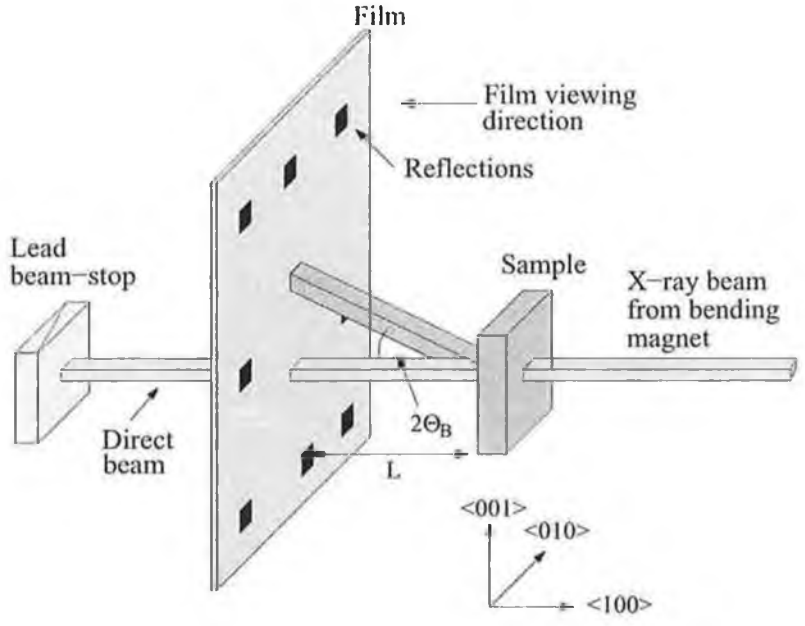

Figure 7.1: Large area transmission topography experimental configuration. Only one diffracted beam has been drawn for clarity.

An example of a large area transmission topograph is shown in Figure 7.2. This topograph was recorded from a 1.135 mm thick <111> oriented silicon substrate with a

145 μm thick epilayer grown on top. Stress at the interface between the substrate and epilayer is being relieved by the formation of misfit dislocations. The misfit dislocations in turn induce threading dislocations to propagate into the substrate.

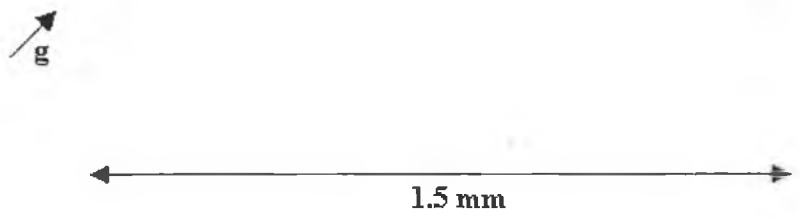

Figure 7.2: $24\bar{2}$ large area transmission topograph from a silicon sample. $\vec{g}$ is the diffraction vector.

7.2.2 Section Transmission Topography

Section transmission topography uses an arrangement similar to its large area counterpart, only in this case the incoming beam is collimated into a narrow ribbon by a slit typically 10–15 μm in height. A set of Laue case section topograph images of sample cross-section is produced and, provided the Bragg angle is not too small, the image gives detailed information about the energy flow within the crystal and direct depth information on the defects present within a particular crystal slice [77, 123]. The height of the slit in section topography should not be more than 20 μm, because im-

ages of the defects begin to overlap and the depth distribution of the defects is lost. Slit heights less than 10 μm are impractical, as longer exposure times are required. The experimental configuration is shown in Figure 7.3.

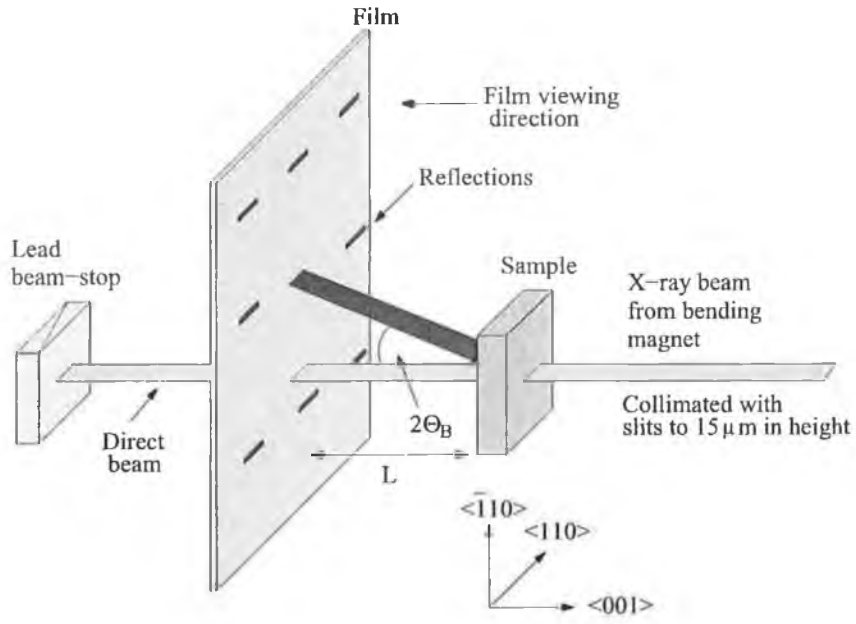

Figure 7.3: Section transmission topography experimental configuration. Only one diffracted beam has been drawn for clarity.

For crystalline materials with very small defect densities, Pendellösung or Kato fringes may be recorded on the film as an interference pattern. The explanation of the interference pattern was presented in Chapter 5 Section 5.3.4. Figure 7.4 is a 044 section transmission topograph from a silicon wafer wherein interference of the wavefields from different branches of the dispersion surface took place at the exit surface, resulting in Pendellösung fringes being recorded [124–126].

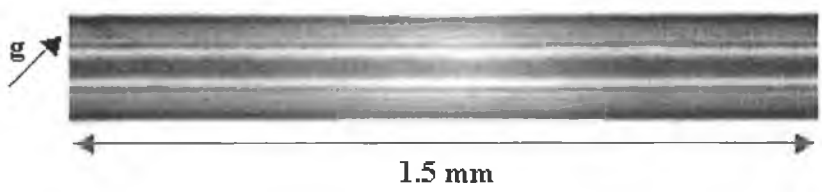

Figure 7.4: 044 section transmission topograph possessing Pendellösung fringes. $\vec{g}$ is the diffraction vector.

7.2.3 Large Area Back Reflection Topography

In large area back reflection topography, the incoming beam is collimated in size similar to its large area transmission counterpart. The beam passes through a hole in the film cassette, and in general, impinges perpendicularly upon the sample. Diffraction occurs and the back reflected topographs are recorded on the film. As this is a reflection geometry, low energy photons satisfy the Bragg diffraction criterion. Therefore the penetration depths are often quite shallow, making this technique quite advantageous for the analysis of epilayers and surface structures. When large area transmission topography is not possible, for example in the case of the microchip bonded to a ceramic package, back reflection topography proves quite useful. The imaging mechanism for one reflection is shown in Figure 7.5.

Figure 7.6 is an 822 back reflection topograph from a packaged erasable read-only memory (EPROM) silicon based integrated circuit. Here the X-rays yield stress information from a penetration depth of 62 μm, as calculated using Equation (5.34).

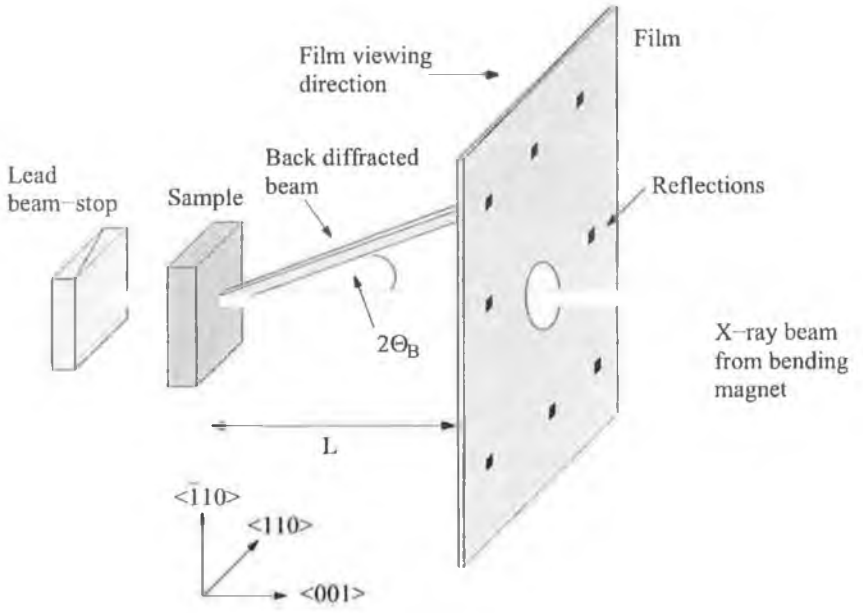

Figure 7.5: Large area back reflection topography. Only one diffracted beam has been drawn for clarity.

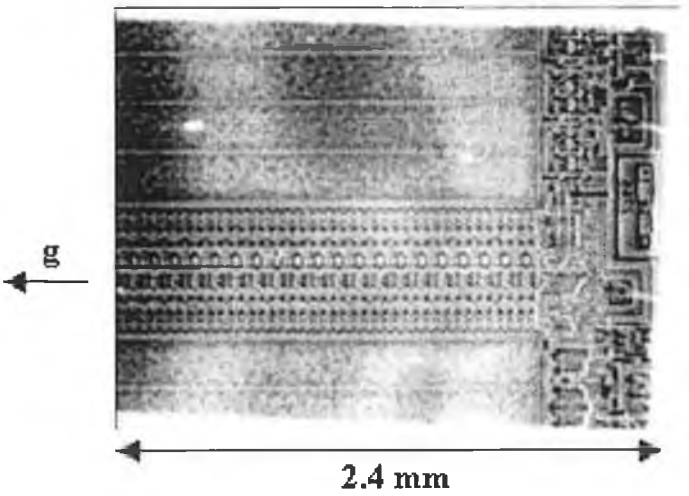

Figure 7.6: 822 large area back reflection topograph from a silicon based EPROM integrated circuit. $\vec{g}$ is the diffraction vector.

7.2.4 Back Reflection Section Topography

As with section transmission topography the incoming beam is collimated to 10–15 μm in height. A set of Bragg case section topographs of sample cross section are produced. The linear absorption coefficient of most semiconductor materials is so large that the X-ray beam generally does not penetrate through the thickness of the sample. Back reflection section topography therefore provides a sectional image from the upper regions of a sample or a device [127]. The experimental configuration is demonstrated in Figure 7.7.

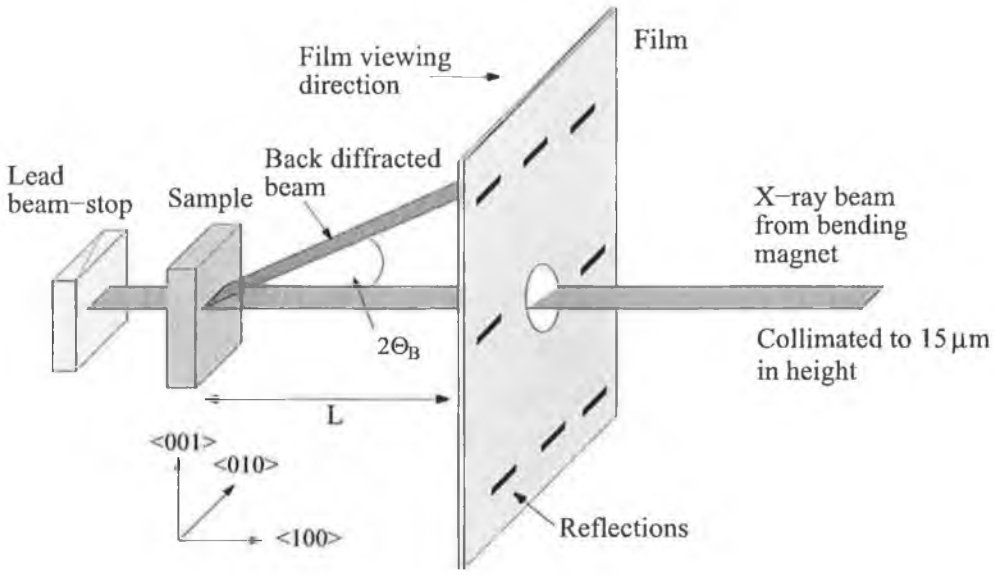

Figure 7.7: Back reflection section topography experimental configuration. Only one diffracted beam has been drawn for clarity.

Figure 7.8 is a 511 back reflection section topograph recorded from a patterned boron doped <100> oriented silicon wafer. The stress due to the patterning on the wafer surface is indicated in the figure by arrow P. In this case the X-rays have penetrated

through the sample and hence the back side is discernible (arrow B).

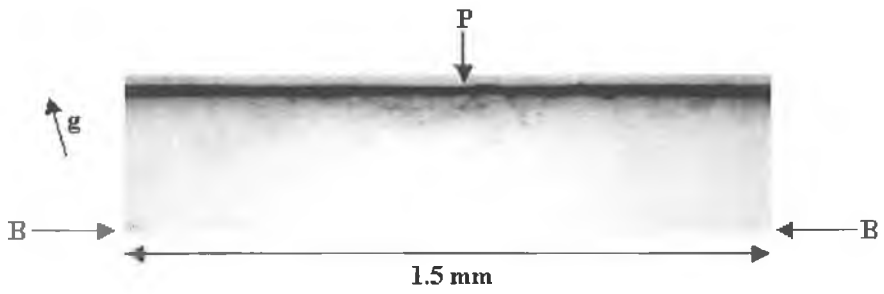

Figure 7.8: 511 back reflection section topograph from a silicon wafer. $\vec{g}$ is the diffraction vector.

7.2.5 Grazing Incidence and Total External Reflection Topography

In the grazing incidence geometry shown in Figure 7.9 the incident X-ray beam impinges on the sample at an angle greater than the critical angle ω_c for total external reflection [128]. By varying the incidence angle, the penetration depth can be varied according to Equation (5.34). At angles close to the critical angle the penetration depth varies rapidly. When the incident angle is smaller than the critical angle total external reflection occurs and the scattering depth is given by Equation (5.61) [129].

Figure 7.10 shows a grazing incidence diffraction topograph from a 0.25 μm CMOS process wafer. The circuit topography is visible via imposed strain on the underlying silicon.

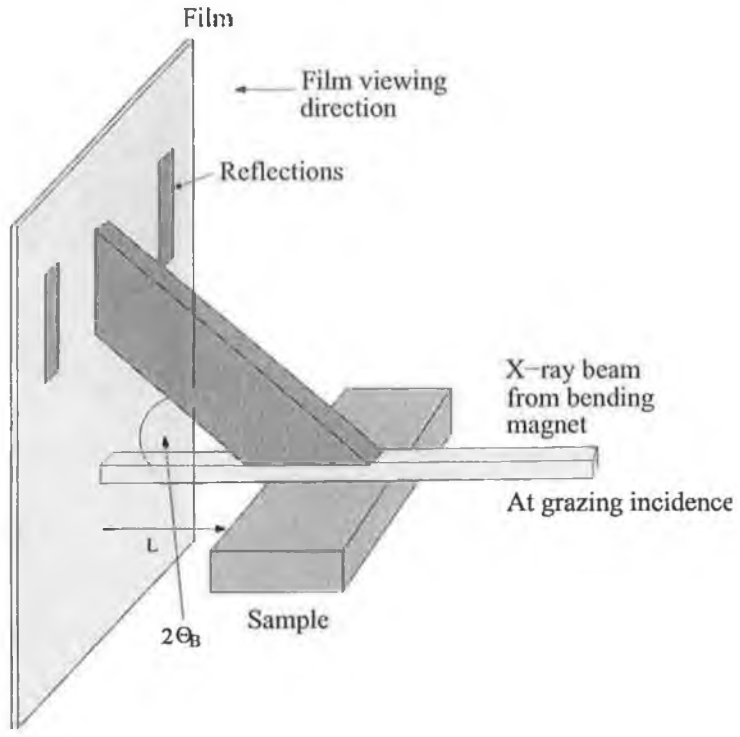

Figure 7.9: Grazing incidence topography experimental configuration. Only one diffracted beam has been drawn for clarity.

Figure 7.10: Grazing incidence diffraction topograph from a 0.25 μm CMOS process wafer. $\vec{g}$ is the diffraction vector.

7.3 Synchrotron Radiation Applied to X-ray Topography

Of all the properties of synchrotron radiation investigated in Chapter 6 Section 6.2, the most important for X-ray topography are the intensity and divergence of the beam. The intensity governs directly the exposure time and the resolution of the technique is limited by the beam divergence.

7.3.1 Exposure

The exposure time is principally determined by a combination of the photon flux provided by the source, be it a bending magnet or insertion device, the sample under investigation, the topographic technique used and the photographic film on which the topograph is recorded.

From Chapter 6 it is known that the intensity of the source is related to the beam current. As the positrons or electrons lose momentum in the storage ring, the intensity falls off accordingly. For topographic studies of similar samples, the same integrated exposure is used. This implies the exposure time has to be increased as the beam current falls off. For example, for a large area transmission topograph of a 500 μm thick silicon sample, the nominal integrated exposure is 100 mAmin for a high resolution film. This yields exposure times of 1 minute and 1 minutes 30 seconds when the beam current is 100 mA and 66 mA, respectively.

As dislocations of the order of a micrometre and greater are imaged at unity magnification by X-ray topography and subsequently optically enlarged, the photographic

film must have a comparable resolution. The high resolution films used in this thesis, Geola VRP-M holographic film and Kodak SO-343 photographic film, have emulsion grain sizes of 35 nm and 50 nm, respectively. The grain size of the standard resolution film, Kodak Industrex industrial X-ray film, is 180 nm. The exposure speed for the high resolution films is ten times slower than that of the standard resolution film.

The exposure time also depends on the technique. Prieur [130] developed an approximate ratio between the exposure times for large area τ_{LAT} and section transmission topography τ_{ST} to be

$$\frac{\tau_{\mathrm{ST}}}{\tau_{\mathrm{LAT}}} = \frac{t}{h}\left[\tan\left(2\theta \mp \varphi\right) \pm \tan\varphi\right] \tag{7.1}$$

where t is the thickness of the sample, h is the height of the beam, 2θ is the angle between the direct and diffracted beam, and, φ is the angle between the incident beam and the normal to the sample surface. The alternating $\pm$ operators account for the position of the diffracted beam with respect to the sample normal. The sign in the first term is $+$ if the image and the incident beam are below the surface normal.

Having exposed the film it is worth mentioning briefly the development procedure. For all the aforementioned films, the process is identical. The films are placed in an aqueous solution of Kodak D-19 developer, the temperature of the bath at the time of mixing being a constant 38 °C. After five minutes, the development process is stopped by dipping the films in a 3% acetic acid aqueous solution. Fixing is then performed using Kodak sodium fixer solution for ten minutes. The films are placed in a dryer for 30 minutes.

7.3.2 Resolution

The spatial resolution or minimum strain field size that can be observed using X-ray topography depends on the angular divergence of the incident beam $\Delta\theta_0$ and the sample to detector distance L, according to the simple formula:

$$r = L\Delta\theta_0 \tag{7.2}$$

At beamline F-1 at HASYLAB am DESY, the horizontal divergence of the beam is 0.4 mrad and the vertical divergence is 0.0238 mrad [131]. As it is larger, the horizontal divergence places a lower limit on the minimum detectable strain field size. For a sample to detector distance of 10 mm, $r = 4$ μm. Improved spatial resolution can be found at the undulator beamline BW-1 where the horizontal divergence of the beam is 0.317 mrad.

The geometrical resolution R on a topographic image is governed by the source size S, the sample to detector distance L and the sample to source distance D, according to the formula:

$$R = \frac{SL}{D} \tag{7.3}$$

The sample to source distance at beamline F-1 is $D = 35$ m. The source size in the horizontal and vertical extents measures $S = 1.224$ mm $\times$ 0.510 mm. Once again the limiting resolution is imposed by the larger horizontal source size. Therefore, for a sample to film distance of 10 mm, the lateral geometrical resolution is 0.3 μm. At the 900 m long coherent X-ray optics beamline at Spring8, Japan, the spatial resolution

is an amazing 14 nm [132]. Note, however, that this is not generally achievable since the actual resolution will be limited by the spatial extent of the strain fields and the thickness of the film emulsions through which the diffracted photons pass.

7.4 Merits of White Beam X-ray Diffraction Topography

Possibly the greatest advantage of X-ray diffraction topography when used with a synchrotron source is its experimental simplicity. The apparatus consists of little more than a goniometer on which the sample is mounted and an X-ray transparent cassette to hold the film during exposure. Even the most esoteric crystalline samples or devices can be inserted into the beam and diffraction will occur. This avoids the relatively more complex alignment procedures that are often associated with monochromatic topography.

Several reflections may be recorded simultaneously and in some favorable cases, an instantaneous Burgers vector $\vec{b}$ assignment may be possible [133]. For example, suppose the diffraction vector is known to be $\vec{g} = [100]$ and a defect is observed in all images bar one. In the image from which the defect is absent, the condition $\vec{g} \cdot \vec{b} = 0$ is satisfied and thus $\vec{b}$ may be evaluated.

One disadvantage of X-ray diffraction topography is that the exposure is integrative in nature i.e. an image due to wavelength λ may also have contributions from harmonics that are not structure factor forbidden. This implies small details may be averaged out or the image may appear blurred as occurred in [134]. This problem can be circumvented in monochromatic topography by detuning the monochromator slightly from

the exact Bragg condition. As the width of the rocking curve is much larger for the fundamental reflexion than for the higher order harmonics, only the fundamental will be passed with any appreciable intensity.

For white-beam topography one can calculate the relative intensities due to the various wavelengths that are recorded during exposure [24, 25, 128]. Phenomenologically, the number of photons $N_{\text{abs}}(\lambda)$ recorded on the film associated with a given harmonic can be calculated through a knowledge of the spectral photon brightness of the source $N_0(\lambda)$ and the scattering power of the diffracting planes through a structure factor related term $f_1(\lambda)$. In the calculations, absorption by the various materials found in the beam path e.g. air, beryllium, aluminum foils and the cassette envelope, is accounted for through the term $f_2(\lambda)$. Finally absorption in the film itself is accounted through the term $f_3(\lambda)$. The harmonic content of each individual reflection is calculated and no comparison with other topographs is made. Therefore geometrical factors such as polarisation do not have to be considered. The total number of photons associated with wavelength λ absorbed in the film during an exposure can be estimated by

$$N_{\text{abs}}(\lambda) = N_0(\lambda) f_1(\lambda) f_2(\lambda) f_3(\lambda) \tag{7.4}$$

where

$$f_1(\lambda) = P(\lambda) F_{hkl} \lambda^3 \tag{7.5}$$

$$f_2(\lambda) = \prod_i e^{-\mu_i x_i} \tag{7.6}$$

$$f_3(\lambda) = 1 - e^{-\mu_f x_f} \tag{7.7}$$

In equations (7.5)–(7.7), $P(\lambda)$ is the intensity of the radiation at wavelength λ with respect to the bending magnet spectrum as obtained from Figure 6.3 in Chapter 6, F_{hkl} is the structure factor associated with the diffracting planes, μ_i and x_i are the effective linear absorption coefficients and thicknesses of the i$^{\text{th}}$ absorbing layer, and, μ_f and x_f are the effective linear absorption coefficients and thicknesses of the film.

7.5 Contrast Formation

X-ray diffraction topographs are essentially maps of the scattering power of the sample under examination as a function of position across the diffracted X-ray beam. The observed contrast is therefore related to the properties of both the incident beam and its interaction with the sample. Contrast formation in a topograph may be broken down into three broad categories, each of which will now be examined in turn.

7.5.1 Structure Factor Contrast

Structure factor contrast arises from samples wherein different regions possess different structure factors. In terms of the kinematical theory of X-ray diffraction (see Section 5.2), the diffracted intensity is proportional to the square of the structure factor. Therefore, a change in the structure factor induces a change in intensity. It commonly arises in magnetic materials and twinned crystals [135]. Figure 7.11 demonstrates structure factor contrast from the II-VI semiconductor compound CdTe. This very rare sample was grown from the melt by the Bridgman method during the space shut-

tle flight STS-95 [136]. The topograph demonstrates two regions twinned about the {111} boundary.

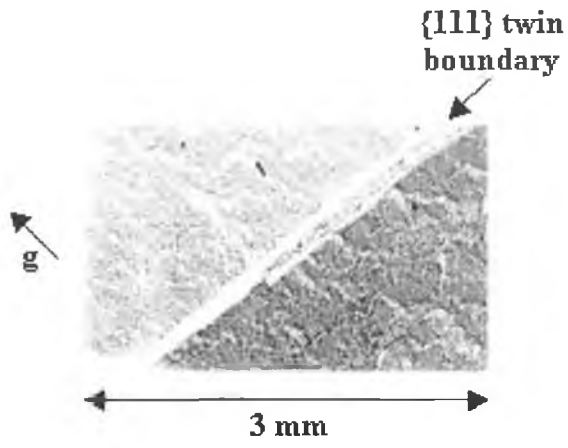

Figure 7.11: $0\,\bar{2}\,\bar{2}$ back reflection topograph demonstrating structure factor contrast in cadmium telluride. $\vec{g}$ is the diffraction vector.

7.5.2 Orientation Contrast

Orientation contrast occurs where part of the crystal is misoriented such that, in the case of monochromatic topography, diffraction cannot occur as Bragg's law is not satisfied. Therefore, no photons will reach the film from the misoriented region and this corresponds to the zero intensity or white region in the topographic image. Diffraction from the perfect region of the sample will expose the film leaving the respective region black.

For white beam topography, the situation is somewhat more complicated. The perfect and imperfect regions of the sample will satisfy Bragg's law for different wavelengths. These wavelengths will then travel toward the film at different Bragg angles and there-

fore, there will be a loss or gain in recorded intensity in regions corresponding to the boundary of a misoriented region. Boundaries producing divergent beams lead to a loss of intensity and thus stronger contrast than convergent boundaries. The width of the region of intensity gain or loss is determined by the angle of misorientation and the sample to film distance [137]. By taking topographs at two sample-to-film distances the misorientation component in the plane of incidence can be measured. For both monochromatic and polychromatic topography the effective misorientation of the region must be greater than the divergence of the beam, otherwise, the sample region will appear perfect with respect to the incident beam and diffract accordingly [138].

An example of orientation contrast is shown in Figure 7.12. The sample was a 2.20 μm thick gallium nitride layer grown on sapphire. The GaN epilayer is observed as the wavy structure indicated by arrow O. The growth uniformity of the epilayer was less than 5%. Consequently, the strain and misorientational contrast is also non-uniform across the sample.

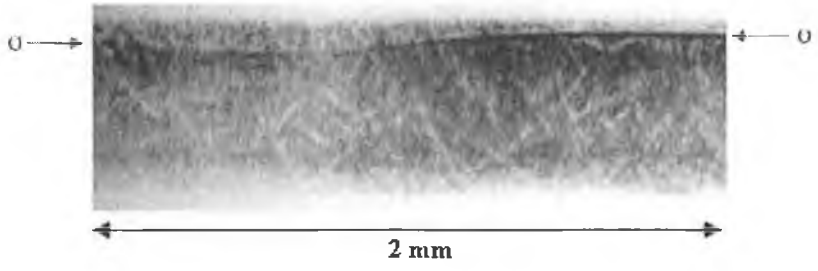

Figure 7.12: Orientation contrast example in gallium nitride grown on sapphire. The misoriented epilayer is indicated by arrow O.

7.5.3 Extinction Contrast

The structure factor and orientational contrast mechanisms can be explained quite simply from the kinematical theory of X-ray diffraction. The last contrast mechanism, called extinction or diffraction contrast, appeals to dynamical theory for its explanation.

7.5.3.1 Direct Image

One of the fundamental problems discussed in Chapter 5 with the kinematical theory was that for a perfect crystal it predicted a delta function type rocking curve. In his early attempts to formulate a dynamical theory of X-ray diffraction, Darwin assumed partial reflection and transmission of the incident radiation by the lattice planes [13, 14]. Therefore the incident radiation is being continuously Bragg scattered as one progresses down into the crystal. For this reason, the *extinction* depth to which the beam penetrates, is generally far less in a perfect crystal than the penetration depth in an imperfect crystal.

In a near perfect crystal, where the product of the linear absorption coefficient μ_0 and the sample thickness t is less than unity, the direct image is formed when the incident X-ray beam intercepts the defect within the crystal [139]. Therefore the X-rays do not suffer extinction and for this reason their contrast is always higher than for a perfect crystal i.e. direct images are seen as black on a grey background. This is the most common type of image observed in white beam topography.

7.5.3.2 Dynamical Image

The dynamical image is formed when a wavefield propagating inside a crystal intercepts the defect. It is most easily observed under conditions of high absorption, where normal absorption destroys the direct image i.e. $\mu_0 t > 1$ [140]. Now a resulting loss in intensity is recorded on the film as the wavefield cannot propagate to the exit surface of the crystal. The dynamical image is often seen as a white shadow beside the direct black image.

7.5.3.3 Intermediary Image

The third and final diffraction imaging mechanism is termed the intermediary image [140]. This image arises from the interference at the exit surface of the new wavefields created at the defect site with the original wavefields propagating along other ray paths. Intermediary images are normally not easy to see in integrated wave topographic images and usually manifest themselves through bead like contrast along the direct image of the defect. The intermediary image thus has an alternating black-white oscillatory contrast.

An example of all three types of extinction contrast mechanisms may be seen in Figure 7.13.

7.6 Summary

X-ray diffraction topography and its application to the visualisation of strain within semiconductor materials and devices was introduced. The fundamental experimental

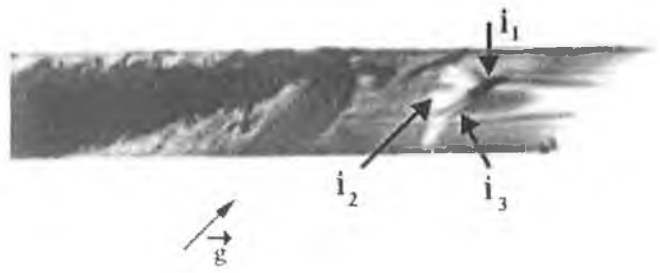

Figure 7.13: Extinction contrast imaging mechanism in silicon. 022 section transmission topograph. $\vec{g}$ is the diffraction vector, i_1 the direct image, i_2 the dynamical image and i_3 the intermediary image.

methods, their usage and merits were discussed. At each stage indicative topographs were presented to help the reader understand and appreciate the beauty of the technique. To date, no detailed, all encompassing review of the techniques of X-ray topography appears to exist in the literature. Factors governing the spatial and geometrical resolution were discussed. The same formulae apply to all X-ray radiation sources. Therefore, when one considers that fourth generation free electron X-ray lasers with their tiny source size, truly negligible divergence, magnificent intensities and femtosecond time structure are on the horizon, whole new avenues of experimental investigation may be opened up for X-ray topography.

As the number of topics that have been studied to date with X-ray diffraction topography is so diverse, only a very basic introduction to the principle imaging mechanisms was provided. This diversity will hopefully become clear in the chapters that follow, wherein several independent topographic investigations of crystalline materials and their constituent devices are preformed. Where necessary, the experimental and theoretical underpinnings considered thus far will be expanded.

Chapter 8

Electrical Stressing of Light Emitting Diodes

8.1 Introduction

In recent years the demand for high-power semiconductor light emitting diodes has increased significantly in tandem with their applicability in a myriad of environments. For example, high-power light emitting diodes offer a much cheaper alternative to their incandescent electrical bulb counterparts. Device efficiency and operation are limited by dislocation and other defect formation due to inhomogeneous strain which can induce subsequent device failure [141]. In addition to the laterally homogeneous biaxial strain built into the layered structure of the devices, strain can also be introduced by the metallization and insulating layers, and by mounting and contact processes. Finally, these high power devices suffer from strain induced by thermal expansion during operation. Consequently, an understanding of the strain evolution and distribution within these devices is vital if increased efficiency and performance are to be obtained. In this chapter, the change in strain within, and output optical emission spectra of ultra bright light emitting diodes, under varying degrees of electrical stress, will be examined using synchrotron X-ray topography and optical emission spectroscopy.

8.2 Experimental

Three ultra-bright light emitting diode arrays were examined in the study: green (565 nm), red (660 nm) and infrared (890 nm). Typical arrays consisted of five diodes recessed in a dual inline package. The red and infrared LED active regions were constructed from proprietary epitaxial layers of the III-V compound semiconductors GaAs and AlGaAs, grown on a (001) GaAs substrate. The active region of the green LED was nitrogen-doped GaP. The substrate was attached to the IC package bulk using bonding epoxy. Connection of the diodes to the legs of the dual inline package was achieved using gold wire and ball-bonding techniques.

Back reflection topographs in large-area and section mode were produced as described in Chapter 7. For the large-area topographs, the incident beam was collimated to 0.75 mm $\times$ 0.75 mm and for the section topographs, the height of the beam was reduced to approximately 15 μm. The topographs were recorded on either Kodak SO-181 professional X-ray or Geola VRP-M holographic high-resolution films. The sample to film distance in both geometries was 40 mm.

The optical output of the diodes was monitored using a DIGITWIN optical emission spectrometer manufactured by SOFIE Instruments. The spectrometer had a spectral accuracy of 0.1 nm in the wavelength range 200 nm to 900 nm. Prior to data acquisition the spectrometer was calibrated using a mercury lamp.

Using a conventional laboratory power supply, the power supplied to each device was increased until failure occurred. The failure point was defined as the point where a

sudden and complete loss of light occurred. At each stage back reflection topographs and plots of the relative output intensity versus wavelength were recorded using X-ray topography and optical emission spectroscopy, respectively.

8.3 Results

8.3.1 X-ray Topography

Figures 8.1–8.3 depict the devices under normal operation: green LED – ca. 66 mW/device; red LED – ca. 57 mW/device; infrared – ca. 70 mW/device. The ball bond and accompanying gold wire are observed via absorption (reduced intensity, i.e. white contrast) of X-rays. The increase in intensity along the underside edges of the LEDs is related to the increase in stress due to the adhesion of the device substrate to the IC package bulk as indicated in the figures by the arrows labeled X. Strain due to the metallization layers is present, albeit difficult to observe. In the green LED it is indicated by the arrow Y; however, due to the limited number of useful reflections that were imaged for the red and infrared diodes, it is indiscernible. In the topographs of the red and infrared LEDs, it would appear that there are two gold wires attached to the devices. One is actually seeing a "shadow" of the diffracted X-ray beam as it propagates from the device to the film and not a second wire.

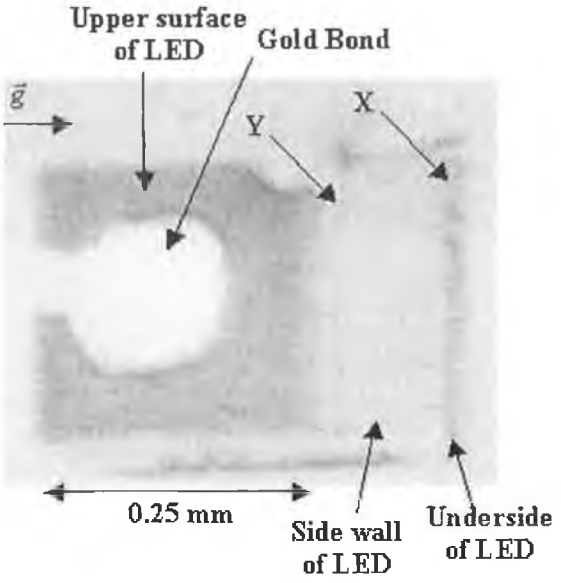

Figure 8.1: 1 1 7 large area back reflection topograph from green LED under normal operation (66 mW/device).

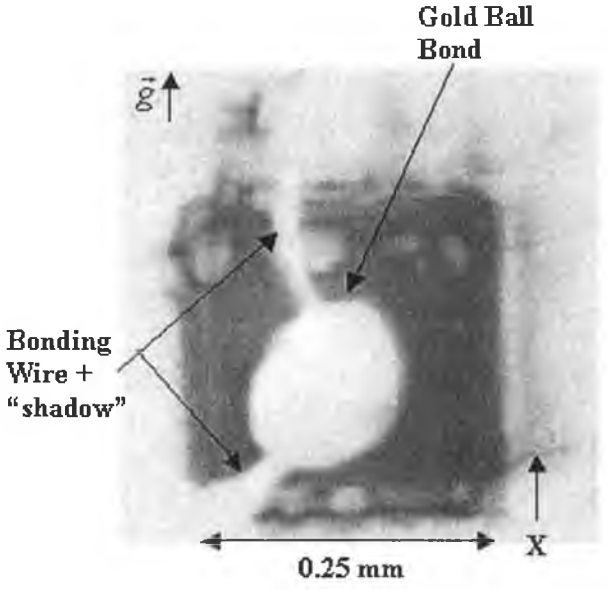

Figure 8.2: 1 $\bar{1}$ 7 large area back reflection topograph from red LED under normal operation (57 mW/device).

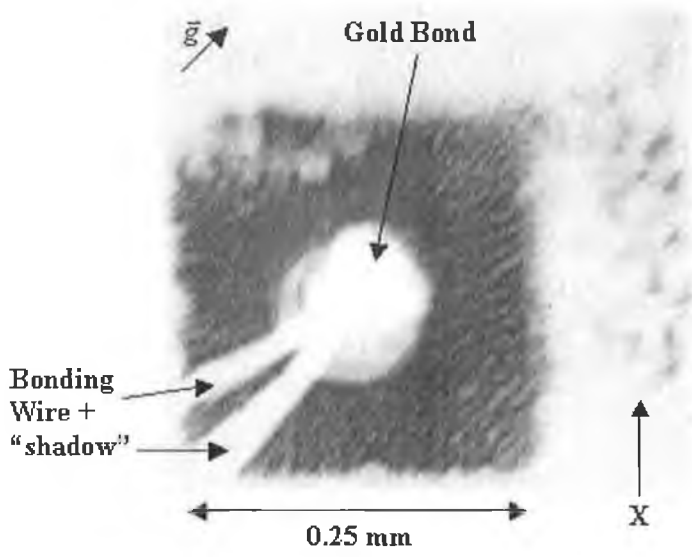

Figure 8.3: 6 0 2 large area back reflection topograph from infrared LED under normal operation (70 mW/device).

It was noticed that as the power supplied to the diodes was increased, the consequent temperature rise and increased lattice vibration caused a reduction in the X-ray topographic definition of the strain induced by the metallization layers, up to the point of failure. The increased electrical stressing enhanced the stress generation around the ball bond regions of the devices through a change in the topology of the ball bond region from circular to elliptical. These features are presented in Figures 8.4–8.6.

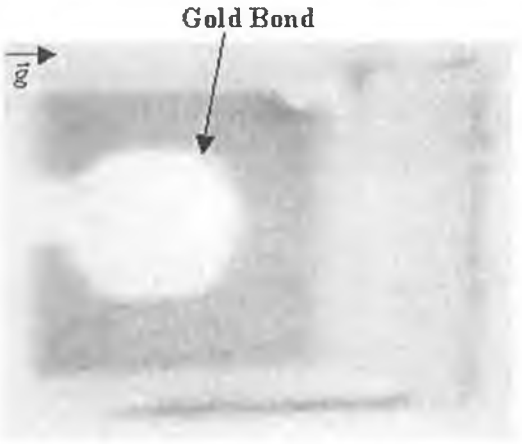

Figure 8.4: 1 1 7 large area back reflection topograph from green LED at elevated powers (602 mW/device).

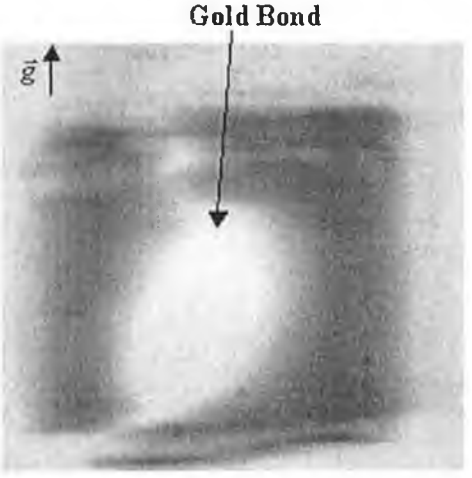

Figure 8.5: 1 $\bar{1}$ 7 large area back reflection topograph from red LED at elevated powers (500 mW/device).

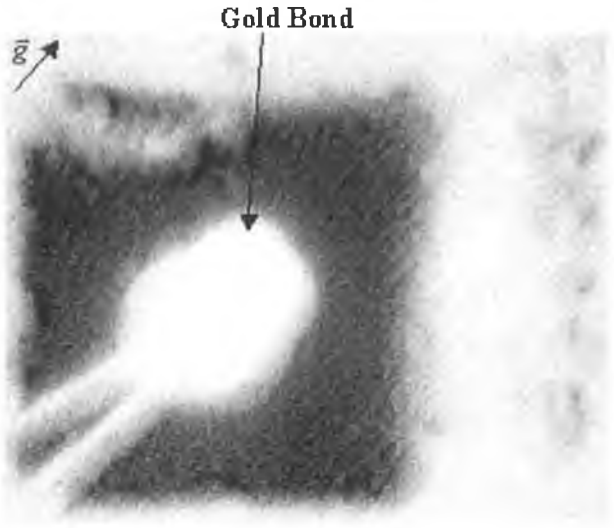

Figure 8.6: 6 0 2 large area back reflection topograph from infrared LED at elevated powers (745 mW/device).

Surprisingly, the ultra-bright LEDs continued to work at powers approximately 25 times greater than their maximum rated working power. Once catastrophic failure occurred, the topographic images of the LEDs became severely warped and distorted around the gold bond regions as shown in Figures 8.7–8.9. The distortion is due to the build-up of large stresses, which are presumably related to the thermally induced lattice deformation. The lattice distortion was greatest for the red LED; upon failure the topographic image appears to display three distinct and completely misoriented "sub-grains" denoted by the solid oval lines in Figure 8.8. One can observe a cellular dislocation structure within each sub-grain, which is indicative of LEC substrate growth [142]. The large void in the centre of the image, denoted by the dotted oval lines in Figure 8.8 is presumably due to the gold bond. However, as with the ball bond regions for the green and infrared LEDs (Figures 8.7 and 8.9), it has now lost its dis-

tinct spherical shape. This is most likely due to thermal relaxation/creep of the gold bond on the surface of the LED.

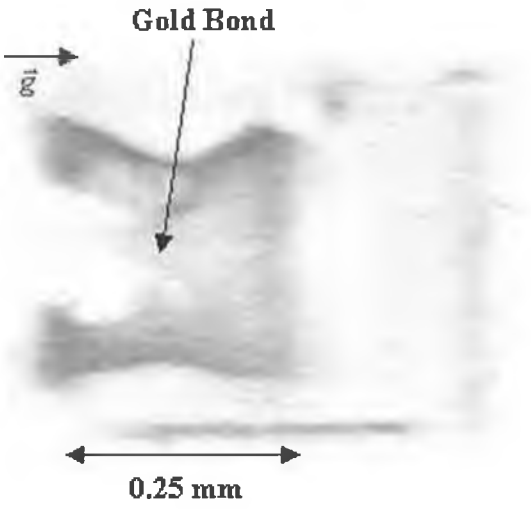

Figure 8.7: 1 1 7 large area back reflection topograph from green LED upon failure.

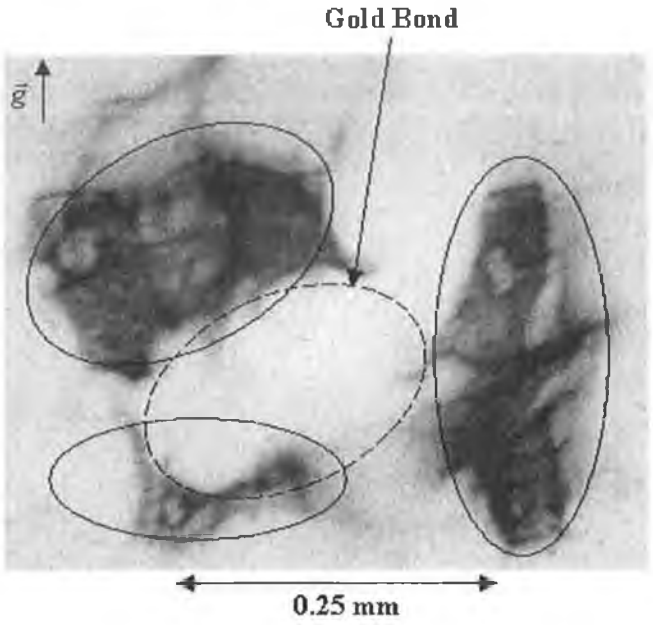

Figure 8.8: 1 $\bar{1}$ 7 large area back reflection topograph from red LED upon failure.

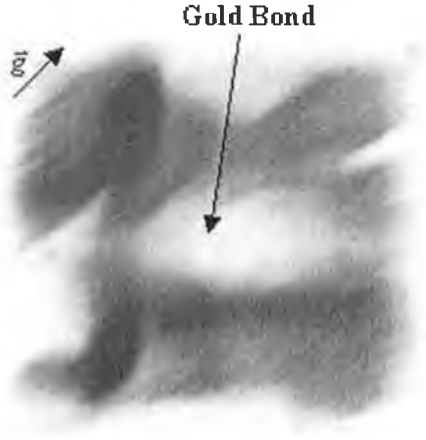

Figure 8.9: 6 0 2 large area back reflection topograph from infrared LED upon failure.

Optical micrographs indicated that the structure of the device remained spatially unaltered although the gold bond wire became detached upon failure. Consider for example the red diode, as shown in Figure 8.10.

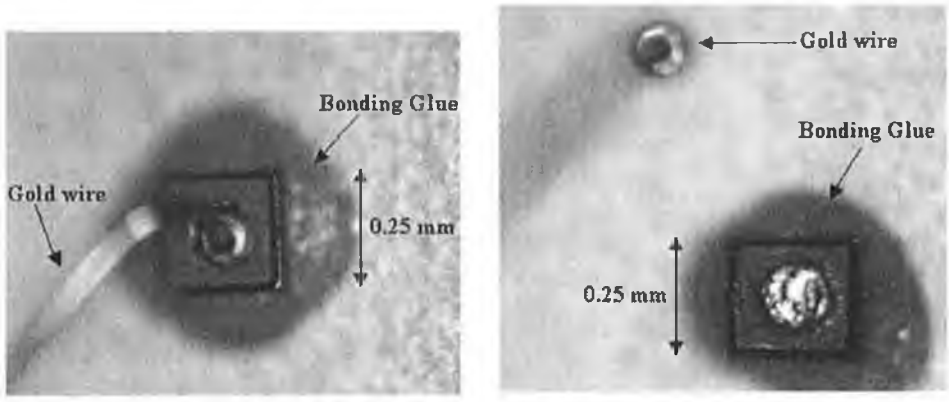

Figure 8.10: Optical micrographs of induced failure in a red (660 nm) LED. (a) An optical micrograph before power up (magnification = 100×), while (b) shows that the device remains spatially unaltered although the ball bond has been removed upon failure.

After failure, the devices were allowed to cool. Upon cooling, large residual strain fields due to the thermal stressing remain. The strain due to the device attachment to the IC package bulk, metallization layers and heteroepitaxial interfaces have increased dramatically as arrows X, Y and Z portray in Figures 8.11–8.13. Post failure examination of the red LED indicated that the cellular dislocation structure imaged in Figure 8.8 manifests itself as a direct consequence of the gold bond being completely removed with little or no residual gold remaining; consequently the X-rays were able to penetrate below the active region to the device substrate as indicated by arrow C in Figure

8.12. Large localised leakage currents around the gold bond may have caused severe thermal lattice vibration and consequent surface damage as indicated by arrow D.

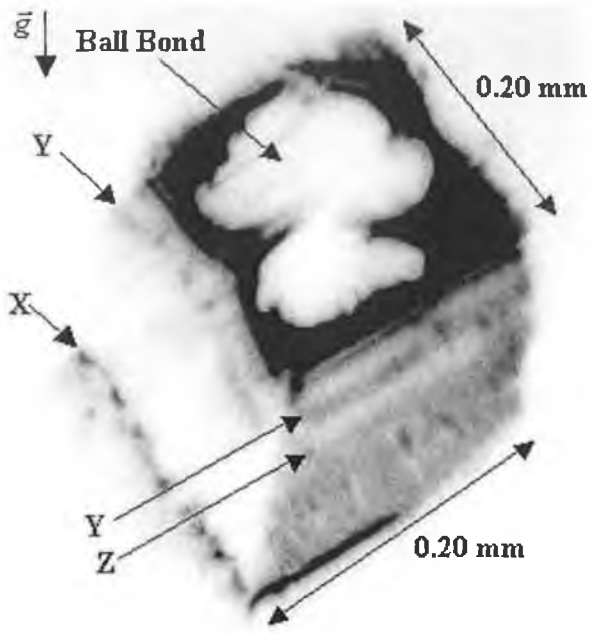

Figure 8.11: Post failure $\bar{2}$ 2 12 large area back reflection topograph from green LED.

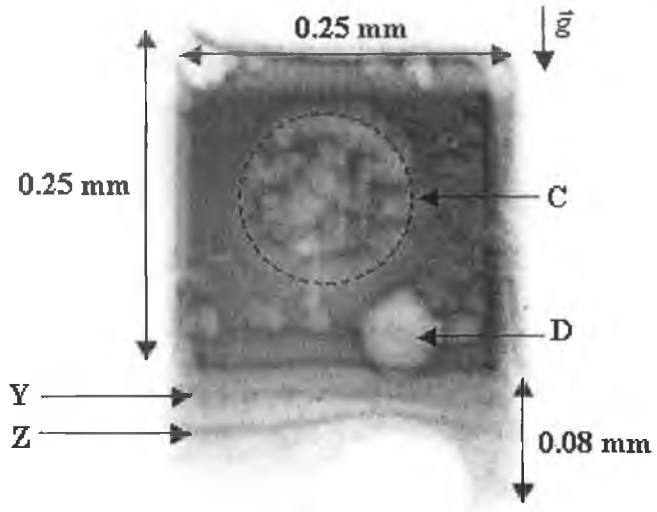

Figure 8.12: Post failure $\bar{1}$ 1 5 large area back reflection topograph from red LED.

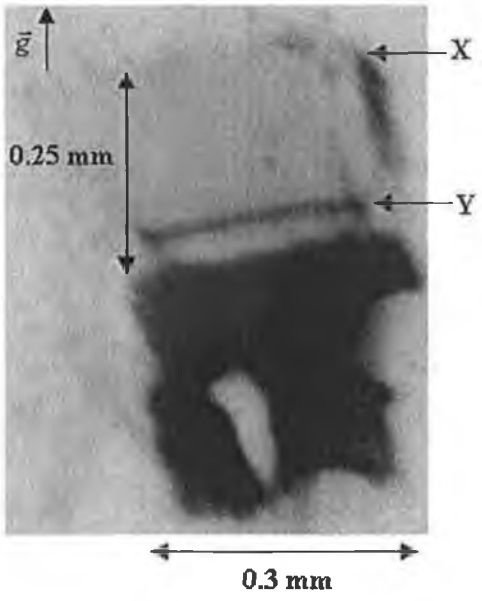

Figure 8.13: Post failure 1 $\bar{1}$ 3 large area back reflection topograph from infrared LED.

In the post failure topograph of the green LED (Figure 8.11) the gold bond is once more observed via absorption contrast due to the presence of residual gold from the gold bond. This was confirmed by back reflection section topography wherein the X-rays wre unable to penetrate below the active region of the device, due to the X-ray absorption of the residual gold in conjunction with the metallization layers, as indicated by arrow C in the 2 2 12 reflection shown in Figure 8.14. This mechanism is explained in Figure 8.15. For the red LED a smaller amount of residual gold remained and consequently the X-rays were able to penetrate deeper into the device structure (Figure 8.16). In the case of the infrared LED, presented in Figure 8.17, much of the gold remained and only the active region could be imaged in the back reflection section topograph.

Within the back reflection topographs, one can see large strain fields in the side walls of the devices (arrow B in Figure 8.14) and at the heteroepitaxial layer interfaces (arrows Y and Z in Figure 8.16). Interestingly the active region of the devices possesses distinctly misorientated features, indicated by arrows A, that arise out of a misorientational contrast mechanism. Using the effective misorientation $2\Delta\theta$ of an imperfect region, it is possible to estimate the maximum magnitude of stress at the edges of the gold bond. The effective misorientation of an imperfect region is associated with the departure of strained lattice planes from the exact Bragg angle. This effective misorientation [143, 144] in real space can be defined as

$$\Delta\theta = \frac{\Delta d}{d}\tan\theta + \alpha = |\epsilon_{\perp}|\tan\theta + \alpha \qquad (8.1)$$

where θ is the Bragg angle, α is the component of the rotation of the lattice planes around the normal to the plane of incidence i.e. tilt, $\epsilon_{\perp}$ is the component of strain perpendicular to the diffracting planes, d is the distance between the diffracting planes and Δd is the deflection of the planes parallel to the diffraction vector $\vec{g}$. Assuming a limiting misorientation based solely upon lattice dilatation, one can relate the misorientation parameter to the stress σ through Young's modulus Y.

$$\Delta\theta \approx |\epsilon_{\perp}| \tan\theta = \frac{|\sigma|}{Y} \tan\theta \tag{8.2}$$

Similarly, assuming the misorientation is based solely upon tilt of the lattice planes yields:

$$\Delta\theta \approx \alpha = \frac{|\sigma_{xy}|}{Y} \tag{8.3}$$

where σ_{xy} is the shear stress. The estimation of the magnitude of stress/strain at the edge of the ball bond region for the diodes is summarised in Table 8.1 based upon the limiting misorientations.

Diode	Stress (MPa)	Strain $\lvert\epsilon\rvert$ (%)
Green (565 nm)	39 – 166	0.04 – 0.19
Red (660 nm)	40 – 70	0.05 – 0.08
Infrared (850 nm)	83 – 236	0.09 – 0.27

Table 8.1: Estimation of the magnitude of stress/strain at edge of the ball bond region.

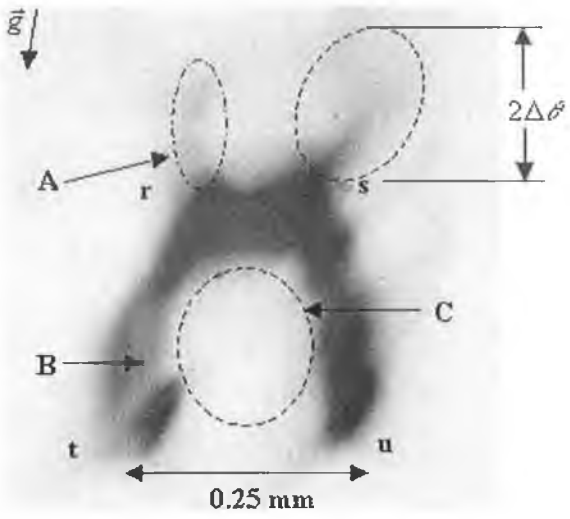

Figure 8.14: Post failure $\bar{2}$ 2 12 back reflection section topograph from green LED.

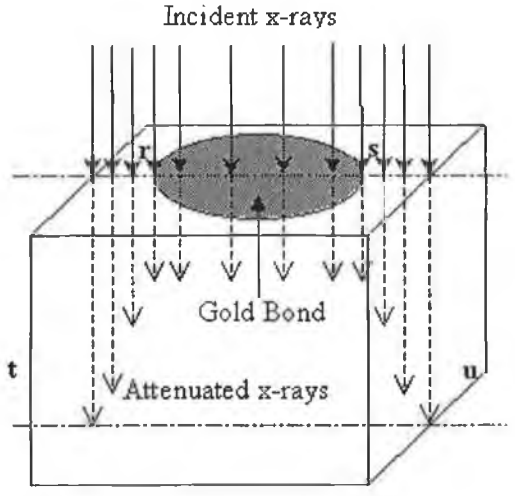

Figure 8.15: Mechanism of X-ray attenuation by gold bond and metallisation layers in back reflection section images. The X-rays experience increased absorption under the gold bond region in comparison to regions at the edge of the device, due to greater cumulative attenuation from the residual gold and semiconductor material. Consequently, the X-rays penetrate deeper into the device at edges that in the centre.

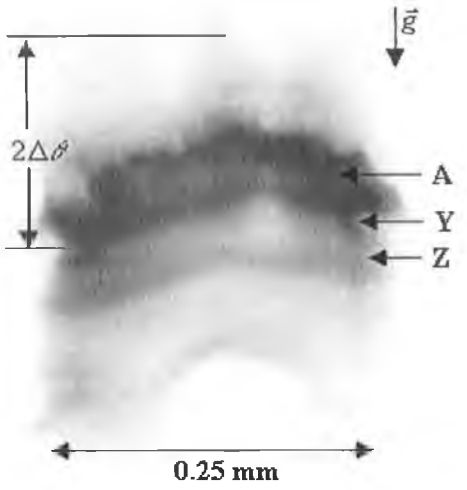

Figure 8.16: Post failure $\bar{4}$ 4 10 back reflection section topograph from red LED.

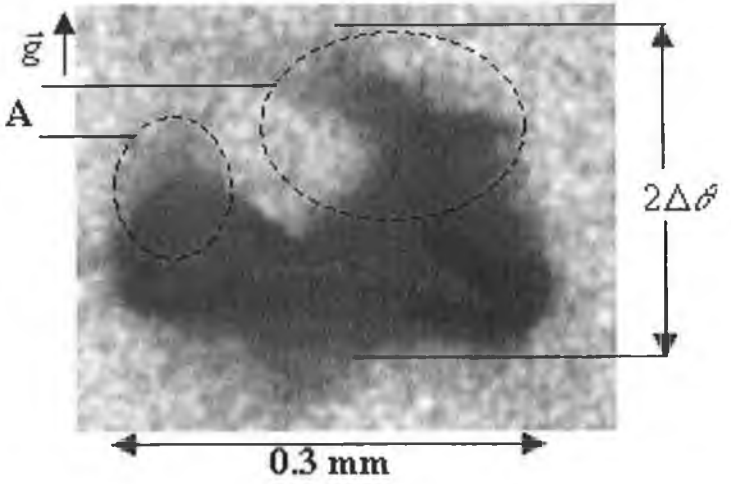

Figure 8.17: Post failure 1 $\bar{1}$ 3 back reflection section topograph from infrared LED.

8.3.2 Optical Emission Spectroscopy

Measured optical emission spectra of the recombinative bandgaps using optical emission spectroscopy (OES) revealed a narrowing of the bandgap for the green and red LEDs as the power to, and hence temperature of, each device is increased, whereas a broadening occurred for the infrared LED. Under normal operation the red LED exhibited a distorted Gaussian spectrum centered at 649 nm. As the power was increased the peak wavelength changed to 741 nm with the introduction of a sidelobe at 715 nm. Conversely, under normal operation, the green LED demonstrated a peak wavelength at 567 nm with a secondary peak at 561 nm. As the power was increased the presence of the secondary peak receded, yielding a distorted Gaussian spectrum centered at 661 nm prior to failure. Figures 8.18 and 8.19 display the change in output optical spectra as a function of power supplied to the device for the green and red diodes respectively. Please note, the spectra have not been normalised with respect to one another and therefore, only the position of the peak wavelength can be used for meaningful comparisons.

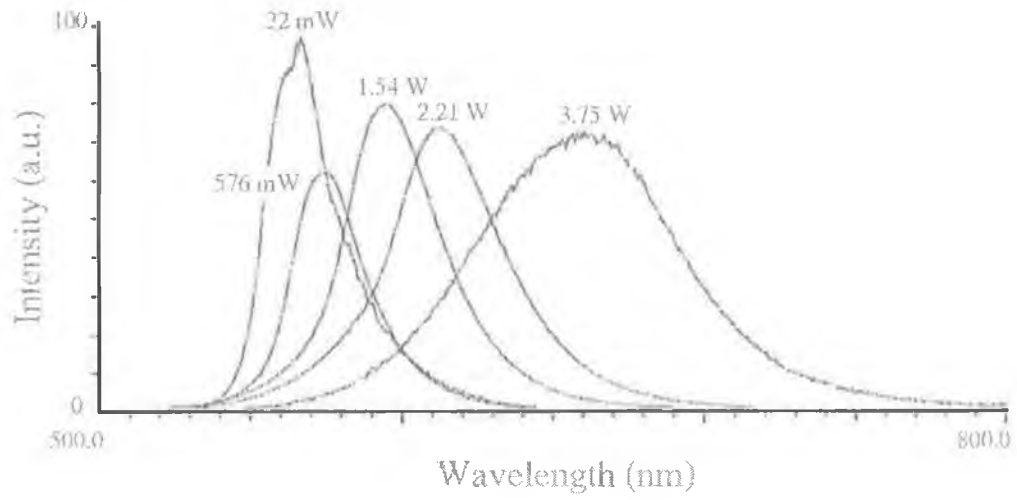

Figure 8.18: Change in output optical emission spectrum as a function of power supplied for green LED.

The narrowing of the bandgap, which is of the order of -240 meV for the green LED and -300 meV for the red LED, cannot be completely accounted for by the temperature dependence of the bandgap as the optical properties of highly excited semiconductors are strongly influenced by many-particle effects. The generation of a dense electron-hole system, for example, caused by the application of a high voltage, leads to significant modifications of the band structure. Bandgap renormalisation [145, 146] for single-particle energies occurs as a consequence of this. The bandgap renormalisation to a first order may be explained as follows: through a collective screening mechanism each carrier in the system repels all others with the same charge. The resulting localised decrease in charge density may be conceived of in terms of a virtual charge of the opposite sign counterbalancing the build-up of charge. Coupled with this mechanism is an exchange interaction which evolves from the Pauli exclusion princi-

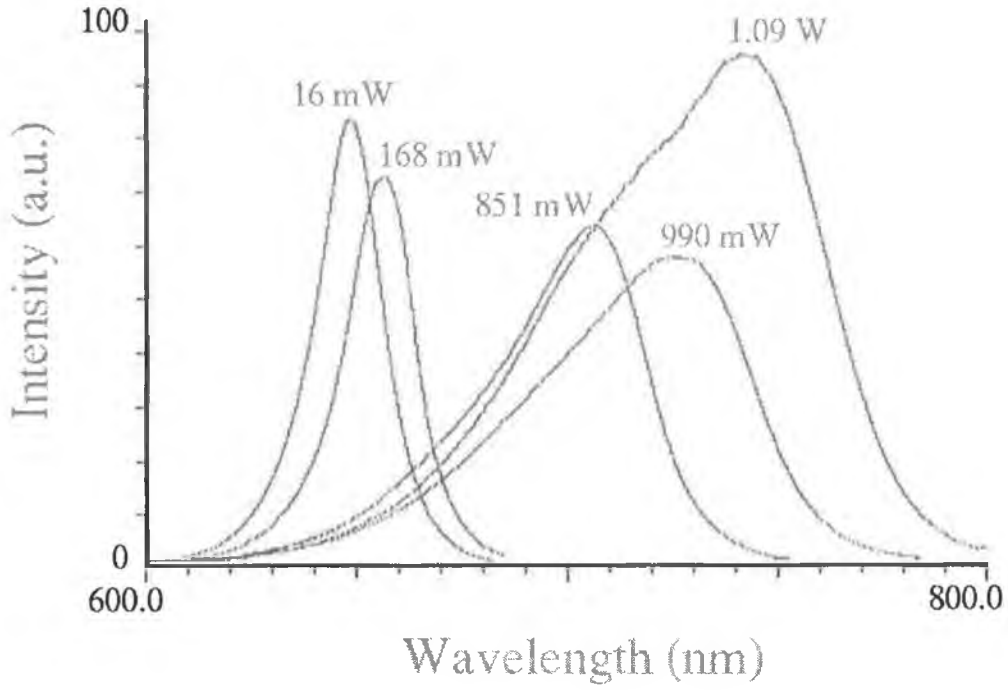

Figure 8.19: Change in output optical emission spectrum as a function of power supplied for red LED.

ple. The electrons in a high carrier-concentration semiconductor spread their momenta such that overlapping of the individual electron wavefunctions is avoided, i.e. fermions with the same spin are prevented from occupying the same position. The spatial separation is thus larger than expected from a purely classical analysis; hence the reduction in the strength of the Coulomb force. The result in the semi-classical approximation is a narrowing of the band gap in the highly excited semiconductor with respect to the unexcited state.

The infrared LED displayed the most unusual spectrum of all. Under normal operation (see Figure 8.20), a dominant peak at 841 nm in concurrence with a tertiary peak at

810 nm was observed. At elevated powers (1.93 W per device) it was observed that the 810 nm peak had moved to 806 nm and dominated the 841 nm peak which had shifted to 830 nm. This suggests that the high-power induced damage is introducing a defect level within the band structure that provides for alternative radiative recombination paths. The possibility of such a level is not inconceivable considering post failure analysis of the device using back reflection section topography revealed large stresses (nominal $|\sigma|$ =83–236 MPa) around the gold bond.

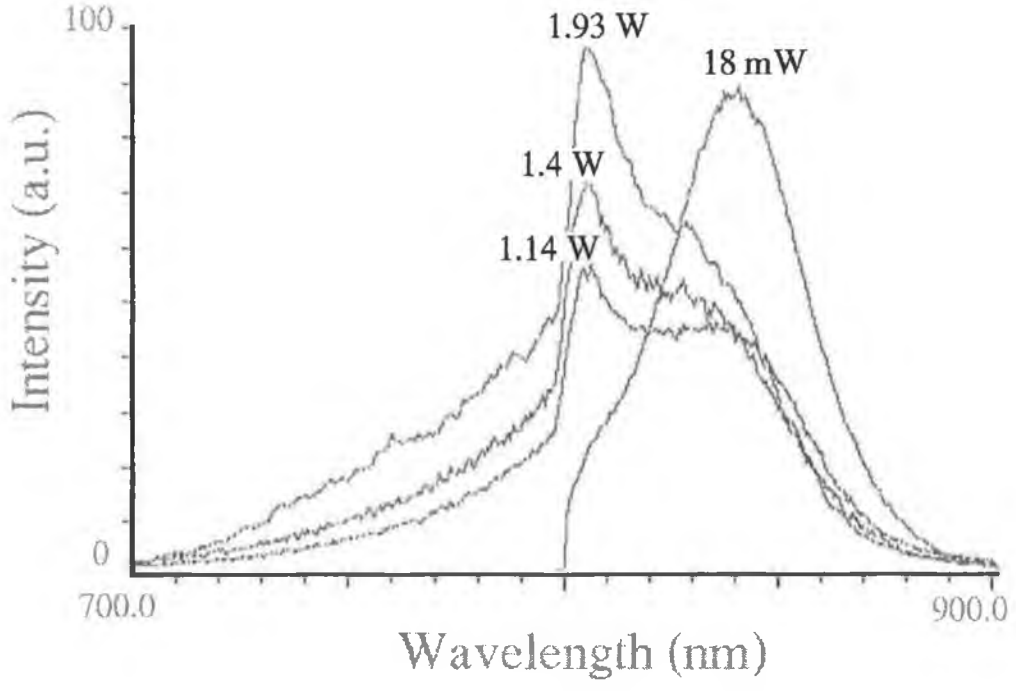

Figure 8.20: Change in output optical emission spectrum as a function of power supplied for infrared LED.

8.4 Conclusions

Synchrotron X-ray topography has been applied to the study of the failure of ultra-bright LEDs under varying degrees of electrical stress. It was observed that the increased thermal load caused an increase in strain around the ball bond regions of the devices as they were stressed to the point of near failure. When complete failure occurred in the samples, it was observed that large lattice deformations of the original device structure took place.

An attempt was made to evaluate the stress distribution within the active region of the devices using micro-Raman spectroscopy. Unfortunately, this did not yield any data due to reflection of the optical photons from the metallic layers in close proximity to the active region. This problem was circumvented through an order of magnitude estimate of the stress using the effective misorientation of the lattice planes. In the analysis the limiting magnitude of stress, based solely on dilatation and tilt of the lattice, was evaluated. With the data obtained in this study, it is not possible to resolve the individual stress components arising from dilatation and tilt of the lattice. However, should the reader wish to ascertain a more accurate value of the stress, then the four-azimuth topographic technique method suggested in [147] could be used to accurately resolve the stress components associated with lattice dilatation and tilt. Alternatively, conventional triple-axis diffractometry could be used.

Optical emission spectroscopy demonstrated a shift of the dominant peak towards long wavelengths for the green and red LEDs as applied power is increased. This has been

explained by a bandgap renormalization mechanism accounting for a decrease in the electron-electron Coulombic particle interaction via the Pauli exclusion principle. The shift toward short wavelengths with increased applied power for the infrared LED is suggestive of a defect level providing an alternative recombination path.

Chapter 9

Strain Induced by Epitaxial Lateral Overgrowth of GaN on Sapphire

9.1 Introduction

Group III-nitrides are presently a promising system for semiconductor device applications, especially for the development of blue- and UV-light emitting diodes. The III-V nitrides, gallium nitride, aluminium nitride and indium nitride are particularly interesting for optoelectronic applications at such photon energies as they form a continous alloy system whose direct optical bandgaps range from 1.9 eV to 6.2 eV [75]. These wide bandgap materials offer other advantages including high mechanical and thermal stability in conjunction with chemical inertness at high temperature. At present, research is ongoing in the development of these materials and the devices constructed out of same.

One particular difficulty in the growth of thin films of these materials is the lack of sufficiently large substrates for homoepitaxial growth. Thus up to now, heteroepitaxial growth is a practical necessity and the choice of substrate is critical. At present, sapphire and silicon carbide are the most popular substrate materials. The lattice mis-

match between hexagonal wurtzite α-phase GaN and the underlying rhombohedral (hexagonal) α-sapphire can achieve values as high as 13.9%; consequently standard epitaxial deposition of GaN on Al_2O_3 can lead to very high threading dislocation densities [75]. Epitaxial lateral overgrowth (ELO) holds out the potential for significant reductions in threading dislocation densities for mismatched hexagonal-GaN on sapphire epitaxy [148–150]. Using openings in a relatively thick SiO_2 mask a new metalorganic vapour phase epitaxy (MOVPE) GaN growth is carried out. After an initial phase of vertical growth upward through the mask window, the growth then proceeds laterally over the mask itself. It is thought that a significant reduction in threading dislocation densities can be achieved via mask blocking of vertically propagating dislocations and by means of a redirection of the propagation of some dislocations at the growth front [151, 152]. Studies have shown that the ELO technique can result in dislocation densities almost three orders of magnitude lower than in the non-ELO case, wherein typical densities of approximately 1×10^{10} cm^{-2} are often observed [150]. GaN-based optoelectronic and electronic devices are expected to benefit from this reduction in dislocation density and this technique has recently been applied to GaN blue laser production [153, 154]. However, an understanding of the processes active during the ELO procedure, and their impact on strain and dislocation generation, is still far from complete. In this chapter, synchrotron X-ray topography in section transmission geometry has been applied to the evaluation of ELO GaN on Al_2O_3.

9.2 Experimental

The growth of the GaN films was carried out in a vertical rotating disk MOVPE reactor manufactured by Thomas Swan & Co. operated at a pressure of 100 Torr. Initially, a low temperature thin (50 nm) GaN buffer layer was grown on the 400 μm thick c-plane sapphire substrate at 500 °C [155]. On top of this, a 0.85 μm GaN epilayer was deposited. In both cases, trimethylgallium (TMG) and ammonia (NH_3) were used as the gallium and nitrogen precursors. This constitutes the non-ELO sample as shown in Figure 9.1.

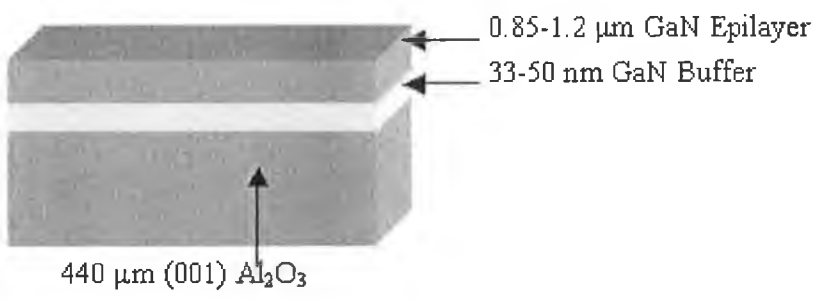

Figure 9.1: Schematic of the non-ELO GaN sample (not drawn to scale).

Subsequently, 100 nm thick SiO_2 stripes were deposited using plasma enhanced chemical vapour deposition (PECVD) followed by conventional photolithography and dry etching. The wafers were divided into four regions according to their respective fill factor

$$f = \frac{W}{W + L} \tag{9.1}$$

where SiO_2 stripe widths (W) of 2 μm and 3 μm were applied and the window open-

ings (L) were varied between 3 μm and 5 μm. In order to achieve large lateral growth rates the stripes were oriented in the $<1\bar{1}0>$ direction relative to the GaN epilayer. A summary of this information is presented in Table 9.1. A schematic outline of the lo-

Sample region	Window Opening W (μm)	SiO_2 stripe width L (μm)	Fill factor f
A	5	3	0.625
B	4	3	0.571
C	4	2	0.667
D	3	3	0.500

Table 9.1: Sample region and fill factor data for ELO wafer.

cation of sample regions A–D, together with the stripe orientation, is shown in Figure 9.2.

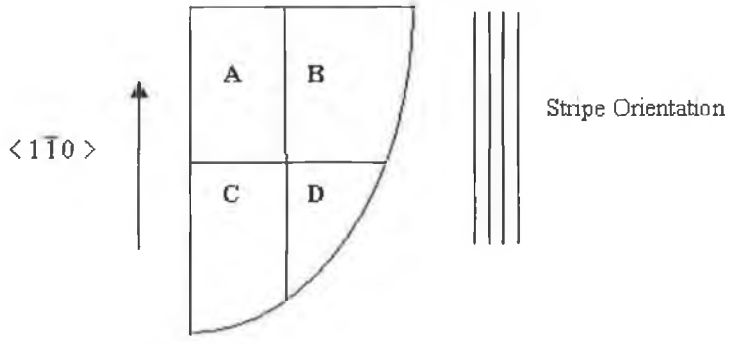

Figure 9.2: Wafer regions differing according to fill factor.

Prior to the actual ELO growth the sample was dipped for 5 s in a 1:4 solution of $HF:H_2O$ to remove the surface oxide. Using H_2 as the carrier gas and the aforementioned precursors, the ELO growth took place at 1080 °C. Typical flow rates for the TMG and NH_3 were 23.7 μmol/min and 5 l/min, respectively. The thickness of the resulting ELO layer was 6.8 μm. The ELO structure is shown in Figure 9.3.

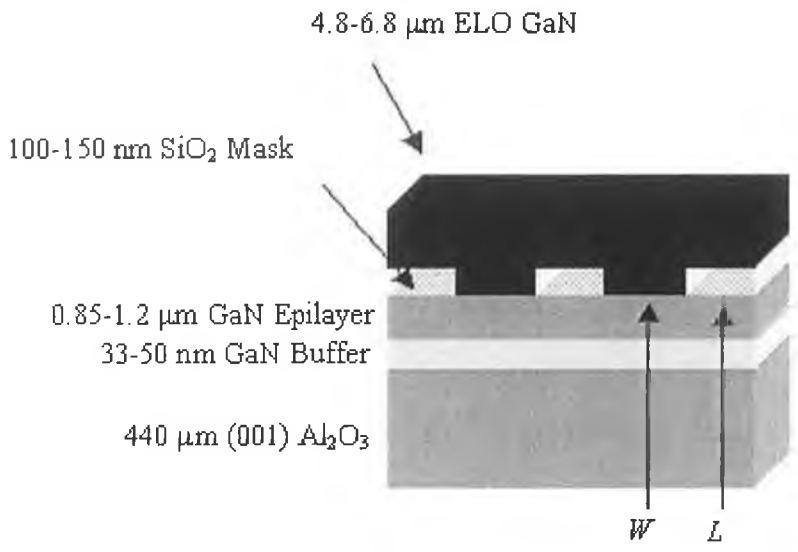

Figure 9.3: Schematic of the ELO GaN sample (not drawn to scale).

Section transmission X-ray topography was applied to the study of the GaN samples. The (001) sample surface was set at a tilt angle of 18° with respect to the vertical plane perpendicular to the incident beam. The Laue patterns of topographs were recorded either on Kodak High-Resolution SO-343 X-ray film or Geola VRP-M holographic film. This method and the corresponding view on the X-ray film is depicted in Figure 9.4. The sample to film distance D was 50 mm.

X-ray diffraction (XRD) measurements were performed using a Bede Model 150 double crystal diffractometer. (004) double crystal X-ray diffraction FWHM reflection measurements were obtained for the non-ELO and ELO samples as a function of fill factor f. For the purpose of this measurement the non-ELO sample was defined as having a fill factor $f = 1$. Experimental data obtained using these techniques were

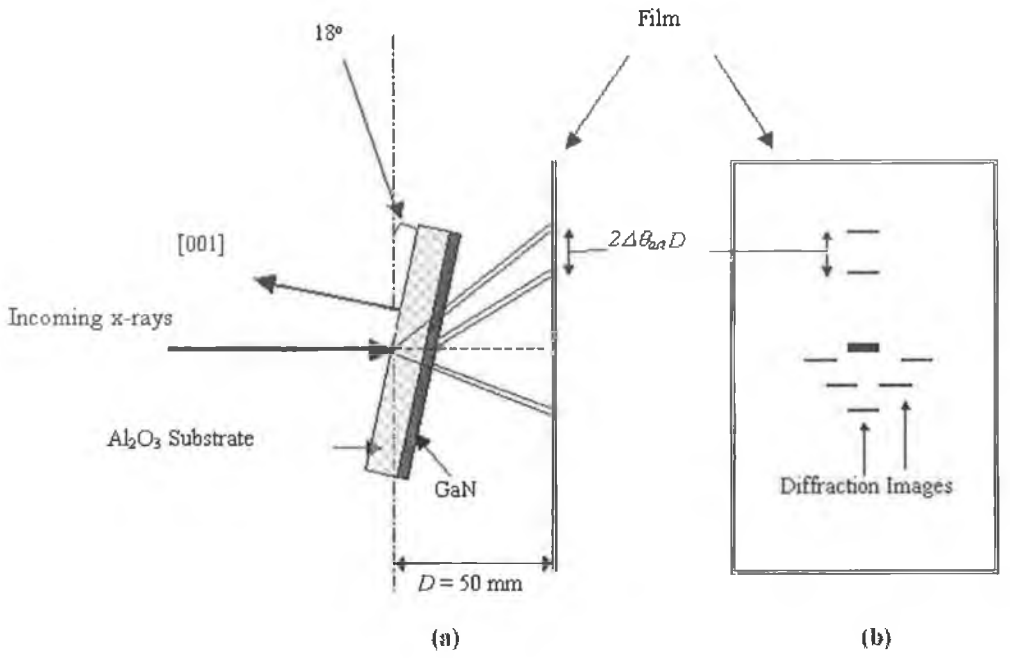

Figure 9.4: (a) Section transmission topography experimental setup. (b) Laue picture recorded on film from section transmission topography experiment.

complimented with transmission electron micrographs.

9.3 Results

Figure 9.5 (a) illustrates the Laue pattern taken from a complete film of the non-ELO GaN on Al_2O_3 sample. This Laue arrangement is composed of two sets of topographic images, the first from the sapphire substrate and the second from the GaN epilayer. An indexed schematic reconstruction of this film is shown in Figure 9.5 (b). In certain cases, a number of substrate and epilayer topographs overlap e.g. the $\bar{1}\,\bar{1}\,0$ Al_2O_3 and the $0\bar{1}0$ GaN reflections.

However, for other topographs the image of the substrate and its corresponding epilay-

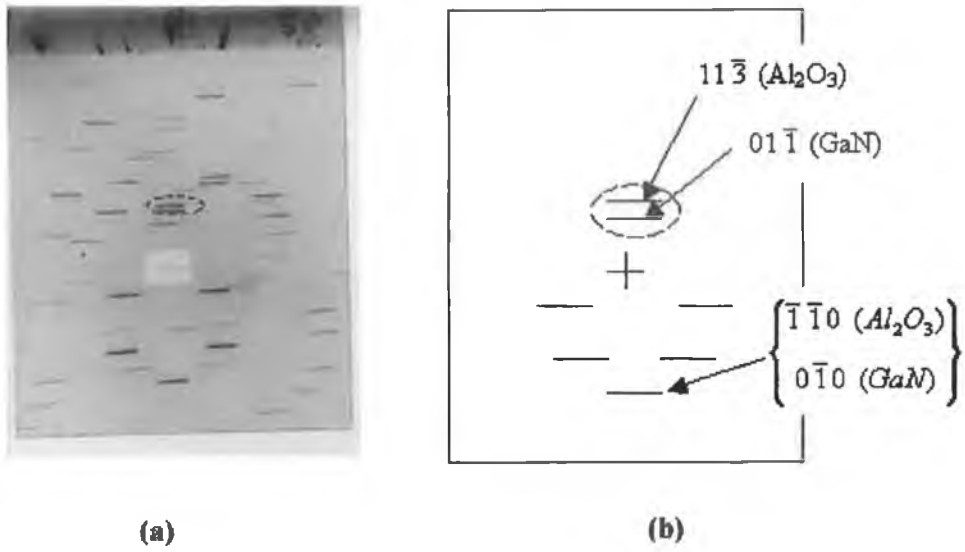

Figure 9.5: (a) KODAK SO-343 film wherein a set of substrate and epilayer reflections were recorded in section transmission mode. (b) An indexed schematic corresponding to (a).

ers are separated from one another, e.g. the $11\bar{3}$ Al_2O_3 and the $01\bar{1}$ GaN reflections. Inherent in the growth of GaN on sapphire is a 30° rotation of the epilayer with respect to the substrate. Consequently, a small separation is expected between certain reflections. This is indicated by $2\Delta\phi = 1.48°$ in Figure 9.6, a magnified image of the reflections highlighted in Figure 9.5. The measured angular separation indicated by $2\Delta\theta_{act}$ is much greater. It was found that this excess in misorientation for the non-ELO GaN sample was $2\Delta\theta_{act} = 1.68°$. This observed separation or misorientation between the substrate and the epilayer is primarily due to lattice mosaicity and tilt between the substrate and epilayer.

In the case of strained layer GaN epitaxy, the lattice dilatation may be understood in

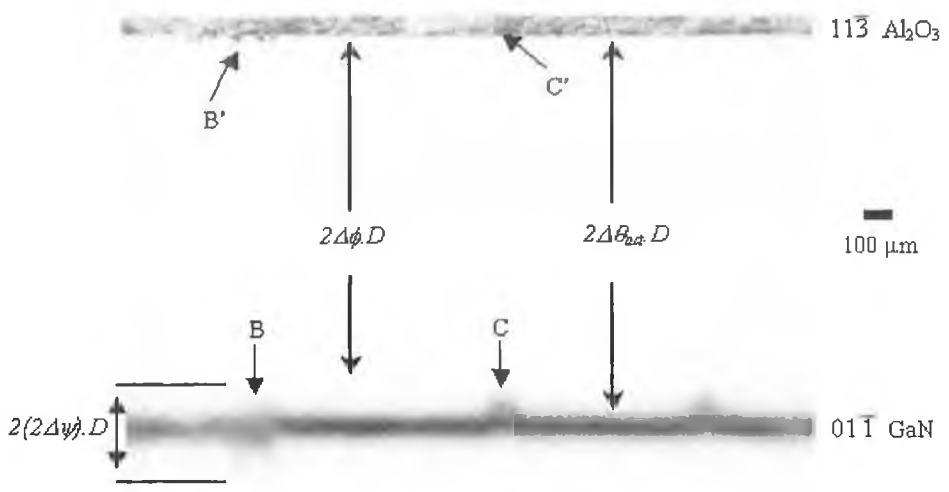

Figure 9.6: Section transmission topograph from non-ELO sample.

terms of a change in the perpendicular component of the lattice parameter whilst the parallel component remains unchanged [156]. This results in a tilt of the relative positions of the lattice planes in the epilayer with respect to the substrate. Thus, along directions where the diffraction vector $\vec{g}$ and the vector $\vec{h}$ running normal to the distortion vector are perpendicular, there will be an observed shift in the position of the diffracted image of the epilayer with respect to the substrate. This condition is satisfied when

$$\vec{g} \cdot \vec{h} = 0 \tag{9.2}$$

The quality of the GaN epilayer is rather poor as one can see that the image of the epilayer is severely broadened and appears to be almost as thick as the substrate itself. Since the epilayer and substrate are approximately 6.8 μm and 400 μm thick,

respectively, this cannot be the case. This effect is most likely due to the fact that the epilayer is far from perfect and this manifests itself via local deviations from lattice coherence throughout the epilayer. Various regions in the epilayer, each slightly misoriented with respect to its neighbour, though macroscopically aligned, will each contribute to a topographic image in a manner similar to a mosaic structure with a high dislocation density. Each of these regions will produce images at slightly different locations on the films. If it is assumed that these deviations are symmetrically distributed around the nominal crystallographic positions, the measured broadening of the epilayer in the section topograph is given by $2\Delta\psi$. For the example presented in Figure 9.6, we find that these local lattice misorientational deviations give values of $2\Delta\psi = \pm 0.177^{\circ}$ across an 8.5 mm length of epilayer. This is principally due to the apparent growth of highly misoriented features within the epilayer as indicated by arrows B and C. These features correspond directly to highly misorientated features on the substrate (arrows B' and C'). Additionally, it has previously been observed in the case of GaAs ELO on GaAs [157], that the ELO SiO_2 stripes can produce very high stresses in the underlying semiconductor. This can be observed as an array of vertically orientated stripes of the order of hundreds of microns long. This mechanism may also be contributing to the apparent broadening of the image of the ELO GaN, though resolving individual stripe effects is nearly impossible, given the 2 μm to 3 μm stripe widths used in this study.

For the ELO GaN sample $2\Delta\theta_{act}$ varied as a function of the fill factor as shown in Figure 9.7. It was observed that the misorientation increased monotonically with the fill factor. The increase in misorientation is attributable to a possible combination of

lattice misfit at the interface plane (which is due to the difference in lattice constants: $a_0 = 3.189$ Å, $c_0 = 5.185$ Å for GaN and $a_0 = 4.785$ Å, $c_0 = 12.991$ Å for α-phase Al_2O_3) and the hexagonal deformation into the c-direction [001] resulting from the strain. Further experiments will be required to determine which, if either, mechanism is dominant and if a limiting misorientation may be reached. Kobayashi and co-workers [158] studied the variation in basal plane rotation and tilt for MOVPE-ELO grown GaN films. They observed that the tilt and rotation angles for ELO grown films were always less than for the non-ELO reference sample and depended on the stripe direction of the mask pattern. Their results demonstrated that the c-axis tilts mainly along the $<1\bar{1}0>$ normal to the stripe pattern.

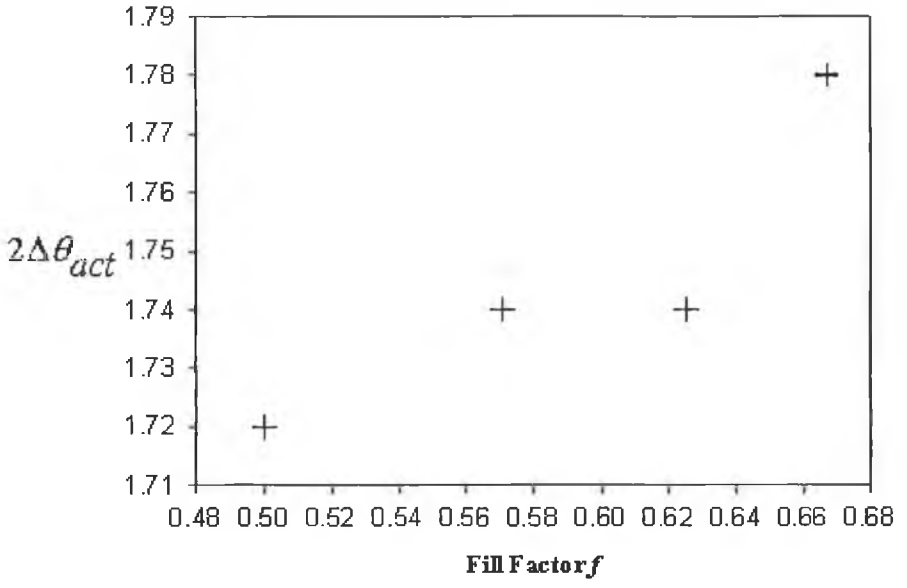

Figure 9.7: Plot of misorientation $2\Delta\theta_{act}$ versus fill factor f for the non-ELO GaN sample.

The variation in measured separation $2\Delta\theta_{act}$ as a function of fill factor becomes especially apparent when one compares two regions on the ELO mask with greatly differing fill factors. An example of this is conveyed by Figure 9.8, which is a section transmission topograph of the ELO GaN epilayer recorded from regions C and D simultaneously. There exists a 33% difference between the fill factors of the two regions and this is directly correlated with the unambiguous shift in the separation of the two regions of the epilayer with respect to the substrate. Region D displays a slightly greater misorientation than region C. This difference is indicated on Figure 9.8 by the measured angle $2\Delta\omega = 0.04°$. This argument is further substantiated when one examines the case where the difference in fill factor between the two regions is not significantly large; an example being regions A and B. The difference in fill factor is only 9.5% and a negligible misorientation with respect to the two regions could be measured, as one would expect having examined Figure 9.7.

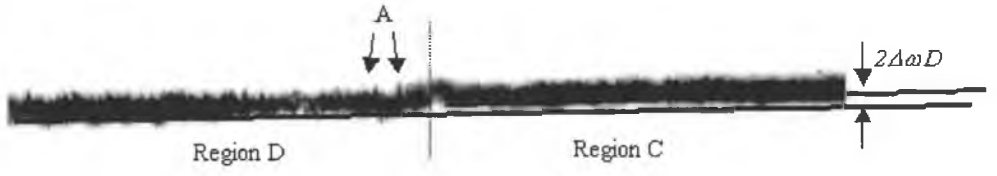

Figure 9.8: $01\bar{1}$ transmission section topograph of GaN epilayer simultaneously recorded from regions C and D. The substrate which appears above the epilayer has been omitted for clarity.

In region D large spikes are observed, indicated by the arrows A in Figure 9.8. These spikes are most probably due to the build-up of strain/misorientation at the SiO_2 stripe edges, which was mentioned previously. Since the dimensions of the stripes in this

region are close to the vertical threshold of resolution for SXRT (circa 4 μm at the F-1 beamline at HASYLAB), it is difficult to discern individual windows. However, this argument is supported by the fact that these features are not easily seen for region C, wherein the stripe widths are reduced by 33%. Similar features have been observed for the ELO growth of GaAs [157].

The quality of the ELO GaN sample is superior to the non-ELO sample. This is evident by comparing a section transmission topograph from region A of the ELO sample (Figure 9.9) with Figure 9.6. The substrate in this sample is far superior to the non-ELO analogue; no major regions of strain/misorientation present themselves. In conjunction, the local lattice misorientational deviations give values $2\Delta\psi = \pm 0.118^{\circ}$ across an 8.5 mm length of epilayer. This is much smaller than the value recorded for the non-ELO sample. The lattice misorientational deviation parameter $2\Delta\psi$ portrays the superior quality of the ELO epilayer over its non-ELO counterpart. A comparison of the epilayer qualities based solely on the misorientation parameter $2\Delta\theta_{act}$ is not sufficient, as notable differences in sample structure exist to make the comparison on this basis misleading. Rather the lattice misorientation parameter $2\Delta\psi$ when considered with $2\Delta\theta_{act}$ can aid in a more definitive evaluation.

Within the bounds of one standard deviation of measurement error $\pm 0.003^{\circ}$, it was not possible to discern any difference in local lattice misorientation for each of the different fill factor regions in the ELO sample. Therefore, epilayer quality superiority between the regions was evaluated in terms of the misorientation parameter $2\Delta\theta_{act}$ as the strain due to lattice mosaicity and misorientation is infused in this parameter.

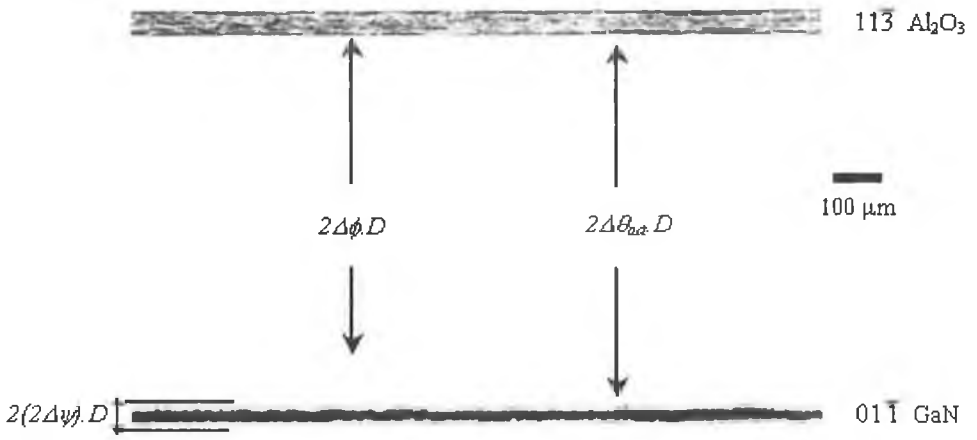

Figure 9.9: Section transmission topograph from region A of the ELO sample.

The arguments presented in the preceding paragraphs were further substantiated by (004) double crystal X-ray diffraction FWHM reflection measurements. An improvement of the crystalline quality of the ELO layer compared to the non-ELO sample became clear when plotting the rocking curve FWHM as a function of fill factor as shown in Figure 9.10. The dependence upon the fill factor is not completly understood at present but the FWHM is always lower than in samples possessing a fill factor of 1. However, Ferrari *et al.* [159] have identified that the Bragg peak width in III-V semiconductor heterostructures increases due to a correlated effect between the strain and tilt (or mosaicity) of lattice planes in the directions parallel to the hetero-interface. Clearly the epitaxial overgrowth possesses a smaller interface strain field than the non-ELO sample as conveyed by the topographic images; consequently our results are in agreement with [159]. It should be stressed that for the XRD measurements of the ELO regions, the large area of the impinging beam averages across material above and

between the stripes, and given that FWHM measurements are taken, the measured misorientations using XRD will be different than for SXRT. This is indeed the case albeit the trend is similar for both measurements. Similar trends were observed in [160] for both the local lattice misorientation parameter $2\Delta\psi$ and the macroscopic misorientation factor $2\Delta\theta_{\text{act}}$.

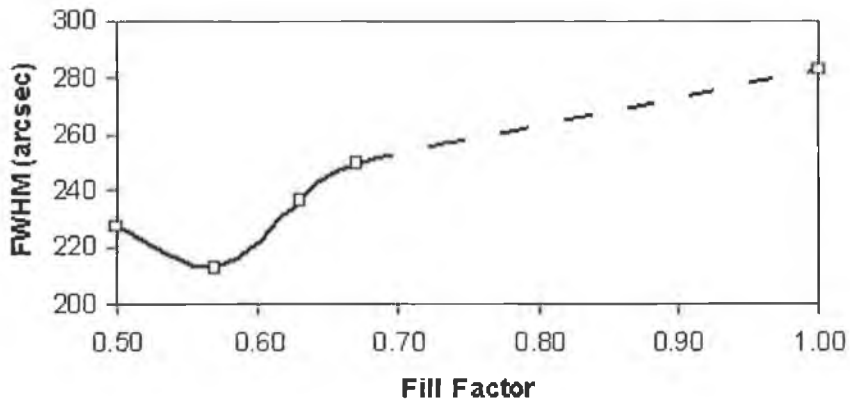

Figure 9.10: (004) double crystal X-ray diffraction FWHM reflection measurements for the ELO GaN on sapphire samples as a function of fill factor (solid line). Also included is the non-ELO sample, designated as having a fill factor $f = 1$.

Transmission electron microscopy measurements for the ELO sample showed a significant degradation in crystallinity for the non-ELO layer when compared with the ELO region as shown in Figure 9.11. Large threading dislocations can be seen propagating vertically in the non-ELO GaN region. However, for regions above the SiO_2 mask a significant reduction in their density is observed consistent with a redirection of the propagation of some dislocations at the growth front [151, 152].

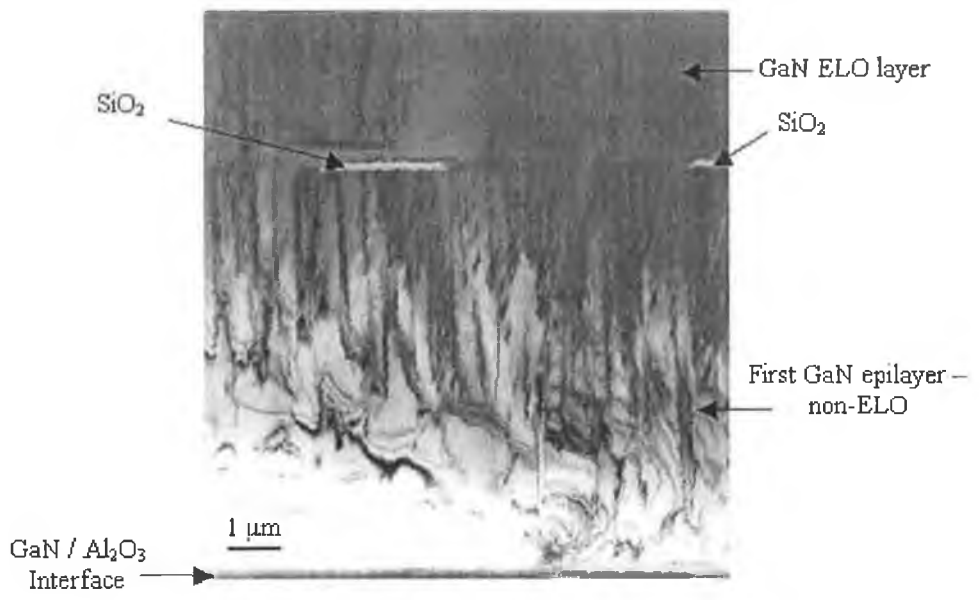

Figure 9.11: A transmission electron micrograph of a representative ELO sample.

9.4 Conclusions

White beam synchrotron X-ray topography in section transmission mode was used to monitor the improvement in quality of ELO GaN on sapphire when compared to non-ELO material. Strain at the epilayer-substrate interface was observed via an orientational contrast mechanism. Measurements of the observed misorientation of the GaN epilayer with respect to the substrate produce values which are larger in the ELO sample than for the non-ELO sample. However, this misorientation does not directly enable qualitative comparisons between the two samples as sufficient structural differences exist to make this information misleading. Rather local deviations from lattice coherence within the epilayers serve as better means of comparision: the ELO re-

gions displayed smaller deviations than the non-ELO sample ($2\Delta\psi = \pm 0.118^{o}$ versus $2\Delta\psi = \pm 0.177^{o}$ across an 8.5 mm length of epilayer). Topographic measurements also revealed variations in the ELO epilayer quality as the fill factor was varied. Moreover, they clearly displayed the enhanced quality of the ELO sample with respect to the non-ELO material. Furthermore, the decreasing FWHM of the rocking curves with decreasing fill factor and the imaging of dislocations by TEM near ELO and non-ELO interfaces demonstrate the better quality of the ELO samples versus the non-ELO sample. The results agree qualitatively with other studies performed on similar samples.

Chapter 10

Rapid Thermal Processing of Silicon Wafers

10.1 Introduction

Rapid thermal processing (RTP) is an important technology for VLSI chip manufacturing, and is increasingly replacing conventional furnace processing. Tighter process reproducibility and stricter control during device fabrication, coupled with the continued downscaling of VLSI device dimensions, has driven the demand for very short high-temperature processing steps. Low dopant distribution and accurate control of oxide growth cycles [161] are some of the major advantages offered by rapid thermal doping (RTD) and rapid thermal oxidation (RTO).

However, RTP is not without its disadvantages. Radiative cooling mechanisms inherent in the process, along with greater localised cooling at the wafer edge result in thermal gradients and therefore thermal stress within the sample. These thermal non-uniformities have made it difficult for RTP systems to meet both stress and film thickness uniformity requirements [162]. Thermal stress within the sample can be relieved by the formation of slip lines [163]. Stress-induced defects influence physical processes, such as diffusion of dopant species and recombination times of charge car-

riers. Greater process yield and enhanced device operation can be achieved through an understanding of the strain generation mechanisms within the constituent materials.

Several models have been proffered to explain the formation and relief of thermal stress within silicon wafers which have undergone proximity RTP. Using a simple two-dimensional reactor scale model and assuming axisymmetric temperature profiles, Lord [164] modelled the wafer temperature and stress distribution for unpatterned silicon wafers during RTP. Bentini *et al.* [165] evaluated the topographic distribution of slip lines in silicon wafers where plastic deformation had occurred. Deaton *et al.* [166] used this model coupled with [167], to estimate the oxide distribution in a silicon wafer after various RTO options. In this chapter, a quantitative and qualitative comparison is made with the theory developed by Bentini and co-workers, using micro-Raman spectroscopy and synchrotron X-ray topography experimental measurements of the stress in silicon samples that have undergone various RTD and RTO processing options.

Raman scattering is a very sensitive technique to probe local atomic environments, be they crystalline or amorphous, through their vibrational modes [168]. The surroundings of a particular atom have a strong influence on its dynamics; therefore, defects and/or structures inducing strain within the material will cause a change in the Raman spectra. This spectral shift with respect to the unstrained material can be related to the local stress through the appropriate Raman tensor. The quantitative information provided by Raman spectroscopy regarding the stress in the sample is limited by the penetration depth of the excitation source. Conventional laboratory laser sources can achieve penetration depths between circa 6 nm and 600 nm. As the active regions

of most integrated circuits lie within 500 nm of the substrate surface, Raman spectroscopy is therefore a suitable tool for analysis of stress distributions in these devices. Micro-Raman spectroscopy has been applied to the study of local mechanical stress in microelectronic devices and structures [169, 170]. Recently, this technique has also been used to study the stress generated in silicon by proximity rapid thermal diffusion [171].

With spatial resolutions better than 1 μm, X-ray topography and micro-Raman spectroscopy can yield complimentary information about the location and nature of stress within a sample. Thus their applicability to the focus of this chapter, the investigation of strain induced by rapid thermal processing of silicon wafers, is ideal.

10.2 Theoretical Description of Stress in RTP Wafers

In their analysis of rapid isothermal annealing of silicon wafers, Bentini *et al.* [165] modelled the topographic distribution of slip lines in thermally stressed <100> wafers. By assuming a free standing wafer of radius a, uniformly irradiated on one side by a lamp, they evaluated the temperature distribution in the wafer assuming the principal mechanism of heat loss from the sample to the ambient was attributable to radiation. Consequently, different regions of the sample, radiating at different rates will give rise to thermal gradients. As silicon has a high thermal diffusivity (0.87 cm^2s^{-1}), heating through the thickness of the wafer may be assumed instantaneous on the time scale of the thermal processing and thermal gradients within the thickness of the sample h can be neglected.

Bentini and co-workers ascertained the radial temperature distribution to be

$$T(r) = T_0 - \frac{H_0 l}{K(T)} \frac{I_0(r/l)}{I_1(a/l)} \tag{10.1}$$

where T_0 represents the steady-state temperature in the sample and $K(T)$ is the thermal conductivity of the sample at temperature T. I_0 and I_1 are modified Bessel functions of the first kind of order zero and one, respectively. H_0 governs the rate at which the surfaces radiate to the ambient in accordance with the Stefan-Boltzmann law. The parameter

$$l = \sqrt{\frac{K(T)h}{8\sigma\epsilon T_0^3}} \tag{10.2}$$

describes the distance over which the cooler area extends from the wafer edge i.e. it governs the length of the thermally stressed region and the length of the stress relieving dislocations. σ is Stefan's constant and ϵ is the emissitivity of the material. For a 150 mm diameter, 500 μm thick silicon wafer heated to 1050 °C, $l = 4.1$ mm.

The radial σ_r and tangential σ_θ components of the thermally induced stresses were computed using [172] (see Figure 10.1).

$$\sigma_r = -\frac{\alpha Y H_0 l^2}{K} \left(\frac{1}{a} - \frac{1}{r} \frac{I_1(r/l)}{I_1(a/l)} \right) \tag{10.3}$$

$$\sigma_t = -\frac{\alpha Y H_0 l^2}{K} \left(\frac{1}{a} + \frac{1}{r} \frac{I_1(r/l)}{I_1(a/l)} - \frac{1}{l} \frac{I_0(r/l)}{I_1(a/l)} \right) \tag{10.4}$$

where Y is Young's modulus and α is the thermal coefficient of linear expansion. Inherent in the term describing Young's modulus is a quasi-isotropic approximation

wherein the average value of Young's modulus for the <100>, <111> and <110> directions is used.

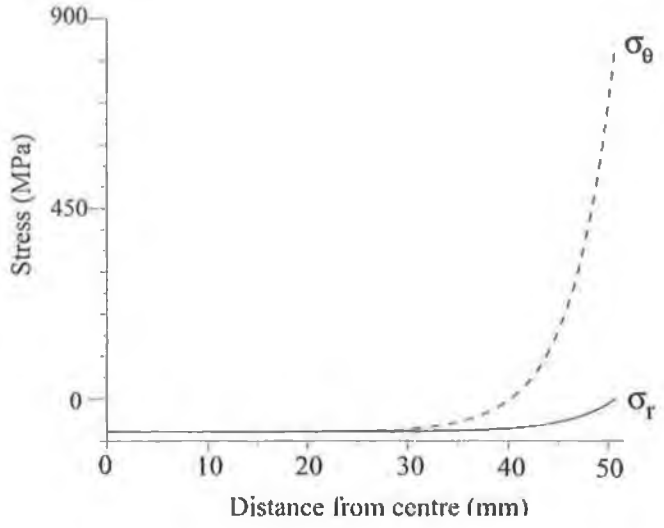

Figure 10.1: Radial σ_r and tangential σ_t stress components as a function of distance from centre of wafer; 150 mm diameter <001> n-type wafer, T_0 = 1050 °C.

Equations (10.3) and (10.4) were converted to Cartesian coordinates to appeal to the crystallographic symmetry of the silicon lattice in this coordinate system.

$$\sigma_{xx} = \frac{\sigma_r + \sigma_\theta}{2} + \frac{\sigma_r - \sigma_\theta}{2}\cos(2\theta) \tag{10.5}$$

$$\sigma_{yy} = \frac{\sigma_r + \sigma_\theta}{2} - \frac{\sigma_r - \sigma_\theta}{2}\cos(2\theta) \tag{10.6}$$

$$\sigma_{xy} = \frac{\sigma_r - \sigma_\theta}{2}\sin(2\theta) \tag{10.7}$$

where θ is the angle measured counterclockwise from the 110 axis as shown in Figure 10.2.

When the thermally induced stress is larger than the yield stress of silicon σ_Y, then slip of the {111} planes in the <110> direction ensues. Using the data of Schröter in [173], the yield stress of silicon at 1050 °C was computed to be $\sigma_Y = 208$ MPa. Bentini *et al.* [165] cited 12 positions on the wafer where the stress concentration is expected to exceed the elastic limit as illustrated in Figure 10.2. The maximum resolved stresses $|S_i|$ may be computed using Equations (10.8)–(10.12)

$$|S_1| = \sqrt{\frac{2}{3}}|\sigma_{xy}| \tag{10.8}$$

$$|S_2| = \sqrt{\frac{1}{6}}|\sigma_{xx} + \sigma_{xy}| \tag{10.9}$$

$$|S_3| = \sqrt{\frac{1}{6}}|\sigma_{xx} - \sigma_{xy}| \tag{10.10}$$

$$|S_4| = \sqrt{\frac{1}{6}}|\sigma_{yy} + \sigma_{xy}| \tag{10.11}$$

$$|S_5| = \sqrt{\frac{1}{6}}|\sigma_{yy} - \sigma_{xy}| \tag{10.12}$$

When the thermally induced stress component S_1 exceeds the elastic limit by 20%, conjugate glide on two glide systems results, causing steps on the wafer edge, with no visible effect on the wafer surface. The stress components S_2 to S_5 give rise to slip lines, which should be visible on the polished surface of the wafer.

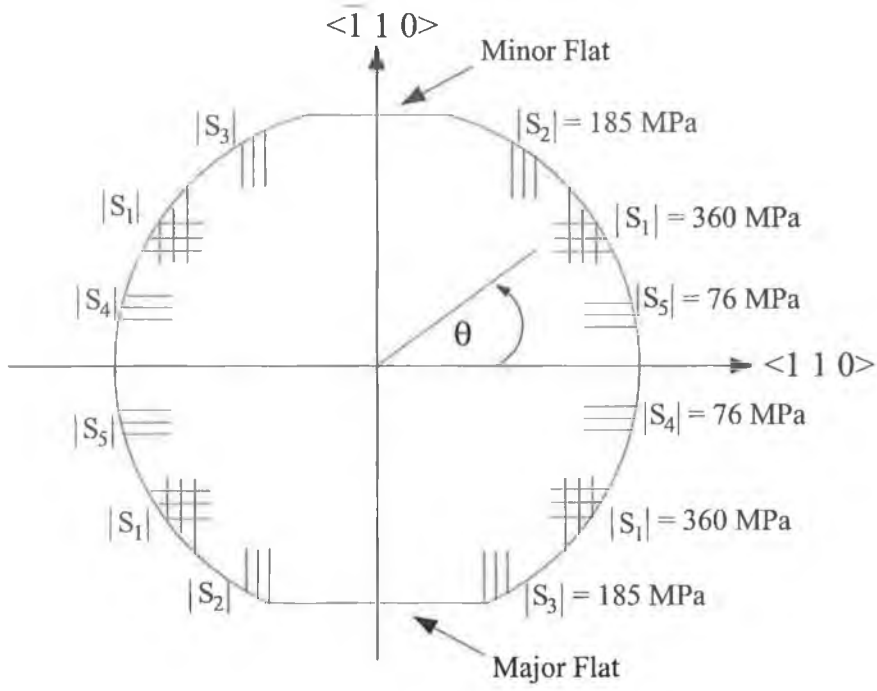

Figure 10.2: Locations of the maxima of the thermally induced stresses and the corresponding slip line directions on a <001> n-type silicon wafer. θ is measured counterclockwise from the <110> axis. The stresses $|S_i|$ were calculated using Equations (10.8)–(10.12).

10.3 Experimental

10.3.1 Sample Preparation

Several different wafers were prepared for the proximity rapid thermal processing options: rapid thermal oxidation and rapid thermal doping of 150 mm diameter Czochralski grown n-type silicon wafers [171, 174]. The <001> oriented wafers used throughout the study possessed a nominal resistivity of $9 - 15\ \Omega$ cm. The as-received wafers were cleaned using $H_2SO_4 : H_2O_2$ followed by a dip in HF. This constituted the reference wafer.

For the RTO process, the samples were fabricated by stacking a clean silicon reference wafer in close proximity to the silicon product wafer in the RTP furnace. The source wafer and product wafer were separated by 0.5 mm silicon spacers. In doing so, the product wafer experienced the same temperature profile as the RTD process, thereby minimising experimental variations between doped and oxidised wafers. Using the Deal-Grove [175, pp. 313–322] first order growth kinetic model of oxidation, the thickness of the silicon dioxide layer formed on the sample surface could be estimated (see Table 10.1).

For the RTD process, boron doped spin-on dopant B153 (SOD) manufactured by Filmtronics, USA, was spun onto the wafer at 6000 rpm for 15 s. The wafers were then baked at 200 °C to evaporate moisture and light organics from the SOD. Next, the SOD layer was cured at 900 °C for 45 s to convert it to a borosilicate glass dopant source. This dopant source was stacked in close proximity (0.5 mm) to an initially un-doped silicon reference wafer in the RTP furnace. During RTD, boron trioxide (B_2O_3) evaporates from the dopant source at a temperature of 1000 °C, across the separation gap, where it is adsorbed on the surface of the product wafer. Boron diffusion is then accomplished by means of a surface oxidation-reduction reaction between the boron trioxide and the silicon wafer [176], as shown in Equation (10.13).

$$2B_2O_3 + 3Si \leftrightarrow 4B + 3SiO_2 \tag{10.13}$$

In this reaction, doped silicon dioxide is formed on the surface of the product wafer and

becomes a dopant source for elemental boron, which diffuses into the silicon substrate. Excessive amounts of boron trioxide in the dopant source can lead to the formation of a *boron skin* composed of silicides and other boron compounds on the silicon surface. By performing the reaction in an oxidising ambient this can be avoided. At 1050 °C boron has a diffusivity $D = 47 \times 10^{-15}$ cm^{2}s^{-1} in silicon [175, pp. 380–391]; consequently for the maximum processing times used in this study (166 s), the diffusion distance of the boron atoms is of the order of 0.2 μm.

The RTP options were performed using a Sitesa rapid thermal processor with a maximum operating temperature of 1200 °C. The RTP furnace consists of a water-cooled, highly reflective stainless steel, double-sided casing. The product and dopant wafers were supported on three quartz pins inside a quartz chamber contained within the furnace. A bank of twenty four tungsten-halogen lamps mounted above and below the wafers constituted the heat source. The intensity of the lamps was determined by two thermocouples. One thermocouple was used to monitor the temperature of the process wafer and the second thermocouple was used to monitor a control section of the wafer. The control thermocouple provided feedback to maintain the temperature of the lamps. To ensure repeatability, the wafers were always inserted into the chamber with the major flat parallel to the furnace door. At a given temperature, there existed a 90 °C temperature variation across the 150 mm diameter; the temperature at the furnace door being cooler than at the back of the chamber. This anomalous temperature profile was found to be due to a variation in the power supply of the halogen lamps. All the rapid thermal processing was performed in an oxidising ambient of 25% O_2: 75% N_2; with

an RTP ramp-up rate of 48 °C/s and a ramp-down rate of 60 °C/s. For both processing options, the wafers were held at a peak temperature of 1050 °C for periods of 5 s, 16 s and 166 s. A summary of the processing options is presented in Table 10.1 and the RTP tool configuration may be seen in Figure 10.3. In this chapter, only the silicon reference and product wafers were analysed for stress.

Wafer	Rapid Thermal Process	Temperature (°C)	Duration (s)
A	Oxidation	1050	5
B	Oxidation	1050	16
C	Oxidation	1050	166
D	Diffusion	1050	5
E	Diffusion	1050	16
F	Diffusion	1050	166

Table 10.1: Rapid thermally processed samples. The oxidation process resulted in SiO_2 layers 1.2 Å, 4 Å and 40 Å thick for the respective oxidation times.

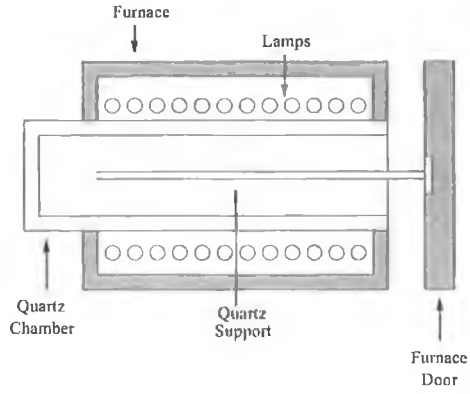

(a)

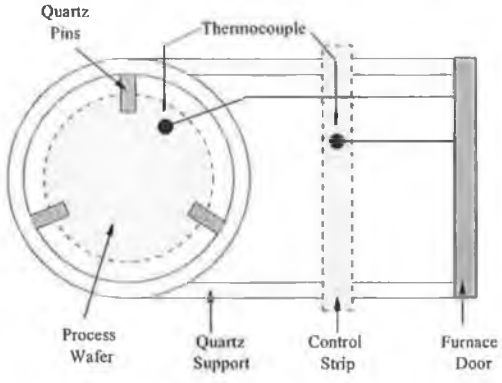

(b)

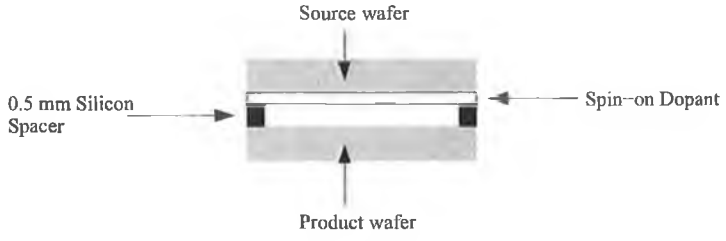

(c)

Figure 10.3: RTP tool configuration for doping and oxidation. (a) Side-view of RTP furnace (b) Plan-view of RTP furnace and (c) doping sample configuration. The dopant source is borosilicate glass on a silicon substrate. The heat is provided by twenty four tungsten-halogen lamps situated above and below the wafers. At 1000 °C, boron evaporates across the 0.5 mm gap and is adsorbed by the silicon product wafer. For the RTO process, the source wafer is replaced by a silicon reference wafer. Drawings not to scale.

10.3.2 Micro-Raman Spectroscopy

The micro-Raman measurements [171] were performed in backscattering mode on a *Renishaw Raman microscope system 1000*. The 514.5 nm line of the Ar^{+} laser, yielding stress information from a penetration depth of approximately 541 nm, at a power of 25 mW was used as the excitation source. The incident light was polarised parallel to the width of the line and the scattered light from the polariser was not analysed. Two objective lenses (40×, 4×), located outside the microscope, were used in conjunction with a pinhole having a diameter of 10 μm to expand the laser spot size. The light was then focused onto the sample using a 50× objective lens mounted on an *Olympus BH-2* optical microscope. The size of the laser spot incident on the sample was approximately 1 μm. A Peltier cooled CCD detector with 1 cm^{-1} spectral resolution was used to analyse the spectrum.

The sample was placed underneath the objective lens on an X-Y translation stage. The sample was moved using the X-Y stage and at ten positions on the wafer a Raman spectrum was recorded. The positions are illustrated in Figure 10.4. The crystalline silicon Raman spectrum in a phonon region mainly consists of a narrow peak at 520 cm^{-1} with a full width of about 4.18 cm^{-1}, arising out of scattering of incident light by long wavelength transverse optical phonons [177]. At each point on the sample, the phonon vibration peak was recorded along with the exciting line peak, in order to avoid inaccuracy in the peak position due to drift of the calibration frequency.

Background baseline removal, followed by a line fit using a Lorentzian function, allows

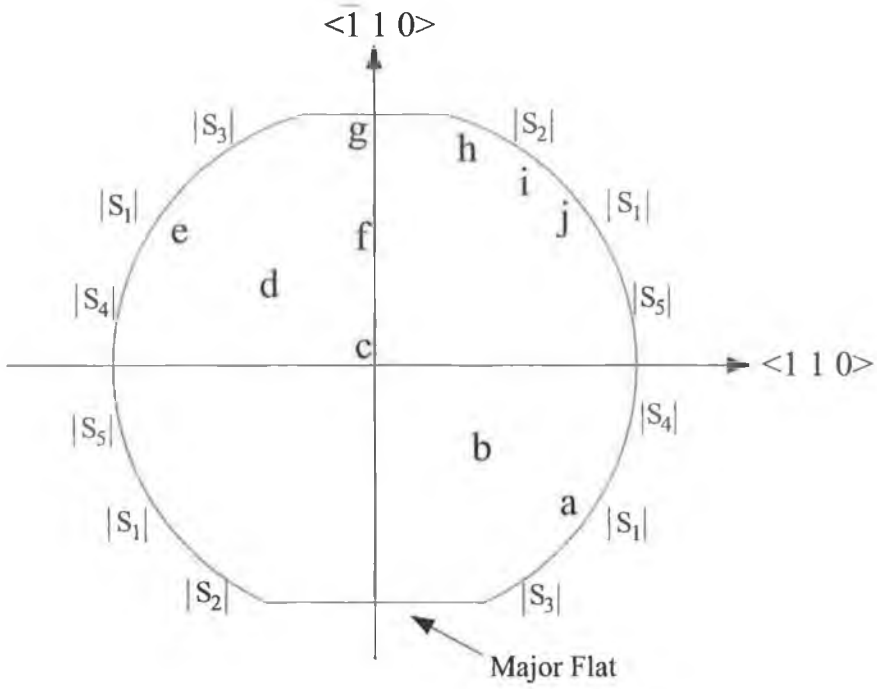

Figure 10.4: In accordance with the theoretical review of Section 10.2, Raman spectra were recorded at ten positions (a-j) on the RTP wafers.

three components of the Raman spectrum to be determined i.e. intensity, full width and position. Variations in the aforementioned are related to the composition, defect density and magnitude of stress in the sample under investigation. With a state-of-the-art spectrometer, it is possible to identify a shift in the Raman band of the order 0.01 cm^{-1}. By assuming a uniaxial stress along the [100] direction, DeWolf [169] obtained a relationship between the stress, σ (in Pa) and the Raman shift, $\Delta\omega$ (in cm^{-1}) for a strained silicon crystal.

$$\sigma = B\left(\omega_{\text{stress}} - \omega_{\text{ref}}\right) \tag{10.14}$$

where $B = -500 \times 10^6$, ω_{stress} (in cm^{-1}) is the peak frequency of the phonon band of

silicon under stress and ω_{ref} (in cm^{-1}) is the peak frequency of the phonon band of the stress-free silicon wafer. A positive or negative shift in the Raman peak position from the unstressed value corresponds to a compressive or tensile stress, respectively. Using the current experimental arrangement, the minimum detectable stress $|\sigma_{min}| = 5$ MPa.

10.3.3 Synchrotron X-ray Topography

Two white beam X-ray topographic imaging modes were employed in this study: large-area back reflection topography and section transmission topography (see Chapter 7). For the large area back reflection experiments the beam impinging perpendicularly on the sample was collimated to 3 mm × 3 mm. For the section transmission topographs the incident beam was collimated into a narrow ribbon by a slit typically 10 - 15 μm in height by 3 mm in width. The sample was tilted at 18° to optimise the imaging of the 040 and 044 set of reflections. The aforementioned topographic images were recorded on Kodak SO-181 high resolution professional X-ray film, having an emulsion grain size of about 0.05 μm. The distance from the sample to film was 40 mm in both imaging geometries. Table 10.2 summarises the topographic measurements.

Wafer	Regions Studied	RTP Process @ 1050 °C
Reference	–	–
C	h	Oxidation 166 s
D	h, c	Diffusion 5 s
F	h	Diffusion 166 s

Table 10.2: Samples studied using X-ray topography. The sample regions are those of Figure 10.4.

10.4 Results

The reference sample, possessing a Raman phonon peak at 520 cm^{-1} and a full width at half maximum Γ = 4.2 cm^{-1}, demonstrated excellent crystallinity. This was confirmed by the presence of Pendellösung fringes in the section transmission topograph of Figure 10.5. From Chapter 5 it is known that Pendellösung fringes occur due to the interference of the X-ray wavefields propagating within the crystal [178]. The number of fringes n in a perfect crystal

$$n = \frac{t_0}{\Lambda_0} \tag{10.15}$$

where t_0 is the thickness of the crystal and Λ_0 is the Pendellösung distance [126, 179]. For the 044 reflection of a 505 μm thick silicon wafer $n = 16.62$. For the topograph illustrated in Figure 10.5, sixteen fringes were counted using an optical microscope. Hence, the starting material for the RTP process is of superior quality.

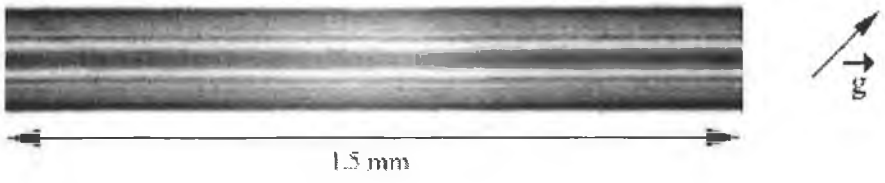

Figure 10.5: 044 section transmission topograph of reference sample. The interference pattern (Pendellösung Fringes) is indicative of excellent sample crystallinity. $\vec{g}$ is the diffraction vector.

As indicated by Table 10.3, an increase in thermal stress was observed in the RTO wafers A-C with increased oxidation time. The only exceptions to this were positions f and g, whereby stress reduction in these regions was attributed to the RTP tool con-

figuration i.e. the 90 °C temperature variation across the 150 mm diameter. Positions e and i in Table 10.3 correspond to the position of the stresses S_1 and S_2 in Figure 10.2 respectively. After 166 s of oxidation, the measured stresses at these positions, $\sigma_i = -320$ MPa and $\sigma_e = -135$ MPa, were found to be in excellent agreement with the theoretical values $|S_1| = 360$ MPa and $|S_2| = 185$ MPa. The slight differences in these results may be accredited to the assumption in Equation (10.14) that the stresses measured using micro-Raman spectroscopy were uniaxial in nature.

Wafer position	Wafer A	Wafer B	Wafer C
a	0.12	0.20	0.59
b	0.09	0.20	0.29
c	0.09	0.35	0.63
d	0.01	0.20	0.44
e	0.18	0.19	0.27
f	0.03	0.20	0.07
g	0.06	0.15	0.04
h	0.04	0.06	0.38
i	0.23	0.24	0.64
j	0.03	0.10	0.31

Table 10.3: Measured shift in Raman peak $\Delta\omega$ (cm^{-1}) in RTO wafers (A-C) with respect to reference wafer.

Section transmission X-ray topographs taken from the wafer edge (region h) after 166 s RTO, demonstrated a reduced number of Pendellösung fringes with respect to the reference material. The reduction in fringe density and sharpness as shown in Figure 10.6, is indicative of a degradation in crystallinity due to the prolonged oxidation.

Micro-Raman measurements of the RTD wafers demonstrated a commensurate increase in strain with time, prior to plastic deformation of the lattice. The results are summarised in Table 10.4. The stress in wafers D and E is greater than their oxidised counterparts for the same process interval. This is due to the presence of boron in the

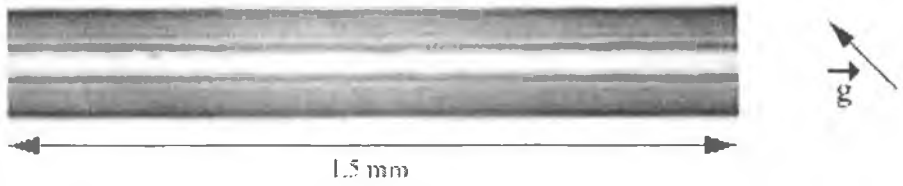

Figure 10.6: $0\bar{4}4$ section transmission topograph of wafer C from region h. A reduction in the number of Pendellösung fringes with respect to the reference material is indicative of crystallinity degradation. $\vec{g}$ is the diffraction vector.

silicon lattice. After 5 s of the RTD process, boron adsorbed on the wafer surface in accordance with Equation (10.13), induced large strain fields that penetrate approximately 120 μm into the wafer bulk. It is important to note that one is only imaging the impact of the strain due to the adsorbed boron in the section topograph of Figure 10.7 (a) and not the actual diffusion of boron within the lattice. Evidence of oxygen related defects within the wafer can be seen in Figure 10.7 (b).

Distortion of the silicon lattice must occur to accommodate dopant impurity atoms. Silicon has a tetrahedral radius of 1.18 Å. Boron has a tetrahedral radius of 0.88 Å, corresponding to a misfit $\epsilon = 0.254$. Since boron is smaller than silicon, the presence of boron in the silicon wafer induces lattice contraction and enhances stress generation. Therefore, the induced stress in a doped wafer is expected to exceed the yield strength more quickly than in an undoped wafer. This was found to be the case through an investigation of the Raman shift for the RTD wafer F, which underwent a long thermal anneal of 166 s. A smaller stress was found in this wafer compared to those that underwent shorter RTD processes, allowing one to conclude that the wafer had relaxed through plastic deformation.

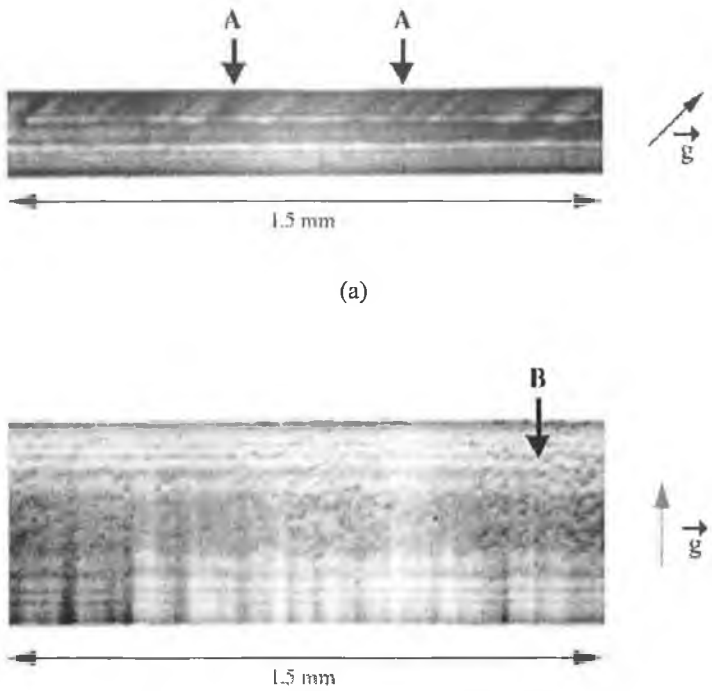

Figure 10.7: (a) 044 and (b) 004 section transmission topographs of wafer D from region c. Adsorbed boron on the wafer surface induces strain fields propagating approximately 120 μm into the wafer bulk as indicated by arrows A. Oxygen related defects are shown in the 004 reflection with arrows B. $\vec{g}$ is the diffraction vector.

A comparison of the stress in wafers C and F confirmed this result. The stress in the oxidised wafer had not been relieved to any significant degree; consequently greater stress was demonstrated across wafer C. Wafer C demonstrated a compressive topology in comparison to the relaxed wafer F, which was found to be compressive at the edges and tensile in the centre. These results contradict those obtained by Deaton *et al.* [166]. Deaton observed that the temperature gradient induced a stress distribution that was compressive at the centre and tensile towards the edges of the wafer. At

Wafer position	Wafer D	Wafer E	Wafer F
a	0.15	0.17	0.32
b	0.16	0.29	0.17
c	0.14	0.53	-0.01
d	0.15	0.19	0.04
e	0.14	0.35	0.15
f	0.16	0.23	0.08
g	0.18	0.41	0.23
h	0.19	0.46	0.24
i	0.34	1.04	0.44
j	0.15	0.36	0.14

Table 10.4: Measured shift in Raman peak $\Delta\omega$ (cm^{-1}) in RTD wafers (D-F) with respect to reference wafer.

present, this anomalous result is thought to be due to a variation in the temperature gradient within the RTP oven and/or some other specific effect of our RTP tool. Further investigations will be required to ascertain which mechanism, if either, is dominant. The self-consistent results presented within this chapter identify that to a first order, the model proposed by Bentini and co-workers [165] is accurate.

Slip lines due to stress palliation measuring 0.3 mm, 5 mm and 25 mm were observed in region a of wafers C, E and F respectively. Wafer E is in closest agreement with the theoretical prediction of the slip line length $l = 4.1$ mm. Optical microscopy demonstrated that the topological distribution of the stress in the wafer agrees with [165]. An analysis of the Raman full widths provides an insight regarding the structural deformation of the crystal from the RTP process. Using Table 10.5 to compare the full width at half maximum for the RTO wafer C, which underwent oxidation for 166 s, with the reference wafer ($\Gamma = 4.18$ cm^{-1}), substantiates the previous results that the oxidation process induces only minor lattice perturbations. Short RTD processes wherein boron adsorbed on the wafer surface induces strain fields within the sample, were observed

to induce slight structural disorder within the lattice. Compare for example, the Raman full widths for wafer D with the section topographic image of Figure 10.7 (a). The formation of slip dislocation lines increased with increased time at the peak temperature. Lord [164] predicts that the ramp rates are not the cause of the most damaging stresses in the wafer; it is the temperature non-uniformity at the peak temperature that tends to stress the wafers beyond the yield stress. Due to the strong temperature dependence of the silicon critical yield stress, the extent of slip line formation depends on both the peak wafer temperature and the time spent at this temperature. For the case of wafer F there is a very noticeable increase in the Raman full width, which proves that a significant structural disorder exists in this wafer. This is not surprising considering that

Wafer position	Wafer C	Wafer D	Wafer F
a	4.19	4.20	4.65
b	4.14	4.18	4.72
c	4.18	4.19	5.21
d	4.22	4.19	5.26
e	4.09	4.23	5.14
f	4.18	4.18	5.32
g	4.17	4.25	4.86
h	4.19	4.20	4.95
i	4.18	4.24	5.06
j	4.17	4.25	5.17

Table 10.5: Measured Raman full width at half maximum Γ (cm^{-1}) for wafers C, D and F. Wafer C underwent RTO for 166 s; wafers D and F underwent RTD for 5 s and 166 s respectively.

slip lines measuring 25 mm in length, far greater than those theoretically predicted, propagated at the wafer surface. The section topograph of Figure 10.8 (a) illustrates the lattice disorder. In the right hand side of the topograph, where the doping process was blocked due to the silicon spacer, slightly distorted Pendellösung fringes can be seen which are suggestive of reasonable wafer quality. However, the boron doped re-

gion (left hand side) possesses a dense dislocation array. These dislocations are also evident in Figure 10.8 (b) which is a back reflection topograph of the same sample.

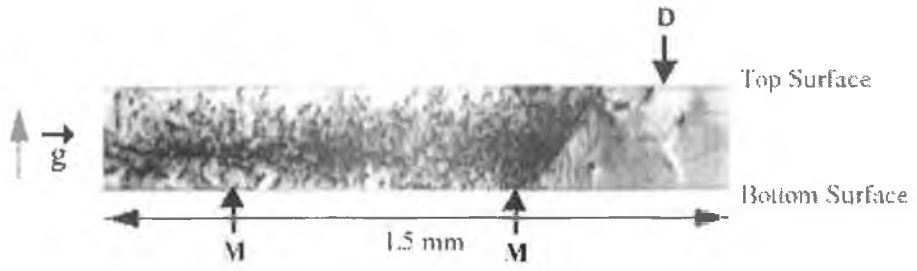

(a)

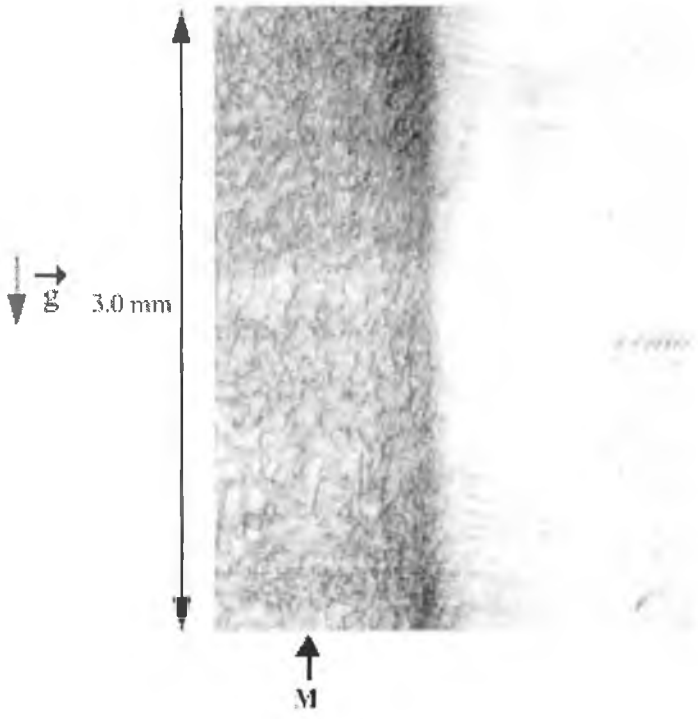

(b)

Figure 10.8: (a) 004 section transmission and (b) 602 back reflection topographs from wafer F which underwent RTD for 166 s. A dense dislocation network arising out of stress relief may be seen on the left hand side of the topographs (arrow M). The right hand side of the sample was covered by a silicon spacer during the doping process; consequently very few boron atoms induced strain in this region. The defect imaged at D has a partial dynamical contrast (see text). The information in (b) was recorded from a penetration depth $t_p = 27$ μm. $\vec{g}$ is the diffraction vector.

10.4.1 Kinematical, Dynamical and Intermediate Imaging of Defects

The imaging mechanism of the dislocations in the section transmission topograph of Figure 10.8 (a) is kinematical. However, the undoped region of the wafer (right hand side) revealed the presence of a defect whose origin was partially dynamical (arrow D). Dynamical imaging can arise when the product $\mu_0(\lambda)t_0 > 1$. In the interval between kinematical and strict dynamical imaging, $1 \leq \mu_0(\lambda)t_0 \leq 6$, an intermediate image is formed and all three types of images may be observed simultaneously [180]. For the (022) family of reflections $\mu_0 t_0 = 1.17$. When the incident X-ray beam impinged on a strongly deformed region of the crystal associated with the defect, the kinematical image i_1 was formed as shown in the 022 section transmission topograph of Figure 10.9 (a). In its stereographic partner, the $0\bar{2}2$ reflection of Figure 10.9 (b), the dislocation did not intersect the direct beam and therefore no kinematical imaging occurred. An important feature of the kinematical or direct image is that it is localised with respect to the incident beam and consequently corresponds to the depth of the defect within the crystal. However, when an X-ray strikes a crystal, energy flow in the crystal occurs within a triangular volume bounded by the diffracted and forward diffracted beams [181]. This is the Borrman fan. Independent of the kinematical image formation, wavefields propagating within the Borrman fan are deviated or stopped when they reach the defect. The resulting lack of intensity creates the dynamical image i_2. When interbranch scattering occurs between wavefields at the site of a defect, new wavefields may be created and these may propagate through the crystal forming the intermediary image i_3. Due to the location of the defect with respect to the Borrman

triangle associated with the incident beam, the dynamical and intermediary images in the $0\bar{2}2$ reflection are less pronounced than in the 022 reflection.

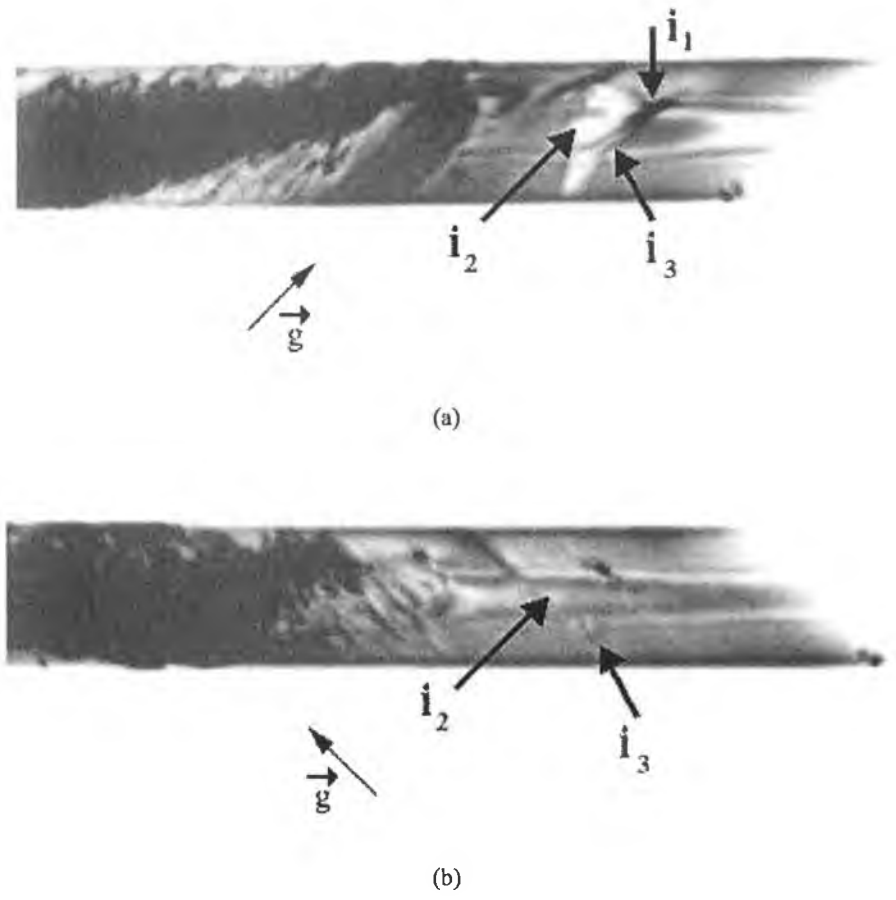

Figure 10.9: Stereo pair of section transmission topographs from wafer F with diffraction vector $\vec{g}$ (a) parallel to 022 and (b) parallel to $0\bar{2}2$. The imaging mechanisms are: i_1 kinematical image; i_2 dynamical image and i_3 intermdediary image.

10.5 Summary

Thermal stress and boron induced strain generated during the RTO and RTD of silicon wafers has been investigated using micro-Raman spectroscopy and X-ray topography.

Thermal stress increased with processing time until relaxation of the lattice occurred. For the RTO samples, close agreement was found with the theoretical predictions of Bentini *et al.* [165]. The RTD samples did not agree with the theory as sizable lattice relaxation occurred via slip line and dislocation formation. The introduction of boron within the lattice caused lattice contraction and reduced the time taken to exceed the yield stress. The results clearly demonstrated that slip line formation was dependent on the peak temperature of the wafer and the time spent at same.

Chapter 11

Characterisation of High Energy Diamond Monochromator Crystals

11.1 Introduction

The Deutsches Elektronen Synchrotron (DESY) facilitates scientific investigations in the fields of particle physics and synchrotron radiation. Nominal experiments performed using the 920 GeV HERA particle accelarator include investigations of: the structure of the protron via colliding positron-proton beams, electron-proton interactions, the quark-gluon structure of matter and CP–violation [113]. Originally used as a Positron-Electron Tandem Ring Accelerator facility, the PETRA synchrotron is now used to preaccelerate particles for use in high energy experiments at HERA and as a positron synchrotron radiation source for HASYLAB test experiments.

The energy of the PETRA storage ring can be ramped between 7 GeV and 12 GeV, facilitating the production of photons using a 121 pole hybrid undulator within the spectral range of 14 keV to 150 keV [182]. A diamond crystal in the Laue geometry, situated approximately 106 m downstream of the undulator, splits the undulator radiation into a "low-energy" branch and a "high-energy" branch as illustrated in Fig-

ure 11.1. The low energy photons diffracted from this pre-monochromator possess-

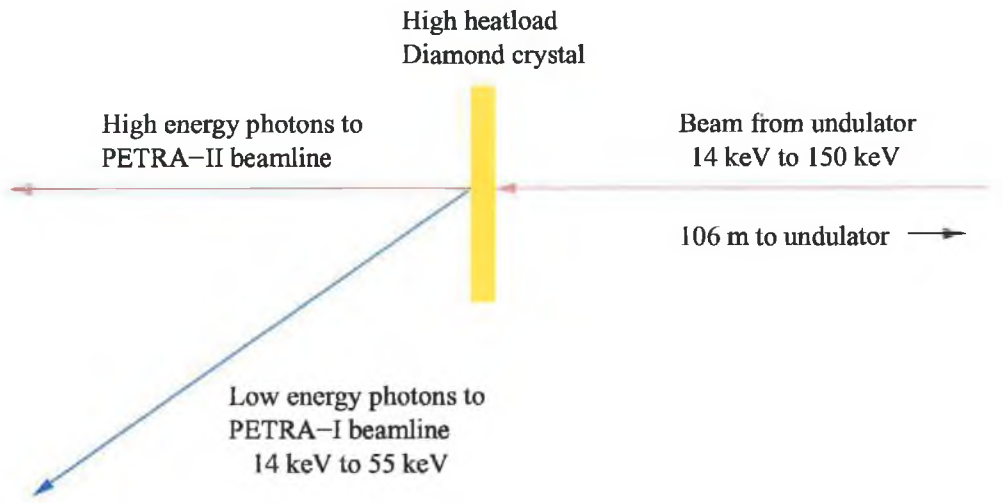

Figure 11.1: High heatload pre-monochromator for PETRA-1 beamline.

ing photon energies from 14 keV to 55 keV are typically used at beamline PETRA-1 for Mössbauer spectroscopy; whilst the high energy photons transmitted through the crystal are used at the PETRA-II beamline in diffraction and scattering experiments pertaining to structural studies of condensed matter.

Considering the nominal power density radiated from the undulator is 512 kW/mrad^2 at a synchrotron energy of 12 GeV, this implies that only diamond, possessing a large thermal conductivity (nominally 600 – 1000 W/m/K at room temperature), high transparency from UV to IR, radiation hardness and chemical inertness, is suitable for use in the pre-monochromator. It is the purpose of this chapter to assess the crystalline quality of several synthetic diamonds, obtained from Drukker in Holland, for potential use in the pre-monochromator.

11.2 Experimental

Type Ib diamonds, wherein the major impurity is nitrogen, possessing a nominal sample size of 4 mm × 8 mm × 2 mm were grown under high pressure and high temperature [183].

X-ray diffraction rocking curve measurements and white beam X-ray topography techniques were performed at beamlines PETRA-1 and HASYLAB F-1 respectively. For the XRD measurements the undulator gap was adjusted to 14.8 mm, yielding a 14.45 keV beam impinging upon the 111 diamond crystal of the pre-monochromator. The beam was deflected into the experimental hutch of beamline PETRA-1 using a 220 Ge crystal. The width of the Bragg reflectivity curve as a function of energy at a fixed angle of incidence is about 2 eV, whose wings show a $(\Delta E)^2$ type dependency. These wings can be supressed and the energy resolution of the beam improved to approximately 150 meV using 14 bounces from the 333 reflexion of a 111 Si channel cut monochromator [184]. This is demonstrated in Figure 11.2. The channel cut was arranged in a (+n,+m) dispersive geometry relative to the Ge crystal. The resulting 1 mm^2 highly monochromatised beam, at a wavelength of 0.8581 Å, impinged upon the diamond sample mounted on a Huber four circle diffractometer. The sample was oriented about the 220 reflection using the θ and ϕ circles. By varying the vertical and lateral displacements of the diffractometer mounting table about a nominal sample centre, a raster scan of the rocking curve as a function of sample position was obtained. The experimental configuration is shown in Figure 11.3.

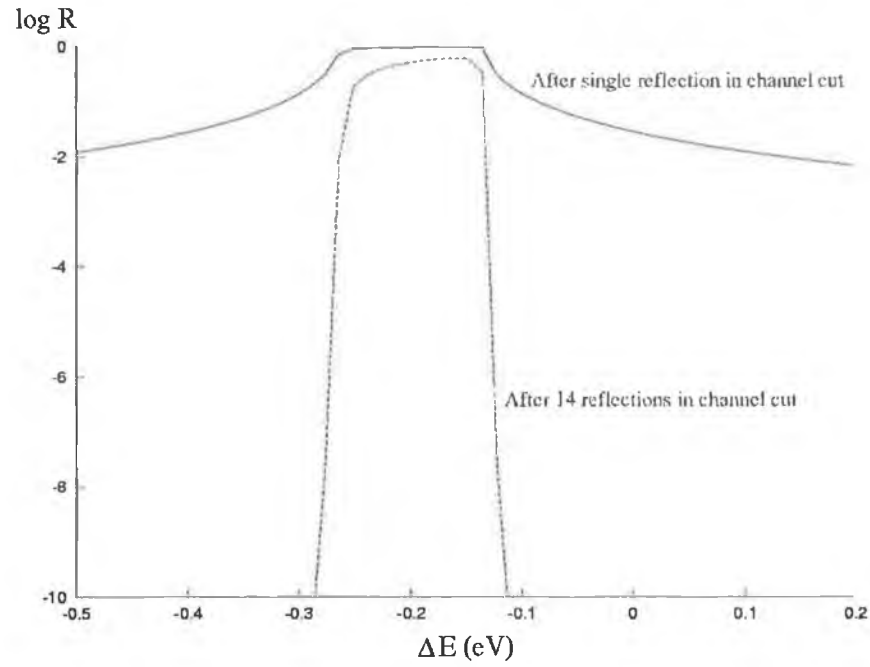

Figure 11.2: Increased energy resolution using channel cut to suppress wings of rocking curve. Decadic logarithm of the Bragg reflectivity of Si (333) at Bragg angle $\theta_B = 24°13'$ for 14.45 keV photon energy plotted as a function of energy difference from 14.45 keV. Calculated according to [92].

White beam back reflection x-ray topography in large area and section modes (as described in Chapter 7) was used to visualise the strain within the samples. The Bragg pattern of topographs was recorded on Geola VRP-M Holographic X-ray film. The distance from the sample to the film was 40 mm in both geometries. The incident beam was collimated to 3.5 mm^2 for large area, whilst the height of the beam was reduced to 15 μm for the section studies.

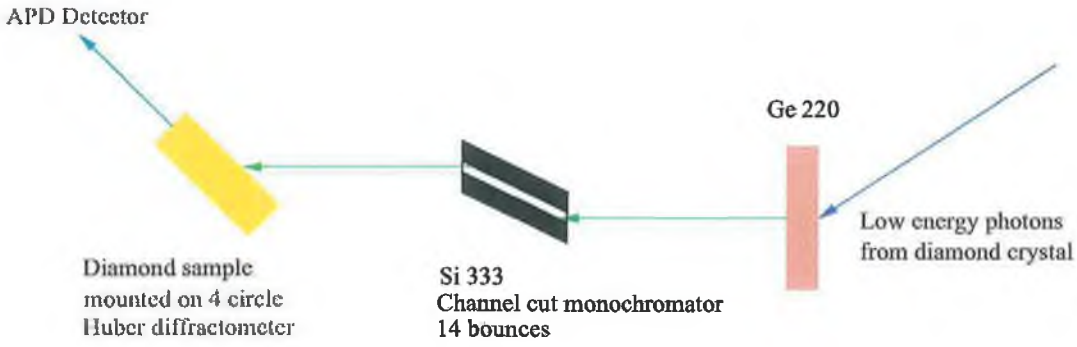

Figure 11.3: XRD measurement configuration.

11.3 Results

Figure 11.4 shows the Full Width at Half Maximum (FWHM) as a function of position about the nominal sample centre for a typical diamond sample. Regions that produced no reflections possess a zero FWHM. The heterogeneous strain within the sample manifests itself via a broadening of the rocking curve width. The source of this strain is possibly due to a combination of curvature and mosaic spread of the lattice planes as a shift in the rocking curve peak towards larger values of θ is witnessed as one progresses from the top toward the bottom of the sample as conveyed in Figure 11.5.

To first order, the curvature R may be evaluated through a knowledge of the beam diameter s and measurement of the shift $\delta\theta$ in the absolute position of the Bragg peak over a distance x on the sample [185]. This measures the curvature about an axis perpendicular to the dispersion plane i.e. cylindrical curvature.

$$R = \frac{s}{\delta\theta} \tag{11.1}$$

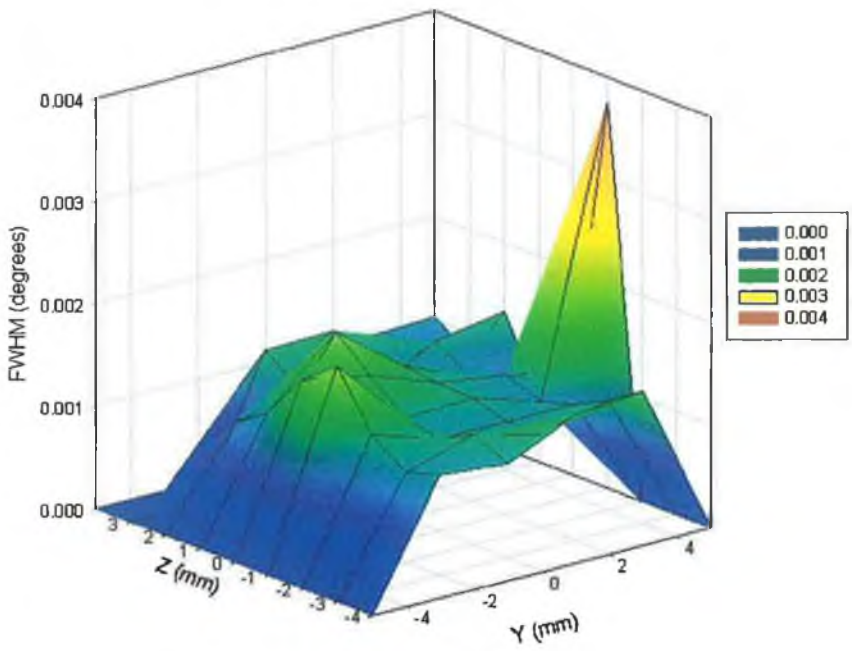

Figure 11.4: FWHM measured in degrees as a function of position about a nominal sample centre.

The radius of curvature along the central vertex of the sample was found to be $R = 4.4$ m. The thickness and Young's modulus of the sample in conjunction with its radius of curvature facilitates an estimation of the maximum stress $|\sigma_{\max}| = 208$ MPa.

The large area back reflection topographs revealed the presence of void like defects and occlusions within the upper regions of the sample, wherein nominal penetration depths $t_p = 1.18$ mm were obtained. These are indicated by arrow A in Figure 11.6.

A laminar strain gradient was observed within the sample using back reflection section topography (arrow B in Figure 11.7). This is suggestive of a tiered stacking fault induced by inhomogeneous growth of the crystal lattice. The presence of a dislocation propagating from the surface of the sample toward the bottom (arrow C) appears to

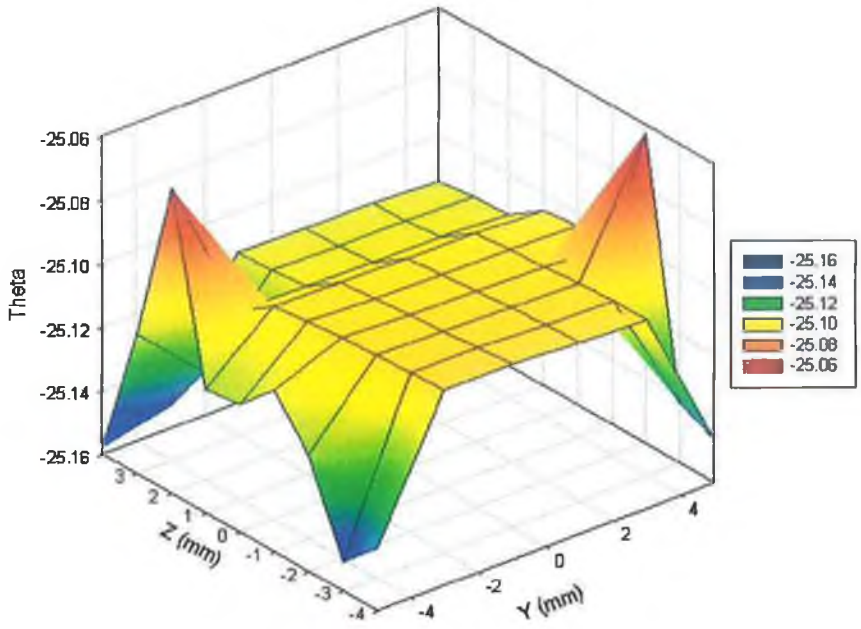

Figure 11.5: Variation in rocking curve peak as a function of position about a nominal sample centre.

effect a dislocation jog at the region depicted by arrow D. This possibly mixed dislocation could consist of a screw and edge dislocation. The large strain fields and defect structures within the sample are not surprising when one considers the mean FWHM over the entire sample is 4.45 arcseconds; this is far greater than the Darwin width $w = 0.9$ arcseconds (calculated using [184]).

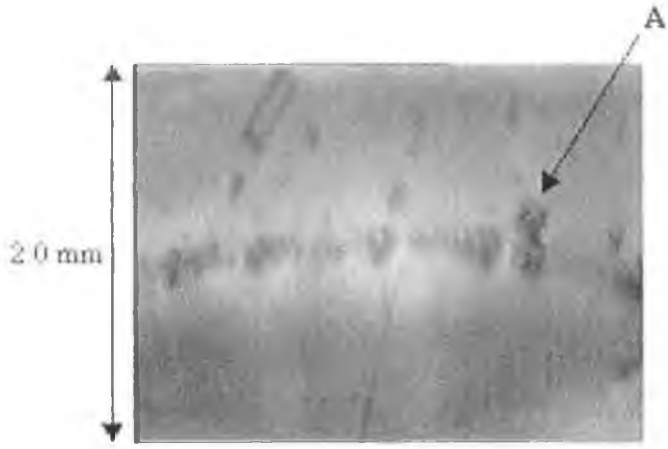

Figure 11.6: $\bar{3}17$ large area back reflection topograph.

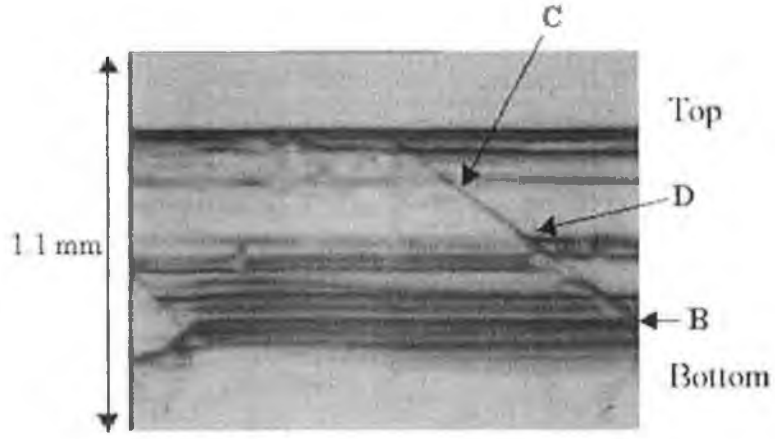

Figure 11.7: $\bar{3}19$ back reflection section topograph.

11.4 Conclusions

The interest in diamond crystals for use in x-ray optics applications has increased dramatically in the past number of years. For example, comparing theoretical data for diamond and single silicon crystals one finds that diamond (111) is competitive with silicon (220). The reflection properties of diamond are slightly higher than silicon coupled with the advantage that diamond will also absorb less heat [119, pp. 248–249]. However, their application is presently limited to situations where their mosaicity (of the order of a couple of arcseconds) is acceptable. The inhomogenous strain conveyed through the variation in FWHM and peak position in the rocking curve as a function of sample position, in conjunction with the presence of defects in the x-ray topographs, demonstrate that the samples examined in this study are a long way from the perfection required for use at conventional third generation beamlines. In a recent and much more comprehensive study performed in a collaboration between the European Synchrotron Radiation Facility (ESRF), De Beers Industrial Diamonds Ltd. and the University of Witwatersrand [183] similar results were obtained. In particular, the nitrogen impurity concentration distribution obtained by optical spectroscopy was superimposed on the defect structure determined by X-ray diffraction. A direct correlation between the nitrogen impurities and raw defect structure was obtained. The findings in this chapter are also supported by Kowalski *et al.* [186].

Due to the tremendous heat load associated with fourth generation X-ray Free Electron Lasers (XFELs) it is obvious that diamond will be the material of choice for use

in monochromators and X-ray photonic delay lines [119, pp. 266]. However, dramatic increases in crystalline quality are required before such implementations will be possible.

Chapter 12

Misfit Dislocations in Si/SiGe Heterostructures

12.1 Introduction

There has been a growing interest over the past decade or so in the use of grazing incidence diffraction (GID) X-ray topographic techniques for the analysis of thin surface crystal layers [128, 187–189]. For strained or dislocation single crystal materials Dudley, Wu and Yao [190] have shown that the kinematical theory determines the penetration depth. For semiconductor materials, grazing incidence angles of the order of 0.1°–1° are typically used. These angles tend to be greater than the critical angle α_c for Fresnel reflection and consequently information about strain, defect or dislocation distributions at penetration depths of the order of micrometres is obtained. However, in many modern epitaxial systems, very thin mismatched layers are grown close to the surface of the substrate, and the overall thickness of such layers, which themselves may be heavily dislocated or strained, may be much smaller than the smallest achievable penetration depth using conventional GID topography. One such system is that of the heteroepitaxy of thin $Si_{1-x}Ge_x$ layers on mismatched Si substrates.

In the past, a number of authors have used variants of the GID topography scheme,

wherein grazing incidence angles below the appropriate critical angles are used to image structures at or near the surface of the sample. For example, Afanasev *et al.* [191] used a non-synchrotron X-ray source to image etched topographical features in Si wafers. Images from the upper 140 nm of the Si surface were presented, though a precise interpretation of these was difficult. Kitano and co-workers [192] availed of a synchrotron X-ray source in double crystal geometry to produce specular reflections at a fixed wavelength to image scratches, mechanochemical polishing damage and growth swirl patterns in Si surfaces. However, no estimation of the depths of the observed features below the Si surface was provided. Using an X-ray tube as a radiation source, Imamov *et al.* [193] used extremely asymmetric Bragg diffraction with grazing angles less than the critical angle for total external reflection to image surface layer amorphisation due to Pb ion implantation in Si.

In the total external reflection domain, as described in Chapter 5, the incident photons with incident angle α_o less than the critical angle α_c, give rise to a specularly reflected Fresnel wave in conjunction with an evanescent wave within the sample whose electric field is exponentially damped within the "scattering depth" [98]

$$\Lambda = \frac{\lambda}{2\pi\left(l_o + l_h\right)} \tag{12.1}$$

where

$$l_{o,h} = \sqrt{\frac{\left(2\delta - \sin^2\alpha_{o,h}\right) + \left[\left(\sin^2\alpha_{o,h}\right)^2 + (2\beta)^2\right]^{\frac{1}{2}}}{2}} \tag{12.2}$$

In equation (12.2) the subscripts o and h refer to the incident and diffracted beams respectively, λ is the wavelength of the incident photons,

$$\beta = \frac{\lambda\mu(\lambda)}{4\pi}$$

$$\delta = \frac{\overline{\rho_e} e^2 \lambda^2}{2m_e\epsilon_0 (2\pi c)^2}$$

$\mu_0(\lambda)$ is the linear absorption coefficient of the material, $\overline{\rho_e}$ is the mean electron density, m_e is the rest mass of the electron, e is the elementary unit of charge, ϵ_0 is the vacuum permittivity and c is the speed of light.

At this point, it is worth re-iterating the differences between the scattering depth Λ and the penetration depth t_p. The scattering depth is the distance the evanescent wave propagates perpendicularly from the surface into the sample bulk. *In this situation the incident beam is not transmitted into the material.* The penetration depth is characterised by the depth at which the intensity of the outgoing reflected beam has dropped to $\frac{1}{e}$ times that of the incident beam due to photoelectric absorption. *Here the incident beam penetrates into the crystal.* For a sufficiently strained material with an angle of incidence greater than the critical angle, kinematical theory applies and the penetration depth [190] is given by

$$t_p = \left[\mu_0(\lambda)\left(\frac{1}{\sin\alpha_o} + \frac{1}{\sin\alpha_h}\right)\right]^{-1} \tag{12.3}$$

Within the volume governed by the scattering and penetration depths, diffraction may

occur. When $\alpha_o < \alpha_c$ radiation only penetrates a few nanometres into the sample. As the value of α_o approaches α_c the scattering depth increases rapidly due to constructive interference between the phases of the incident and specular electric fields [194]. However, depth control is quite difficult because the scattering depth varies over several orders of magnitude for a slight change in α_o. At values $\alpha_o > \alpha_c$ control of the penetration depth is quite easy as t_p increases rather slowly with increasing α_o [128]. Therefore, the technique of Total External Reflection X-ray Topography (TERXT) combined with conventional GID topography potentially provides an imaging mechanism sensitive to strain features associated with, or in very close proximity to, the sample surface. It is the purpose of this chapter to investigate the strain induced by the heteroepitaxial growth of thin $Si_{1-x}Ge_x$ layers on mismatched Si substrate's using TERXT.

12.2 Experimental

Three samples were created for the study. The first, referred to as SiGe 720, consists of a silicon substrate with a ~ 1.7 μm buffer layer of $Si_{1-x}Ge_x$ wherein the germanium concentration varies linearly from 13.5% to 42% over the thickness of the layer. On top of the buffer layer, a ~ 0.3 μm thick $Si_{0.6}Ge_{0.4}$ active layer was grown. The sample was grown at 800 °C by low pressure chemical vapour deposition (LPCVD). The second sample, referred to as SiGe 774, was formed by growing a ~ 1.36 μm $Si_{1-x}Ge_x$ buffer layer on top of a silicon substrate. The germanium concentration varied from 12% to 42%, in steps of 6% throughout the layer. A ~ 0.3 μm thick $Si_{0.65}Ge_{0.35}$ active layer was grown on the buffer layer. The last sample, SiGe 775, consisted of a ~ 1.36 μm

buffer layer of $Si_{1-x}Ge_x$ wherein the germanium concentration varied linearly from 12% to 42%. The structure was completed by adding a $\sim$ 0.3 μm thick $Si_{0.65}Ge_{0.35}$ active layer to the structure. Samples SiGe 774 and SiGe 775 were grown at 750 °C. All samples were grown in the [001] direction. The total sample thickness in all three cases was $\sim$ 535 μm.

A combination of grazing incidence diffraction topography (see Chapter 7) and total external reflection topography was used to image the strain within the samples. From the analysis of Chpater 5 it is known that for a given wavelength of radiation λ incident upon a sample, the critical angle can be calculated using

$$\alpha_c = \lambda\sqrt{\frac{r_e F_0}{\pi V}} \tag{12.4}$$

where r_e is the classical electron radius, F_0 is the structure factor for the incident beam and V is the volume of the unit cell. For 19 keV photons (λ = 0.6526 Å) incident on a silicon sample this results in $\alpha_c \approx 0.12°$. Accordingly, the angle of incidence was varied from $\alpha_o = 0.05°$ (total external reflection) to $\alpha_o = 10°$ (deeper penetration depths) in the experiment. The stepping motors used to drive the goniometer on which the sample was mounted possessed step sizes of 0.1 μm for the x-, y- and z-axis motions. The goniometer was capable of providing full revolutions of the sample about the y-axis with a precision of 0.01°. The Bragg pattern of topographs were recorded on Kodak SO-343 and SO-181 high resolution professional X-ray films. The distance from the sample to film was 70 mm.

Atomic force microscopy images were obtained for the three samples using a Top-Metrix TMX2000 Discoverer scanning probe microscope. Nominal scans speeds were 50 μm/s for sample SiGe 720 and 100 μm/s for samples SiGe 774 and SiGe 775. The images were used to evaluate the average roughness and root mean square of the surface roughness. Back reflection section topography was used to obtain sectional information about the strain in the upper regions of the system. The sample to film distance in this geometry was 40 mm.

12.3 Results

Previous studies of these samples demonstrated that the $Si_{1-x}Ge_x$ virtual substrates had relaxed from misfit strain at the heterointerface. As a result, a well-defined cross-hatch pattern, with ridges running along two perpendicular <011> directions on the surface (001) plane was observed using Nomarski differential interference contrast microscopy and transmission electron microscopy [195].

Three sets of figures were obtained using the grazing incidence diffraction and total external reflection topography techniques. Figures 12.1–12.3 were taken in the reflection domain at an incidence angle $\alpha_o = 0.05°$. Figures 12.10–12.12 and 12.13–12.15 were recorded in the grazing incidence geometry with incidence angles $\alpha_o = 1.0°$ and $\alpha_o = 10°$, respectively. A scale bar appropriate to each image is shown in Figure 12.1.

Figures 12.1–12.3 are 115 total external reflection topographs, wherein the incidence angle $\alpha_o = 0.05°$ is smaller than the critical angle $\alpha_c = 0.12°$. Accordingly equation 12.1 yielded a scattering depth $\Lambda = 1.29$ Å. Surprisingly there are no clear images of

the misfit dislocations as one would have expected based on the previous results [195]. However, each image possesses a "bumpy" structure, which is presumably related to the underlying misfit dislocations. It has been observed that, for some strained epitaxial systems, the surface layer develops roughness or waviness, correlated spatially with the positions of the underlying misfit dislocations, which partially relax the elastic mismatch strain [196–198]. For example, Fitzgerald *et al.* [198] noted the presence of ridges on the surface of a strained layer InGaAs/GaAs system, which correlated in position with misfit dislocations at the strained layer-substrate interface. In the total external reflection topographs depicted in Figures 12.1–12.3 it is most likely that the strain fields due to this type of waviness are now being imaged.

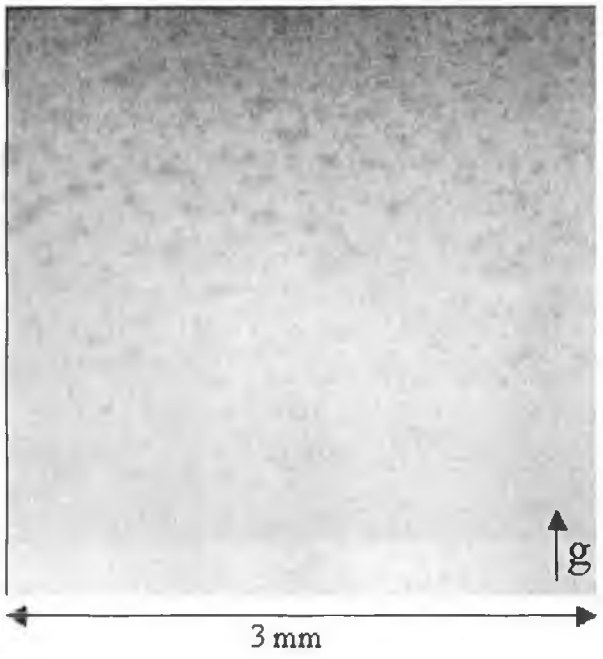

Figure 12.1: 115 total external reflection topograph for sample SiGe 720. Incidence angle $\alpha_o = 0.05°$. Scattering depth $\Lambda = 1.29$ Å.

Figure 12.2: 115 total external reflection topograph for sample SiGe 774. Incidence angle $\alpha_o = 0.05°$. Scattering depth $\Lambda = 1.29$ Å.

Figure 12.3: 115 total external reflection topograph for sample SiGe 775. Incidence angle $\alpha_o = 0.05°$. Scattering depth $\Lambda = 1.29$ Å

Figures 12.4–12.6 display the corresponding three dimensional atomic force microscopy images for these samples. The strain induced surface waviness is easily observed in each image, with the surface bumps running along the direction of the <011> family of misfit dislocations. From the AFM analysis, the following root mean square values of surface roughness were obtained: (a) Sample SiGe 720 – ca. 70 nm; (b) Sample SiGe 774 – ca. 7 nm; (c) Sample SiGe 775 – ca. 20 nm. These results are consistent with the fact that sample SiGe 720 was grown at the highest temperature and presents a high density of misfit dislocation pile-ups extending well into the layer of constant germanium concentration at the top, thus creating higher strain fields at the surface. This also accounts for the lower observed roughness in samples SiGe 774 and SiGe 775 since these were grown at lower temperatures. On the larger scale of the total external reflection topography images, no apparent reduction in surface strain or bumpiness is observed. Since the lateral limit in geometrical resolution for the current experimental setup at beamline F-1 at HASYLAB am DESY is approximately 4 μm, the total external reflection topography technique is not capable of resolving the small-scale structure necessary to observe this reduction in surface roughness.

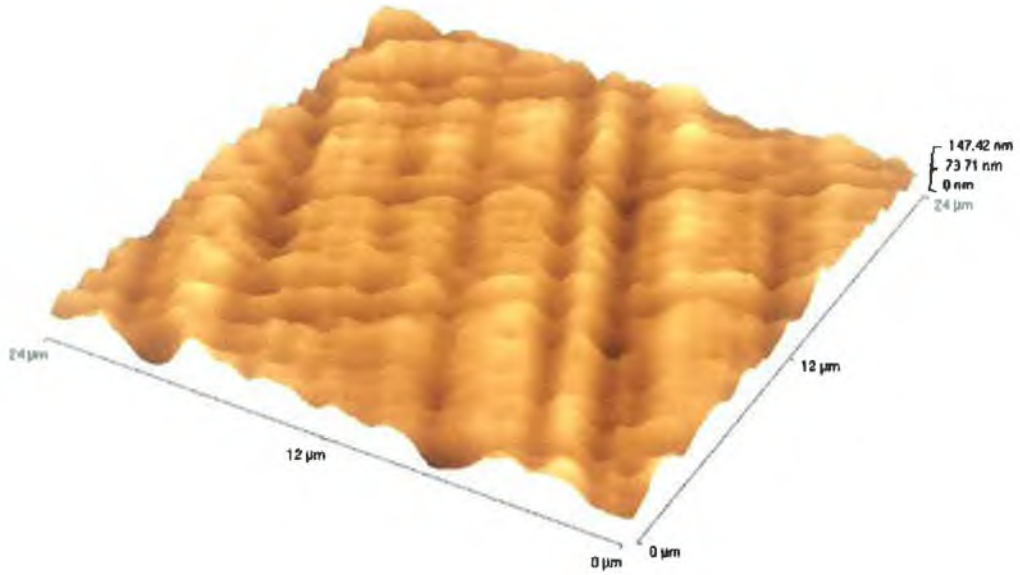

Figure 12.4: 3-D atomic force microscopy image of sample SiGe 720.

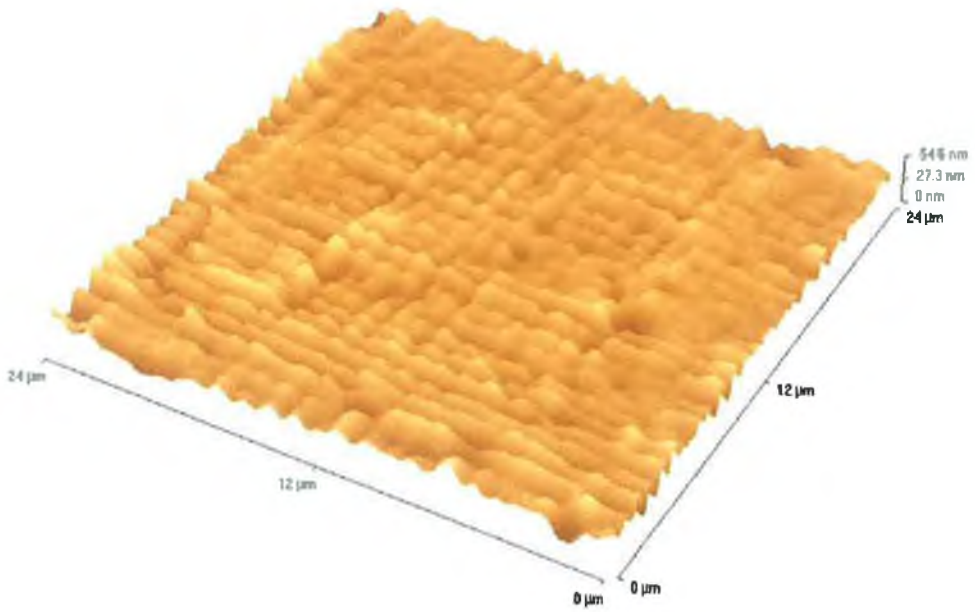

Figure 12.5: 3-D atomic force microscopy image of sample SiGe 774.

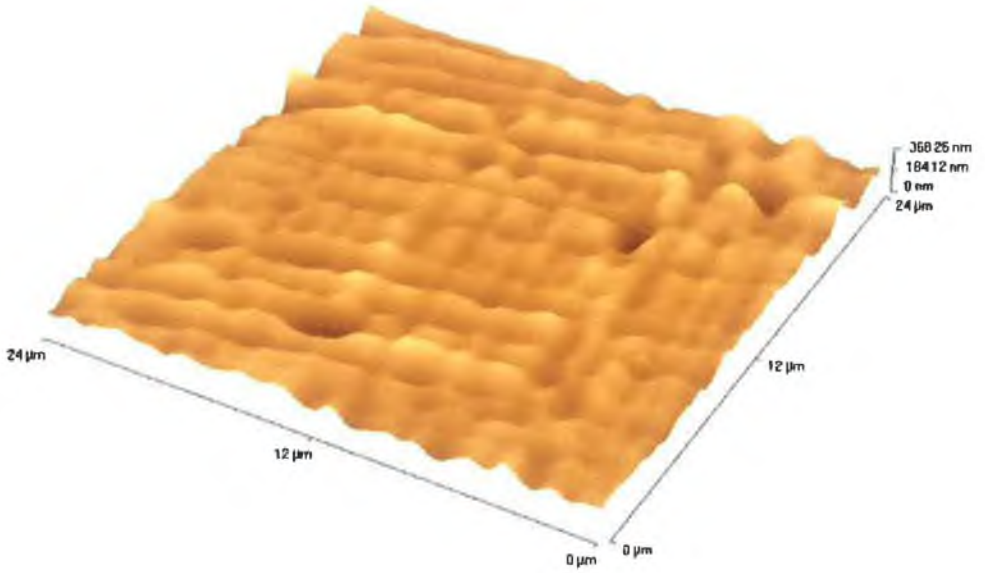

Figure 12.6: 3-D atomic force microscopy image of sample SiGe 775.

The strain induced surface waviness was also imaged using back reflection section topography. The topographs of Figures 12.7–12.9 capture details of the strain/defects from the top surface through to the backside, producing an image of a slice right through the crystal. The severe strain inhomogeneity present near the surface manifests itself through long range "looped" strain features (indicated by arrow Q in the images) that propagate to penetration depths of the order of 100 μm into the substrate. In the centre of all three topographs, there is a reduction in definition of the strain (arrows C). This would seem to suggest that the localised strain fields may be attributable to an inhomogenous lateral variation in the germanium concentration. However, further experiments will be required to test this hypothesis.

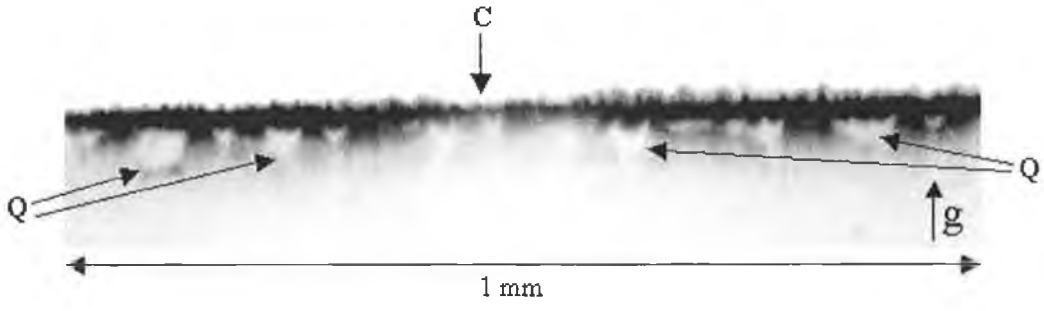

Figure 12.7: 103 back reflection section topograph for sample SiGe 720.

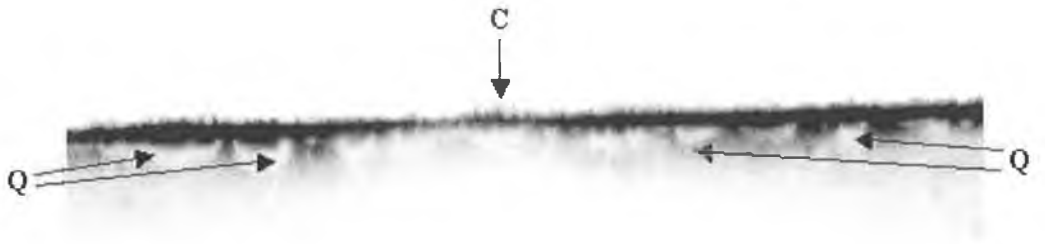

Figure 12.8: 103 back reflection section topograph for sample SiGe 774.

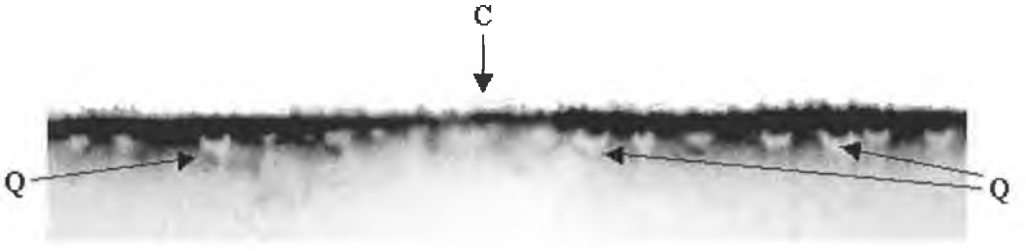

Figure 12.9: 103 back reflection section topograph for sample SiGe 775.

The fact that the images of Figures 12.1–12.3 are indeed surface images (i.e. $\Lambda < 10$ Å) is confirmed by the fact that the images of these wavy structures disappear in the grazing incidence topographs where the penetration depths are much larger. One can observe this in the series of topographs shown in Figures 12.10–12.12. Nominal penetration depths $t_p = 0.27$ μm were obtained for these 115 reflections with radiation incident at $\alpha = 1.0°$. The cross-hatched array of misfit dislocations is clearly seen, running parallel to the <011> directions, and the surface structure has almost completely disappeared.

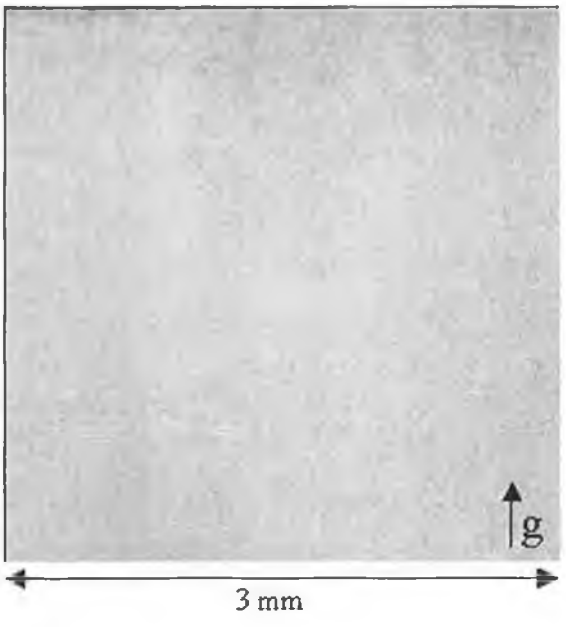

Figure 12.10: 115 grazing incidence diffraction topograph for sample SiGe 720. Incidence angle $\alpha_o = 1.0°$. Penetration depth $t_p = 0.27$ μm.

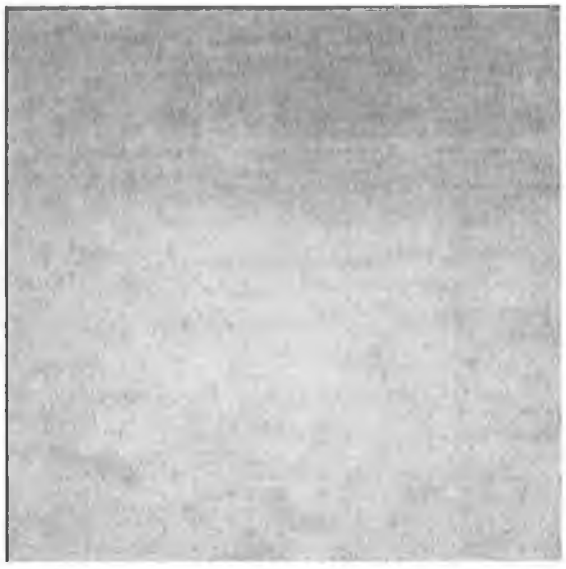

Figure 12.11: 115 grazing incidence diffraction topograph for sample SiGe 774. Incidence angle $\alpha_o = 1.0°$. Penetration depth $t_p = 0.27$ μm.

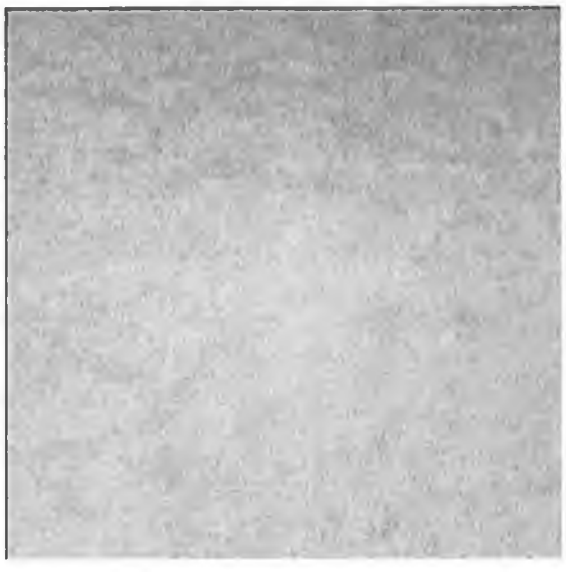

Figure 12.12: 115 grazing incidence diffraction topograph for sample SiGe 775. Incidence angle $\alpha_o = 1.0°$. Penetration depth $t_p = 0.27$ μm.

The misfit dislocation arrays are even more prominent in Figures 12.13–12.15 (all 117 reflections with $\alpha_o = 10°$), wherein $t_p = 21.6\ \mu$m. At these penetration depths the recorded intensity from the wavy surface features, though still present, does not make up the largest contribution to the image, since a far greater underlying volume of sample is also diffracting.

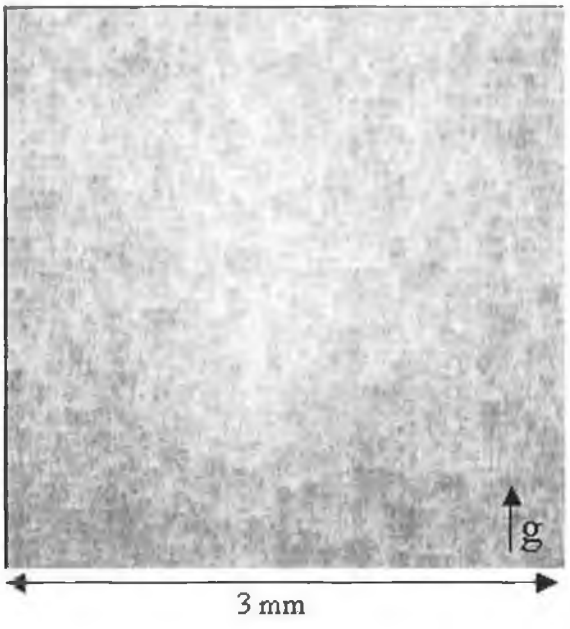

Figure 12.13: 117 grazing incidence diffraction topograph for sample SiGe 720. Incidence angle $\alpha_o = 10°$. Penetration depth $t_p = 21.6\ \mu$m.

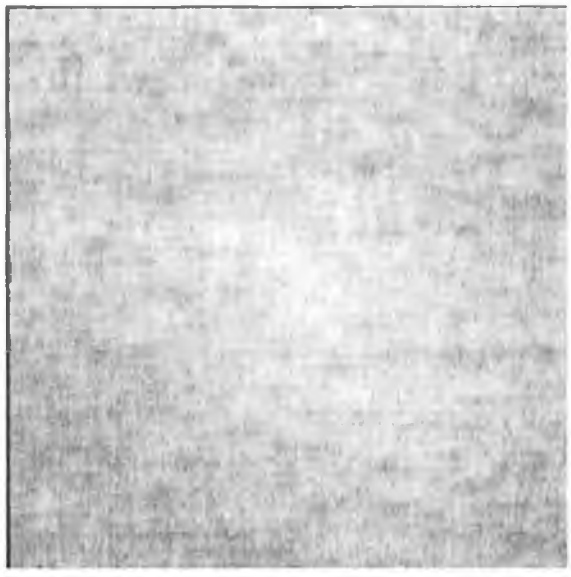

Figure 12.14: 117 grazing incidence diffraction topograph for sample SiGe 774. Incidence angle $\alpha_o = 10°$. Penetration depth $t_p = 21.6$ μm.

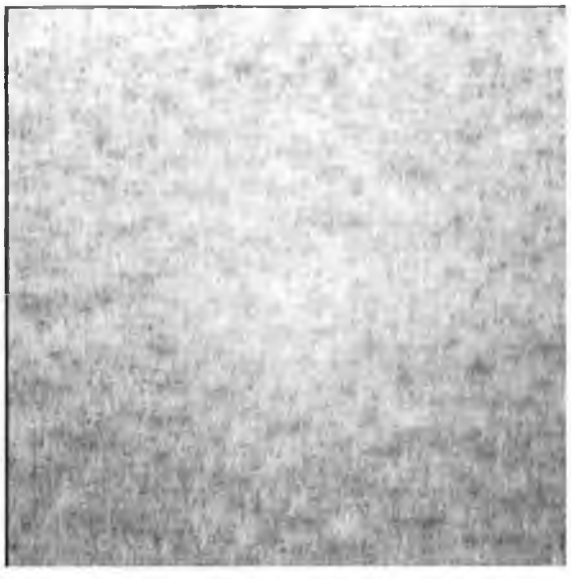

Figure 12.15: 117 grazing incidence diffraction topograph for sample SiGe 775. Incidence angle $\alpha_o = 10°$. Penetration depth $t_p = 21.6$ μm.

12.4 Conclusions

Synchrotron X-ray topography in total external reflection and grazing incidence diffraction modes has been used to observe strain induced surface waviness and bumps in a silicon–silicon germanium heterostructure, whose origin most likely is associated with the existence of misfit dislocations at the heterointerface. For a number of reflections, the impinging X-rays approached the sample at angles less than the critical angle yielding information on strain features no more than nominally 10 Å from the sample surface. These features displayed a remarkable resemblance to the surface bumpiness observed by atomic force microscopy, albeit on a much larger lateral length scale. The strain induced surface waviness was also evident in the back reflection section topographs. Stress originating at the heterointerface was seen to induce large strain fields that propagated into the silicon substrate. The fact that total external reflection topographic mode images were taken was confirmed by the observation of clear and conventional grazing incidence topographic images of misfit dislocations in all samples when the incidence angle became greater than the critical angle.

Chapter 13

Microdefects in Nearly Perfect Silicon

13.1 Introduction

Extremely pure and perfect silicon single crystals are needed for an accurate determination of the Avogadro constant and a redefinition of the unit of mass, the kilogramme. The lattice parameter, impurity content, isotropic composition and self-point defect concentration of silicon crystals grown by the float-zone technique are constant within a relative uncertainty of a few parts in 10^{-7}. However, to replace the present kilogramme artifact by the mass of a certain number of silicon atoms requires, within a relative uncertainty of a few parts in 10^{-8}, the knowledge of the total number of silicon atoms in a certain crystal volume [199].

To date, investigations have been ongoing in an attempt to reduce this relative uncertainty level. Evidence suggestive of absent material has been obtained by the use of X-ray diffraction topography with synchrotron radiation [200, 201]. In an experiment at the National Synchrotron Light Source (NSLS) in Brookhaven, the incident beam was monochromatized to 8 keV using a double crystal monochromator composed of two asymmetrically cut silicon (111) crystals. The sample investigated was prepared

at the National Institute of Standards and Technology (NIST), USA from a silicon crystal grown at Shin-Etsu Handotai Co., Japan. This material was used for the Avogadro project at the National Research Laboratory of Metrology (NRLM), Japan [202]. The topographs of this (110) silicon crystal, having a density approximately 3×10^{-6} smaller than other similar samples, showed clear round topographic images displaying a black-white contrast. It was assumed that the images of these microdefects corresponded to the location of absent material.

In this chapter, the theory of anomalous transmission of X-rays in elastically deformed crystals, developed by Penning and Polder in 1961 [203], will be reformulated in a form that is more amenable to understanding the imaging mechanism of these microdefects in nearly perfect silicon crystals. This theory will then be applied to recent results that have been obtained from both float-zone and Czochralski grown silicon wafers.

13.2 Theory of tie point migration in strained crystals

The salient features of the Penning-Polder theory are as follows. The coupling of energy between the diffracted and forward diffracted beams is characterised through the ratio of the amplitudes of their respective electric fields. Microdefects within the lattice introduce short range strain fields which cause a migration of the tie point characterising each wave at the site of the defect. Consequently, the energy coupling is modified and this manifests itself as a variation in the recorded intensity on the topograph. The strain fields are assumed to be sufficiently small that an Eikonal approximation is still

valid. An expression for the migration of the tie point due to the defect is obtained, and this is used to explain the images of precipitates and voids that will be presented in the results. An important point to note is the diffracted beam is anomalously transmitted through the crystal and therefore only branch one of the dispersion surface is excited. No inter branch scattering is induced by the defect.

13.2.1 Characterisation of plane-waves propagating in a perfect crystal

From Chapter 5 we know that incident photons with wavelength $\lambda = 1/k$ generate under the two-beam approximation, two wavefields within the crystal. The fields associated with the diffracted $\vec{k}_H$ and forward-diffracted $\vec{k}_O$ beams may be described using Equations (5.63) and (5.64) re-iterated here:

$$\left[k^2\left(1+\chi_O\right)-\left(\vec{k}_O\vec{k}_O\right)\right]E_O+k^2C\chi_{\overline{H}}E_H=0 \tag{13.1}$$

$$k^2C\chi_HE_O+\left[k^2\left(1+\chi_O\right)-\left(\vec{k}_H\vec{k}_H\right)\right]E_H=0 \tag{13.2}$$

where χ is the dielectric susceptibility, E the electric field amplitude and C is the polarisation constant.

Defining ζ as the ratio of the diffracted and forward diffracted electric field amplitudes enables us to rearrange equations (13.1) and (13.2) to solve for k^2.

$$k^2=|\vec{k}_O|^2-k^2\chi_O-k^2C\chi_H\zeta \tag{13.3}$$

$$k^2 = |\vec{k}_H|^2 - k^2\chi_O - \frac{k^2 C \chi_H}{\zeta} \tag{13.4}$$

Using equations (13.3) and (13.4) to solve for ζ one obtains:

$$\frac{\zeta^2 - 1}{\zeta} = \frac{1}{k^2\chi_H}\left[|\vec{k}_O|^2 - |\vec{k}_H|^2\right] \tag{13.5}$$

13.2.2 Dispersion relations determining validity of Eikonal theory:

Case I. Perfect crystal

A beam, characterised by wave vector $\vec{k}_O$, arriving at a position $\vec{r}$ in the crystal will propagate further over a distance dl in the direction of the group velocity.

$$d\vec{r} = \frac{1}{|\nabla_{\vec{k}_O}\omega|} dl \nabla_{\vec{k}_O}\omega \tag{13.6}$$

At the new location $\vec{r} + d\vec{r}$, the reciprocal lattice vector $\vec{G}$ will have changed by

$$d\vec{G} = (d\vec{r} \cdot \nabla_{\vec{r}})\,\vec{G}$$

$$d\vec{G} = \frac{1}{|\nabla_{\vec{k}_O}\omega|} dl \left(\nabla_{\vec{k}_O}\omega \cdot \nabla_{\vec{r}}\right)\vec{G} \tag{13.7}$$

For the Eikonal ray theory to be valid $d\omega = 0$. This implies that there is no spreading out of the $\vec{k}$-values in $\vec{k}$-space and a given mode remains on the same branch of the

dispersion surface. This is valid if the following condition is satisfied:

$$d\vec{k}_O \cdot \nabla_{\vec{k}_O}\omega + d\vec{G} \cdot \nabla_{\vec{G}}\omega = 0 \tag{13.8}$$

Substitution of equation (13.7) into (13.8) yields

$$d\vec{k}_O = -\frac{1}{|\nabla_{\vec{k}_O}\omega|} dl \nabla_{\vec{r}} \left(\vec{G} \cdot \nabla_{\vec{G}}\omega\right) \tag{13.9}$$

Equation (13.9) describes the allowable change in $\vec{k}_O$ such that the Eikonal approximation remains valid. Similar analysis yields the following expression for the diffracted beam $\vec{k_H}$.

$$d\vec{k}_H = -\frac{1}{|\nabla_{\vec{k}_H}\omega|} dl \nabla_{\vec{r}} \left(\vec{G} \cdot \nabla_{\vec{G}}\omega\right) \tag{13.10}$$

13.2.3 Dispersion relations determining validity of Eikonal theory: Case II. Strained crystal

In a perfect crystal with reciprocal lattice vector $\vec{h}$ and real space vector $\vec{R}$ Bragg's Law implies

$$\vec{R} \cdot \vec{h} = 2m\pi \qquad m \in \mathbb{Z}$$

A lattice deformation can be introduced through a locally varying vector $\vec{u}$. Consequently a position $\vec{r}$ in the strained crystal may be defined as

$$\vec{r} = \vec{R} + \vec{u}$$

Bragg's Law will now be satisfied for the case

$$\vec{r} \cdot \vec{h} - \vec{u} \cdot \vec{h} = 2m\pi$$

Consequently, the reciprocal lattice vector describing this strained lattice may be written as

$$\vec{G} = \vec{h} - \nabla_{\vec{r}} \left(\vec{u} \cdot \vec{h} \right) \tag{13.11}$$

Assuming ω is constant with respect to $\vec{r}$

$$\Rightarrow \vec{h} \cdot \nabla_{\vec{G}} \omega = 0 \tag{13.12}$$

Substituting equation (13.11) into equation (13.9) and using the result of equation (13.12) yields

$$d\vec{k}_O = \frac{1}{|\nabla_{\vec{k}_O} \omega|} dl \nabla_{\vec{r}} \left(\nabla_{\vec{G}} \omega \cdot \nabla_{\vec{r}} \right) \left(\vec{u} \cdot \vec{h} \right) \tag{13.13}$$

Substitution of equation (13.11) into equation (13.7) yields

$$d\vec{G} = \frac{1}{|\nabla_{\vec{k}_O} \omega|} dl \left(\nabla_{\vec{k}_O} \omega \cdot \nabla_{\vec{r}} \right) \left[\vec{h} - \nabla_{\vec{r}} \left(\vec{u} \cdot \vec{h} \right) \right]$$

and using the result of equation (13.12)

$$\Rightarrow d\vec{G} = -\frac{1}{|\nabla_{\vec{k}_O} \omega|} dl \nabla_{\vec{r}} \left(\nabla_{\vec{k}_O} \omega \cdot \nabla_{\vec{r}} \right) \left(\vec{u} \cdot \vec{h} \right) \tag{13.14}$$

13.2.4 Migration of tie point due to strain

To see how the tie point moves under the influence of strain, we differentiate equation (13.5) with respect to ζ and apply the formulae derived in the previous subsection to ensure the Eikonal approximation remains valid.

$$\frac{1}{k^2\chi_H}\frac{d}{d\zeta}\left[|\vec{k}_O|^2 - |\vec{k}_H|^2\right] = \frac{d}{d\zeta}\frac{\zeta^2-1}{\zeta} \tag{13.15}$$

We can differentiate the right hand side using the quotient rule

$$\frac{d}{d\zeta}\frac{\zeta^2-1}{\zeta} = \frac{\zeta^2+1}{\zeta} \tag{13.16}$$

For diffraction to occur

$$\vec{k}_H = \vec{k}_O - \vec{G}$$

$$\Rightarrow d\vec{k}_H = d\vec{k}_O - d\vec{G}$$

Solving the left hand side of equation (13.15)

$$\begin{aligned}
\frac{d}{d\zeta}\left[|\vec{k}_O|^2 - |\vec{k}_H|^2\right] &= 2\vec{k}_O\frac{d\vec{k}_O}{d\zeta} - 2\vec{k}_H\frac{d\vec{k}_H}{d\zeta} \\
&= 2\vec{k}_O\frac{d\vec{k}_O}{d\zeta} - 2\vec{k}_H\left(\frac{d\vec{k}_H}{d\zeta} - \frac{d\vec{G}}{d\zeta}\right) \\
&= 2\vec{k}_O\frac{d\vec{k}_O}{d\zeta} - 2\vec{k}_H\frac{d\vec{k}_O}{d\zeta} + 2\vec{k}_H\frac{d\vec{G}}{d\zeta} \\
&= \frac{1}{d\zeta}\left[2\left(\vec{k}_O - \vec{k}_H\right)d\vec{k}_O + 2\vec{k}_H d\vec{G}\right] \\
&= \frac{1}{d\zeta}\left[2\vec{G}\cdot d\vec{k}_O + 2\vec{k}_H\cdot d\vec{G}\right]
\end{aligned}$$

$$\Rightarrow \frac{1}{k^2\chi_H}\frac{d}{d\zeta}\left[|\vec{k}_O|^2 - |\vec{k}_H|^2\right] = \frac{1}{k^2\chi_H}\frac{2}{d\zeta}\left[\vec{G}\cdot d\vec{k}_H + \vec{k}_H \cdot d\vec{G}\right] \tag{13.17}$$

Inserting the results of equations (13.16) and (13.17) into equation (13.15) yields

$$d\zeta = \frac{2}{k^2\chi_H}\frac{\zeta}{\zeta^2+1}\left[\vec{G}\cdot d\vec{k}_H + \vec{k}_H \cdot d\vec{G}\right] \tag{13.18}$$

To elucidate the effect of strain on the migration of the tie points substitute equations (13.14) and (13.13) into equation (13.18)

$$d\zeta = \frac{2}{k^2\chi_H}\frac{\zeta}{\zeta^2+1}\frac{dl}{|\nabla_{\vec{k}_O}\omega|}\left[\vec{G}\nabla_{\vec{r}}\left(\nabla_{\vec{G}}\omega\cdot\nabla_{\vec{r}}\right)\left(\vec{u}\cdot\vec{h}\right) - \vec{k}_H\nabla_{\vec{r}}\left(\nabla_{\vec{k}_O}\omega\cdot\nabla_{\vec{r}}\right)\left(\vec{u}\cdot\vec{h}\right)\right] \tag{13.19}$$

Two particular cases of stress within the sample are worth mentioning at this point. The first, the case of no stress implies $\vec{u} = 0$ and therefore $d\zeta = 0$ as one would expect. The second case, where the strain is perpendicular to the diffracting planes $\vec{u}\cdot\vec{h} = 0$, also does not alter the character of the mode.

13.2.5 Image formation

Consider the presence of a void introducing tensile stress within the lattice as indicated in Figure 13.1. The crystal is sufficiently thick such that anomalous transmission occurs. Therefore, only wavefields associated with the first branch of the dispersion surface close to the exact Bragg condition are present and the energy flow is parallel to the lattice planes. As the beam passes the void, $d\zeta$ will change from positive to negative on one side, whilst the converse will take place on the opposite side of the void i.e.

the branch one wavefields follow the curvature of the lattice. Thus tie point migration is in opposite sense on either side of the void. Close to the exact Bragg condition the angular amplification A, defined as the ratio of the angular divergence of the wavefields inside the crystal to the angular divergence of the incident wave-packet, is extremely large. Hence very small lattice distortions give rise to appreciable changes in the direction of energy flow. In the centre of the reflection domain the angular amplification is at a maximum [204].

$$A_{\max} = \frac{\pi V}{2d_{hkl}^2 r_e |C| \sqrt{F_H F_{\overline{H}}}} \tag{13.20}$$

where V is the volume of the unit cell, d_{hkl} is the interplanar spacing of the unstrained diffracting planes, r_e is the classical electron radius, C is the polarisation constant and F is the structure factor. $A_{\max}$ possesses values upwards of 10^4 for most reflections in silicon. It is also known from Chapter 5 Equation (5.81) that the anomalous absorption coefficient in the case of a symmetric reflection has the following dependence on the real part of the deviation parameter η_R

$$\mu_j = \mu_0 \left[1 \mp \frac{|C| \Im\mathrm{m}(\chi_H)/\Im\mathrm{m}(\chi_O) \cos\psi}{\sqrt{1+\eta_r^2}} \right] \tag{13.21}$$

where μ_0 is the linear absorption coefficient and ψ is the phase difference between the real and imaginary parts of the dielectric susceptibility for the given reflection. The upper sign corresponds to branch one and the lower sign to branch two of the dispersion surface. Consequently, any deviation from the Bragg angle induced by a lattice distortion, will lead through the angular amplification, to a significant increase

in the absorption coefficient associated with the corresponding wavefield. Therefore the deflected rays are absorbed and there is a loss in intensity from both sides of the defect. Hence the long-range image of a void within the crystal bulk appears as a white image in the transmission topograph.

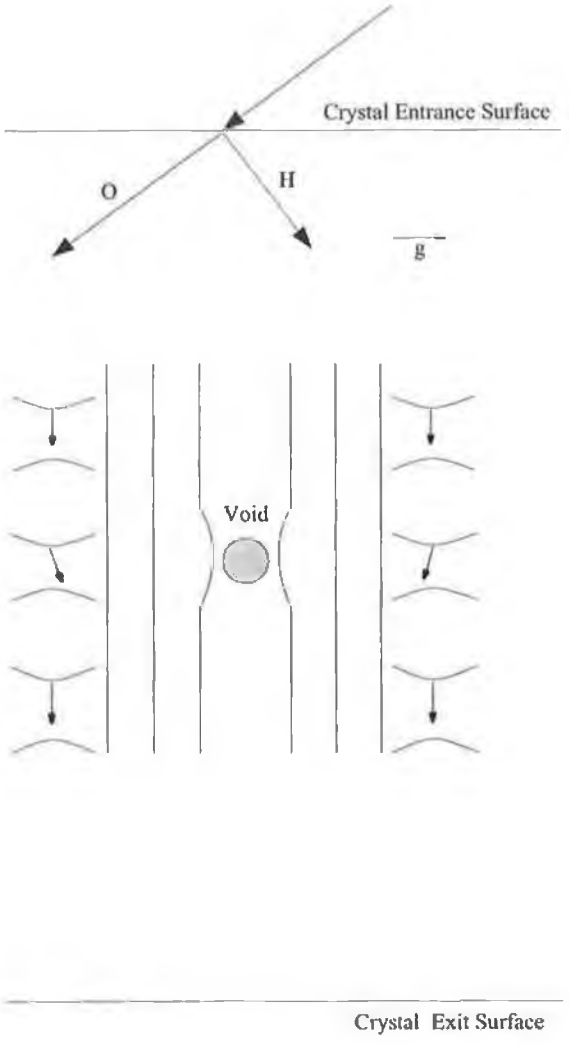

Figure 13.1: Image formation due to void within crystal bulk in transmission geometry.

Conversely, a precipitate within the bulk of the crystal would also give rise to a similar

white image. Therefore, when white defects manifest themselves in the topographs it is not possible to state categorically whether they are accreditable to the presence of voids or precipitates within the crystal bulk.

Consider now the case of a void located near the exit surface of the crystal as illustrated in Figure 13.2. On the left-hand side of the void, the tie point moves toward the void, producing greater diffracted intensity ($d\zeta > 0$ and $\zeta \to \infty$) at the exit surface. However, on the right-hand side of the void, the tie point also moves towards the void, but in this case it produces a reduced diffracted intensity ($d\zeta < 0$ and $\zeta \to 0$) at the exit surface. The image of the void in this situation will consist of two contrasting components, one black on the negative of the diffraction vector $\vec{g}$, the other white on the positive side of the same $\vec{g}$ vector. As the defect is close to the surface, the lattice planes rotate rapidly and thus the Eikonal approximation breaks down as Equation (13.8) is no longer satisfied. Consequently, the X-rays exit the crystal without further diffraction.

It is worth mentioning that the black-white contrast reverses if the lattice around the defect is compressed. Such images have been found and they have been interpreted as dynamical images of precipitates near the exit surface of a rare earth vanadate [205]. It is also worth mentioning that the dynamical black-white image contrast of nearly screw dislocations in potassium dihydrogen phosphate has been explained using ray theory [206].

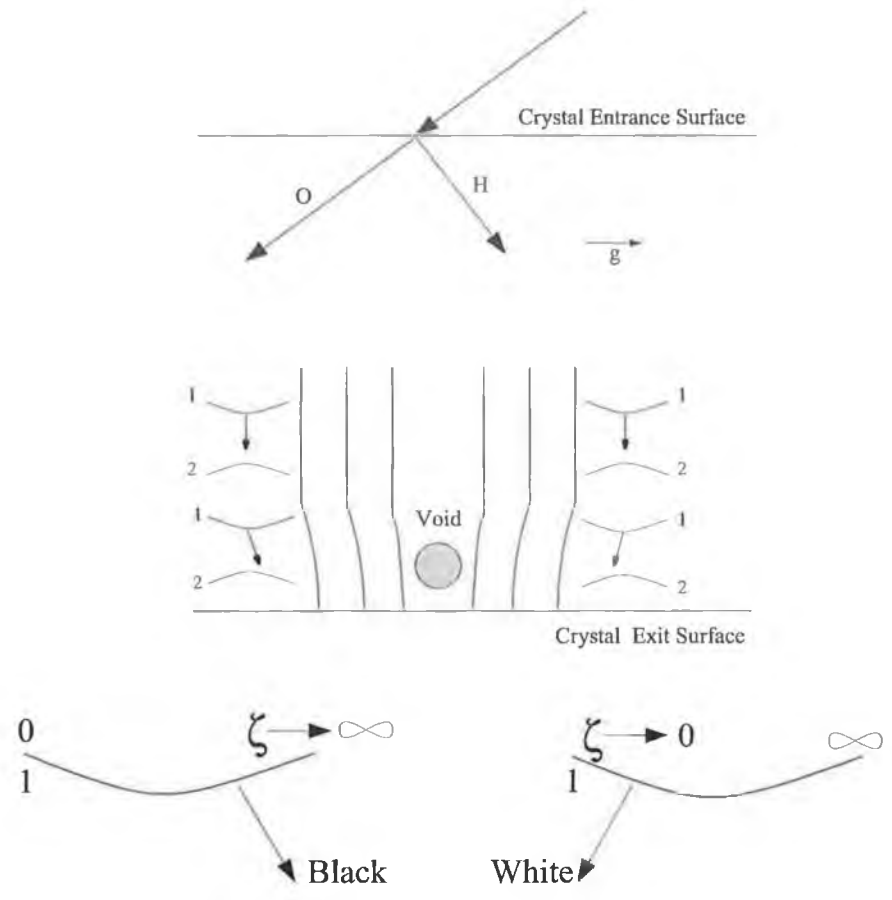

Figure 13.2: Image formation due to void near exit surface of crystal in transmission geometry.

13.3 Experimental

Two sets of experiments pertaining to this work will be discussed in this chapter. The first, which gave a null result, was performed at the bending magnet beamline F-1 at HASYLAB am DESY. In this experiment, the sample referred to in the introduction and henceforth known as sample FZ-NIST, was a 0.5 mm thick (110) silicon crystal grown by the float-zone technique. The sample was inserted into the beam in the large area transmission geometry as described in Chapter 7. The sample was tilted at 18°

with respect to the incident beam that was collimated to 3 mm in the horizontal plane by 1 mm in the vertical plane. The sample to film distance was 50 mm.

In the second experiment, wherein images of the microdefect voids and precipitates were recorded, the experiment was performed at the undulator beamline BW-1 at HASYLAB am DESY [207]. The undulator spectrum was optimised to the third harmonic at 10.5 keV by adjusting the undulator gap to 15 mm in accordance with Figure 6.4. The beam was further conditioned by reflecting the beam off two flat gold-coated mirrors in a grazing incidence geometry to produce energies smaller than 13 keV. Four samples were investigated: the first, sample FZ-NIST referred to in the last paragraph; the second, a (110) float-zone grown silicon sample produced from the same material as sample FZ-NIST by the Physikalisch-Technische Bundesanstalt, Germany, referred to as sample FZ-PTB; the third, a (100) Czochralski grown sample manufactured by Wacker-Siltronic will be referred to as CZ-Wacker; and the fourth, a (100) Czochralski grown silicon sample manufactured by Okmetic, Finland, will henceforth be called CZ-Okmetic. All samples were approximately 0.5 mm thick. The samples were tilted at 18° to facilitate the recording of the $\{110\}$ set of reflections for the float-zone samples and the 400 reflection for the Czochralski samples. The sample to film distance was 25 mm. The Laue set of section and large area transmission topographs were recorded on Geola VRP-M high resolution holographic film.

13.4 Results and Discussion

The 5 $\bar{1}$ $\bar{3}$ large area transmission topograph shown in Figure 13.3 recorded from the float-zone sample FZ-NIST at the bending magnet beamline did not demonstrate the presence of any void or precipitate like images. Using the values of linear absorption coefficient in [208], a value of $\mu_0 t = 0.36$ was calculated. Therefore, the imaging mechanism may be considered kinematical. The reason for the null result is most likely that either the kinematical image contrast based on primary extinction or the orientational image contrast based on lattice plane curvature without angular amplification is not large enough to be resolved. The sharp black dots in the image are artefacts of the X-ray film; they are not defects in the sample.

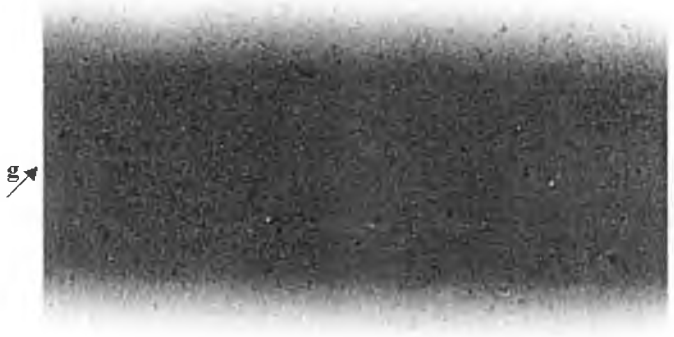

Figure 13.3: 5 $\bar{1}$ $\bar{3}$ large area white beam transmission topograph recorded from (110) float-zone silicon sample FZ-NIST.

Figure 13.4 (a) shows a 1 $\bar{1}$ $\bar{1}$ large-area transmission topograph from sample FZ-NIST and Figure 13.4 (b) its $\bar{1}$ 1 $\bar{1}$ stereo pair topograph enlarged from the same X-ray film. These and the remaining images presented in the remainder of the chapter

were generated at the undulator beamline. Two rather large round images are the most striking features in the topographs. They have a black-white contrast and a diameter about 40 μm. Black corresponds to increased diffraction intensity. The black-white image contrast follows the diffraction vector $\vec{g}$ and is enhanced on the negative side of $\vec{g}$.

Values of $\mu_0 t = 1.9$ were obtained for these topographs, justifying the application of the dynamical theory of X-ray diffraction. The X-rays are anomalously transmitted through the crystal. The anomalous absorption coefficient for each branch of the dispersion surface was calculated using equation (13.21). For branch one of the dispersion surface, $\mu_1 t = 0.58$ and for the second branch $\mu_2 t = 3.3$. The weakly absorbed wavefield pertaining to branch one is transmitted through the crystal and the voids were imaged according to the Penning-Polder explanation of Section 13.2.5. For these reflections the maximum angular amplification was calculated using Equation (13.20) to be 1.5×10^4.

The fact that anomalous transmission occurred and a justification of the application of the dynamical theory, was found simply and elegantly by obtaining a section transmission topograph from the $1\ \bar{1}\ \bar{1}$ reflection for the sample. No Pendellösung fringes can be seen in the topograph of Figure 13.5. This is attributable to the propagation of only one wavefield within the crystal. Therefore no interference (or coupling of energy) is possible between the α and β branches of the dispersion surface. This last point is very important as similar features attributable to the presence of voids have been observed in previous work by Krylova and Shulpina [209,210]. In their experiment a molybdenum

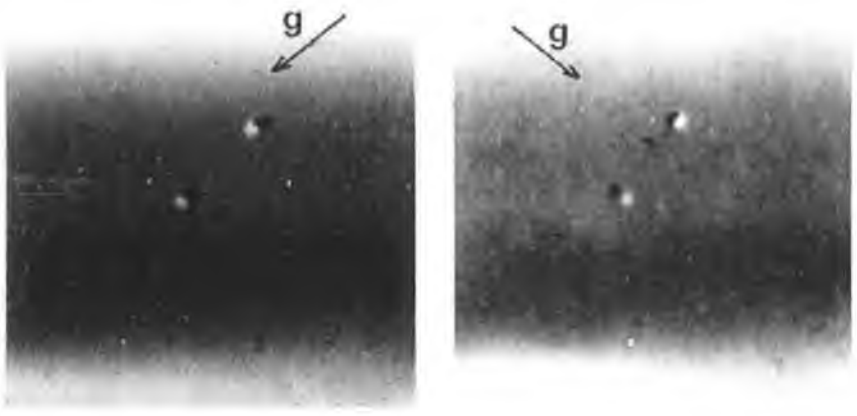

(a) (b)

Figure 13.4: Stereo pair of synchrotron X-ray undulator topographs from nearly perfect (110) silicon single crystal sample FZ-NIST with diffraction vector $\vec{g}$ (a) parallel to 1 $\overline{1}$ $\overline{1}$ and (b) parallel to $\overline{1}$ 1 $\overline{1}$.

Kα_1 radiation source was used with a silicon 444 double crystal monochromator and topographs were recorded from the silicon samples at various points on the rocking curve. Their results demonstrated a change in the contrast from black-white to white-black as they moved across the rocking curve. This was attributable to the change in the absorption coefficient for the two branches of the dispersion surface as the deviation parameter η was varied. The image formation in this case, which relies on two wavefields propagating within the crystal, is completely different from that described in Section 13.2.5.

Voids were also imaged in sample FZ-PTB. Figure 13.6 demonstrates the presence of three large voids in the $\overline{2}$ 2 0 reflection; the largest void possesses a diameter of approximately 60 μm. For this reflection $\mu_0 t = 4.3$. The "hairy" structure present in

Figure 13.5: Section transmission topograph from 1 $\bar{1}$ $\bar{1}$ reflection of sample FZ-NIST. No Pendellösung fringes are seen in the image as only the branch one wavefield propagates within the crystal.

the image is attributable to the beam and not the sample itself.

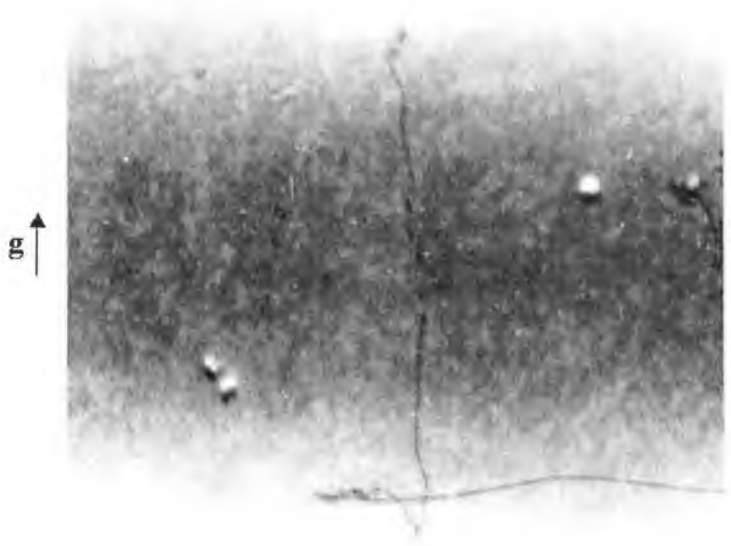

Figure 13.6: $\bar{2}$ 2 0 large area transmission topograph from sample FZ-PTB.

Recent work by Basile and co-workers [199] has revealed that the origin of the voids in the float-zone samples is due to the presence of hydrogen in the growth atmosphere. This was originally speculated by Deslattes *et al.* in their pioneering topographic work with these samples [200]. The samples were made from a polycrystalline silane (SiH_4)

source. During the growth, a significant percentage of the "intrinsic" hydrogen is set free from the source material and is responsible for the void formation in the lattice. These voids have reduced the density of the samples by approximately 3 ppm in comparison to samples that were grown from a trichlorosilane ($SiHCl_3$) source. Thus far, X-ray topography has been the only method capable of imaging the voids. Other techniques such as infrared tomography have failed as the voids are smaller than the limiting resolution of those techniques. Interestingly, Basile *et al.* venture to estimate the size of the voids based upon the "missing" molar volume. Their calculations estimate the size of the nano-holes to be approximately 3 nm^3. If one considers the maximum angular amplification for the $\bar{2}$ 2 0 reflection is $A_{max} = 3.57 \times 10^4$, then one can estimate a lower limit on the size of the lattice distortion which is responsible for the void with a diameter of 60 μm in Figure 13.6 to be approximately 2.5 nm^3. This is in good agreement with the estimation of Basile *et. al.*

A partial pressure of 5 mbar hydrogen in the growth atmosphere is sufficient to induce void formation [199]. Prior to investigation one did not expect to image microdefects of this nature in the Czochralski samples, as a relatively higher partial pressure of 20 mbar is required. However, in the CZ-Wacker sample, the presence of both voids and precipitates were detected. Both the voids and the precipitate shown in Figure 13.7 have a diameter of approximately 10 μm. $A_{max} = 8.54 \times 10^4$ for this 4 0 0 reflection and therefore, the distorted volume that gave rise to these defect images, would be potentially commensurably smaller than those imaged for the float zone samples in Figures 13.4 and 13.6.

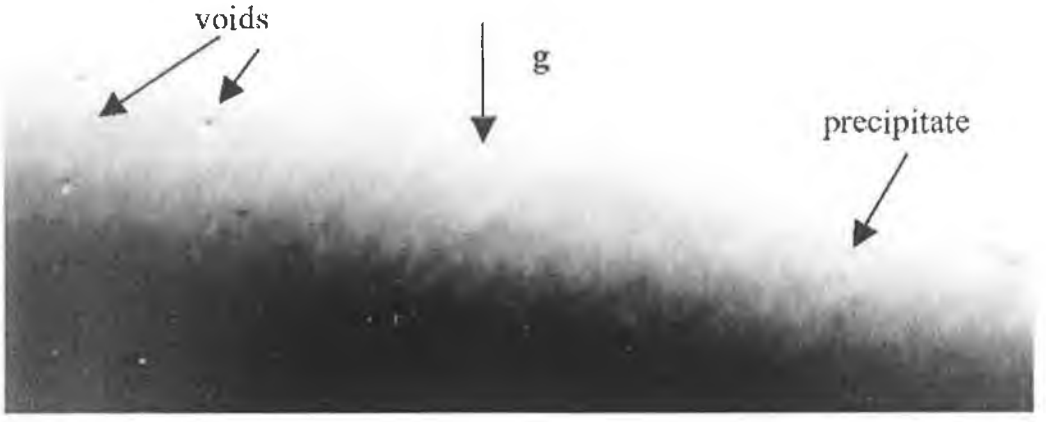

Figure 13.7: 4 0 0 large area transmission topograph from Czochralski sample manufactured by Wacker-Siltronic.

The second Czochralski sample to be studied, that of CZ-Okmetic, demonstrates potentially the presence of microdefects within the bulk of the sample. These are highlighted in the 4 0 0 topograph of Figure 13.8 by the dashed circular lines. These defects, with an average size of 20 μm, should be treated with a certain amount of circumspection as the "hairy" structure associated with the beam used to generate these topographs could be the cause. One should also remember from the discussion of Section 13.2.5 that as defects within the bulk only give rise to a white contrast, it is not possible to state whether the defect images have arisen from voids or precipitates.

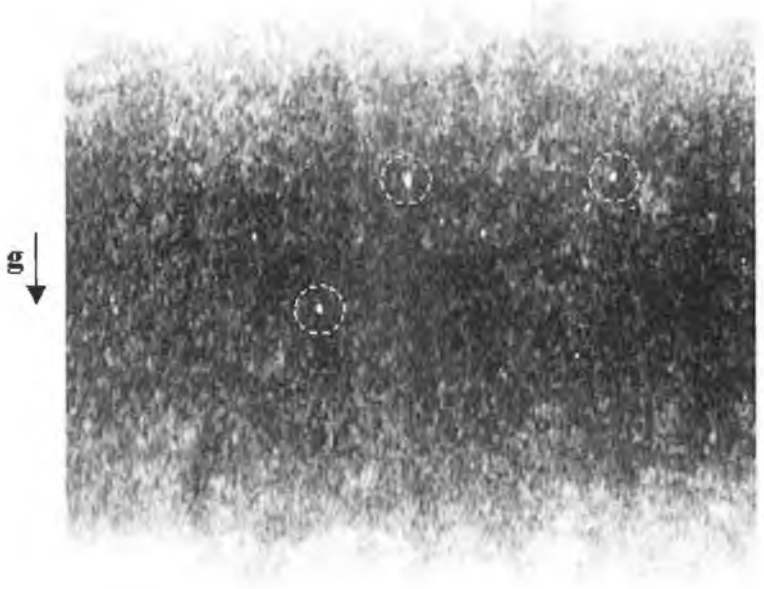

Figure 13.8: 4 0 0 large area transmission topograph from Czochralski sample manufactured by Okmetic.

13.5 Conclusions

X-ray dynamical diffraction has proved to be a useful tool for the imaging of microdefects in ultra-pure silicon crystals. Starting with the fundamental equations describing the wavefields within a crystal, the Penning-Polder theory was re-formulated, and applied qualitatively to describe the diffraction images formed by voids and precipitates in the bulk and the near surface regions of a crystal. Both voids and precipitates have been observed in float-zone and Czochralski grown silicon samples. This chapter contains some of the first images of microdefects of this nature imaged in Czochralski silicon. No other technique to date has successfully imaged these defects.

The interested reader may have pondered the following: why was the Penning-Polder description used in preference to the more popular Takagi theory [17,211]? The answer lies in the formulation of both theories. In Takagi theory, the distortion is represented by a slowly varying dielectric susceptibility in the Bloch function representative of the wavefield propagating in the crystal. By substitution of the equation for the wavefield into the Schrödinger equation one may obtain, in the two-beam case, a set of coupled differential equations describing the evolution of the Bloch waves in the crystal. The concept of the dispersion surface is thus lost in Takagi theory and, in general, no analytical solution exists for all but the most banal situations of lattice distortion. Therefore, with Takagi theory it is not possible to get an easy qualitative description for the diffracted image formation by simple investigation of the differential equations.

The discussion of the previous paragraph becomes important when one considers the

current status of the topographic investigation. The topography results demonstrated a clear correlation between the volume of these defects, as anticipated by the crystal manufacturers, and that measured, when the angular amplification for the associated reflection was taken into consideration. However, two pervasive questions are in the minds of the topographers and crystal growers associated with this work: what is the size of the actual core volume that gives rise to the diffracted image and how many of these defects are there (to account for the density discrepancies)?

One may have thought the first question had already been answered. As the angular amplification is super sensitive to the deviation from the Bragg angle, even the slightest deviation from the diffraction condition will lead to an appreciable change in the size of the void or precipitate imaged on the X-ray film. Therefore, the values for the core of the defects presented in the results should only be treated as estimates. In regard to the second question, which is now compounded by the previous statement, let us presume the following situation: only voids exist within the crystal. Therefore, in principle one only needs to image a specific volume of the crystal and evaluate the number of black-white and white images to ascertain the answer. If the voids are statistically distributed through the crystal, then one would envisage a certain number of white and black-white images would be recorded on the X-ray film. In a recent, as yet unpublished study performed at beamline ID-19 at the ESRF, in which the quality of the beam was superb, only black-white images were recorded. No white images attributable to defects within the crystal bulk were found. This result suggests the following: either no defects exist within the bulk or some alteration to the theoretical

description is necessary.

The answer to these questions, the author believes, is couched in the Penning-Polder and Takagi theories. To accurately determine the size of the defect and rule out the ambiguity associated with the angular amplification, a change in the $\vec{u} \cdot \vec{h}$ term of Equation (13.19) needs to be induced. Experimentally and theoretically, the easiest way of achieving this would be to introduce a large thermal gradient across the sample. Thus by superimposing a new "controllable" strain $\vec{u'}$ on top of $\vec{u}$ one can investigate the tie point migration due to strain in a manner that is independent of the angular amplification. The results of such a study could then be fed into the lattice distortion parameters necessary for a numerical simulation of the Takagi equations. The reward for such an endeavor would yield a virtual experiment that could be used by the crystal growers to further improve the quality of these nearly perfect silicon crystals.

PART III

Conclusions

Chapter 14

Conclusions

In this thesis an exploration of the optoelectronic and structural properties of semiconductor materials and devices has been performed using different parts of the electromagnetic spectrum. In the optical regime, photoacoustic studies of the non-radiative de-excitation processes in silicon, gallium arsenide and gallium nitride were performed. Utilising X-ray radiation with a wavelength comparable to the inter-atomic dimension, white beam diffraction topographs were recorded to elucidate the stress in common crystalline semiconductor materials such as silicon germanium and devices such as ultra-bright light emitting diodes.

The most prevalent theories of the photoacoustic effect in semiconductor materials were reviewed. Using an isobaric adiabatic approximation, one learned from the Rosencwaig Gersho theory that following light absorption heat is generated within the sample, which in turn generates heat in the photoacoustic cell gas column by convective processes. The resulting "thermal piston" induces the acoustic wave within the gas column that can be detected with a microphone. The expression for the pressure variation is dependent upon the thermal diffusion mechanisms, specific heats and densities of the gas, sample and cell backing materials. Using physical insight into the

sample under examination one can simplify the expression for the pressure variation in the gas column. For example, in the case of an optically opaque thermally thin sample such as carbon black or silicon, the pressure variation was shown to be inversely proportional to the chopping frequency and directly proportional to the intensity of the incident light. This was verified experimentally over the frequency range 25 Hz to 350 Hz.

The generalised and extended classical theories of the photoacoustic effect were found to contain particular guidelines for the design of a photoacoustic cell. In particular, high frequency effects such as cellular resonance and thermo-viscous damping, in conjunction with low frequency influences on the photoacoustic signal such as reflected thermal and acoustic waves from the optical window, have to be taken into consideration. A photoacoustic spectrometer was constructed according to these theoretical guidelines for the characterisation of non-radiative de-excitation processes in narrow and wide bandgap semiconductors. In accordance with the predictions of Bandeira, Closs and Ghizoni an increase in the photoacoustic signal amplitude was found due to thermalisation and non-radiative recombination of electrons with sufficient energy to cross the electronic bandgap. The optical absorption spectrum near the intraband transition was evaluated using the normalised photoacoustic amplitude and thermal diffusion length of the sample. Through a knowledge of the optical absorption spectrum in the Urbach region, the bandgap energy was evaluated for silicon, gallium arsenide and gallium nitride. An excellent agreement was found between the measured optical absorption spectrum and bandgap energies with the data in the literature. Thus, the

motivating aims for Part I of the thesis have been fulfilled.

Theoretical modifications of the photoacoustic effect due to structural strain were briefly discussed and the dearth of theories for such mechanisms highlighted. This is an obvious area for exploration, both theoretically and experimentally, in the future. The effect of dislocation density which is related to strain was seen experimentally in what is potentially the first study of the non-radiative de-excitation processes in gallium nitride using photoacoustic spectroscopy. A gallium nitride sample grown by pendeo-epitaxy demonstrated a sharper bandgap transition and larger optical absorption coefficient compared to a standard hetero-epitaxial gallium nitride on sapphire sample. The higher dislocation density in the reference material provided a greater number of non-radiative de-excitation centres. To date very little research has been undertaken in establishing relationships between non-radiative de-excitation processes and structural defect distributions. Thus far, the spectrometer constructed in this thesis has not been used for spatially resolved photoacoustic studies. In the future, such studies will be undertaken and correlated with defect distributions from X-ray topography measurements.

For the future several modifications should be made to the spectrometer to increase its efficiency and range of applicability. At present the signal to noise ratio is so low that spectral averaging and filtering are required to obtain usable data. Therefore, any modifications to the spectrometer must increase the signal to noise ratio. From the theoretical discussions it is known that the photoacoustic effect is directly proportional to the intensity of the incident light. Apparently the most obvious way of increasing the

signal to noise ratio would be to increase the intensity of the arc lamp. However, the intensity of the light reaching the sample is fundamentally dependent on the irradiance of the lamp, which in turn depends on the size of the arc and the power supplied to it. This spectrometer was designed to operate from the infrared to ultraviolet regions of the spectrum and at present, it is quite difficult to acquire a lamp with significantly greater irradiance over this spectral range. Hence an increase in the intensity is not possible.

Returning to the theory of the photoacoustic effect, it is also known that the photoacoustic signal is inversely proportional to the ambient temperature and directly proportional to the thermal conductivity and pressure of the gas. Therefore, the best method of increasing the signal to noise ratio is to re-design the photoacoustic cell. Construction of a low-temperature photoacoustic cell of the gas-microphone type will be complicated by the operating temperature range of the microphone. The microphone will have to be housed in an antechamber at room temperature and the photoacoustic signal transmitted through a capillary tube that isolates regions of the cell operating at different temperatures. Using gases with higher thermal conductivities and pressures will entail nothing more than fitting the cell with entrance and exit gas ports. During the discussion on the design of the photoacoustic cell it was also pointed out that by adding the photoacoustic signal from a number of microphones one can also increase the signal to noise ratio. Given the minute size of the electret microphones used in this thesis it would be quite easy to use an array of twenty microphones thus increasing the signal to noise ratio by a factor of approximately five. A combination of all these

modifications to the photoacoustic cell will significantly enhance the operation of the spectrometer.

Features of the kinematical and dynamical theories of X-ray diffraction applicable to this thesis were reviewed at the start of Part II, as this knowledge is fundamental to an understanding of X-ray diffraction topography. Kinematical theory applies to sufficiently thin samples, i.e. when the thickness of the sample is less than the Pendellösung distance, or to heavily dislocated samples where each scattering centre behaves independently of the rest. For all other situations, dynamical theory must be applied to account for the coupling of energy between the diffracted and forward diffracted X-ray beams inside the crystal. By solving Maxwell's equations under the two beam approximation the concept of the dispersion surface was introduced. The propagation of the allowable wavefield(s) inside the crystal can be described by the appropriate tie-point(s) on the dispersion surface which in turn are selected according to the boundary conditions. Thus, three diffraction scenarios were considered: (i) Laue diffraction, (ii) Bragg diffraction and (iii) total external reflection. Other dynamical effects such as anomalous transmission were examined.

The properties of relativistically charged particles moving in a curved trajectory were examined as a prologue to the techniques of synchrotron X-ray topography. The low divergence, high intensity and small source size of a synchrotron X-ray beam facilitate the production of X-ray topographs with high spatial and geometrical resolution within very short exposure times. The principal transmission, reflection and grazing incidence topographic techniques were reviewed with a focus on their applicability to analysis of

stress in semiconductor materials and devices.

Several detailed topographic investigations were performed. The main results now follow. The failure of ultra-bright light emitting diodes under varying degrees of electrical stress was observed. The increased thermal load caused an increase in strain around the ball bond regions of the devices, as the devices were stressed to the point of near failure. Upon failure large lattice deformations of the original device structure took place. Back reflection section topographs facilitated an estimation of the stress around the ball bond region via misorientational contrast.

Strain at the interface of a gallium nitride epilayer and sapphire substrate was examined using section transmission topography. The quality of epitaxial lateral overgrown (ELO) gallium nitride was shown to be superior to non-ELO material through measurements of local deviations from lattice coherence. Although it was an unrelated study, photoacoustic spectroscopy demonstrated that the pendeo-epitaxy gallium nitride sample possessed fewer non-radiative de-excitation centres in comparison to the reference material. This has been attributed to the reduced dislocation density in the pendeo-epitaxy material. In the future a complete study of the ELO and non-ELO materials will be performed using photoacoustic spectroscopy and the results will be correlated with the current topography data.

Thermal stress and boron induced strain generated during the rapid thermal oxidation and doping of silicon wafers was investigated using X-ray topography and micro-Raman spectroscopy. It was observed that thermal stress increased with processing time until relaxation of the lattice occurred. The measured values of stress were found

to be in close agreement with the theoretical predictions for the oxidised wafers. The doped samples did not agree with the theory as sizable lattice relaxation occurred through slip line and dislocation formation.

The crystal quality of synthetic type Ib diamonds was evaluated using X-ray diffraction rocking curve measurements and back reflection topography. The poor quality of the samples was demonstrated through the rather large rocking curve full width half maximum which was nominally four to five times greater than the Darwin width of the reflection being measured. These findings were supported by the presence of stacking faults and occlusions in the topographic images.

Using grazing incidence diffraction topography and total external reflection topography, strain induced surface waviness in a silicon-silicon germanium heterostructure was observed. The origin of the strain was attributed to the presence of misfit dislocations at the hetero-interface. The results of the topographic investigation were found to be in agreement with data yielded by atomic force microscopy.

In the final study, microdefects in nearly perfect float-zone and Czochralski grown silicon samples were imaged using anomalous transmission of X-rays. The imaging mechanism was explained qualitatively using the Penning Polder theory. Essentially, the microdefects cause migration of the tie-point characterising the single anomalous wavefield propagating in the crystal. If the defect is present in the crystal bulk, the subsequent deviation from the ideal Bragg condition leads to an increase in the effective absorption coefficient and the wavefield is absorbed; this being recorded as a white image on the X-ray topograph. For voids located near the exit surface of the crystal a

black-white image, which is enhanced on the negative side of the diffraction vector, is observed. This image arises from angular amplification of the X-rays on either side of the defect. On one side of the defect the tie-point migrates causing increased diffracted intensity and the opposite happens on the other side. The defect core size was estimated based on the angular amplification and a close agreement was found with the values suggested by the crystal manufacturers on the basis of missing sample matter. Future directions of investigation were suggested. These consisted of altering the strain field around the microdefects by application of a thermal gradient and simulation of the observed features using the Takagi-Taupin formalism.

These studies have clearly demonstrated that synchrotron X-ray topography is capable of imaging stress and defect distributions in semiconductor materials and devices. Thus the goals of Part II of this thesis have been reached.

Looking at the long-term focus of the research of which this thesis is a part, i.e. to determine the interrelationship between non-radiative de-excitation processes and structural defects in semiconductor materials, one can clearly see that the techniques of photoacoustic spectroscopy and X-ray topography are particularly suited to this task. It is envisaged that whilst data from these techniques will provide its own insight into the physical mechanisms, it will also support findings from more conventional experimental methods such as deep level transient spectroscopy, photoluminescence, Raman spectroscopy and transmission electron microscopy. The cumulative knowledge gained from these investigations will surely serve to enhance our understanding of the structural and optoelectronic properties of semiconductor materials and devices.

Bibliography

[1] V. Bakshi, D. Youngson, and R. Goodall, "300 mm moves into the next century," *Semiconductor International*, vol. 22, no. 8, pp. 92–98, 1999.

[2] A. Tam, "Applications of photoacoustic sensing techniques," *Review of Modern Physics*, vol. 58, no. 2, pp. 381–431, 1986.

[3] H. Winick and S. Doniach, eds., *Synchrotron Radiation Research*, ch. 18, pp. 607–638. Plenum Press, 1980.

[4] A. Rosencwaig, *History of photoacoustics*, ch. 2, pp. 7–14. John Wiley & Sons, 1980.

[5] A. Parker, "Optical absorption in glass: Investigation using an acoustic technique," *Applied Optics*, vol. 12, no. 12, pp. 2974–2977, 1973.

[6] A. Rosencwaig and A. Gersho, "Theory of the photoacoustic effect with solids," *Journal of Applied Physics*, vol. 47, no. 1, pp. 64–69, 1976.

[7] F. McDonald and G. Wetsel, "Generalized theory of the photoacoustic effect," *Journal of Applied Physics*, vol. 49, no. 4, pp. 2313–2322, 1978.

[8] P. Korpiun and B. Buchner, "On the thermodynamics of the photacoustic effect of condensed matter on gas cells," *Applied Physics B*, vol. 30, pp. 121–129, 1983.

[9] P. Korpiun, B. Buchner, A. Tam, and Y. Wong, "Effect of coupling gas viscosity on the photoacoustic signal," *Applied Physics Letters*, vol. 46, no. 11, pp. 1039–1041, 1985.

[10] I. Bandeira, H. Closs, and C. Ghizoni, "Study of the photoacoustic effect in semiconductors. Effect of an applied DC- electric field.," *Journal of Photoacoustics*, vol. 1, no. 2, pp. 275–290, 1982.

[11] W. Röntgen, "On a new kind of rays," *Nature*, vol. 53, p. 274, 1896. Translated by Stanton, A.

[12] D. Bowen and B. Tanner, *High Resolution X-ray Diffractometry and Topography*, ch. 1, pp. 1–2. Taylor & Francis, 1998.

[13] C. Darwin, "The theory of X-ray reflexion," *Philosophical Magazine*, vol. 27, pp. 315–333, 1914.

[14] C. Darwin, "The theory of X-ray reflexion. Part II.," *Philosophical Magazine*, vol. 27, pp. 675–690, 1914.

[15] D. Cruickshank, H. Juretschke, and N. Kato, eds., *P.P. Ewald and his Dynamical Theory of X-ray Diffraction*, ch. 1, pp. 3–23. Oxford University Press, 1992.

[16] A. Authier, *Dynamical Theory of X-ray Diffraction*, ch. 1,3, pp. 1–32,43–62. Plenum Press, 1996.

[17] S. Takagi, "A dynamical theory of diffraction for a distorted crystal," *Journal of the Physical Society of Japan*, vol. 26, no. 5, pp. 1239–1253, 1969.

[18] N. Kato, "Dynamical diffraction theory of waves in distorted crystals. I. General formulation and treatment for perfect crystals," *Acta Crystallographica*, vol. A16, pp. 276–290, 1963.

[19] J. Härtwig, "Hierarchy of dynamical theories of x-ray diffraction for deformed and perfect crystals," *Journal of Physics D: Applied Physics*, vol. 34, no. 10A, pp. A70–A77, 2001.

[20] A. Lang, "The early days of high-resolution x-ray topography," *Journal of Physics D: Applied Physics*, vol. 26, no. 4A, pp. A1–A8, 1993.

[21] W. Berg, "Uber eine rontgengraphishce methode zur unterschung von gitterstorung in kristallen," *Naturwissenschaften*, vol. 19, p. 391, 1931.

[22] A. Lang, *Techniques and interpretation in X-ray topography*, pp. 623–713. Diffraction and Imaging Techniques in Materials Science, North-Holland Publishing Company, 1978.

[23] U. Bonse and H. Klapper, "Rontgengraphische abbildung des verzerrungsfeldes einzelner versetzungen in germanium-einkristallen," *Zeitug für Naturforschein Teil A*, vol. 13, p. 348, 1958.

[24] T. Tuomi, N. Naukkarinen, and P. Rabe, "Use of synchrotron radiation in x-ray diffraction topography," *Physica Status Solidi (a)*, vol. 25, pp. 93–106, 1974.

[25] M. Hart, "Synchrotron radiation – its application to high-speed, high-resolution x-ray diffraction topography," *Journal of Applied Crystallography*, vol. 8, pp. 436–444, 1975.

[26] L. Kreuzer, "Ultralow gas concentration infrared absorption spectroscopy," *Journal of Applied Physics*, vol. 42, no. 7, pp. 2934–2943, 1971.

[27] A. Rosencwaig, "Theoretical aspects of photoacoustic spectroscopy," *Journal of Applied Physics*, vol. 49, no. 5, pp. 2905–2910, 1978.

[28] A. Rosencwaig, "Photo-acoustic spectroscopy of solids," *Review of Scientific Instruments*, vol. 48, no. 9, pp. 1133–1137, 1977.

[29] P. Korpiun and B. Buchner, "Photoacoustic signal in gas-microphone cells for all thermal lengths below acoustic resonance," *Journal De Physique*, vol. 44, no. 10, pp. C6–85–C6–89, 1983.

[30] L. Kinsler and A. Frey, *Fundamentals of Acoustics*, ch. 9, pp. 237–242. John Wiley & Sons, 1962.

[31] L. Miranda, "Theory of the photoacoustic effect in semiconductors influence of carrier diffusion and recombination," *Applied Optics*, vol. 21, no. 16, pp. 2923 - 2928, 1982.

[32] V. Sablikov and V. Sandomirskii, "Theory of the photoacoustic effect in semiconductors," *Soviet Physics of Semiconductors*, vol. 17, no. 1, pp. 51–53, 1983.

[33] A. Vasil'ev and V. Sandomirskii, "Photoacoustic effect in semiconductors subjected to an alternating electric field," *Soviet Physics of Semiconductors*, vol. 18, no. 11, pp. 1221–1223, 1984.

[34] A. Vasil'ev and V. Sandomirskii, "Photoacoustic effects in finite semiconductors," *Soviet Physics of Semiconductors*, vol. 18, no. 10, pp. 1095–1099, 1984.

[35] V. Sablikov and V. Sandomirskii, "The photoacoustic effect in semiconductors," *Physica Status Solidi (b)*, vol. 120, pp. 471–480, 1983.

[36] P. Poulet, J. Chambron, and R. Unterreiner, "Quantitative photoacoustic spectroscopy applied to thermally thick samples," *Journal of Applied Physics*, vol. 51, no. 3, pp. 1738–1742, 1980.

[37] J. Fesquet, B. Girault, and M. Razafindrandriatsimaniry, "Determination of absorption coefficients of thick semiconductor samples using photoacoustic spectroscopy," *Applied Optics*, vol. 23, no. 16, pp. 2784–2787, 1984.

[38] J. Pankove, *Optical Processing in Semiconductors*. Dover, 1975.

[39] A. Zegadi, M. Slifkin, M. Djamin, R. Tomlinson, and H. Neumann, "Photoacoustic spectroscopy of defect states in $CuInSe_2$ single crystals," *Solid State Communications*, vol. 83, no. 8, pp. 587–591, 1992.

[40] T. Toyoda and K. Shinoyama, "Photoacoustic spectroscopy of Cu impurities in ceramic ZnS," *Japanese Journal of Applied Physics*, vol. 36, no. 5B, pp. 3300–3302, 1997.

[41] T. Ikari, A. Fukuyama, and Y. Akashi, "Investigation of deep levels in semi-insulating GaAs by means of a thermally activated piezoelectric photoacoustic measurements," *Materials Science in Semiconductor Processing*, vol. 4, pp. 253–255, 2001.

[42] D. Todorović, P. Nikolić, A. Bojićić, and K. Radulović, "Thermoelastic and electronic strain contributions to the frequency transmission photoacoustic effect in semiconductors," *Physical Review B*, vol. 55, no. 23, pp. 15631–15642, 1997.

[43] D. Todorović, P. Nikolić, and A. Bojićić, "Photoacoustic frequency transmission technique: Electronic deformation mechanism in semiconductors," *Journal of Applied Physics*, vol. 85, no. 11, pp. 7716–7726, 1999.

[44] K. Muratikov, A. Glazov, D. Rose, and J. Dumar, "Photoacoustic effect in stress elastic solids," *Journal of Applied Physics*, vol. 88, no. 5, pp. 2948–2955, 2000.

[45] R. Muller and T. Kamins, *Device electronics for integrated circuits*, ch. 1, p. 56. John Wiley & Sons, 1986.

[46] A. Zegadi, M. Slifkin, and R. Tomlinson, "A photoacoustic spectrometer for measuring subgap absorption spectra of semiconductors," *Review of Scientific Instruments*, vol. 65, no. 7, pp. 2238–2243, 1994.

[47] A. Zegadi, *Photoacoustic study of $CuInSe_2$ single crystals*. PhD thesis, Department of Electronic and Electrical Engineering, University of Salford, England, 1993.

[48] D. Cahen, E. Lerner, and A. Auerbach, "Simple setup for single and differential photoacoustic spectroscopy," *Review of Scientific Instruments*, vol. 49, no. 8, pp. 1206–1209, 1978.

[49] R. Gray, V. Fishman, and A. Bard, "Simple sample cell for examination of solids and liquids by photoacoustic spectroscopy," *Analytical Chemistry*, vol. 69, no. 6, pp. 697–700, 1997.

[50] W. Ferrell and Y. Haven, "High-performance cell for photoacoustic spectroscopy," *Applied Physics*, vol. 48, no. 9, pp. 3984–3985, 1977.

[51] J. McClelland and R. Kniseley, "Scattered light effects in photoacoustic spectroscopy," *Applied Optics*, vol. 15, no. 12, pp. 2967–2968, 1976.

[52] T. Diószeghy, "Photoacoustic response of condenser microphones," *Journal of Applied Physics*, vol. 61, no. 1, pp. 449–450, 1987.

[53] I. Calasso and M. Sigrist, "Selection criteria for microphones used in pulsed nonresonant gas-phase photoacoustics," *Review of Scientific Instruments*, vol. 70, no. 12, pp. 4569–4578, 1999.

[54] Knowles Electronics, "FG Series Data Sheet," 1998.

[55] H. Bennett and R. Forman, "Photacoustic methods for measuring surface and bulk absorption coefficients in highly transparent materials: theory of a gas cell," *Applied Optics*, vol. 15, no. 10, pp. 2405–2413, 1976.

[56] Oriel Instruments, "The Book of Photon Tools," 1999.

[57] H. Young and R. Freedman, *University Physics*, ch. 35, pp. 1085–1117. Addison Wesley, 9 ed., 1996.

[58] E. Hecht and A. Zajac, *Optics*, ch. 5–6, pp. 99–195. Addison Wesley, 1979.

[59] J. Murphy and L. Aamodt, "The photothermophone, a device for absolute calibration of photoacoustic spectrometers," *Applied Physics Letters*, vol. 31, no. 11, pp. 728–729, 1977.

[60] Stanford Research Systems, "SR830 DSP Lock-in Amplifier Operational Manual," 1998.

[61] Stanford Research Systems, "Scientific and engineering instruments," 1998.

[62] Stanford Research Systems, "SR550 Voltage Pre-Amplifier Data Sheet," 1993.

[63] National Instruments, "The Measurement and Automation Catalog 2000," 2000.

[64] National Instruments, "LabView Users Manual," 1998.

[65] W. Press, S. Teukolsky, W. Vetterling, and B. Flannery, eds., *Numerical Recipes in C*, ch. 14, pp. 650–655. Cambridge University Press, 1992.

[66] J. Murphy and L. Aamodt, "The photothermophone, a device for absolute calibration of photoacoustic spectrometers," *Applied Physics Letters*, vol. 31, no. 11, pp. 728–730, 1977.

[67] G. Jellison and F. Modine, "Optical absorption of silicon between 1.6 and 4.7 eV at elevated temperatures," *Applied Physics Letters*, vol. 41, no. 2, pp. 180–182, 1982.

[68] G. Macfarlane, T. McLean, J. Quarrington, and V. Roberts *Journal of Physics and Chemistry of Solids*, vol. 8, pp. 388–392, 1959.

[69] S. Sze, *Physics of Semiconductor Devices*. John Wiley & Sons, 1981.

[70] A. Fukuyama, Y. Morooka, Y. Akashi, K. Yoshino, K. Maeda, and T. Ikari, "Effect of the carbon acceptor concentration on the photoquenching and following enhancement of the photoacoustic signals in semi-insulating GaAs," *Journal of Applied Physics*, vol. 81, no. 11, pp. 7567–7574, 1997.

[71] A. Fukuyama, A. Memon, K. Sakai, Y. Akashi, and T. Ikari, "Investigation of deep levels in semi-insulating GaAs by means of the temperature change piezoelectric photo-thermal measurements," *Journal of Applied Physics*, vol. 89, no. 3, pp. 1751–1754, 2001.

[72] T. Ikari, K. Miyazaki, A. Fukuyama, H. Yokoyama, K. Maeda, and K. Futagami, "Piezoelectric detection of the photoacoustic signals of n-type GaAs single crystals," *Journal of Applied Physics*, vol. 71, no. 5, pp. 2408–2413, 1992.

[73] M. Sturge, "Optical absorption of gallium arsenide between 0.6 eV and 2.75 eV," *Physical Review*, vol. 127, no. 3, pp. 768–773, 1962.

[74] H. Casey, D. Sell, and W. Wecht, "Concentration dependence of the absorption coefficient for n- and p- type GaAs between 1.3 eV and 1.6 eV," *Journal of Applied Physics*, vol. 46, no. 1, pp. 250–257, 1975.

[75] O. Ambacher, "Growth and applications of Group III-nitrides," *Journal of Physics D: Applied Physics*, vol. 31, pp. 2653–2710, 1998.

[76] R. Davis, T. Gehrke, K. Linthicum, P. Rajagopal, A. Roskowski, T. Zheleva, E. Preble, C. Zorman, M. Mehregany, U. Schwarz, J. Schuck, and R. Grober, "Review of pendeo-epitaxial growth and characterisation of thin films of GaN and AlGaN alloys of 6H-SiC(0001) and Si(111) substrates," *Materials Research Society Internet Journal of Nitride Semiconductor Research*, vol. 6, no. 14, 2001.

[77] P. McNally, T. Tuomi, D. Lowney, K. Jacobs, A. Danilewsky, R. Rantamäki, M. O'Hare, and L. Considine, "Epitaxial lateral overgrowth of GaN on sapphire – An examination of epitaxy quality using synchrotron X-ray topography," *Physica Status Solidi (a)*, vol. 185, no. 2, pp. 373–382, 2001.

[78] K. Linthicum, T. Gehrke, D. Thomson, E. Carlson, P. Rajagopal, T. Smith, D. Batchelor, and R. Davis, "Pendeoepitaxy of gallium nitride thin films," *Applied Physics Letters*, vol. 75, no. 2, pp. 196–198, 1999.

[79] R. Davis, T. Gehrke, K. Linthicum, T. Zheleva, E. Preble, P. Rajagopal, C. Zorman, and M. Mehregany, "Pendeo-epitaxial growth of thin films of gallium nitride and related materials and their characterization," *Journal of Crystal Growth*, vol. 225, no. 2–4, pp. 134–140, 2001.

[80] A. Hoffmann, L. Eckey, M. Maxim, J. Holst, T. Heitz, D. Hofmann, D. Kovalev, G. Stevde, D. Volm, and B. Meyer, "Dynamical study of the yellow luminescence band in GaN," *Solid State Electronics*, vol. 41, no. 2, pp. 275–278, 1997.

[81] H. Marchand, N. Zhang, L. Zhao, Y. Golan, S. Rosner, G. Girolami, P. Fini, J. Ibbetson, S. Keller, S. DenBaars, J. Speck, and U. Mishra, "Structural and optical properties of GaN laterally overgrown on Si(111) by metalorganic chemical vapor deposition using an AlN buffer layer," *Materials Research Society Internet Journal of Nitride Semiconductor Research*, vol. 4, no. 2, 2001.

[82] T. Sugahara, H. Sato, M. Hao, Y. Naoi, S. Kurai, S. Tottori, K. Yamashita, K. Nishino, L. Romano, and S. Sakai, "Direct evidence that dislocations are

non-radiative recombination centers in GaN," *Japanese Journal of Applied Physics*, vol. 37, no. 4A, pp. L398–L400, 1998.

[83] K. Lee and K. Auh, "Dislocation density of GaN grown by hydride vapor phase epitaxy," *Materials Research Society Internet Journal of Nitride Semiconductor Research*, vol. 6, no. 9, 2001.

[84] T. Miyajima, T. Tojyo, T. Asano, K. Yanashima, S. Kijima, T. Hino, M. Takeya, S. Uchida, S. Tomiya, K. Funato, T. Asatsuma, T. Kobayashi, and M. Ikeda, "GaN-based blue laser diodes," *Journal of Physics: Condensed Matter*, vol. 13, no. 32, pp. 7099–7114, 2001.

[85] O. Ambacher, W. Rieger, P. Ansmann, H. Angerer, T. Moustakas, and M. Stulzman, "Sub-bandgap absorption of gallium nitride determined by photothermal deflection spectroscopy," *Solid State Communications*, vol. 97, no. 5, pp. 365–370, 1996.

[86] J. Muth, J. Lee, I. Shmagin, R. Kolbas, H. Casey, B. Keller, U. Mishra, and S. DenBaars, "Absorption coefficient, energy gap, exciton binding energy, and recombination lifetime of GaN obtained from transmission measurements," *Applied Physics Letters*, vol. 71, no. 18, pp. 2572–2574, 1997.

[87] S. Mohammad, A. Salvador, and H. Morkoc, "Emerging gallium nitride based devices," *Proceedings of the IEEE*, vol. 83, no. 10, pp. 1306–1355, 1955.

[88] P. Ewald, "Zur Begründung der Kristalloptik. III. Röntgenstrahlen," *Annalen der Physik*, vol. 54, pp. 519–597, 1917.

[89] M. Laue, "Die dynamische Theorie der Röntgenstrahlinterferenzen in neuer Form," *Naturwissen*, vol. 10, pp. 133–158, 1931.

[90] W. Zachariasen, *Theory of X-ray diffraction in crystals*, ch. III, pp. 82–155. Dover, 1945.

[91] L. Azároff, R. Kaplow, N. Kato, R. Weiss, A. Wilson, and R. Young, eds., *X-Ray Diffraction*. McGraw-Hill, 1974.

[92] B. Batterman and H. Cole, "Dynamical diffraction of X-rays by perfect crystals," *Reviews of Modern Physics*, vol. 36, no. 3, pp. 681–717, 1964.

[93] A. Authier, S. Lagomarsino, and B. Tanner, eds., *X-Ray and Neutron Dynamical Diffraction: Theory and Applications*, vol. 357 of *NATO ASI Series*, ch. 1, pp. 1–32. Plenum, 1996.

[94] A. Authier, "Dynamical theory of X-ray diffraction: Plane wave case," in *International Summer School on X-ray Dynamical Theory and Topography*, (Limoges, France), pp. A1–A24, August 1975.

[95] A. Authier, *Dynamical Theory of X-Ray Diffraction*. Oxford Science Publications, 2001.

[96] J. Sutter, *Applications of special X-ray diffraction cases in silicon crystals*. PhD thesis, Department of Physics, Purdue University, West Lafayette, Indiana, U.S.A., 2000.

[97] J. Jackson, *Classical Electrodynamics*, ch. 9, pp. 407–413. John Wiley & Sons, Inc., 1999.

[98] H. Dosch, B. Batterman, and D. Wack, "Depth-controlled grazing-incidence diffraction of synchrotron X radiation," *Physical Review Letters*, vol. 56, no. 11, pp. 1144–1147, 1986.

[99] J. Sutter, E. Alp, M. Hu, P. Lee, H. Sinn, W. Sturhahn, T. Toellner, G. Bortel, and R. Colella, "Multiple-beam x-ray diffraction near exact backscatterig in silicon," *Physical Review B*, vol. 63, no. 9, pp. 094111–1–094111–12, 2001.

[100] J. Watson and F. Crick, "Molecular structure of nucleic acids," *Nature*, vol. 171, pp. 737–738, 1953.

[101] R. Haensel and C. Kunz *Z. Angew. Phys.*, vol. 23, p. 276, 1967.

[102] J. Jackson, *Classical Electrodynamics*, ch. 14, pp. 661–707. John Wiley & Sons, Inc., 1999.

[103] H. Winick and S. Doniach, eds., *Synchrotron Radiation Research*, ch. 2, pp. 11–25. Plenum Press, 1980.

[104] H. Winick, *Synchrotron Radiation Sources: A Primer*. World Scientific Publishing Co., 1995.

[105] J. Schwinger, "On the classical radiation of accelerated electrons," *Physical Review*, vol. 75, no. 12, pp. 1912–1925, 1949.

[106] B. Martin and G. Shaw, eds., *Particle Physics*, ch. 3, pp. 49–51. Wiley, 1992.

[107] R. Whatmore, P. Goddard, B. Tanner, and G. Clark, "Direct imaging of travelling Rayleigh waves by stroboscopic X-ray topography," *Nature*, vol. 299, pp. 44–46, 1982.

[108] L. Emery and M. Borland, "Top-up operation experience at the Advanced Photon Source," in *Proceedings of the 1999 Particle Accelerator Conference* (A. Luccio and W. MacKay, eds.), vol. 1, pp. 200–202, IEEE, 1999.

[109] D. Bowen and B. Tanner, *High Resolution X-ray Diffractometry and Topography*, ch. 2, pp. 15–16. Taylor & Francis, 1998.

[110] C. Rose-Petruck, R. Jimenez, T. Guo, A. Cavalleri, C. Siders, F. Ráksi, J. Squier, B. Walker, K. Wilson, and C. Barty, "Picosecond-milliångström lattice dynamics measured by ultrafast X-ray diffraction," *Nature*, vol. 398, pp. 310–312, 1999.

[111] D. Riley, N. Woolsey, D. McSherry, I. Weaver, A. Djaoui, and E. Nardi, "X-ray diffraction from a dense plasma," *Physical Review Letters*, vol. 84, no. 8, pp. 1704–1707, 2000.

[112] H. Wiedemann, "Design of low emittance storage rings," *Nuclear Instruments and Methods in Physics Research A*, vol. 246, pp. 4–11, 1986.

[113] "Executive summary," in *TESLA: The Superconducting Electron-Positron Linear Collider with an Integrated X-Ray Laser Laboratory. Technical Design Report* (F. Richard, J. Schneider, D. Trines, and A. Wagner, eds.), vol. 5, Deutsches Elektronen-Synchrotron, March 2001.

[114] M. Sanchez del Rio and R. Dejus, "XOP: Recent developments," *Proceedings of SPIE*, vol. 3448, pp. 340–345, 1998.

[115] P. Iinksi, R. Dejus, E. Gluskun, and T. Morrison, "Practical aspects of undulator radiation properties," *Proceedings of SPIE*, vol. 2856, pp. 15–25, 1996.

[116] J. Pflüger and M. Tischer, "Undulator systems for the TESLA X-FEL," *Nuclear Instruments and Methods in Physics Research A*, vol. in press, 2002.

[117] J. Lewellen *et al.*, "Present status and recent results from the APS SASE FEL," *Nuclear Instruments and Methods in Physics Research A*, vol. in press, 2002.

[118] W. Brefeld *et al.*, "Development of a femtosecond X-ray SASE FEL at DESY," *Nuclear Instruments and Methods in Physics Research A*, vol. in press, 2002.

[119] "The X-Ray Free Electron Laser," in *TESLA: The Superconducting Electron-Positron Linear Collider with an Integrated X-Ray Laser Laboratory. Technical Design Report* (G. Materlik and T. Tschentscher, eds.), vol. 5, Deutsches Elektronen-Synchrotron, March 2001.

[120] C. Barrett, "Laue spots from perfect, imperfect, and oscillating crystals," *Physical Review*, vol. 38, no. 4, pp. 832–833, 1931.

[121] E. Talik, A. Winiarski, B. Kotur, and W. Suski, "Growth and X-ray characterization of $ScFe_4Al_8$ single crystals," *Crystal Research Technology*, vol. 36, no. 8–10, pp. 1119–1122, 2001.

[122] T. Tuomi, M. Tilli, and O. Anttila, "Detection of defect-free zone in annealed Czochralski silicon with synchrotron section topography," *Journal of Applied Physics*, vol. 57, no. 4, pp. 1384–1386, 1985.

[123] B. Tanner, "X-ray topography and precision diffractometry of semiconducting materials," *Journal of the Electrochemical Society*, vol. 136, no. 11, pp. 3438–3443, 1989.

[124] N. Kato, "Spherical-wave theory of dynamical X-ray diffraction for absorbing perfect crystals. I. The crystal wave fields," *Journal of Applied Physics*, vol. 39, no. 5, pp. 2225–2230, 1968.

[125] N. Kato, "Spherical-wave theory of dynamical X-ray diffraction for absorbing perfect crystals. II. Iintegrated reflection power," *Journal of Applied Physics*, vol. 39, no. 5, pp. 2231–2237, 1968.

[126] J. Partanen and T. Tuomi, "An experimental and theoretical study of Pendellösung fringes in synchrotron section topographs of silicon wafers," *Journal of X-Ray Science and Technology*, vol. 2, no. 3, pp. 165–171, 1990.

[127] R. Rantamäki, T. Tuomi, Z. Zytkiewicz, D. Dobosz, P. McNally, and A. Danilewsky, "Epitaxial lateral overgrowth of gallium arsenide studied by synchrotron topography," in *Epitaxial Growth* (T. Pearsall, A. Barabasi, and G. Maracas, eds.), vol. 570, pp. 181–186, Materials Research Society, 1999.

[128] R. Rantamäki, T. Tuomi, P. McNally, J. Curley, and A. Danilewsky, "Grazing incidence synchrotron x-ray topography as a tool for denuded zone studies of silicon wafers," *Journal of X-Ray Science and Technology*, vol. 8, pp. 159–169, 1998.

[129] P. McNally, G. Dilliway, J. Bonar, A. Willoughby, T. Tuomi, R. Rantamäki, A. Danilewsky, and D. Lowney, "On the use of total reflection x-ray topography for the observation of misfit dislocation strain at the surface of a Si/Ge-Si heterostructure," *Applied Physics Letters*, vol. 77, no. 11, pp. 1644–1646, 2000.

[130] E. Prieur, *Synchrotron Radiation of Semiconductors*. PhD thesis, Optoelectronics Laboratory, Helsinki University of Technology, Finland, 1996.

[131] http://www hasylab.desy.de.

[132] http://www.spring8.co.jp.

[133] F. Vallino, A. Jacques, and A. George, "Non-planar slip and cross-slip at the onset of plastic deformation in silicon," *Physica Status Solidi (b)*, vol. 222, no. 1, pp. 51–62, 2000.

[134] P. McNally, R. Rantamäki, T. Tuomi, A. Danilewsky, D. Lowney, J. Curley, and P. Herbert, "Mapping of mechanical, thermomechanical and wire-bond strain fields in packaged Si integrated circuits using synchrotron white beam X-ray topography," *IEEE Transactions on Components and Packaging Technologies*, vol. 24, no. 1, pp. 76–83, 2001.

[135] H. Klapper, *Progress in Crystal Growth and Characterisation*, vol. 14, pp. 367–401. Oxford, 1987.

[136] M. Fiederle, T. Feltgen, J. Joerger, K. Benz, T. Duffar, P. Dussere, E. Dieguez, J. Launay, and G. Roosen, "Detached growth of CdTe:Zn:V (STS-95): preliminary results," *Proceedings of SPIE*, vol. 3792, pp. 147–153, 1999.

[137] B. Tanner, D. Midgley, and M. Safa, "Dislocation contrast in X-ray synchrotron topographs," *Journal of Applied Crystallography*, vol. 10, pp. 281–286, 1997.

[138] M. Dudley, X. Huang, and W. Huang, "Assessment of orientation and extinction contrast contributions to the direct dislocation image," *Journal of Physics D: Applied Physics*, vol. 32, pp. A139–A144, 1999.

[139] F. Zontone, L. Mancini, R. Barrett, J. Baruchel, J. Härtwig, and Y. Epelboin, "New features of dislocation images in third-generation synchrotron radiation topographs," *Journal of Synchrotron Radiation*, vol. 3, pp. 173–186, 1996.

[140] A. Authier, *Dynamical Theory of X-Ray Diffraction*, pp. 546–549. Oxford Science Publications, 2001.

[141] U. Zeimer, T. Baumbach, J. Grenzer, D. Lubbert, A. Mazuelas, U. Pietsch, and G. Erbert, "In situ characterization of strain distribution in broad-area high-power lasers under operation by high-resolution x-ray diffraction and topography using synchrotron radiation," *Journal of Physics D: Applied Physics*, vol. 32, no. 10A, pp. A123–A127, 1999.

[142] E. Prieur, T. Tuomi, J. Partanen, E. Yli-Juuti, and M. Tilli, "Synchrotron topographic study of defects in liquid-encapsulated Czochralski-grown semi-insulating gallium arsenide wafers," *Journal of Crystal Growth*, vol. 32, pp. 599–605, 1993.

[143] A. Zarka, "X-ray topography," *Scanning Microscopy Supplement*, vol. 7, pp. 221–242, 1993.

[144] P. McNally, J. Curley, M. Bolt, A. Reader, T. Tuomi, R. Rantamäki, A. Danilewsky, and I. Dewolf, "Monitoring of stress reduction in shallow trench isolation CMOS structures via synchrotron X-ray topography, electrical data and Raman spectroscopy," *Journal of Materials Science: Materials in Electronics*, vol. 10, pp. 351–358, 1999.

[145] H. Kalt and M. Rinker, "Band-gap renormalization in semiconductors with multiple inequivalent valleys," *Physical Review B*, vol. 45, no. 3, pp. 1139–1154, 1992.

[146] J. Singh, *Physics of Semiconductors and Their Heterostructures*, ch. 8, pp. 272–273. McGraw-Hill, 1993.

[147] W. Wierzchowski, M. Moore, A. Makepeace, and A. Yacoot, "X-ray topographic studies and measurement of lattice parameter differences with synthetic diamonds grown by the reconstitution technique," *Journal of Crystal Growth*, vol. 114, no. 1–2, pp. 209–227, 1991.

[148] Y. Kato, S. Kitamura, K. Hiramatsu, and N. Sawaki, "Selective growth of wurtzite GaN and $Al_xGa_{1-x}N$ on GaN sapphire substrates by metalorganic vapor-phase epitaxy," *Journal of Crystal Growth*, vol. 144, pp. 133–140, 1994.

[149] D. Kapolnek, S. Keller, R. Ventury, R. Underwood, P. Kozody, S. Den Barrs, and U. Mishra, "Anisotropic epitaxial lateral overgrowth in GaN selective area epitaxy," *Applied Physics Letters*, vol. 71, no. 9, pp. 1204–1206, 1997.

[150] A. Usui, H. Sunkawa, A. Sakai, and A. Yamaguchi, "Thick GaN epitaxial growth with low dislocation density by hydride vapor phase epitaxy," *Japanese Journal of Applied Physics*, vol. 36, no. 7B, pp. L899–L902, 1997.

[151] O. Nam, M. Bremser, T. Zheleva, and R. Davis, "Lateral epitaxy of low defect density GaN layers via organometallic vapor phase epitaxy," *Applied Physics Letters*, vol. 71, no. 18, pp. 2638–2640.

[152] A. Sakai, H. Sunkawa, and A. Usui, "Defect structure in selectively grown GaN films with low threading dislocation density," *Applied Physics Letters*, vol. 71, no. 16, pp. 2259–2261, 1997.

[153] S. Nakamura, M. Senoh, S. Nagahama, N. Iwasa, T. Yamada, T. Matsushita, H. Kiyoku, Y. Sugimoto, T. Kozaki, H. Unemoto, M. Sano, and K. Chocho, "InGaN/GaN/AlGaN – based laser diodes with modulation-doped strained-layer superlattices grown on epitaxially laterally overgrown GaN substrate," *Applied Physics Letters*, vol. 72, no. 2, pp. 211–213, 1998.

[154] S. Nakamura, M. Senoh, S. Nagahama, N. Iwasa, T. Yamada, T. Matsushita, Y. Sugimoto, and H. Kiyohu, "High-power, long-lifetime InGaN multi-quantum-well structure laser diodes," *Japanese Journal of Applied Physics*, vol. 36, no. 8B, pp. L1059–L1061, 1997.

[155] L. Considine, E. Thrush, J. Crawley, K. Jacobs, W. Stricht, I. Moerman, P. Demeester, G. Park, S. Hwang, and J. Song, "Growth and in-situ monitoring of GaN using IR interference effects," *Journal of Crystal Growth*, vol. 195, pp. 195–198, 1998.

[156] D. Bowen and B. Tanner, *High Resolution X-ray Diffractometry and Topography*, ch. 3, pp. 50–68. Taylor & Francis, 1998.

[157] R. Rantamäki, T. Tuomi, Z. Zythiewicz, D. Dobosz, and P. McNally, "Synchrotron x-ray topography analysis of GaAs layers grown on GaAs substrate by liquid phase epitaxial lateral overgrowth," *Journal of Physics D: Applied Physics*, vol. 32, no. 10A, pp. A114–A118, 1998.

[158] K. Kobayashi, A. Yamaguchi, S. Kimura, H. Sunakawa, A. Kimura, and A. Usui, "X-ray rocking curve determination of twist and tilt angles in GaN films grown by an epitaxial-lateral-overgrowth technique," *Japanese Journal of Applied Physics*, vol. 38, no. 6B, pp. L611–L613, 1999.

[159] C. Ferrari, L. Francesio, P. Franzosi, and S. Gennari, "High resolution x-ray diffraction study of the Bragg peak width in highly mismatched III-V heterostructures," *Applied Physics Letters*, vol. 69, no. 27, pp. 1233–1235, 1996.

[160] P. Fini, H. Marchand, J. Ibbetson, S. Den Baars, U. Mishra, and J. Speck, "Determination of tilt in the lateral overgrowth of GaN using x-ray diffraction," *Journal of Crystal Growth*, vol. 209, pp. 581–590, 2000.

[161] M. Moslehi, "Process uniformity and slip dislocation patterns in linearly ramped-temperature transient rapid thermal processing of silicon," *IEEE Transactions on Semiconductor Manufacturing*, vol. 2, no. 4, pp. 130–140, 1989.

[162] R. Perkins, T. Riley, and R. Gyurcsik, "Thermal uniformity and stress minimization during rapid thermal processes," *IEEE Transactions on Semiconductor Manufacturing*, vol. 8, no. 3, pp. 272–279, 1995.

[163] J. Zöllner, G. Eichhorn, V. Cimalla, J. Bozmarov, P. Zaumseil, and H. Kürschner, "Slip generation during rapid thermal processing," *Physica Status Solidi (a)*, vol. 156, pp. 63–70, 1996.

[164] H. Lord, "Thermal and stress analysis of semiconductor wafers in a rapid thermal processing oven," *IEEE Transactions on Semiconductor Manufacturing*, vol. 1, no. 3, pp. 105–114, 1988.

[165] G. Bentini, L. Correra, and C. Donolato, "Defects introduced in silicon wafers during rapid isothermal annealing: Thermoelastic and thermoplastic effects," *Journal of Applied Physics*, vol. 56, no. 10, pp. 2922–2929, 1984.

[166] R. Deaton and H. Massoud, "Effect of thermally induced stresses on the rapid-thermal oxidation of silicon," *Journal of Applied Physics*, vol. 70, no. 7, pp. 3588–3592, 1991.

[167] H. Massoud and J. Plummer, "Analytical relationship for the oxidation of silicon in dry oxygen in the thin-film regime," *Journal of Applied Physics*, vol. 62, no. 8, pp. 3416–3423, 1987.

[168] S. Jimenez-Sandoval, "Micro-Raman spectroscopy: a powerful technique for materials research," *Microelectronics Journal*, vol. 31, pp. 419–427, 2000.

[169] I. DeWolf, "Micro-Raman spectroscopy to study local mechanical stress in silicon integrated circuits," *Semiconductor Science and Technology*, vol. 11, pp. 139–154, 1996.

[170] S. Webster, D. Batchelder, and D. Smith, "Submicron resolution measurement of stress in silicon by near-field raman spectroscopy," *Applied Physics Letters*, vol. 72, no. 12, pp. 1478–1480, 1998.

[171] M. Nolan, T. Perova, R. Moore, C. Moore, K. Berwick, and H. Gamble, "Micro-Raman study of stress distribution generated in silicon during proximity rapid thermal diffusion," *Materials Science & Engineering B*, vol. 73, no. 1-3, pp. 168–172, 2000.

[172] B. Boley and J. Weiner, *Theory of thermal stresses*, p. 290. Wiley, New York, 1960.

[173] W. Schröter, H. Brion, and H. Siethoff, "Yield point and dislocation mobility in silicon and germanium," *Journal of Applied Physics*, vol. 54, no. 4, pp. 1816–1820, 1983.

[174] M. Nolan, *Fabrication of ultra-shallow boron junction using proximity rapid thermal diffusion*. PhD thesis, Electronic & Electrical Engineering, University of Dublin, Trinity College, Dublin 2, Ireland, 2000.

[175] J. Plummer, M. Deal, and P. Griffin, *Silicon VLSI Technology*. Prentice Hall, 2000.

[176] S. Ghandhi, *VLSI Fabrication Principles*, pp. 210–211. John Wiley & Sons, Inc., 1994.

[177] G. Cardona, M. anf Güntherodt, ed., *Light Scattering in Solids II*, p. 19. Springer, Heidelberg, 1982.

[178] N. Kato, "The determination of structure factors by means of Pendellösung fringes," *Acta Crystallographica*, vol. A25, pp. 119–128, 1969.

[179] J. Patel and N. Kato, "X-ray diffraction topographs of silicon crystals with superposed oxide fim. II. Pendellösung fringes: comparison of experiment with theory," *Journal of Applied Physics*, vol. 44, no. 3, pp. 971–977, 1973.

[180] A. Authier, *Dynamical Theory of X-Ray Diffraction*, p. 527. International Union of Crystallography (IUCr), Oxford University Press, 2001.

[181] D. Bowen and B. Tanner, *High resolution X-ray diffractometry and topography*, p. 84. Taylor & Francis, 1998.

[182] H. Franz, E. Gerdau, H. Schulte-Schrepping, and Y. Shvyd'ko, "Prospects of synchrotron Mößbauer experiments at PETRA," *HASYLAB Jahresbericht*, vol. Part 1, pp. 55–58, 1998.

[183] J. Hoszowska, A. Freund, E. Boller, J. Sellschop, G. Level, J. Härtwig, R. Burns, M. Rebak, and J. Baruchel, "Characterization of synthetic diamond crystals by spatially resolved rocking curve measurements," *Journal of Physics D: Applied Physics*, vol. 34, pp. A47–A51, 2001.

[184] A. Authier, *Dynamical Theory of X-Ray Diffraction*, pp. 456–458,572. Oxford Science Publications, 2001.

[185] D. Bowen and B. Tanner, *High Resolution X-ray Diffractometry and Topography*, ch. 3, pp. 58–59. Taylor & Francis, 1998.

[186] G. Kowalski, M. Moore, G. Gledhill, and Z. Marlcic, "Double-crystal diffractometric and topographic studies of (111) oriented synthetic diamonds," *Journal of Physics D: Applied Physics*, vol. 29, pp. 793–800, 1996.

[187] C. Kuo and J. Bilello, "Depth profiling of defects in epilayer semiconductor materials by using synchrotron x-radiation topography," *Journal of Applied Physics*, vol. 62, no. 1, pp. 137–144, 1987.

[188] G. Yao, M. Dudley, and J. Wu, "Synchrotron white beam topographic imaging in grazing Bragg-Laue geometries," *Journal of X-Ray Science and Technology*, vol. 2, pp. 195–213, 1990.

[189] D. Novikov, M. Ohler, R. Köhler, and G. Materlik, "Observation of defects in crystal surface layers by grazing-incidence diffraction x-ray topography," *Journal of Physics D: Applied Physics*, vol. 28, no. 4A, pp. A84–A87, 1995.

[190] M. Dudley, J. Wu, and G. Yao, "Determination of penetration depths and analysis of strains in single crystals by white beam synchrotron x-ray topography in grazing Bragg–Laue geometries," *Nuclear Instruments and Methods in Physics Research B*, vol. 40/41, pp. 388–392, 1989.

[191] A. Afansaev, P. Aleksandrov, R. Imamov, E. Pashaev, and Polovinkina *Physica Status Solidi (a)*, vol. 90, pp. 419–, 1985.

[192] T. Kitano, T. Ishikawa, J. Matsui, K. Akimoto, J. Mizuki, and Y. Kawase, "Synchrotron plane wave X-ray topography of 6 inch diameter Si crystal," *Japanese Journal of Applied Physics*, vol. 26, no. 2, pp. L108–L110, 1987.

[193] R. Imamov, A. Lomov, and D. Novikov, "Grazing incidence diffraction X-ray topography," *Physica Status Solidi (a)*, vol. 115, pp. K133–K134, 1989.

[194] H. Dosch, "Evanescent absorption in kinematic surface Bragg diffraction," *Physical Review B*, vol. 35, no. 5, pp. 2137–2143, 1987.

[195] G. Dilliway, A. Willoughby, and J. Bonar, "Characterisation of morphology and defects in silicon-germanium virtual substrates grown by low pressure chemical vapour deposition," in 3rd *International Conference on Materials for Microelectronics*, pp. 57–60, The Institute of Materials, IOM Communications Ltd., October 2000.

[196] F. LeGoues, B. Meyerson, and J. Morar, "Anomalous strain relaxation in SiGe thin films and superlattices," *Physical Review Letters*, vol. 66, no. 22, pp. 2903–2906, 1991.

[197] F. Jonsdottir, "Three dimensional surface waviness of an epitaxial layer due to surface diffusion induced by interface misfit dislocations," in *Thin Films: Stresses and Mechanical Properties V* (S. Baker, P. Borgesen, P. Townsend, C. Ross, and C. Volkert, eds.), vol. 356, pp. 45–50, Materials Research Society, 1995. ISBN: 155899257X.

[198] E. Fitzgerald, D. Ast, P. Kirchner, G. Pettit, and J. Woodall, "Structure and recombination in InGaAs/GaAs heterostructures," *Journal of Applied Physics*, vol. 63, no. 3, pp. 693–703, 1998.

[199] G. Basile, P. Becker, H. Bettin, U. Kuetgens, H. Riemann, and L. Jensen, "The influence of hydrogen and nitrogen on the floating zone growth of ultra-pure crystals," *in preparation*, 2002.

[200] R. Deslattes, E. Kessler, S. Owens, D. Black, and A. Henins, "Just how perfect can a perfect crystal be?," *Journal of Physics D: Applied Physics*, vol. 32, no. 10A, pp. A3–A7, 1999.

[201] T. Tuomi, R. Rantamäki, P. McNally, D. Lowney, A. Danilewsky, and P. Becker, "Dynamical diffraction imaging of voids in nearly perfect silicon," *Journal of Physics D: Applied Physics*, vol. 34, no. 10A, pp. A133–A135, 2001.

[202] K. Nakayama, H. Fujimoto, T. Ishikawa, and H. Takeno, "Silicon molar volume discrepancy: Studies of the nrlm crystal," *IEEE Transactions on Instrumentation and Measurement*, vol. 50, no. 2, pp. 601–603, 2001.

[203] P. Penning and D. Polder, "Anomalous transmission of X-rays in elastically deformed crystals," *Philips Research Reports*, vol. 16, pp. 419–440, 1961.

[204] A. Authier, *Dynamical Theory of X-Ray Diffraction*, p. 314. Oxford Science Publications, 2001.

[205] B. Tanner, *X-ray Diffraction Topography*, pp. 75–77. Oxford Science Publications, 1976.

[206] E. Dunia, C. Malgrange, and J. Petroff, "Determination of the sign of the Burgers vector for nearly screw dislocations. A direct application of x-ray dynamical theory.," *Philosophical Magazine A*, vol. 41, no. 3, pp. 291–306, 1980.

[207] "Status of beamline BW1," *HASYLAB Jahresbericht*, vol. 1, pp. 89–94, 1992.

[208] B. Henke, E. Gullikson, and J. Davis, *X-ray interactions: photoabsorption, scattering, transmission, and reflection at E=50–30000 eV, Z=1–92*, vol. 54 of *Atomic Data and Nuclear Data Tables*, pp. 181–342. 1993.

[209] N. Krylova, W. Möhling, I. Shulpina, and E. Sheikhet, "Visualisation and investigation of microdefects in silicon by x-ray topography," *Soviet Physics of the Solid State*, vol. 28, no. 2, pp. 244–248, 1986.

[210] I. Shulpina, "Microdefects investigated by x-ray topography," *Journal of Physics D: Applied Physics*, vol. 26, no. 4A, pp. A82–A85, 1993.

[211] S. Takagi, "Dynamical theory of diffraction applicable to crystals with any kind of small distortion," *Acta Crystallographica*, vol. 15, pp. 1311–1312, 1962.

[212] http://www.goodfellow.com/static, "Goodfellow catalogue," 2002.

[213] V. Bougrov, M. Levinshtein, S. Rumyantsev, and A. Zubrilov, *Properties of Advanced Semiconductor Materials GaN, AlN, InN, BN, SiC, SiGe*, pp. 1–30. John Wiley & Sons, 2001.

Appendix A

Photoacoustic Cell Working Drawings

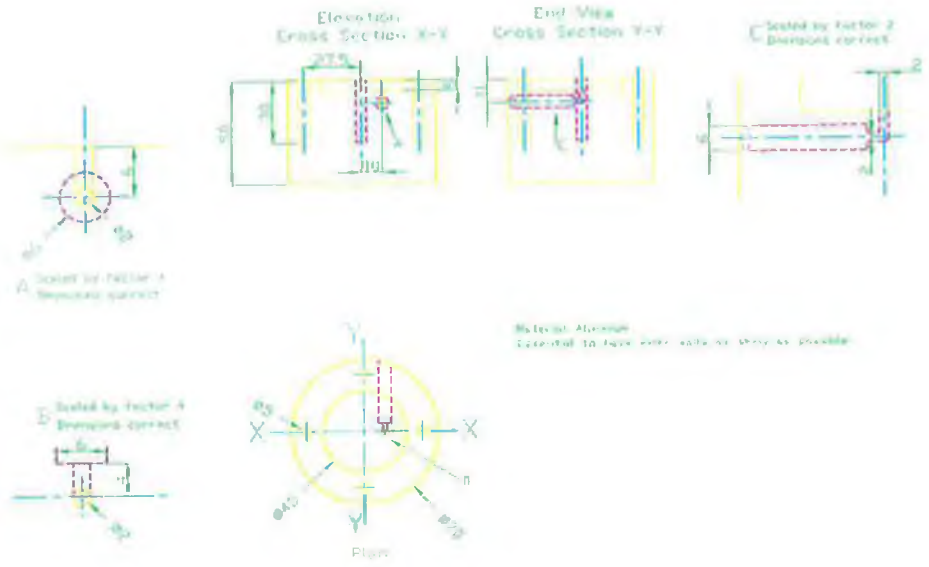

Sample and microphone holder

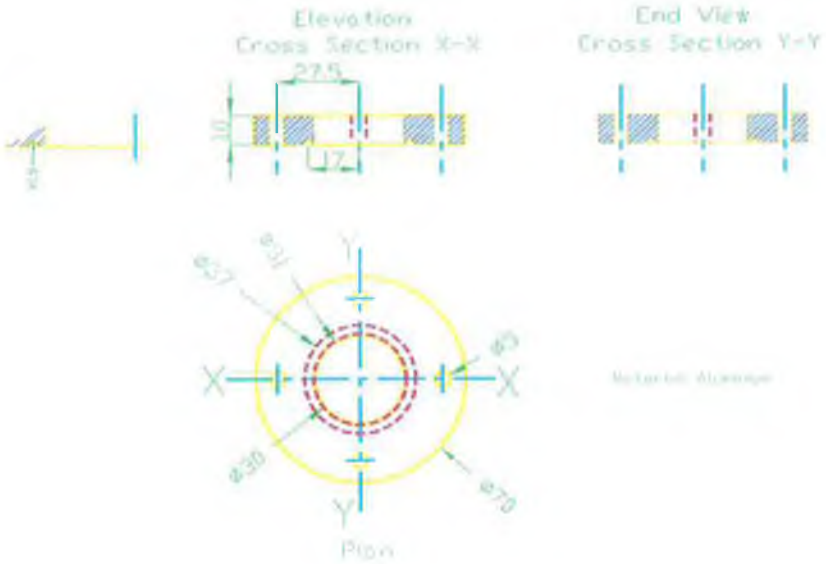

Cell Cover

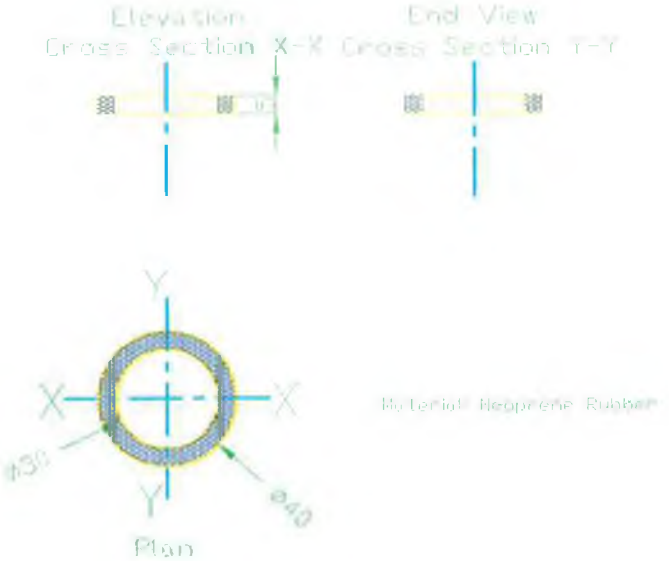

Neoprene cushion

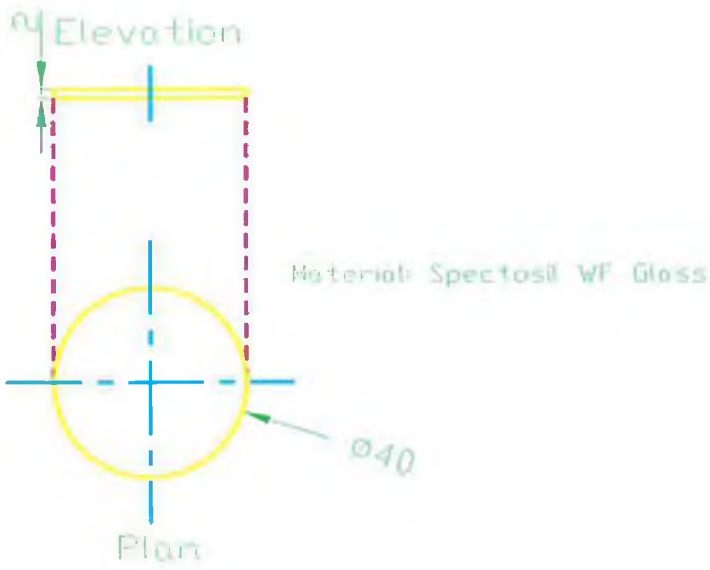

Spectrosil WF Window

Appendix B

Ray Tracing Parameters

Derivation of Δy_{i_1}

The biconcave lens may be considered to be constructed out of two spheres C_1 and C_2, of radii R_1 and R_2 respectively. The point at which the ray from the object hits C_1 and the angle at which it travels through the glass is known. Therefore, simple analytic geometry can be applied to solving the distance traveled by the ray through the lens.

Presume C_1 is located at the origin.

$$C_1 : \qquad x^2 + y^2 = R_1^2 \tag{B.1}$$

Now, in this reference frame C_2 is located at $(R_1 + CT_1 + R_2, 0) \equiv (a, 0)$

$$C_2 : \qquad (x - a)^2 + y^2 = R_2^2 \tag{B.2}$$

The point at which the ray hits C_1 is

$$P_1 : \qquad (x_1, y_1) = (R_1 \cos\alpha_1, R_1 \sin\alpha_1) \tag{B.3}$$

The slope of the ray through the lens is

$$m = \tan\alpha_{t_1} \tag{B.4}$$

Therefore, the equation of the ray through the lens is

$$L_1 : \quad y = \tan\alpha_{t_1} x + R_1 \left(\sin\alpha_1 - \cos\alpha_1 \tan\alpha_{t_1}\right) \tag{B.5}$$

Now

$$c \equiv R_1 \left(\sin\alpha_1 - \cos\alpha_1 \tan\alpha_{t_1}\right) \tag{B.6}$$

The intersection of L_1 with C_2 may be described by the equation

$$L_1 \bigcap C_2 : \qquad \left(m^2 + 1\right) x^2 + (2cm - 2a)\, x + a^2 + c^2 - R_2^2 = 0 \tag{B.7}$$

This quadratic equation in x can now be solved. The point of intersection x_2 should be chosen such that $0 < x_2 < a$. Using Equation (B.5) y_2 can be evaluated. The distance between the points $P_1 = (x_1, y_1)$ and $P_2 = (x_2, y_2)$ can be obtained and

$$\Delta_{y_1} = |P_1 P_2| \sin\alpha_{t_1} \tag{B.8}$$

Derivation of Δy_{i_2}

Suppose the second surface of the biconcave lens C_2 is located at the origin.

$$C_2: \qquad x^2 + y^2 = R_2^2 \tag{B.9}$$

The ray exits the lens at the point

$$P_2: \qquad (x_2, y_2) = (-R_2 \cos\alpha_2, R_2 \sin\alpha_2) \tag{B.10}$$

with slope

$$m = \tan\alpha_{t_2} \tag{B.11}$$

Therefore the equation of the ray between the biconcave and biconvex lens is:

$$L_3: \qquad y = \tan\alpha_{t_2} x + R_2 \left(\sin\alpha_2 + \tan\alpha_{t_2} \cos\alpha_2\right) \tag{B.12}$$

In this reference frame, the biconvex lens will be located at the point

$$\left(d - R_2 + R_3 - \frac{CT_2}{2} - \frac{CT_1}{2}, 0\right) \equiv (a, 0)$$

$$C_3: \qquad (x-a)^2 + y^2 = R_3^2 \tag{B.13}$$

The intersection of L_3 with C_3 may be described by the equation

$$L_3 \bigcap C_3: \qquad \left(m^2+1\right) x^2 + (2cm - 2a)\, x + a^2 + c^2 - R_3^2 = 0 \tag{B.14}$$

This quadratic equation in x can now be solved. The point of intersection x_3 should be chosen such that $0 < x_3 < a$. Using Equation (B.12) y_3 can be evaluated. The distance between the points $P_2 = (x_2, y_2)$ and $P_3 = (x_3, y_3)$ can be obtained and

$$\Delta_{y_1} = |P_2P_3| \sin \alpha_{t_2} \tag{B.15}$$

Derivation of Δy_{i_3}

Suppose the first surface of the biconcave lens C_3 is located at the origin.

$$C_3 : \qquad x^2 + y^2 = R_3^2 \tag{B.16}$$

The ray hits the surface at the point

$$P_3 : \qquad (x_3, y_3) = (-R_3 \cos \alpha_3, R_3 \sin \alpha_3) \tag{B.17}$$

and the slope of the ray through the lens is

$$m = \tan \alpha_{t_3} \tag{B.18}$$

Consequently, the equation of the ray L_4 through the lens is

$$L_4 : \qquad y = \tan \alpha_{t_3} x + R_3 (\sin \alpha_3 + \tan \alpha_{t_3} \cos \alpha_3) \tag{B.19}$$

In this reference frame, the centre of the circle governing the second circle C_4 is located

at

$$(-(R_4 + R_3 - CT_2)) \equiv (-a, 0)$$

$$C_4 : \qquad (x+a)^2 + y^2 = R_4^2 \tag{B.20}$$

The intersection of L_4 with C_4 may be described by the equation

$$L_4 \bigcap C_4 : \qquad \left(m^2+1\right) x^2 + (2cm + 2a)\, x + a^2 + c^2 - R_4^2 = 0 \tag{B.21}$$

This quadratic equation in x can now be solved. The point of intersection x_4 should be chosen such that $x_4 > a$. Using equation (B.19) y_4 can be evaluated. The distance between the points $P_3 = (x_3, y_3)$ and $P_4 = (x_4, y_4)$ can be obtained and

$$\Delta_{y_3} = |P_3 P_4| \sin \alpha_{t_3} \tag{B.22}$$

Derivation of Δy_{i_4}

The lateral distance between the sample and the exit of the ray from the biconvex lens is

$$l = d_s - \frac{CT_2}{2} + R_4 \left(1 - \cos \alpha_4\right) \tag{B.23}$$

$$\Delta y_{i_4} = l \tan \alpha_{t_4} \tag{B.24}$$

Appendix C

Material Parameters

Material	ρ (kg/m^3)	k (W/(m K))	C (J/(kg K))	Data Source
Carbon	2267	160	709	[212]
Silicon	2328	141.2	700	[45]
Gallium Arsenide	5316	455	350	[45]
Gallium Nitride	6150	130	490	[213]

Publications

Refereed Publications

- P.J. McNally, G. Dilliway, J.M. Bonar, A. Willoughby, T. Tuomi, R. Rantamäki, A.N. Danilewsky, and D. Lowney, "Total Reflection X-Ray Topography for the Observation of Misfit Dislocation Strain at the Surface of a Si/Ge-Si Heterostructure", (accepted for publication in *Journal of X-Ray Science and Technology*), 2002.

- P.J. McNally, T. Tuomi, D. Lowney, K. Jacobs, A.N. Danilewsky, R. Rantamäki, M. O'Hare, and L. Considine, "Epitaxial Lateral Overgrowth of GaN on Sapphire – An Examination of Epitaxy Quality Using Synchrotron X-Ray Topography", *Physica Status Solidi (a)*, vol. 185, no. 2, pp. 373–382, 2001.

- W.M. Chen, P.J. McNally, Yu.V. Shvyd'ko, T. Tuomi, M. Lerche, A.N. Danilewsky, J. Kanatharana, D. Lowney, M. O'Hare, L. Knuuttila, J. Riikonen, and R. Rantamäki, "Quality Assessment of Sapphire Wafers for X-Ray Crystal Optics Using White Beam Synchrotron X-Ray Topography", *Physica Status Solidi (a)*, vol. 186, no. 3, pp. 365–371, 2001.

- T. Tuomi, R. Rantamäki, P.J. McNally, D. Lowney, A.N. Danilewsky, P. and Becker, "Dynamical diffraction imaging of voids in nearly perfect silicon", *Journal of Physics D: Applied Physics*, vol. 34, no. 10A, pp. A133–A135, 2001.

- P.J. McNally, R. Rantamäki, T. Tuomi, A.N. Danilewsky, J.W. Curley, P.A.F. Herbert, and D. Lowney, "Mapping of Mechanical, Thermomechanical and Wire-Bond Strain Fields in Packaged Si Integrated Circuits Using Synchrotron White Beam X-Ray Topography", *IEEE Transactions on Components and Packaging Technologies*, vol. 24, pp. 76–83, 2001.

- D. Lowney, P.J. McNally, P.A.F. Herbert, T. Tuomi, R. Ranatamäki, M. Karilahti, M. O'Hare, and A.N. Danilewsky, "Examination of the Structural and Optical Failure of Ultra Bright LEDs under varying degrees of Electrical Stress using Synchrotron X-Ray Topography and Optical Emission Spectroscopy", *Journal of Materials Science: Materials in Electronics*, vol. 12, no. 4/6, pp. 249–253, 2001.

- D. Lowney, P.J. McNally, P.A.F. Herbert, T. Perova, T. Tuomi, R. Rantamäki, M. Karilahti, M. O'Hare, and A.N. Danilewsky, "Failure Analysis of LED Arrays using White Beam Synchrotron X-Ray Topography", in *Proceedings of the* 3^{rd} *International Conference on Materials for Microelectronics,* 16^{th} *to* 17^{th} *October, Dublin Castle, Ireland*, pp. 37–42, 2000.

- M. Nolan, D. Lowney, P.J. McNally, T.S. Perova, A. Moore, H. Gamble, T. Tuomi, R. Rantamäki, and A.N. Danilewsky, "Synchrotron X-Ray Topography and Micro-Raman Spectroscopy of Boron Doped Silicon Wafer Using Rapid Thermal Diffusion", in *Proceedings of the* 3^{rd} *International Conference on Materials for Microelectronics,* 16^{th} *to* 17^{th} *October, Dublin Castle, Ireland*, pp. 147–150, 2000.

- M. O'Hare, P.J. McNally, D. Lowney, T. Tuomi, and R. Rantamäki, "Visualisation and Finite Element Modelling of Strain Fields in Silicon due to Integrated Circuit Metallisation", in *Proceedings of the* 3^{rd} *International Conference on Materials for Microelectronics,* 16^{th} *to* 17^{th} *October, Dublin Castle, Ireland*, pp. 89–92, 2000.

- P.J. McNally, G. Dilliway, J.M. Bonar, A. Willoughby, T. Tuomi, R. Rantamäki, A.N. Danilewsky, and D. Lowney, "Observation of Misfit Dislocation Strain-Induced Surface Features for a Si/Ge-Si Heterostructure Using Total Reflection X-Ray Topography", *Physica Status Solidi (a)*, vol. 180, pp. R1–R3, 2000.

- P.J. McNally, G. Dilliway, J.M. Bonar, A. Willoughby, T. Tuomi, R. Rantamäki, A.N. Danilewsky, and D. Lowney, "On the use of Total Reflection X-Ray Topography for the Observation of Misfit Dislocation Strain at the Surface of a Si/Si-Ge Heterostructure", *Applied Physics Letters*, vol. 77, no. 11, pp. 1644–1646, 2000.

- P.J. McNally, T. Tuomi, R. Rantamäki, K. Jacobs, L. Considine, M. O'Hare, D. Lowney, and A.N. Danilewsky, "Synchrotron X-Ray topography studies of epitaxial lateral overgrowth of GaN on sapphire", in *Wide-Bandgap Semiconductors for High-Power, High-Frequency and High-Temperature Applications*, (Binari, S. and Burk, A. and Melloch, M. and Nguyen, C. eds.), vol. 572, pp. 327–332, Materials Research Society, 1999.

Unrefereed Publications

- W.M Chen, P.J. McNally, K. Jacbos, T. Tuomi, A.N. Danilewsky, D. Lowney, J. Kanatharana, L. Knuuttila, and J. Riikonen, "Wing tilt features in white beam synchrotron X-ray topographs of epitaxial lateral overgrown GaN", *HASYLAB Jahresbericht*, pp. 865–866, 2001.
- T. Tuomi, P.J. McNally, D. Lowney, and P. Becker, "Diffraction imaging of microdefects in Czochralski silicon", *HASYLAB Jahresbericht*, pp. 835–836, 2001.
- T. Tuomi, P. Pohjola, J. Riikonen, L. Knuuttila, M. Sopanen, P.J. McNally, J. Kanatharana, W. Chen, D. Lowney, and A.N. Danilewsky, "Defects in GaInAs quantum dot layers", *HASYLAB Jahresbericht*, pp. 851–852, 2000.
- T. Tuomi, R. Rantamäki, P.J. McNally, D. Lowney, A.N. Danilewsky, and P. Becker, "Dynamical Diffraction Imaging of Voids in Exteremely Pure and Perfect Silicon", *HASYLAB Jahresbericht*, pp. 857–858, 2000.
- J. Riikonen, L. Knuuttila, T. Tuomi, H. Lipsanen, P.J. McNally, J. Kanatharana, W. Chen, D. Lowney, and A.N. Danilewsky, "Epitaxial growth of GaAs on silicon-on-insulator", *HASYLAB Jahresbericht*, pp. 859–860, 2000.
- J. Toivonen, T. Tuomi, J. Riikonen, L. Knuuttila, R. Rantamäki, M. Sopanen, H. Lipsanen, P.J. McNally, J. Kanatharana, W. Chen, and D. Lowney, "Growth and Defects of GaAsN layers on GaAs", *HASYLAB Jahresberict*, pp. 861–862, 2000.
- D. Lowney, P.J. McNally, M. O'Hare, T. Herbert, T. Tuomi, R. Rantamäki, and A.N. Danilewsky, "Structural and Optical Failure Mechanisms of IC LEDs", *HASYLAB Jahresbericht*, pp. 879–880, 2000.
- W.M. Chen, P.J. McNally, Yu.V. Shvyd'ko, M. Lerche, T. Tuomi, A.N. Danilewsky, J. Kanatharana, D. Lowney, M. O'Hare, L. Knuuttila, J. Riikonen, R. Rantamäki, "SXRT Evaluation of Sapphire Wafer Quality Used for Bragg Backscattering Mirrors", *HASYLAB Jahresbericht*, pp. 887–888, 2000.
- A.N. Danilewsky, M. Fiederle, T. Feltgen, K.W. Benz, P.J. McNally, D. Lowney, M. O'Hare, R. Rantamäki, and T. Tuomi, "White Beam Back Reflection Topography of CdTe", *HASYLAB Jahresbericht*, pp. 893–894, 2000.
- J. Kanatharana, P.J. McNally, J.J. Pérez-Camacho, T. Tuomi, A.N. Danilewsky, M. O'Hare, D. Lowney, and W. Chen, "White Beam Synchrotron X-Ray Topography Studies of Pb/Sn Ball Grid Array Induced Srain in Si Substrate", *HASYLAB Jahresbericht*, pp. 895–896, 2000.
- D. Lowney, B. Adams, H. Franz, and P.J. McNally, "Characterisation of Diamond Crystals for use at the PETRA Beamline", *HASYLAB Jahresbericht*, pp. 989–990, 2000.

- D. Lowney, P.J. McNally, M. Nolan, T. Perova, T. Tuomi, R. Rantamäki, and A.N. Danilewsky, "X-Ray Topography Studies of Dislocation Distributions in Si during Proximity Rapid Thermal Diffusion", *HASYLAB Jahresbericht*, pp. 915–917, 1999.

- P.J. McNally, D. Lowney, T. Herbert, M. O'Hare, T. Tuomi, R. Rantamäki, and A.N. Danilewsky, "Synchrotron X-Ray Topography Studies of LED Array Failure", *HASYLAB Jahresbericht*, pp. 911–913, 1999.

Index

REFERENC